ABSTRACT

Title of Dissertation: COLLECTIVE DYNAMICS OF ATOMS COUPLED TO AN OPTICAL NANOFIBER: FROM DISORDERED ENSEMBLES TO TUNABLE ARRAYS

Ahreum Lee
Doctor of Philosophy, 2025

Dissertation Directed by: Professor Steven Rolston
Department of Physics

Quantum emitters coupled to a nanophotonic waveguide have revolutionized quantum science and technology by enabling engineered light-matter interactions. In particular, a system of neutral atoms coupled to an optical nanofiber (ONF) offers a unique platform for quantum optics and quantum computation, as it integrates two well-established technologies: neutral atoms with high-fidelity control and optical fibers with low-loss light propagation. This thesis presents a study of the collective dynamics of ^{85}Rb atoms coupled to an ONF, with a focus on the atomic spatial distribution.

We first present the collective dynamics of V-type multilevel quantum emitters, emphasizing the interaction between multiple excited states and multiple atoms mediated by a common electromagnetic (EM) field mode. Remarkably, we observe quantum beats even in the absence of an initial superposition in the excited states, which arises from vacuum-induced coupling between the excited levels. Although such second-order processes are typically weak, they can

become observable through collective enhancement. We theoretically investigate these collective quantum beats in an extended system of V-type atoms coupled to a waveguide and identify a characteristic length scale that governs the interference in the multi-atom, multi-level emission.

Then, we describe our efforts to observe long-range interaction between macroscopically separated atomic clouds via an optical fiber. We develop a theoretical framework for modeling resonant scattering of an atomic ensemble placed in front of a mirror in the waveguide quantum electrodynamics (QED) setup. We identify the competition of two parameters that govern the scattering process: the drive strength and the strength of time-delayed feedback. Our intensity correlation measurement shows that an atomic cloud coupled to an ONF operates in the independent emission regime, where time-delayed feedback is negligible. This work highlights the need for an ordered atomic array with a lattice constant commensurate with the transition wavelength to collectively enhance cooperativity.

In the final chapter, we present a novel method for creating a tunable-spacing atomic array interfaced with an ONF using a set of binary phase transmission gratings. The optical setup and preliminary results on atom trapping within the lattice are described. Our approach opens the door to high-cooperativity neutral-atom-nanofiber interfaces, paving the way for advances in quantum optics and quantum technology.

COLLECTIVE DYNAMICS OF ATOMS COUPLED TO AN OPTICAL NANOFIBER: FROM DISORDERED ENSEMBLES TO TUNABLE ARRAYS

by

Ahreum Lee

Dissertation submitted to the Faculty of the Graduate School of the
University of Maryland, College Park in partial fulfillment
of the requirements for the degree of
Doctor of Philosophy
2025

Advisory Committee:
Professor Steven L. Rolston, Chair/Advisor
Dr. Fredrik K. Fatemi, Co-Chair/Co-Advisor
Professor Alicia J. Kollár
Professor Nathan Schine
Professor Thomas E. Murphy, Dean's Representative

To my dad, for the love and belief he always placed in me

Acknowledgments

This work would not have been possible without the incredible people who supported me in more ways than one.

I am deeply grateful to my two PIs, Steve Rolston and Fredrik Fatemi. Steve has been an exceptionally patient advisor, accepting my slow progress and mistakes, and giving me the space to explore detours. I have always enjoyed our discussions; I was often impressed by the simple and intuitive picture he used to explain complicated concepts in physics, and my research has greatly benefited from that. Fredrik brought a wealth of knowledge and sharp questions that led to many breakthroughs. I still remember one lab meeting when, after a long discussion, we all left smiling, satisfied and knowing exactly what steps to take next. My graduate research essentially grew out of that moment, and I am grateful to have learned how to move forward as a team.

I am truly grateful to Kanu Sinha, my former senior lab member and current theory collaborator at the University of Arizona. She generously guided me through the foundational theoretical tools of quantum electrodynamics and open quantum systems, and always made time for detailed discussions whenever I needed help with calculations. Beyond her intellectual support, she has been a remarkable mentor, sharing her research experience and communication skills with great generosity. She has also been a wonderful friend, encouraging me whenever I felt uncertain about myself as a researcher.

I can't thank Hyok enough. I was incredibly lucky to learn not only the subtle know-how of

experimental techniques (including the art of screwing), but also his deep and creative reflections on many physics problems. The dad jokes and snacks we shared during long experimental runs are some of the most memorable parts of my graduate life. I am also grateful to Sarthak for our collaboration on the lattice project. He also generously shared advice and insights about both career and life, and introduced me to the exciting world of photonics.

I am grateful to Alicia, Nathan, Trey, Gretchen, and Ian for their guidance at the JQI AMO group meetings. I was extremely fortunate to be a part of such a supportive environment, where we could share our research, discuss technical details, and learn from each other. I also sincerely thank Professor Tom Murphy for generously serving on my thesis committee. I would also like to thank Elizabeth Goldschmidt and Peter Zoller for discussions on non-Markovian correlation functions, and William Phillips, Pablo Solano, Hadiseh Alaeina, and Chen-Lung Hung for insightful conversations on a variety of topics. Thank you so much, Alessandro, for always so cheerfully guiding me through electronics and 3D printing projects. I appreciate Melissa and Josiland for their consistently efficient and warm administrative support.

I owe deep gratitude to the many friends who supported me mentally and emotionally throughout my graduate studies. Thank you so much, Deniz—we began our research journey together on day one, and now we are finishing it side by side. Thank you for being such a wonderful cohort, sharing both struggles and joys along the way. In that same spirit, I also thank Patrick and Yaxin, who stopped by my office (even though you mostly came to visit Deniz) and brought laughter and much-needed breaks to my days. I am thankful to my fellow JQI members, from whom I gained a broader perspective and borrowed experimental equipment: Madi, Peter, Ananya, Yingyue, Nhung, Yuxin, Kevin, Oliver, Yanda, Sarah, Tim, Kayla, Martin, Maya, Kellen, Zhiyin, and Won. I also deeply appreciate the warm interactions with friends I met

at UMD: Jiashen, Yihui, Jason, Kavic, Deric, Sam, Musa, Ben, Jiyeon, Srielkha, Raquel, Gui, Eunji, Hyunwoo, Donghee, Rahul, Khoi, Max, Prajit, Juhyeong, Daeun, Nayeon, and Seongeun. I am grateful to the members of Key Community Church and Diaspora Church for spiritual support and fellowship. Thank you, Kyounghun, for continuously checking in on how I was doing and for sharing what the world is like out there - you were like my personal social network service. Thank you, Donghun, Erica, Sungha, Hyunheung, and Seoyeon, for making College Park feel like my hometown. Thank you, Sara, for the invaluable friendship we shared in God. Thank you, Nayeon and Sunyoung, for your kindness and the fun we shared together. I am also deeply grateful for the support of my friends from Korea. Thank you, Hyunsu and Yeogyeong, for consistently checking in on me and encouraging me. Thank you, Yongjin, Minkyung, Chanoh, Seokyoung, Junseok, and Gaeun - I am thankful for your constant care and all your prayers. Minhee, I'm so grateful that we went through our twenties together and are now both facing major life changes. I cherish our non-decaying, long-range friendship.

Thank you, Mom, for your endless love and warm hugs. Those were the fuel that sustained me throughout my life abroad. Looking back, I now realize how courageous it was for you to let me go. I am always grateful for your understanding and unwavering support. Thank you, my brother, for your constant support. As my connection to Korea has grown weaker, I've often had to rely on you for administrative tasks. Thank you for always helping me so willingly.

Lastly, I thank God in all these matters (and light).

Table of Contents

List of Tables

List of Figures

List of Abbreviations

AOM	Acousto-optic modulator
APD	Avalanche photodiode
AR	anti-reflection
BB	beam block
BIC	bound states in the continuum
BOP	bipolar operational power supply/amplifier (product of Kepco Inc.)
CAS	Chemical Abstracts Service
CCD	charge-coupled device
CF	conflat
DAC	digital-to-analog converter
DDS	direct digital synthesizer
ECDL	extra-cavity diode laser
EM	electromagnetic
emf	electromotive force
FET	field-effect transistor
FFT	fast Fourier transform
HWP	half waveplate
LD	laser diode
MOSFET	metal–oxide–semiconductor field-effect transistor
MOT	Magneto-optical trap
NA	numerical aperture
NI	National Instruments
NIM	Nuclear Instrumentation Module
NIR	near-infrared
OBE	optical Bloch equation

OD	optical depth (OD $= -\ln$ T, where T is the transmission)
ONF	optical nanofiber
Op-amp	operational amplifier
PBS	polarizing beam splitter
PCI	Peripheral Component Interconnect
PCL	plano-convex lens
PD	photodiode
PGC	polarization gradient cooling
PM fiber	polarization maintaining fiber
QED	quantum electrodynamics
QWP	quarter waveplate
Rb	rubidium
SAS	saturated absorption spectroscopy
SM	single-mode
SOM	semiconductor optical modulator
SPCM	single photon counting module
TOF	time of flight
TPA	tapered amplifier
TTL	Transistor-Transistor Logic
UHV	ultra-high vacuum
VBG	volume Bragg grating

Chapter 1: Introduction

The atom-light interaction lies at the heart of the revolution of quantum science and technology [1, 2]. It has long served as a testbed for quantum theories, with examples ranging from the observation of antibunched photons [3, 4], squeezed photons [5], and violation of Bell's inequality [6]. Later on, atom-light interaction has begun to be regarded as a promising platform for a new kind of information processing-quantum computation [7–11]. Atoms provide stationary systems that can store quantum states for a long time, while photons propagate through space carrying quantum states with minimal environmental disturbance. Thus, controlling and engineering interaction between single atoms and single photons have become increasingly critical for the advancement of quantum technologies.

Realistically, atoms and photons exist in an open system, where both atomic and field excitations dissipate into the surrounding bath, gradually losing their ability to participate in coherent interactions. In this context, the atom-light interaction has an appreciable impact only when it is strong enough, so that the interaction rate exceeds the decay rate of the individual quantum systems. In free space, coherent atom-light interaction has been implemented by tightly focusing light using a high-NA optical system [12–15] or interfacing weakly focused light with a large number of atoms [9, 16]. However, achieving strong interaction between single atoms and photons, as well as engineering photon-mediated interactions between atoms, is limited in free

space, as diffraction limits the size of the minimum focal spot of a Gaussian light [17–19] and causes a focused beam to diverge quickly.

In an effort to engineer atom-light interactions in a more useful way, cavity quantum electrodynamics (QED) [20] and waveguide QED [21–23] have been widely employed. In cavity QED, photon travels multiple times before it escapes the cavity, increasing the chance to interact with the atom in the cavity. In waveguide QED, the light is tightly confined along the waveguide, increasing its mode overlap with the quantum emitters. Both schemes offer a way to interface atoms to a photonic environment with high efficiency, opening a pathway to quantum computation [24, 25] and quantum networks [26–28].

In this thesis, we focus on a unique waveguide QED system: neutral atoms coupled to an optical nanofiber (ONF). The ONF enables direct integration of the neutral atom system into an optical fiber network with low transmission loss [29], making it an ideal platform for quantum networking and distributed quantum computing [8, 26–28, 30]. Our study investigates the interaction of a photon in the ONF guided mode and a collection of atoms, whose distribution spans from a disordered ensemble to an ordered array.

1.1 Cooperativity

In achieving a strong atom-light interaction, the figure of merit is the cooperativity parameter. Historically, the term cooperativity was first invented in the context of cavity QED, where the interaction of confined single atoms and photons was considered [20, 31, 32]. The cooperativity

is defined as

$$C = \frac{4g^2}{\kappa\Gamma}, \tag{1.1}$$

where $2g$ is the vacuum Rabi splitting, which signifies the interaction strength between the atom and the cavity field mode, and κ and Γ are the dissipative rates of the photon and the atom, respectively. The cooperativity compares the atom-photon energy exchange rate to the geometric mean of the energy loss rates of the atomic and photonic systems to the surrounding bath. The interaction strength between an atom and a cavity field mode, g, is given by

$$g = d\sqrt{\frac{\omega_0}{2\varepsilon_0\hbar V}}, \tag{1.2}$$

where d is the atomic transition dipole moment, ω_0 is the angular transition frequency, ε_0 is the vacuum permittivity, $\hbar$ is the reduced Plank constant, and V is the cavity mode volume. The cavity linewidth κ is

$$\kappa = \frac{Tc}{L}, \tag{1.3}$$

where T is the transmission of the lossless mirrors forming the cavity, c is the speed of light, and L is the cavity length. The atomic decay rate is

$$\Gamma = \frac{d^2\omega_0^3}{3\pi\varepsilon_0\hbar c^3}. \tag{1.4}$$

The cooperativity can be collectively enhanced. When N atoms couple to the same EM

field mode of the cavity, the cooperativity is enhanced in proportion with N:

$$C^{(N)} = NC. \tag{1.5}$$

Note that the spatial distribution of atoms and their initial phases are important in collectively enhancing the total cooperativity; the atoms must be constructively coupled to the field mode of interest.

Cooperativity is a purely geometrical factor related to the overlap of the atomic scattering cross section and the field mode area [32]. Putting in Eqs. (1.2), (1.3), and (1.4) into Eq. (1.1), we can express the cooperativity in terms of the geometrical parameters:

$$C = \frac{A_{\text{atom}}}{A_{\text{field}}} \frac{1}{T}. \tag{1.6}$$

Here, $A_{\text{atom}} = \sigma_0 = 3\lambda_0^2/(2\pi)$ is the resonant atomic scattering cross section with λ_0 the transition wavelength, and $A_{\text{field}} = V/L = \pi w^2/4$ is the effective field mode area with w the beam waist of the field mode at the position of the atom. Note that an atom positioned at the antinode of the cavity is considered here, thus the effective field mode area is decreased by a factor of 4 considering intensity concentration at antinodes [32]. Eq. (1.6) indicates that the single-atom cooperativity in cavity QED can be regarded as the geometrical overlap of the atomic and field mode areas multiplied by the number of photon roundtrips before it escapes the cavity.

In this geometrical framework, the cooperativity in free space and waveguide QED can be

written as

$$C = \frac{A_{\text{atom}}}{A_{\text{field}}}, \tag{1.7}$$

where $T = 1$ accounts the fact that there is no mirror. Indeed, it has been independently shown that the efficiency of interaction between an atom and a free-space light is determined by the spatial overlap of incident light and atomic dipole radiation pattern, a purely geometrical factor [19, 32].

In waveguide QED, the atom-light strength is typically quantified by the coupling efficiency, which is defined as

$$\beta = \frac{\Gamma_{\text{1D}}}{\Gamma_{\text{rad}} + \Gamma_{\text{1D}}}, \tag{1.8}$$

where Γ_{1D} is the radiative decay rate into the guided modes, and Γ_{rad} is the decay rate into the rest of the free-space modes. Note that the total decay rate $\Gamma_{\text{rad}} + \Gamma_{\text{1D}}$ is different from the decay rate of an atom in the free space, as the waveguide modifies the vacuum mode structure by imposing boundary conditions. The coupling efficiency is connected to the cooperativity parameter by the relation [33]

$$C = \frac{\beta}{1 - \beta}. \tag{1.9}$$

The above equation follows the same intuition as in Eq. (1.1): β represents the amount of interaction between the atom and the guided field mode, and 1-β the amount of incoherent decay to the free-space modes.

1.2 Waveguide QED

Waveguide QED has been widely used to achieve strong atom-light interactions and photon-mediated interactions between multiple atoms [21–23]. In this approach, quantum emitters are coupled to optical waveguides, enabling the use of a vast amount of technologies developed for modern optical communication systems [34–36]. The versatility offered by waveguide QED has attracted significant interest for quantum optics and quantum information research [8, 26–28, 30, 37–39].

Nanophotonic waveguides modify the vacuum mode structure in such a way that quantum emitters can be efficiently interfaced to the guided optical modes. Strong coupling between emitters and guided modes has been demonstrated in various platforms, including atoms coupled to photonic crystals [40–42] or hollow-core photonic crystal fibers [43, 44], quantum dots imbedded in nanowires [10, 45–49], color centers in diamond waveguides [50–52], and superconducting qubits coupled to microwave transmission lines [53, 54].

Beyond strongly coupling single atoms and photons, guided light also naturally facilitates collective dynamics of quantum emitters by providing a shared photonic environment. Collective dynamics mediated by guided modes have been demonstrated across several platforms, including neutral atoms coupled to an optical nanofibers (ONFs) [55] or photonic crystal waveguides [41, 42], and superconducting qubits coupled to transmission lines [54, 56–59]. These collective effects can also lead to novel optomechanical phenomena, such as self-organization of atoms coupled to a nanophotonic waveguide [60, 61].

Importantly, the collective modes can be exploited to enhance the cooperativity, as briefly discussed in Eq. (1.5). However, care must be taken to ensure that the atomic emissions inter-

fere constructively to achieve collective enhancement of cooperativity. If atoms are randomly distributed relative to the EM field mode of interest, their emissions will not exhibit coherent build-up. In contrast, for a regularly spaced atomic array, atoms can collectively couple to a specific scattering mode that has a specific angle relative to the axis of the atomic array. To interface such an array efficiently with a waveguide, one must ensure that the direction of constructive scattering aligns with the guided mode. The collective dynamics in waveguide QED will be discussed in detail in Sec. 1.4.

The one-dimensional nature of guided modes further enables photons to propagate over long distances with minimal loss, allowing for long-range atom-atom interactions [55, 62, 63]. These long-range interactions enable exploration beyond standard assumptions in atom-light interaction, such as the dipole approximation or Markovian approximations. One striking example of the breakdown of dipole approximation is the "giant atom", where a quantum emitter is coupled to a waveguide at multiple points spaced comparably to the resonant wavelength [64, 65]. In this case, the emitter cannot be approximated as a point-like object, as it experiences different optical phases simultaneously. An example of breaking the Markovian approximation is delay-induced non-Markovian dynamics in delocalized emitters coupled to a waveguide [66–70]. In scenarios where emitters couple to multiple locations along a waveguide separated by distances comparable to the coherence length, they experience coherent time-delayed feedback from their past emissions. Such time-delayed feedback introduces memory effects into the emitter dynamics, leading to a breakdown of the Markovian approximation. Since non-Markovian dynamics falls within the scope of this thesis, it is discussed in detail in Sec. 1.5.

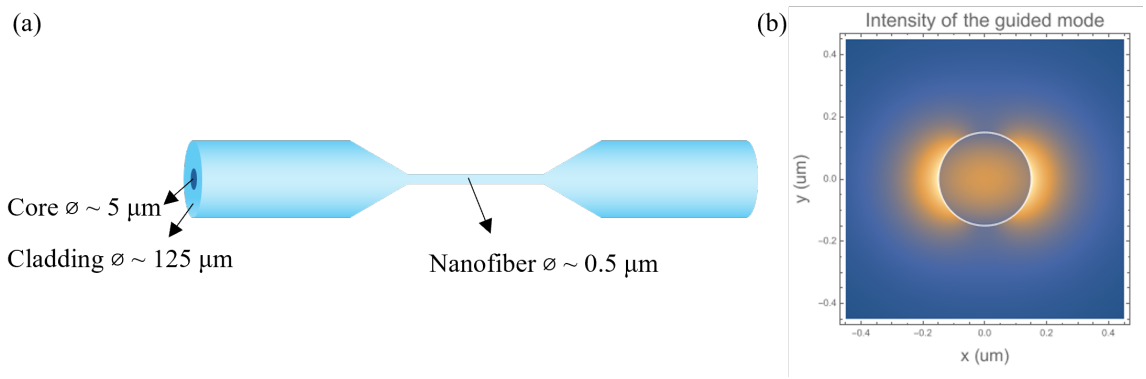

Figure 1.1: (a) Diagram showing geometry of an optical nanofiber (ONF) pulled from a conventional fiber. A typical single-mode fiber has core of diameter ~ 5 μm and cladding of diameter ~ 125 μm. An ONF has diameter $\lesssim 0.5$ μm. (b) A typical guided mode profile showing substantial amount of power being guided outside the fiber.

1.3 Neutral Atoms coupled to an ONF

We consider a unique system of waveguide QED: neutral atoms coupled to an optical nanofiber (ONF) [71–75]. Figure 1.1 (a) illustrates the geometry of an ONF in comparison to the conventional fibers. Conventional near-infrared (NIR) single-mode fibers have a core of diameter $\sim$5 μm and a cladding of diameter $\sim$125 μm. On the other hand, the ONF diameter is typically $\lesssim$500 nm. The sub-wavelength structure allows a significant amount of power to be guided outside the fiber, as shown in Fig. 1.1 (b). A detailed calculation of the guided mode profile is discussed in Appendix A. The evanescent mode can be mode-overlapped with atoms trapped in the vicinity, allowing efficient interfacing of atoms to the fiber modes [76–85].

ONF can be pulled from a commercial optical fiber using a heat-and-pull method using various heat sources including a pure flame [29, 86–89], CO_2 laser [90], ceramic heater [91], and electric strip heater [92]. The glass forms a uniform and smooth surface when it is melted. Thus, the ONF surface smoothness is at the atomic level, and recent measurement shows that the axes length difference of an ONF is within $\sim$ 1 Ångström [93]. The transmission is gov-

erned by the adiabatic transfer of the fiber core mode to the ONF mode, which can be precisely controlled using localized heating techniques [87, 94, 95]. ONFs can be readily fabricated with ultrahigh transmission to conventional optical fibers [29]. Therefore, the atom-ONF interface efficiently integrates neutral atoms into an optical fiber network. This allows scaling up mid-sized, high-fidelity quantum computation with neutral atoms [11, 96, 97] by connecting multiple such quantum systems via optical fibers [28, 80, 85, 98–100].

The ONFs are tapered so thin that the conventional fiber core vanishes, leaving the original cladding to serve as the core of the ONF, and the surrounding vacuum to serve as the cladding. This vacuum-clad structure results in a huge refractive index contrast between the silica core ($n \sim 1.45$) and the vacuum-clad ($n \sim 1$), resulting in strong guiding. The guided mode in the ONF is tightly confined around the core and exhibits a large transverse evanescent field gradient. Such a large field gradient leads to rich physics, including chiral coupling [61, 101–103] and quadrupole transitions with small power [104]. Furthermore, high intensities resulting from strong confinement enable the study of nonlinear processes with small injection powers [105–107].

As the atoms couple to the guided mode evanescently, its coupling efficiency is typically a few percent [76, 77]. However, the ONF can easily host thousands of atoms, opening the possibility to collectively enhance the cooperativity to reach the strong coupling regime [33, 81, 82, 108, 109]. Collective effects such as Bragg reflection [108, 110, 111] and superradiant emission [55, 109, 112], have been investigated in atomic arrays coupled to an ONF.

1.4 Collective Dynamics in Waveguide QED

In 1954, Dicke theoretically demonstrated that spontaneous decay of an atom can be modified by the presence of other atoms [113]. Depending on the initial symmetry in the superposition state, the decay rate of the atom can be either enhanced ("superradiance") or suppressed ("subrdiance"). Since Dicke's pioneering work on collective effects in spontaneous radiaion, it has been central to much quantum optics research [114]. Although Dicke considered a set of co-located atoms when he first predicted such phenomena, it has been demonstrated that the extended systems exhibit more rich interference effects, and that the spatial distribution of the atoms is critical in determining the properties of the collective dynamics [115–117]. With precise spatial arrangement, the dissipative and dispersive couplings between emitters could be fully engineered [54, 57, 59, 118, 119]. Superradiance has been used in the development of narrow-linewidth lasers [120] and in the study of phase transitions [121–123]. Subradiant states are particularly valuable in quantum technologies, as they can be used to protect quantum systems from decoherence due to the coupling to environment [58, 119]. Superradiance and subradiance have been observed in various systems, including atomic clouds [55, 124–126], atoms coupled to photonic crystal waveguides [42], trapped ions [118, 127], quantum dots [128, 129], and superconducting qubits [54, 56–59].

Dimensionality typically plays a significant role in determining the collective behavior. Depending on the dimension of the space, the Green's function, which represents the structure and scaling of the atomic interactions, is modified. Collective dynamics of atoms in one-dimensional space offers a rich and diverse set of physical phenomena, as atoms exhibit long-range interactions [21, 130, 131]. These one-dimensional collective effects can be directly explored in waveg-

uide QED setups. Discussions on collective dynamics in two- and three-dimensional spaces can be found in [132–134].

The critical parameter in determining the collective decay modes in one-dimensional systems is the atomic distribution, as it sets the phase-matching conditions for constructive and destructive interference in the decay process. For a randomly distributed ensemble coupled to a waveguide, the collective modes are typically blurred [135], resulting in a mixture of superradiant and subradiant contributions [55]. However, There is a special EM field mode that is ensured to strongly couple to randomly distributed atoms: the forward scattering mode, which aligns with the propagation direction of the driving laser [115–117]. In this direction, the phases imprinted on the atomic dipoles by the drive field are exactly compensated by the propagation phase of the photon traveling between the atoms, leading to constructive interference and enhanced scattering. Thus, the emission in the forward direction always exhibits collectively enhanced decay rates, and such modes have been observed in waveguide QED systems [109, 112, 136, 137]. For detailed discussions on the collective modes of randomly distributed ensembles, see Appendix B.1.

For ordered arrays of atoms coupled to a waveguide, the collective dynamics becomes richer, as the scattering from each atom can build up. In this case, the interatomic distance d relative to the resonant wavelength λ_0 plays a crucial role in determining the collective behavior. In the dilute regime ($d \gg \lambda_0$), the atoms interact primarily via the guided mode only, and the interaction via free space modes is negligible [33, 56, 110, 130, 131]. In this regime, the atom-atom interaction is mediated solely by the one-dimensional Green's function $G = e^{ik|z_j - z_l|}$, where k is the wave vector of the guided mode and z_j denotes the position of the j-th atom. Consequently, the collective dynamics of the atomic array depends on the lattice constant modulo the transition wavelength. In particular, when the interatomic spacing satisfies $d = n\lambda_0$ (with n an integer),

the atoms couple coherently to the guided mode, leading to collectively enhanced coupling efficiency [33]. The calculation of collective modes of ordered arrays of atoms interacting via the guided mode only is described in Appendix B.2.

As atoms are brought closer together, their interactions can be mediated by both free-space and guided modes [138–141]. In such case, it is helpful to first consider the collective modes of a linear array of atoms in free space [117, 130, 139, 141–143]. There are two resonance involved in such systems: resonance of the periodic structure in the atomic arrangement, and the internal transition resonance of the constituent emitters. We first consider the resonance arising from the periodic structure in spirit of solid-state physics. The collective mode of an infinite chain of an atomic array along z-axis can be depicted as a spin wave with a quasi-momentum k_z [140]:

$$|\Psi\rangle \sim \sum_j e^{ik_z z_j} \hat{\sigma}_j^+ |gg\cdots g\rangle \,, \tag{1.10}$$

where $\hat{\sigma}_j^+$ is the raising operator for the j-th atom and $|gg\cdots g\rangle$ is the state where all the atoms are in the ground state. Note that this quasi-momentum is defined in the first Brillouin zone ($-\pi/d < k_z < \pi/d$). We now consider a resonant emission process of the constituent atoms. The atoms are two-level system with transition wavelength λ_0 with the corresponding wave vector $k_0 = 2\pi/\lambda_0$. For these atoms to emit collectively, the quasi-momentum k_z and the corresponding transverse quasi-momentum $k_\perp$ should satisfy the following wave equation:

$$k_z^2 + k_\perp^2 = k_0^2. \tag{1.11}$$

When the momentum of the spin wave is smaller than the momentum of the resonantly emitted

photon, i.e., $k_z < k_0$, the condition in Eq. (1.11) leads to a real value of $k_\perp$. Therefore, the atoms can collectively radiate into free space. Suppose now the spin wave has a larger momentum than the spontaneously emitted photon, i.e., $k_z > k_0$. In that case, the transverse mode $k_\perp$ should be imaginary, indicating that the corresponding collective mode decays evanescently in the transverse direction. Therefore, such modes are guided along the atomic chain and decoupled from the free space radiative modes. Recall that the maximum value of k_z is π/d in the first Brillouin zone. Therefore, when the atoms are distant, i.e., $d > \lambda_0/2$, the quasi-momentum k_z is always smaller than the resonant frequency k_0 within the first Brillouin zone. In such a case, collective modes are always radiative to free space to some degree. As the atoms enter a sub-diffraction regime, i.e., $d < \lambda_0/2$, the quasi-momentum k_z crosses the light line $k_z = k_0$ within the first Brillouin zone, and subradiant, guided modes arise [139, 140]. These subradiant modes can be thought as spin waves that have a larger spatial frequency than the resonant spatial frequency k_0.

Now consider placing a nanophotonic dielectric waveguide parallel to the atomic chain. Such a system can be analyzed either by adding additional interaction channels between atoms [140, 141], or equivalently, by considering the polaritonic modes between the atomic chain states and the guided mode [139]. A key feature of this setup is that the subradiant states with quasi-momentum $k_z > k_0$ can be radiant with respect to the dielectric waveguide modes. Dielectric waveguides possess higher refractive index for guiding using total internal reflection. Therefore, the resonant wave vector k_0 is enhanced inside the waveguide medium. This enables "selective radiance", where an atomic array is completely decoupled from all radiative modes except the guided mode of a nanophotonic waveguide [140].

1.5 Non-Markovian Dynamics

Waveguide QED enables long-range interactions between emitters through guided photons. This raises a natural question: what happens to collective emission when the atoms are separated by distances so large that a photon emitted from one atom reaches another only after the atoms have already significantly decayed? Such a scenario enters a new regime characterized by non-Markovian dynamics, where memory effects become significant [144–146]. In the typical treatment of open quantum system dynamics, a Markovian approximation is employed, where the system is assumed to interact with the same state of the bath at all times. Therefore, the system evolution depends only on its instantaneous state, and it does not remember any past time evolution. The essential requirement for making such an approximation is that any correlations in the bath decay much faster than the system relaxation time scale. The non-Markovian regime is where this approximation is not valid. The bath retains information of the past states of the system, and thus the system experiences memory effects. Non-Markovian processes typically exhibit the revival of quantum properties such as coherence or correlations [69, 147]. The rich physics in non-Markovian processes can be leveraged to create intricate quantum states [38, 39] and quantum information protocols [148] that are otherwise inaccessible in Markovian processes.

We consider non-Markovian dynamics in a waveguide QED setup, where two distant emitters couple to the guided mode. To understand the non-Markovianity originating from time-delayed interactions between two emitters, one can compare the system relaxation time scale $\tau_R \sim 1/\Gamma$ with the time scale associated with the bath $\tau_B \sim d/v$ to bring information back to the delocalized system. The Markov approximation is no longer valid when τ_B becomes comparable

to τ_R:

$$\tau_B/\tau_R \gtrsim 1 \implies \Gamma d/v \gtrsim 1. \tag{1.12}$$

The above condition illustrates different origins of non-Markovian dynamics in this scenario: 1) delocalized systems (large d), 2) slow bath modes such as the modes near the band gap (small v), and 3) strong coupling (large Γ). In this thesis, we focus on the first case where the emitters are macroscopically separated. The non-Markovian dynamics in separated emitters has been studied theoretically in the model system of two emitters coupled to a waveguide [66–70] or a single emitter placed in front of a mirror [70, 149–151]. The general feature of such delay-induced non-Markovian dynamics is that the system relaxation now deviates from exponential decay – indicating a memory-like effect. The coherent time-delayed feedback exerts a sudden kick on the system, leading to faster-than-superradiant decay [66–68] or bound state in continuum (BIC) [69, 70]. Especially, BIC can be used to suppress decoherence of quantum emitters, as demonstrated in the system of superconducting qubits forming a giant atom [152].

1.6 Thesis Outline and Statement of Contribution

This thesis describes investigations on the interaction of ^{85}Rb atoms mediated by photons traveling in an ONF. In Ch. 2, we describe the apparatus for the integration and control of neutral atoms with ONFs, which involves a vacuum system, coil system, lasers, electronics, and a custom program for experimental control and data acquisition. In Ch. 3, we present a summary of our work on the collective dynamics of multi-level atoms, as presented in [136, 153]. We show that the quantum beats arising from interference of multiple transitions can be collectively enhanced.

We also discuss the effects of photon propagation in such a multi-atom, multi-level system. Ch. 4 describes our investigation on the possible long-range interaction of a multi-atom system through the intensity correlation measurement. A theoretical framework is developed to capture both strong- and weak-coupling regimes. Experimental measurements in the system of neutral atoms coupled to an ONF indicate that the system is in the weak-coupling regime and suggest that achieving strong coupling would require proper spatial ordering of the atoms. In Ch. 5, we present a new approach for making a tunable-spacing atomic array around an ONF, which can enhance cooperativity using collective effects. A summary of the optical setup, as presented in [154], is provided. Preliminary data are presented, demonstrating atoms trapped in tunable-spacing lattice sites and interfaced to the ONF guided mode. Conclusions and outlooks are given in Ch. 6. Appendix A presents the calculation of ONF guided mode profiles along with example plots. Appendix B demonstrates the collective atomic modes mediated by one-dimensional EM field modes. The relevant publications [136, 153, 154] are included at the end of this thesis.

The work presented in this thesis is the result of a collaborative effort involving many people. The construction of the experimental systems described in Ch.2 was primarily carried out by Hyok Han and me. Hyok Han led the chamber design and assembly, as well as the nanofiber fabrication. I was responsible for the design and implementation of the coil systems. The computer-controlled unipolar current control circuit was designed by Alessandro Restelli and me. The control program was initially written by Huan Bui, who implemented communication with NI PCI boards. It was later further developed by Hyok Han and me to incorporate object-oriented principles and multi-threading for better extensibility, as well as to include pseudoclock functionality and automated parameter scanning. In Ch. 3, the experiment was conducted by Hyok Han, and the theoretical work was performed by me with guidance from Kanu Sinha. In

Ch. 4, the initial experiment was conducted by Hyok Han, while the final sets of experiments was carried out by me. The theoretical modeling was also performed by me with guidance from Kanu Sinha. In Ch. 5, the accordion lattice setup was designed by Hyok Han, Sarthak Subhankar, and me. The construction and testing of the optical setup was carried out by Hyok Han. Integration of the optical setup with the ONF and the measurement of atomic data were jointly conducted by Hyok Han and me. All works are advised and led by Steve Rolston and Fredrik Fatemi.

Chapter 2: Apparatus

This chapter describes the setup for experiments with cold, trapped ^{85}Rb atoms interfaced with an ONF. The setup integrates multiple components, including the vacuum system, coil system, fibers, lasers, and experimental control and measurement programs. These components have evolved over time to meet the specific needs of each project. In this section, we describe our experimental system, focusing on key upgrades and the motivations behind them.

2.1 Vacuum System

We describe the components and assembly procedure for an ultra-high vacuum (UHV) system that contains two ONFs and Rb atom sources. The chamber has been re-built after the completion of our first project (observing vacuum-induced quantum beats, described in Sec. 3.1), as the ONFs were broken while changing the Rb dispensers. Figure 2.1 shows the design and photo of the new chamber, where the Rb sources are separated from the main chamber. This prevents the dense Rb atomic flux from directly hitting the ONFs.

The main vacuum chamber is a 6.0" spherical-octagon chamber (Kimball Physics MCF600-SphOct-F2C8), which has two 6.00" conflat (CF) ports and eight 2.75" CF ports. Viewports that are anti-reflection (AR) coated for 780 nm are attached to the flanges, except for two of the 2.75" ports; one is connected to the ONF assembly and the other is attached to a 6-way cross (Kurt J.

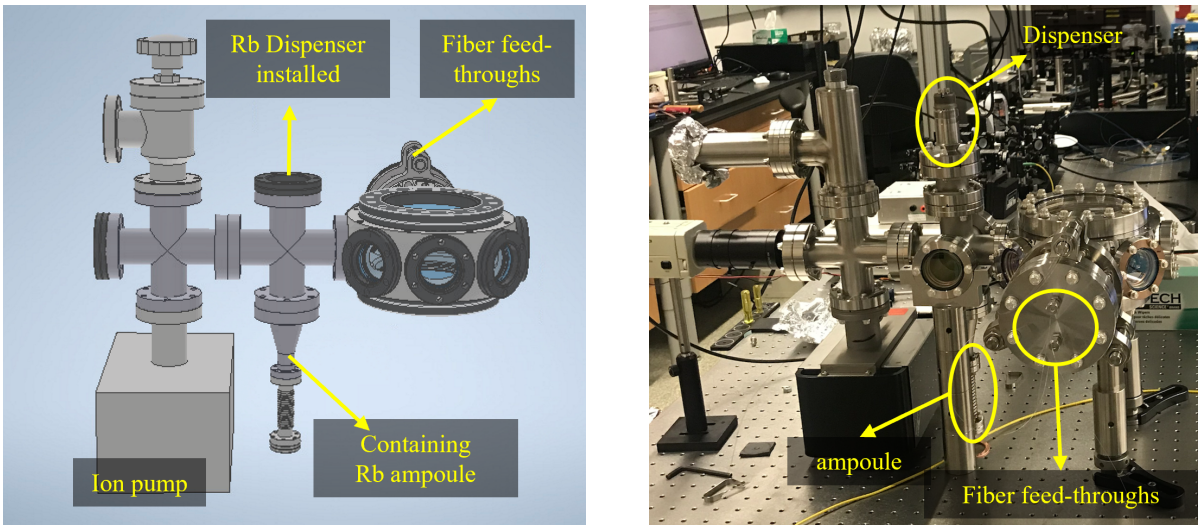

(a) (b)

Figure 2.1: (a) Design of a new chamber, where the Rb sources (dispenser and ampoule) are separated from the main chamber. (b) A photograph of the new chamber.

Lesker C6-0275), which connects to the atomic sources and pumps.

One of the 2.75” ports of the main chamber is used to insert the ONFs. The ONF assembly is shown in Fig. 2.2. A 4.50” flange and CF port aligner (Kurt J. Lesker PA64-H) is adapted by a 4.50” to 2.75” flange adapter (Kimball Physics MCF450-ClsCplr-E1Cr1) to the main chamber. The 4.50” flange is attached to the ONF holder, where the fibers are taken outside the chamber through two fiber feedthroughs installed at the two holes of the 4.50” flange. The fiber can be adjusted by the three knobs in the port aligner. The ONFs are positioned horizontally inside the chamber so that no structure other than a 6.0” viewport is above them, minimizing the probability of dust falling onto the fiber.

The Rb dispensers are installed at the top port of the 6-way cross, in between the ion pump and the main chamber. We spot-welded five Rb dispensers (SAES RB/NF/7/25 FT10+10) onto a 6-pin feedthrough 2.75” CF flange (MDC Precision, Part # 9132003) as in Fig. 2.3. The dispensers are connected in series with electrical access points between them, allowing us to

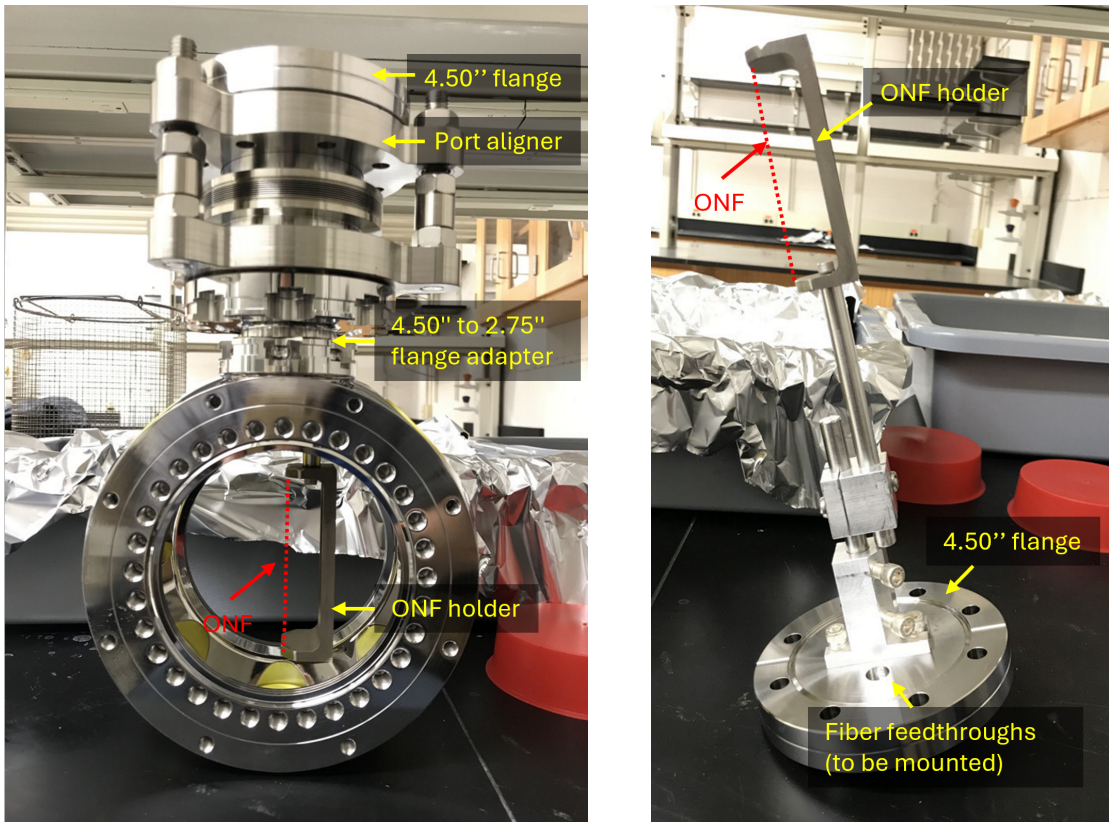

(a) (b)

Figure 2.2: (a) A 4.50" flange is connected to the main chamber via a 4.50" CF port aligner and a 4.50" to 2.75" flange adapter. (b) The ONF holder is fixed to the flange. The position of the ONF is indicated with dashed red line.

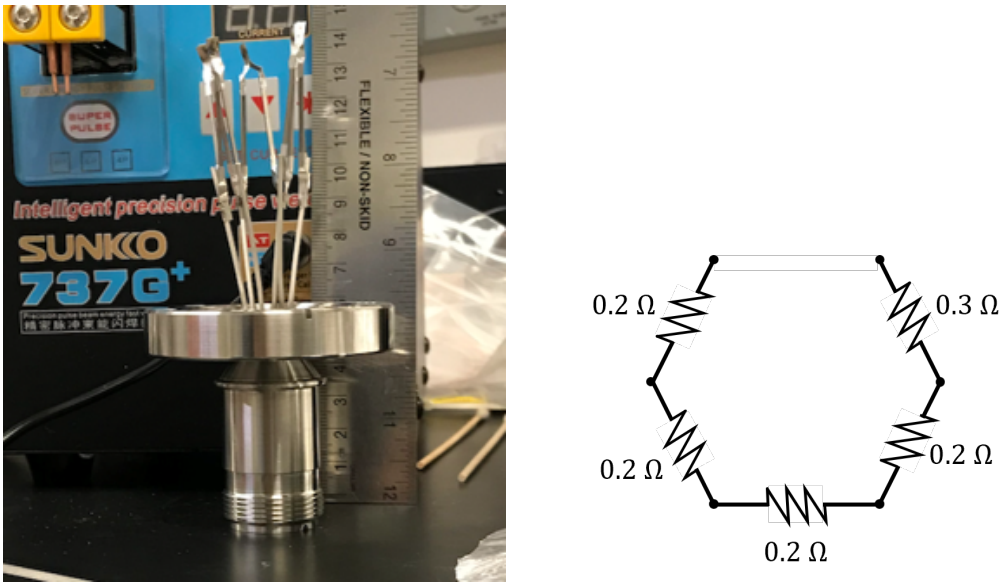

(a) (b)

Figure 2.3: (a) Rb dispensers welded onto a 6-pin feedthrough 2.75" CF flange and (b) their connection diagram. Each resistance indicates the composite resistance of the dispenser and the rod.

apply different currents to each of them and use only one dispenser at a time. The resistance of each getter is about 0.2 Ω. As a backup atomic source, we also put a Rb ampoule (Alfa Aesar, Rubidium, 99.75% (metals basis), CAS: 7440-17-7). The ampoule is housed in a separate bellow, which is connected to the bottom port of the 6-way cross. The bellow can be bent to break the ampoule and release atoms. Once broken, the ampoule can be either heated up or cooled down to control the Rb vapor pressure in the chamber. The ampoule has not been used yet and all experiments so far have been conducted using the Rb dispensers.

The chamber is initially pumped by a roughing turbo pump (HiCube 80 Eco), and the vacuum is maintained by an ion pump (Duniway Varian Classic Style Ion Pump 20 I/s). The turbo pump took one day to reach a pressure of 1.4E-7 mbar. Then we turned on the ion pump and closed the valve to the turbo pump, which further reduced the pressure to 3.5E-9 mbar over two weeks. We did not bake out the chamber due to the risk of ONFs sticking to each other. Glass

generally has lower thermal conductivity than titanium, so there can be a temperature gradient between the ONFs (glass) and the holder (titanium). In the case where the ONFs are at a higher temperature than the holder, they may expand and shift laterally, potentially coming into contact with each other. We observed this once during the cool-down phase of a precious bake-out.

After pumping, we activated a getter by applying a current of 3 A. To suppress the pressure increase caused by outgassing during getter activation, we temporarily turned on the turbo pump. The outgassing acted as a mild bake-out and helped to reduce the vacuum pressure further to 2.4E-9 mbar. The remaining unactivated getters were supplied with 0.7 A to prevent them from catching junk gases. When not in use, the activated getter is applied 1 A (standby mode). Over time, as we turned on the coils and ran experiments, the vacuum level in standby mode further improved to $\sim$1E-10 mbar indicated by ion pump current, due to local bake-out from the heat dissipation of the coils.

2.2 ONF Pulling

We pull a single-mode (SM) fiber (SM800-5.6-125) using the flame brushing method, where the fiber pulling apparatus is built by previous graduate students in the lab [29, 155, 156]. The fiber is pulled in a cleanroom to prevent dust from sitting on the fiber. The schematics of the setup for nanofiber pulling is shown in Fig. 2.4. The general procedure for fiber pulling is summarized here.

The motor stages are pre-aligned using a dummy fiber. The position of the stages are calibrated with respect to the fiber-nozzle distance: The stage is moved to the point where the dummy fiber touches the nozzle, which marks the reference point.

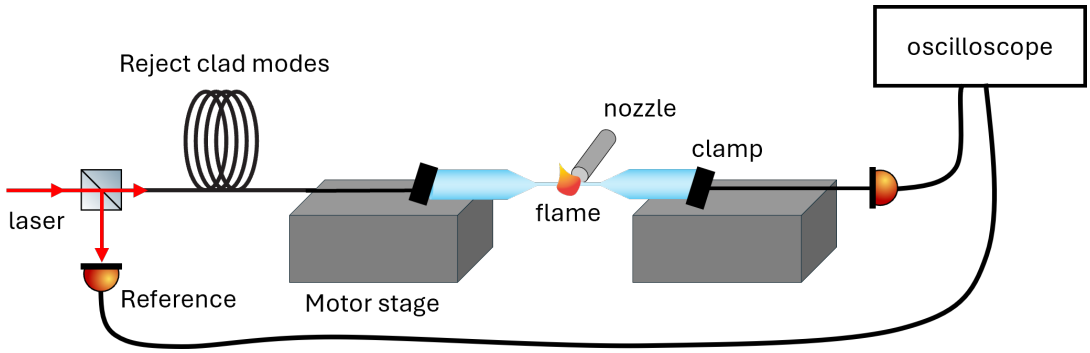

Figure 2.4: A diagram showing ONF pulling process.

The fiber to be pulled is first stripped and cleaned using acetone and isopropyl. It is then mounted on motorized stages, clamped tightly, and tensioned by moving the stages apart. To filter out cladding modes, the upstream section of the fiber is wound around a 1" post ≈ 10 times. This mode purification allows monitoring the adiabatic transfer of the core mode to the tapered region during the pulling process.

The oxygen and hydrogen valves are opened, and the flame is ignited by an electric spark generated by a voltage of $\sim$1 V. The flame is brought to the fiber, which locally melts and tapers the glass. The transmitted optical power is monitored during the pulling process to observe the adiabatic transfer of light into and out of the tapered region. Figure 2.5 shows a typical transmission measurement of the fiber, normalized to its initial value, during the pulling process. As the fiber is thinned out, a portion of the core mode begins to couple to higher-order modes. The interference among these modes gives rise to the beating patterns in the transmission signal. As the fiber is further tapered and reaches the cutoff diameter that supports only the fundamental HE_{11} mode, the beating disappears. The final transmission typically exceeds 99%.

Once pulling is completed, the tapered fiber is carefully inspected to make sure that the tapered region does not have any dust. This is crucial because, once placed in vacuum, even a small dust particle can scatter light, generate local heating, and potentially break the fiber. The

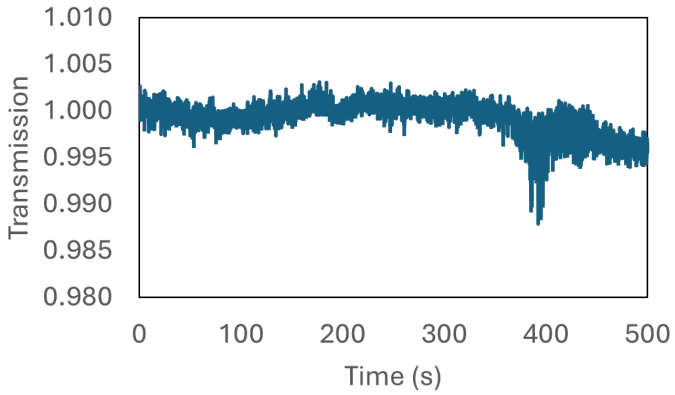

Figure 2.5: Transmission data during the fiber pulling process.

pulled fiber is applied with a small tension and fixed at two points (outside the tapered region) to the holder with vacuum-compatible epoxy (EPO-TEK OG116-31) and UV curing (110 mW/cm^2, 2 minutes) (see Fig. 2.2 (b)).

We pulled two ONFs and fixed them on a titanium holder where the separation between the ONFs is 1 mm. Such a configuration enables us to have two systems of atoms + ONF which may be connected by an optical fiber outside the chamber.

2.3 Coil System

Creating magnetic field gradient and offsetting its zero point are essential in trapping and cooling neutral atoms. We describe the coil and driver system to create desired magnetic fields inside the chamber.

We use two types of coils; an anti-Helmholtz coil and shim coils. The anti-Helmholtz coil is made of a set of parallel coils running the current in the opposite direction. It produces a linear magnetic field gradient around the center. The shim coil is a set of parallel coils as well, but with the current running in the same direction. They are used to offset the zero-field point of the

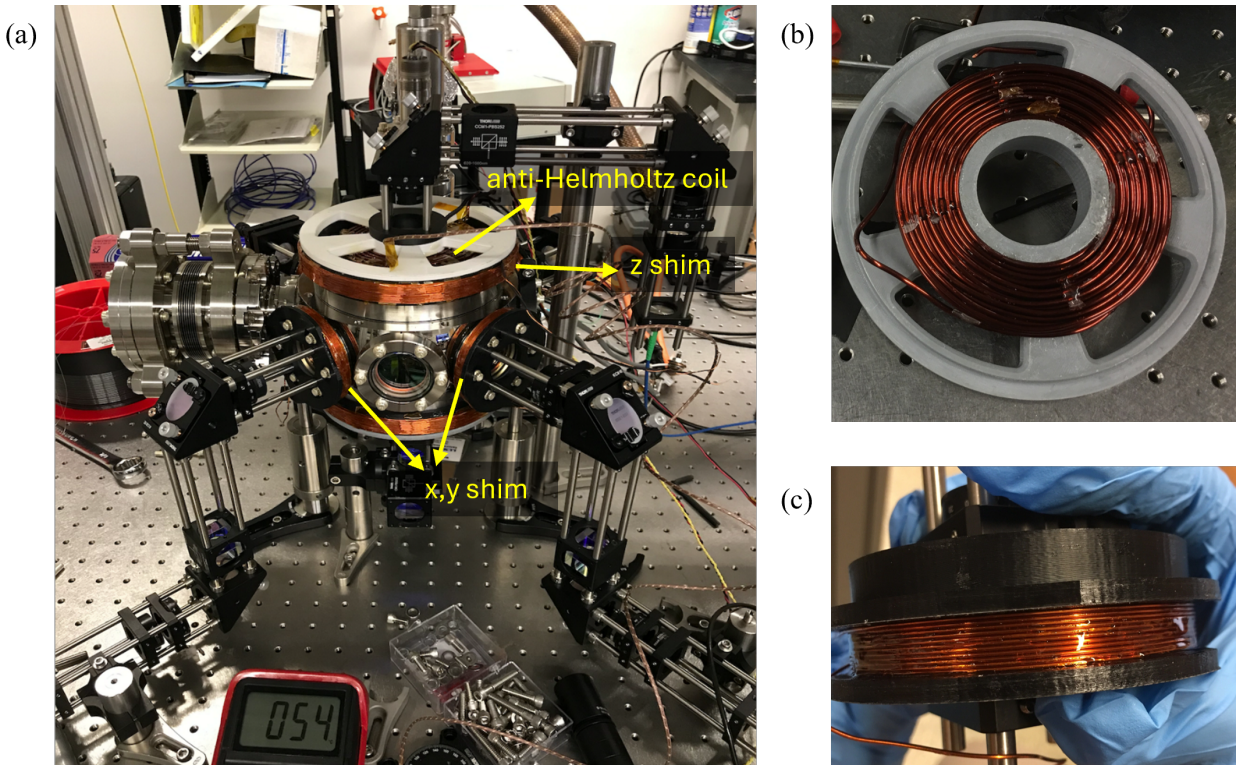

Figure 2.6: (a) The magnetic coils assembled to the chamber. (b) An anti-Helmholtz coil wound around its frame and (c) x- and y-shim coils wound around the frame.

magnetic field gradient created by the MOT coils and cancel the Earth's field. The overview of the coils assembled around the chamber is shown in Fig. 2.6.

2.3.1 MOT Coil

Design Principle

The important parameters for designing a MOT coil are the magnetic field gradient, heat dissipation, and inductance. A typical magnetic field gradient required for a magneto-optical trap of Rb atoms is around 15 G/cm [157]. The power dissipation limit depends on factors such as the surface area of the coil, mounting material, and air flow. Typically, up to 20 W of heat can be safely dissipated with passive air cooling alone. The inductance becomes critical when rapid

ramping of the magnetic field is required. The inductance of a solenoid is given

$$L = \frac{\mu N^2 A}{l} \tag{2.1}$$

where μ is the permeability of the coil material, N is the number of turns, A is the cross-sectional area, and l is the length of the solenoid. Thus, it is generally better to restrict the total number of turns as low as possible.

The magnetic field gradient and the thermal heat generated by the MOT coil are closely correlated; both are determined by the coil geometry (number of turns, radius, and separation) and the current passing through the coils. When the MOT coils are placed closer to the chamber, less current is required to produce the desired magnetic field gradient. However, when it is put close to components such as viewports, the local heat gradient can damage the component. In contrast, putting the coils farther away from the chamber necessitates higher current to make the same magnetic field gradient. But managing heat dissipation becomes much easier and the temperature rise is less critical at a large distance from the chamber.

We decided to make smaller coils on top of the 6" viewport with passive air cooling. The coils are $\sim$ 2 mm air-gapped from the viewport surface to mitigate any local heat gradient in the glass. Our rule of thumb in coil design was to achieve a magnetic field gradient of 15 G/cm using less than 20 A of current, while keeping the power dissipation below 20 W. When we made the coil, we did not need dynamic switching of the coil during the experiment. However, we opted for thicker wire with fewer turns to ensure that the coil could support rapid magnetic field ramps in future experiments.

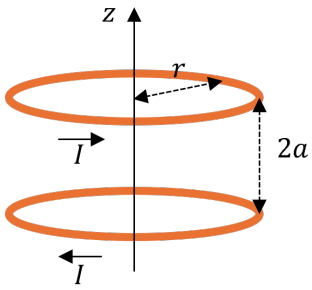

Figure 2.7: Geometry of a MOT coil. The coils of radius r are positioned at $z = \pm a$, carrying currents I in opposite directions.

Magnetic Field Calculation

Now we describe the calculation of the magnetic field gradient and the thermal power generated by a MOT coil. Suppose that two coils of radius r are positioned parallel to each other at $\pm a$ along the z-axis (Fig. 2.7). The current I flows through the two coils in opposite directions. The magnetic field at z is given by:

$$B(z) = \mu_0 I \left(\frac{r^2}{2(r^2 + (z-a)^2)^{3/2}} - \frac{r^2}{2(r^2 + (z+a)^2)^{3/2}} \right), \tag{2.2}$$

where $\mu_0 = 4\pi \times 10^{-7}$ H/m is the vacuum permeability. The derivative of the magnetic field with respect to z gives the magnetic field gradient:

$$\frac{dB(z)}{dz} = \mu_0 I \left(\frac{3r^2(a+z)}{2(r^2 + (z+a)^2)^{5/2}} - \frac{3r^2(z-a)}{2(r^2 + (z-a)^2)^{5/2}} \right). \tag{2.3}$$

The gradient at center is

$$\left.\frac{dB(z)}{dz}\right|_{z=0} = \mu_0 I \frac{3ar^2}{(r^2 + a^2)^{5/2}}. \tag{2.4}$$

Once the geometry is known, we can sum the magnetic field gradient contributions from each segment and calculate the current required to generate 15 G/cm at the center. We then calculate the electric power I^2R where R is the total resistance of the coil.

We opted to use gauge 11 wire since MOT coils require high currents. The coil has inner radius 30 mm, giving optical access for MOT beams. The outer radius is 60 mm, snugly fitting within the viewport diameter. The separation between the coils ($2a$) is 114 mm, which is slightly larger than the chamber height of 100 mm. Each coil consists of 4 layers with 12 turns per layer, totaling 13.3 meters in length. A current of $\approx$ 19 A produces a magnetic field gradient of $\approx$ 15 G/cm at the center and generates $\approx$ 21 W. The inductance of the coil is $\approx$ 2 mH.

2.3.2 Shim Coils

The shim coils are used to shift the atomic position by adjusting the zero field position. The expression for the magnetic field generated by the shim coil is the same as that for the MOT coil, except for a sign difference in the second term:

$$B(z) = \mu_0 I \left(\frac{r^2}{2(r^2 + (z-a)^2)^{3/2}} + \frac{r^2}{2(r^2 + (z+a)^2)^{3/2}} \right). \tag{2.5}$$

The shim coils are designed to make $\pm$ 0.5 cm shift of the magnetic field center. Thus, it should generate $\pm$ 7.5 G in the z-direction, and $\pm$ 3.7 G in the x- and y-direction. Note the factor 2 difference in the magnetic field gradient created by anti-Helmholtz coils in the transverse and axial directions.

The z-shim coil is wound around the 6" viewport. Gauge 20 wire was used, and the coil consists of three layers with 16 turns in each layer. The inner radius is $\approx$ 87 mm and the outer

radius is $\approx$ 90 mm. The separation of the coils ($2a$) is 110 mm. The total wire length is $\approx$ 53 m, corresponding to a resistance of $\approx$ 2 Ω. A current of $\approx$ 2 A generates $\approx$ 7.5 G magnetic field while producing $\approx$ 7 W of heat. The inductance of the z-shim coil is $\approx$ 5 mH.

The x- and y-shim coils are mounted around the 2.75" viewports. The inner radius of each coil is $\approx$ 39 mm, and the outer radius is $\approx$ 44 mm. The separation between the coils is $\approx$ 192 mm. The total wire length is $\approx$ 26 m corresponding to a resistance of $\approx$ 1 Ω. A current of $\approx$ 4 A generates a homogeneous horizontal magnetic field of 3.7 G at the center and produces $\approx$ 17 W of heat. The inductance of the coils is $\approx$ 2 mH.

2.3.3 Mounts

We 3D-printed the frames for coil winding and assembly using Markforged Onyx One. Fig. 2.8 shows the frames and assembly of the z-direction coils including the MOT coil and the z-shim coil. The MOT coil is wound around the center pillar of the frame (Fig. 2.8 (a)). The length of the pillar is a few milimeters longer than the coil, ensuring air gap between the coil and the viewport. The z-shim coil is wound around the bigger frame (Fig. 2.8 (b)). The two frames fits to each other so that they are combined after coil winding and sits on the 6.0" viewport.

The x- and y-shim coils are wound on the frame shown in Fig. 2.9, which is designed to fit onto the 2.75" viewport. The frames are secured by interfacing them with 30 mm cage systems. The frame also serves as an adapter between the 2.75" viewport and the 30 mm cage system.

Note that the frames are designed to mount directly onto the chamber, ensuring that the magnetic system is centered with respect to the chamber. Furthermore, the frame also aligns the cage system to the chamber center, which ensures that the cooling lasers are properly aligned

with both the chamber and the magnetic field center set by the coil.

(a) MOT coil frame

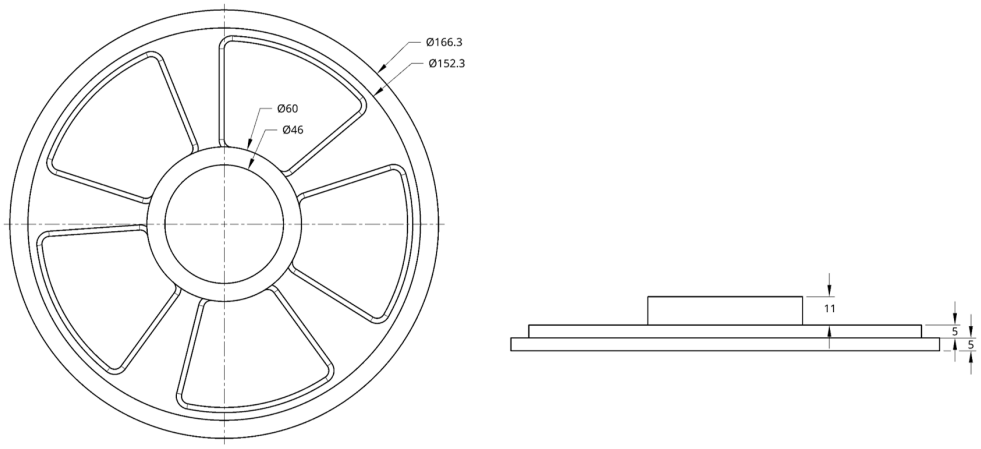

(b) z-shim coil frame

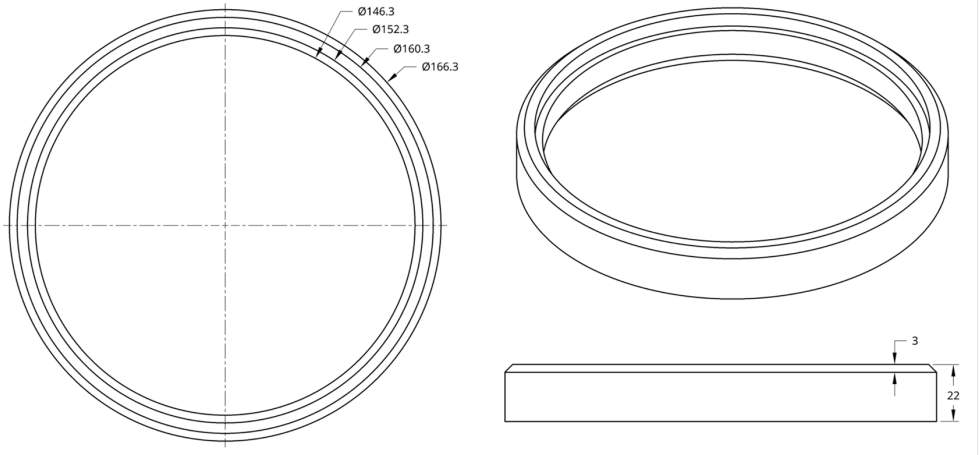

(c) assembly

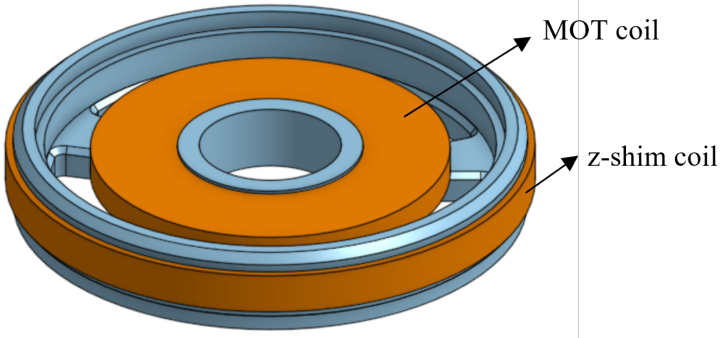

Figure 2.8: MOT coil and z-shim coil assembly.

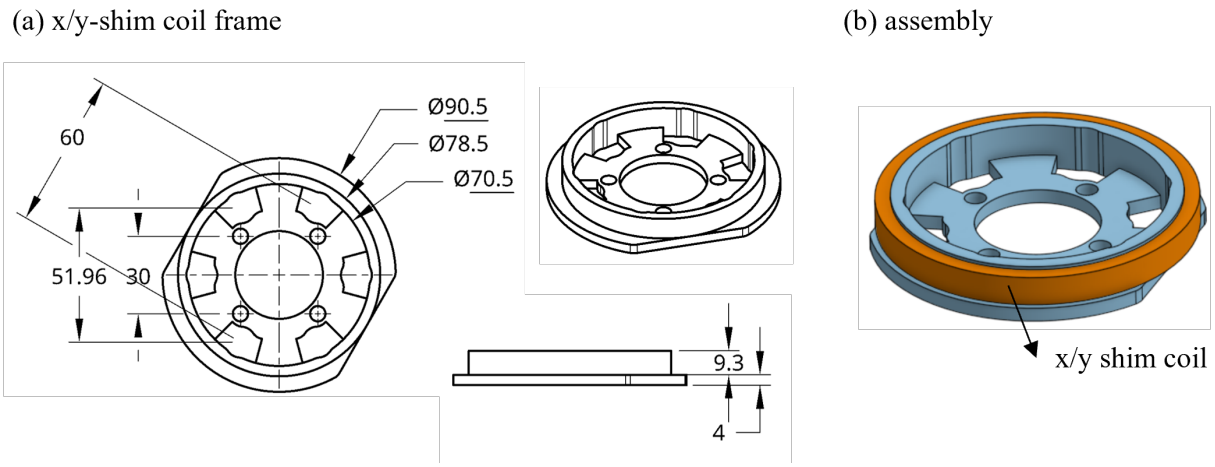

Figure 2.9: x- and y-shim coil assembly.

2.3.4 Computer-controlled Unipolar Current Control Circuit

Previously, the MOT coils were driven using DC power supplies that were manually controlled via front-panel knobs (Topward Dual-Tracking DC Power Supply 6306D). For the new setup, we designed custom electronic circuits to control the current via computer, ensuring better reproducibility. Our circuit takes a digital input and outputs a corresponding current. The schematic of the current control circuit is shown in Fig. 2.10. The full schematics and code can be found in `https://github.com/JQIamo/unipolar-multichannel-current-controller`.

Before explaining the circuit in detail, we note a few of its limitations. First, the update time is approximately one second due to its daisy-chain structure to communicate with the computer. Since the circuit is designed to adjust the static position of the MOT, it does not support dynamic ramping during the experiment. For the same reason, the current output is unipolar, and reversing the direction requires physically switching the wiring. The current output is designed to be in the range $0 \sim 5$ A, although this range could, in principle, be adjusted by tuning certain parameters in the circuit.

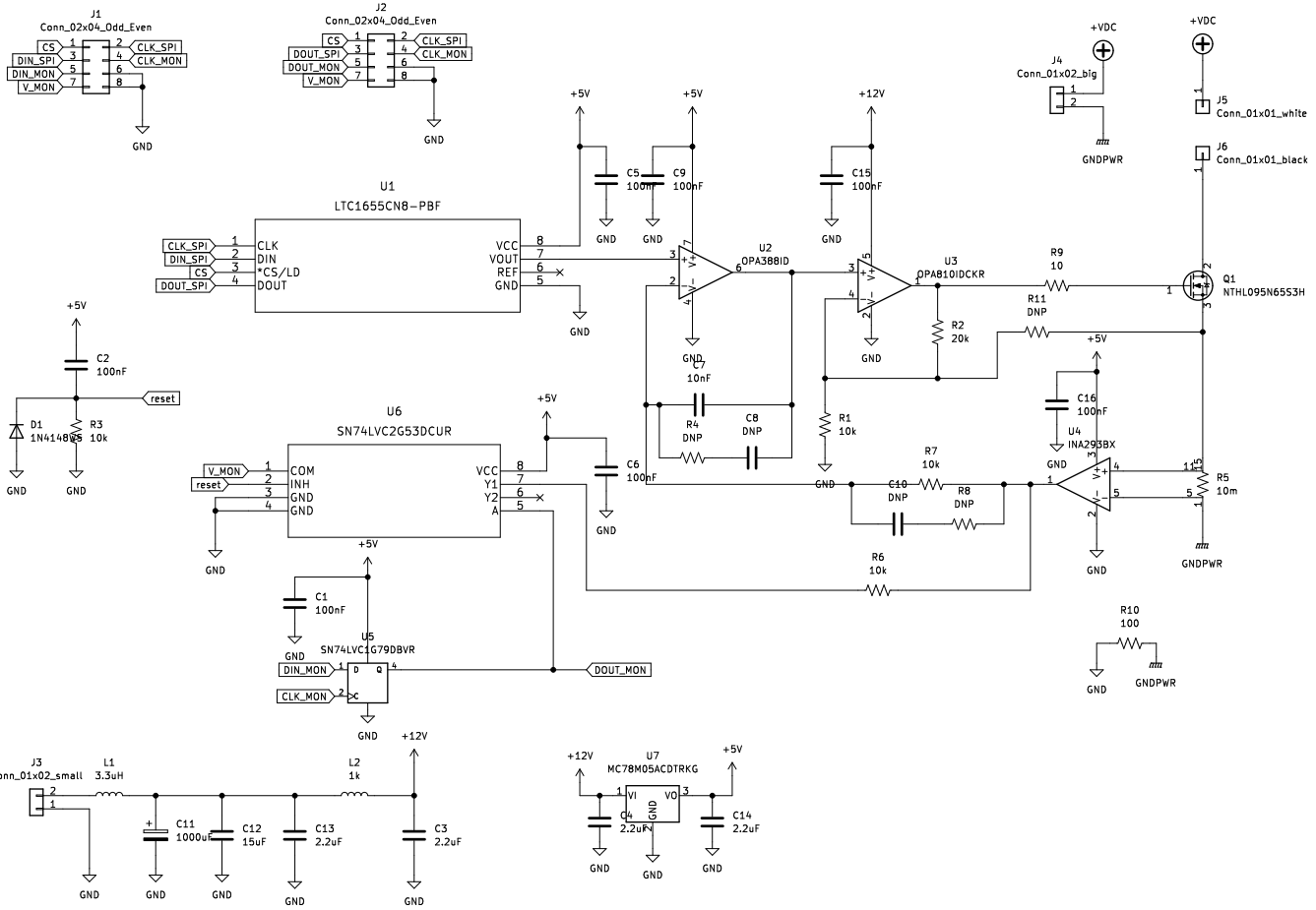

Figure 2.10: Schematics of the unipolar current controller circuit that takes digital input and adjust the current output between 0 to 6 A.

Reference Number	Description	Part Number
U1	DAC	LTC1655CN8#PBF
U2	op-amp	OPA388ID
U3	FET driver op-amp	OPA810IDCKR
U4	instrumentation amplifier (gain=20)	INA293B1IDBVR
U5	D-type flip-flop	SN74LVC1G79DBVR
U6	analog switch	SN74LVC2G53DCUR
U7	linear regulator	MC78M05CDTRKG
D1	diode	1N4148WSFSCT-ND
Q1	MOSFET	NTHL095N65S3H
R5	shunt resistor (0.01 Ω)	FHR4V-0R01F1

Table 2.1: Description of the electrical components in the unipolar current controller circuit in Fig. 2.10.

A description of each component in the current control circuit (Fig. 2.10) is provided in Table 2.1. The basic design principle is as follows. The digital-to-analog converter (DAC) (U1) receives 16-bit digital data and converts it into an output voltage V_{DAC}. This voltage is compared with the sensing voltage V_{sense}, which is measured across the sensing resistor (R5) and amplified by the instrumentation amplifier (U4). The operational amplifier (op-amp) (U2) adjusts its output to minimize the difference between the two inputs, V_{DAC} and V_{sense}. The output of U2 is amplified through the second op-amp (U3) and applied to the gate of the MOSFET (Q1), which controls the current flowing through its drain and source.

The relation of the set voltage, V_{DAC}, and the current flow in the load, I, is determined by the combination of the resistance of the sensing resistor and the gain of the instrumentation amplifier. To ensure precise current output, both components were picked from models having low thermal drift and high accuracy. The sensing resistor has a resistance of 0.01 Ω, and the instrumentation amplifier has a gain of 20. Using the relation $V_{\text{DAC}} = V_{\text{sense}}$, we see that the

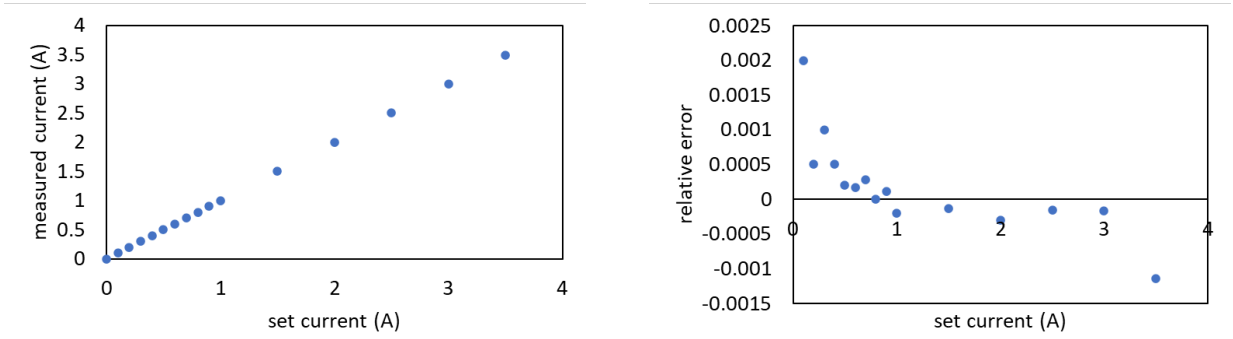

(a) (b)

Figure 2.11: (a) The measured current output for set current from 0 to 4 A. (b) The relative error of the current output.

current flowing through the load, I, is given by

$$I = V_{\text{DAC}} \times 5, \tag{2.6}$$

where I is in amperes and V_{DAC} is in volts. The DAC has an internal reference of 2.048 V, and its output voltage swings from 0 to 4.096 V in steps of $2^{16} = 65536$. Therefore, the digital input to the DAC to set the current to a desired value I_{set} (in amperes) is

$$\text{DIN\_SPI} = \text{round}\left(\frac{I_{\text{set}}}{5} \times \frac{65535}{4.096}\right), \tag{2.7}$$

with the maximum allowable current limited to $5 \times 4.096A = 20.48A$. In practice, I is limited below 5 A in the control program. From calibration, we adjusted the formula to

$$\text{DIN\_SPI} = I_{\text{set}} \times 3205 + 11, \tag{2.8}$$

Fig. 2.11 shows the comparison of the set value and the actual value of the current. Overall, the

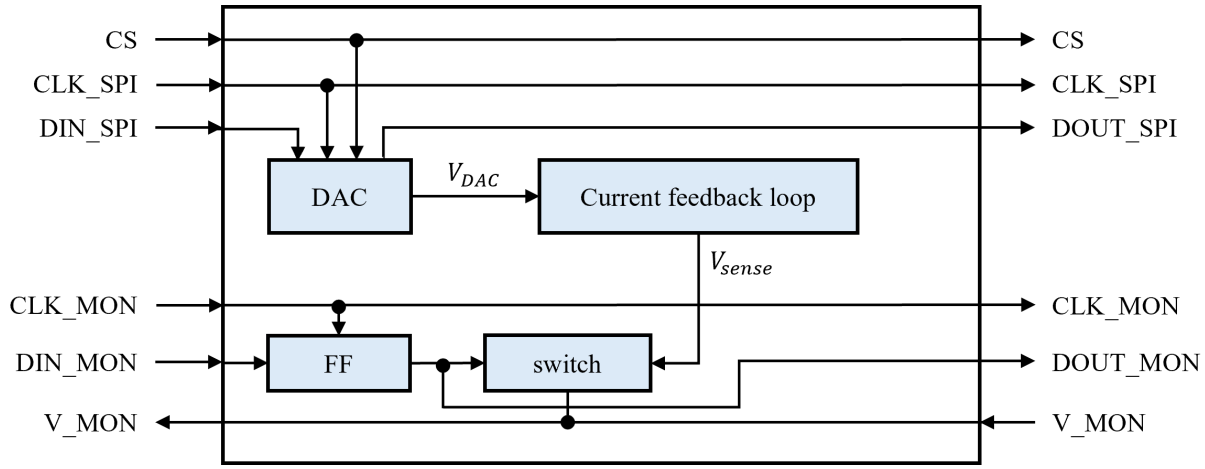

Figure 2.12: Diagram illustrating the data flow into and out of each circuit in the daisy-chain configuration, where the output of a circuit is connected to the input of the next circuit.

relative error is below 0.2 % within the 0 to 4 A range.

To ensure the stability of the feedback circuit, a capacitor (C7) is added between the negative input and the output of U2. The inductance of the coils is $\approx$ 2 mH. Assuming a 10 V supply and a 1 A change in current, the rate of the current change is given by (inductance)$\times$(current change)/(voltage) = 0.2 ms, which corresponds to a frequency of 5 kHz. Thus, the transfer function $(1/R7)/(s \times C7)$ should cross 0 dB below this frequency. We set 0 dB cross at 1 kHz, which implies C7$\approx$ 16 nF. Based on this estimation, a 10 nF capacitor was used.

All components of the circuit, except for the load, MOSFET, and shunt resistor, are powered by a 12 V DC supply provided by an AC-DC converter (ECL15US12-S), which converts the AC power from electric outlet to 12 V DC. The load, MOSFET, and shunt resistor are powered separately via banana connectors. This supply voltage can be adjusted to minimize power dissipation in the MOSFET, since the power dissipated at the MOSFET equals the total supplied power minus the power dissipated in the load. To avoid ground-loop issues, the power grounds of the control circuit and the load are connected at a single point, among multiple circuits.

Our current control box contains five of the current control circuits (Fig. 2.10). The circuits

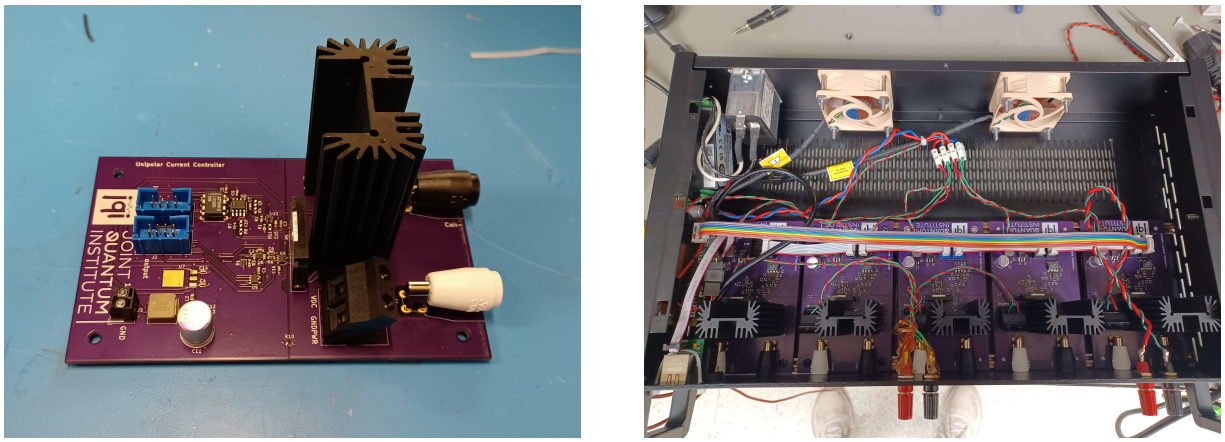

(a) (b)

Figure 2.13: (a) Current control circuit. (b) A housing containing five current control circuits and a microprocessor with USB and Ethernet interfaces.

are controlled and monitored by a microcontroller (Teensy 4.1) using a daisy-chain configuration, in which data is transferred sequentially through the circuits, as shown in Fig. 2.12. The chip select (CS) pin on the DAC determines whether the incoming data is reflected on the output (V_{DAC}) or passed to D_{OUT}. During the data writing phase, CS is pulled low, allowing the data to shift to the next circuit. Once all data has been transferred and each circuit has received its intended value, CS is pulled high, simultaneously updating all DAC outputs.

The sensing voltage V_{sense} is also read out for monitoring purposes. It is routed to one of the inputs of the analog switch (U6). A single low-level monitoring signal propagates through the circuits, activating the switch of the selected circuit and connecting it to V_{mon}. This allows sequential readout of the actual voltage from each circuit.

Fig. 2.13 shows photographs of the current control circuit and a housing containing five circuits connected in a daisy-chain configuration. Power to the load, MOSFET, and shunt resistor is supplied through banana connectors on the front panel. The load power lines are divided into two groups: one for low-power applications, suitable for driving shim coils, and another for

high-power applications, such as powering dispensers or other high-current devices.

2.3.5 Bipolar Operational Power Supply (BOP)

As the experiment progressed to creating an atomic array around an ONF (see Sec. 5), it became necessary to cool the atomic cloud below the Doppler limit, which in turn demanded dynamic ramping of the magnetic field on a millisecond time scale. As a result, the current control circuit described in Sec. 2.3.4 could no longer be used, as its update time was on a second scale.

For dynamics control of the magnetic field during the experiment, a 20 V - 20 A Kepco Bipolar Operational Power Supply/Amplifier (BOP) was employed. Since the maximum output voltage of the BOP is $\pm$ 20 V, the electromotive force (emf) generated during current ramping through the coils must remain within this limit. Generally, driving an inductive load with inductance exceeding 0.5 mH can cause unstable output of BOP. Therefore, it is recommended to place either a capacitor or a capacitor-resistor series circuit in parallel with the load to suppress oscillations.

The output voltage and current of the BOPs were tested using the rear programming unit. This unit enables monitoring of the output current and voltage, as well as adjustment of internal settings. The output current can be monitored through pin 10 on the rear programming unit, which provides a voltage signal ranging from 0 to 10 V, corresponding to an output current range of 0 to 20 A (i.e., 10 V corresponds to 20 A).

Driving the MOT coils was smooth, with no unstable oscillations. However, the shim coils picked up noise at a frequency of approximately 5.625 kHz due to an unfortunate combination

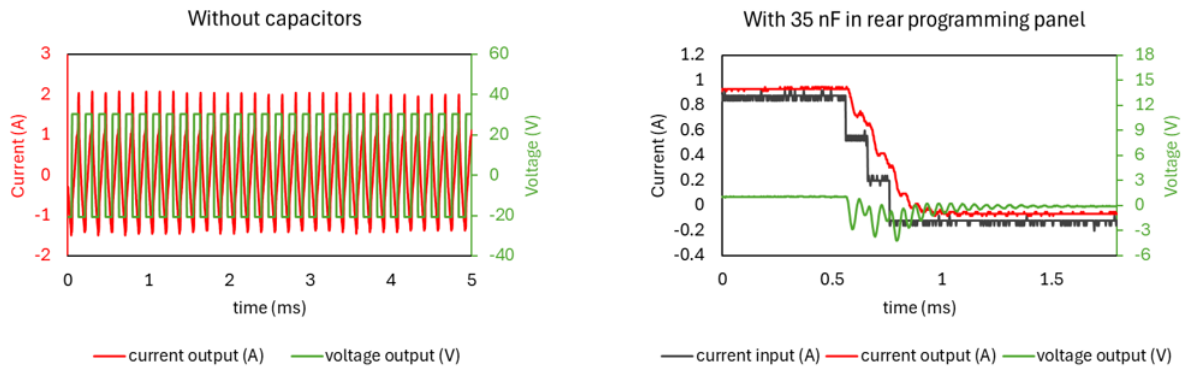

(a) (b)

Figure 2.14: (a) Current (red) and voltage (green) output of a BOP driving a shim coil without any external capacitors. (b) Current ramp-down test (1 A change in 0.2 ms) with 35 nF capacitor connected between pins 16 and 18 on the BOP rear programming unit. The current control signal (black) ramps down by 1 A within 0.2 ms in 0.1 ms steps. The actual current output (red) is smoothened due to the external capacitor placed in the current control circuit. The voltage output (green) swings within 7 V.

of its inductance and stray capacitance, and the resulting emf exceeded the voltage range of the BOP. Fig. 2.14 (a) shows the current and voltage output when the current control input is set to 0 V (no ramp). The shim coil picks up the 5.625 kHz noise and oscillates, causing the BOP to output a voltage exceeding 50 V peak-to-peak. This output was so large that it went beyond the measurable range of the oscilloscope. We first tried placing a 0.39 μF capacitor in parallel with the load. While this initially suppressed the oscillation, the capacitor quickly burned out due to excessive power dissipation. We then tried placing a 35 nF capacitor between pins 16 and 18 (the current-mode compensating terminals) on the rear programming panel. As the power in the control circuit is limited, the capacitor successfully suppressed the oscillation without burning out. We tested a 1 A ramp within 0.2 ms, which is faster than the eddy current timescale associated with magnetic field switching in the actual experiment. The current output was smoothed and the voltage output fluctuated within a 7 V range, as shown in Fig. 2.14 (b). We ultimately soldered 33.8 nF for the MOT coil drivers and 35 nF for the shim coil drivers.

2.4 Laser System

We use lasers to cool, trap, pump, and probe ^{85}Rb atoms interfaced with an ONF. The hyperfine state $\left|5^2S_{1/2}, F = 3\right\rangle$ serves as our ground state. The other hyperfine state, $\left|5^2S_{1/2}, F = 2\right\rangle$, is used as a reservoir where atoms can be pumped and become transparent to the probe beam. The cycling transition $|F = 3\rangle \leftrightarrow |F' = 4\rangle$ in the D_2 line is used to cool and trap the atoms, as well as to probe the atoms. The $|F = 2\rangle \leftrightarrow |F' = 3\rangle$ transition in the D_1 line repumps the atom to the ground state, and the $|F = 3\rangle \leftrightarrow |F' = 3\rangle$ transition in the D_2 line depumps the atom out of the ground state.

The dipole trap beam is far red-detuned (~ 100 GHz) from the D_2 line and does not see the hyperfine structure. However, it still sees the fine structure and is blue to the D_1 transition.

We continuously send heating beams through the ONFs to prevent atoms from adhering to the fiber surface.

2.4.1 Cooling and Pump Beams

The level structure of the ^{85}Rb atom with relevant laser frequencies for cooling, pumping, and probing is shown in Fig. 2.15. The cooling beam is 18 MHz red-detuned from the cycling transition $|F = 3\rangle \leftrightarrow |F' = 4\rangle$ in the D_2 line and sent to the atoms from the three perpendicular directions. The repump beams, resonant with the $|F = 2\rangle \leftrightarrow |F' = 3\rangle$ transition in the D_1 line, co-propagate with the cooling beams to repump atomic population from $|F = 2\rangle$ back to $|F = 3\rangle$ in the ground-state hyperfine manifold.

Figure 2.16 (a) shows the schematic of the preparation of cooling, depump, and probe beams. They all originate from a Toptica TA pro. The 780 nm laser diode (LD) is frequency-

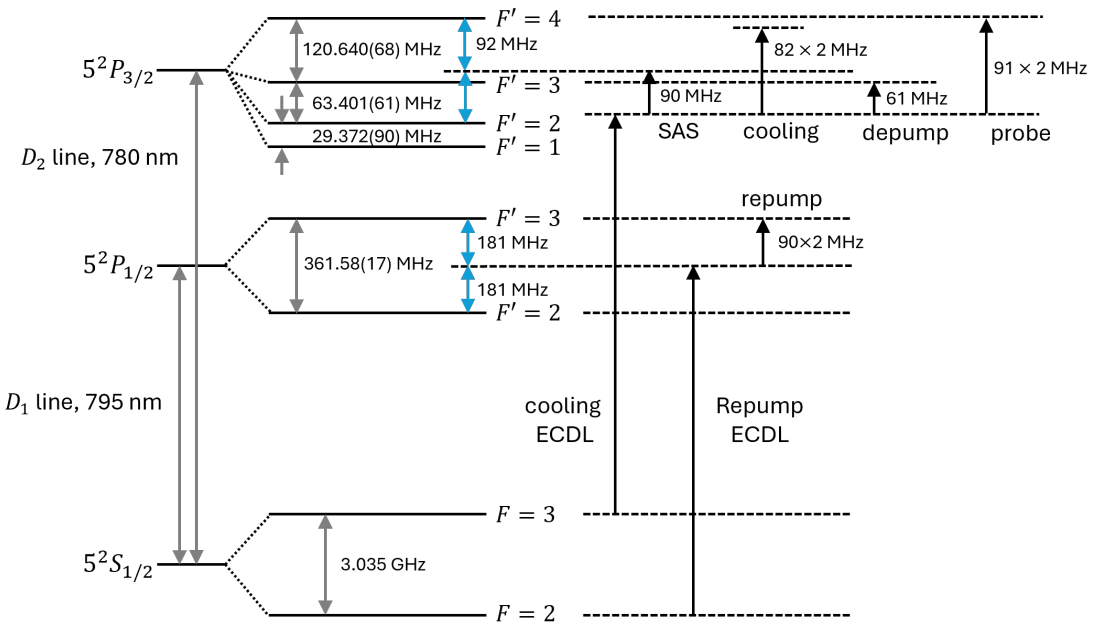

Figure 2.15: ^{85}Rb D_1 and D_2 transitions [158] with relevant laser frequencies for cooling, pumping, and probing atoms. The cooling ECDL is locked to the crossover peak between $|F' = 3\rangle$ and $|F' = 4\rangle$ in the D_2 transition using SAS, where the frequencies of the cooling, depump, and probe beams are shifted accordingly using AOMs. The repump laser is locked to the crossover peak between $|F' = 2\rangle$ and $|F' = 3\rangle$ in the D_1 transition, where an AOM brings the repump beam to resonance.

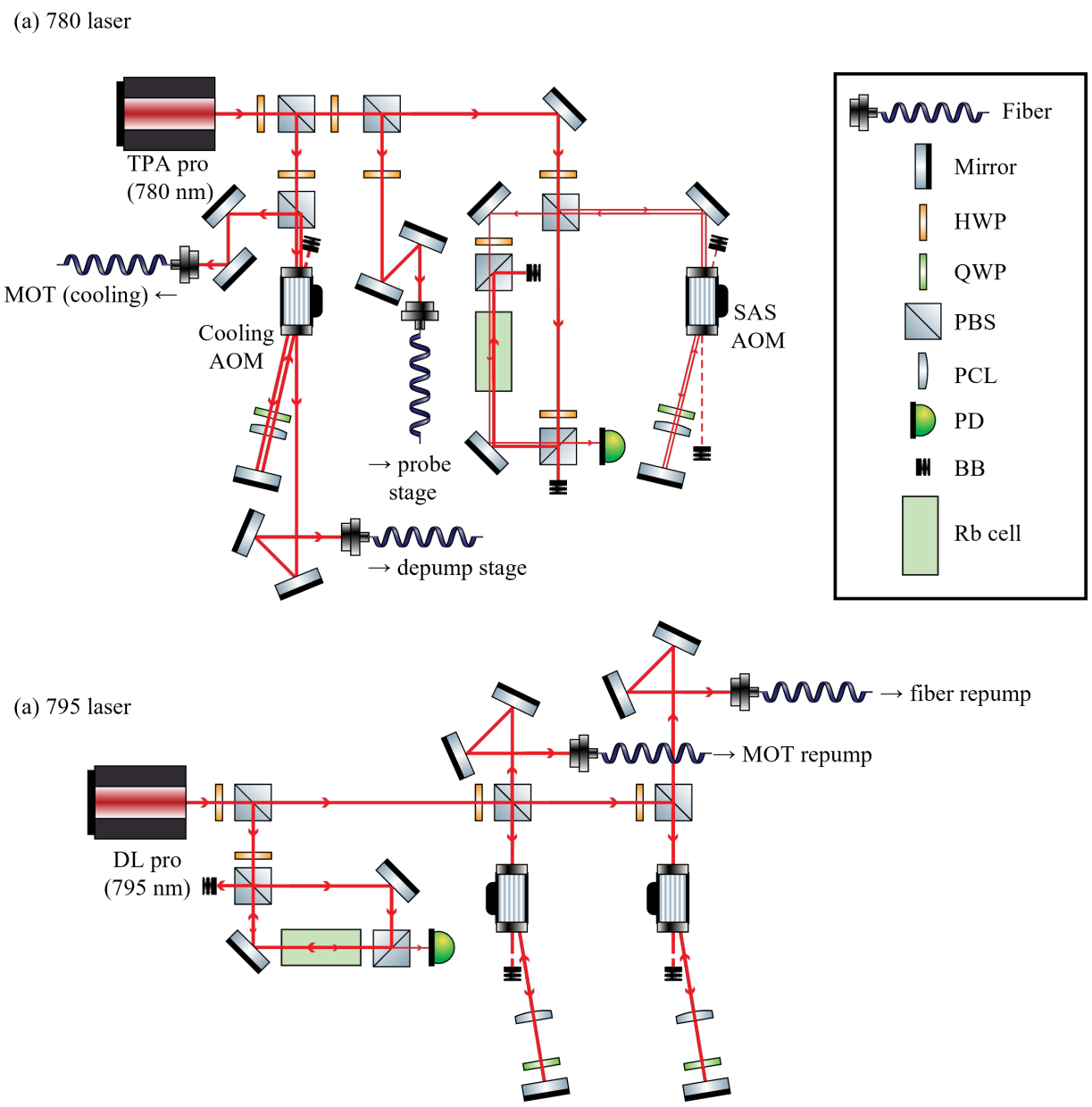

Figure 2.16: Schematics of the laser setup preparing (a) cooling, depump, and probe beams using the ^{85}Rb D_2 line, and (b) repump beams using the D_1 line. In (a), the retro-reflected beams in the double-pass AOM configuration are slightly offset for visualization purposes. The prepared cooling and MOT repump beams are combined and split into three equal powers via a 2×3 fiber multiplexer, then sent to the chamber. The depump and probe beams are routed to additional preparation stages. HWP: half waveplate, QWP: quarter waveplate, PBS: polarizing beam splitter, PCL: plano-convex lens, PD: photodiode, BB: beam block.

locked using saturated absorption spectroscopy (SAS) to the crossover resonance between $|F' = 3\rangle$ and $|F' = 4\rangle$ in the D_2 line. The SAS setup involves a weak probe beam, which is frequency-shifted by +180 MHz via a double-pass AOM configuration, and a strong pump beam. Since the probe and pump beams have different frequencies, they interact with a group of atoms moving with velocity v toward the probe beam. The resonance condition for simultaneous interaction with both beams is given by:

$$\omega_{\text{probe}} - kv = \omega_{\text{pump}} + kv \implies kv = \frac{\omega_{\text{probe}} - \omega_{\text{pump}}}{2}, \tag{2.9}$$

where $k = \omega_{\text{probe}}/c \simeq \omega_{\text{pump}}/c$ is the wave vector of the light. As a result, the Doppler-free peaks appear at a + 90 MHz frequency shift relative to the atomic rest frame. Therefore, the 780 nm LD is locked to a frequency 182 MHz red-detuned from the cycling transition. The cooling beam is generated using a double-pass AOM scheme. It is then combined with the repump beam and split into three equal-power outputs using a 2×3 fiber multiplexer (Evanescent Optics, Polarization Maintaining Couplers). The combined cooling and repump beams are sent to the chamber along three mutually perpendicular directions.

The zeroth order path of the cooling AOM is sent to a separate stage and used as a depump line. We chose such scheme because the depump and cooling is not turned on simultaneously in general, so one can avail maximum power of depump when cooling is turned off. The depump line is tuned resonant to the $|F = 3\rangle \leftrightarrow |F' = 3\rangle$ D_2 transition using a single-pass AOM scheme. The depump beams are either sent from the side or through the fiber.

Figure 2.16 (b) shows the schematic of the repump beam preparation. The repump beam originates from a Toptica DL pro. The repump laser is locked to the crossover peak between

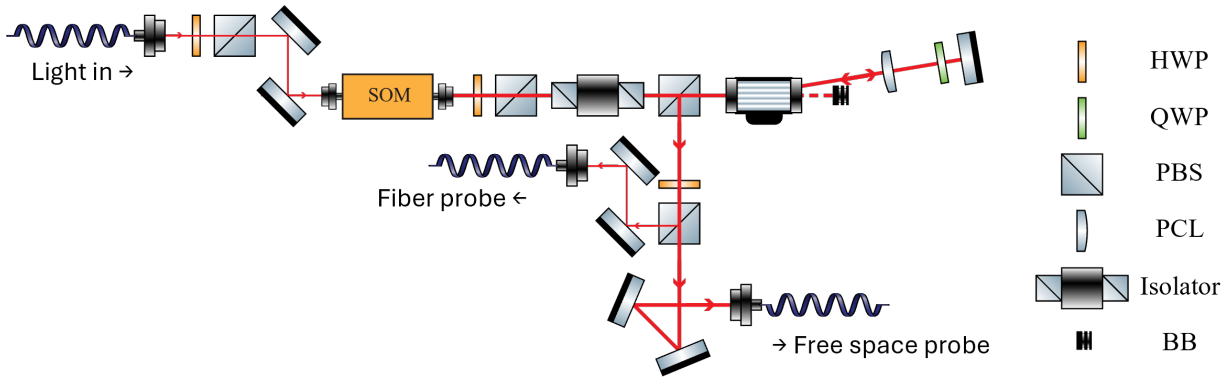

Figure 2.17: Schematics of laser setup for probe beam preparation. SOM: semiconductor optical modulator, HWP: half waveplate, QWP: quarter waveplate, PBS: polarizing beam splitter, PCL: plano-convex lens.

$|F' = 2\rangle$ and $|F' = 3\rangle$ in the D_1 line. The repump beams are brought to resonance with the $|F = 2\rangle \leftrightarrow |F' = 3\rangle$ transition in the D_1 line by double-passing through an AOM.

2.4.2 Probe Beam

The probe light is resonant with the $|F = 3\rangle \leftrightarrow |F = 4\rangle$ transition in the D_2 line. It originates from the main cooling beam preparation stage (see the fiber coupler labeled as "probe stage" in Fig. 2.16 (a)). We send around 2 mW of seed power to a semiconductor optical modulator (SOM) (AeroDiode, SOM-HPP), which both amplifies and switches the optical power. The maximum output power of the SOM is around 40 mW with an operating current of 200 mA. The light is brought into resonance via a double-pass through an AOM and sent to the atoms either through a fiber or through the 2.75" viewports perpendicular to the ONF.

2.4.3 Dipole Trap Beam

For trapping atoms in the optical lattice interfaced around the ONF (see Sec. 5), a dipole trap laser is prepared with a combination of a seed laser (Toptica DL pro) and a tapered amplifier

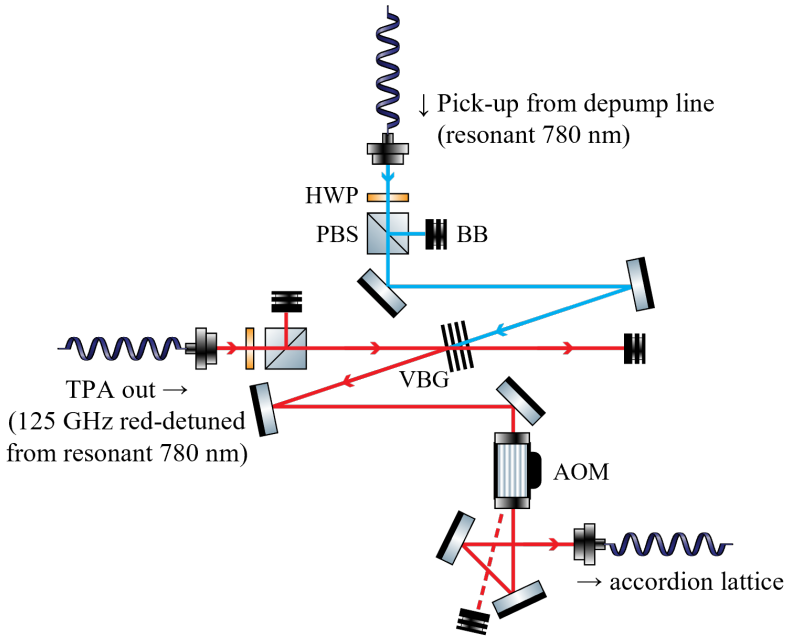

Figure 2.18: Schematics of laser setup for dipole trap beam preparation. The trap beam (red lines) is mixed with a pick-up from the depump line (blue line) via VBG. Since the two beams are separated in frequency by 125 GHz, the depump beam passes through the VBG. The two beams are sent to an AOM and the zeroth order mode is sent to the accordion lattice setup. HWP: half waveplate, PBS: polarizing beam splitter, BB: beam block, VBG: volume Bragg grating.

(TPA) (Thorlabs TPA780P20). The seed laser is 125 GHz red-detuned from depump transition $|F = 3\rangle \leftrightarrow |F' = 3\rangle$ in the D_2 line. The typical power of the seed laser injected into the TPA is ≈ 40 mW, and the typical output is ≈ 900 mW.

Fig. 2.18 shows the schematics of coupling the TPA output to the accordion lattice setup. We first filter the frequency mode with a volume Bragg grating (VBG). Then the beam is passed through an AOM and the zeroth order is fiber-coupled and sent to the optical lattice setup (see Fig. 5.4). The AOM modulates the power of the dipole trap beam by reducing the power to the zeroth order mode. By coupling the zeroth-order mode instead of the first-order mode, more trap beam power can be utilized. Although the AOM efficiency is not perfect, this configuration allows for effective power turnoff; when the AOM is fully driven, the zeroth-order mode becomes distorted, significantly reducing the fiber coupling efficiency. The maximum power at the fiber

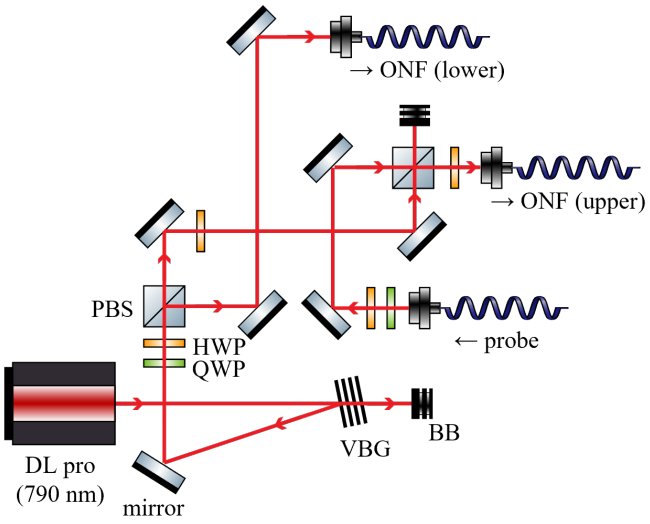

Figure 2.19: Schematics of laser setup for sending heating beams to the ONFs. The heating beam sent to the upper ONF is mixed with the probe beam at PBS.

output is $\approx$ 450 mW.

As can be seen in Fig. 2.18, another beam resonant to the depump transition is mixed into the setup. Since the depump and dipole trap beams are separated by 125 GHz, the depump beam passes through the VBG. This depump beam is blocked during the experiment and is only sent to the accordion lattice setup during alignment with the ONF. Having this additional resonant beam in the same optical path as the trap beam helps in visualizing the beam path, as it excites the ambient Rb vapor. It also assists with alignment to the ONF, since a portion of the lattice beams are coupled into the ONF and can be monitored.

2.4.4 Heating Beam

We continuously send a 790 nm light with a power of approximately 200 μW to the ONFs. This laser heats the ONF surface, preventing the fiber from being coated by Rb atoms. The exact frequency of the heating beam is not important as long as it is far detuned from atomic resonances.

The laser setup for sending the heating beam to the ONF is shown in Fig. 2.19. The heating beam is from Toptica DL pro which is frequency-tuned to 790 nm. It is first frequency filtered by a volume Bragg grating (VBG, bandwidth $\approx$ 50 pm) to suppress any frequency component in the resonant transition $|F = 3\rangle \leftrightarrow |F' = 4\rangle$ in the D_2 line. This is to protect the avalanche photodiode (APD) down the line. Then, the heating beam is separated in two, which are sent to each ONF. The heating beam directed to the upper ONF, which is used in the current experiments, is mixed with the probe beam in orthogonal polarizations. The polarization of the combined heating and probe beams is linearly rotated by the HWP downstream to adjust their orientation in the ONF region (see Sec. 2.5.1).

2.5 Imaging

2.5.1 Fluorescence Imaging

We image the MOT from the bottom and from the top to check its overlap with the ONFs. The setup for bottom-view imaging is shown in Fig. 2.20 (a). The bottom-view imaging setup shares the beam path with the z-direction MOT beams. We put a PBS in between the QWP and the retro-reflecting mirror to pick up the unpolarized MOT fluorescence without affecting the MOT beams. The fluorescent light is $4f$-imaged onto the camera (PointGrey FL3-FW-03S1M-C). We block the DC point in the Fourier plane to reject possible reflection of the MOT beams and get a cleaner image. Fig. 2.20 (b) shows an image taken which shows that MOT is horizontally overlapped with the ONFs.

The side-view imaging setup is shown in Fig. 2.21 (a). We collect the MOT fluorescence with 150 mm PCL. Then the beam passes through PBS, which only transmits vertical polariza-

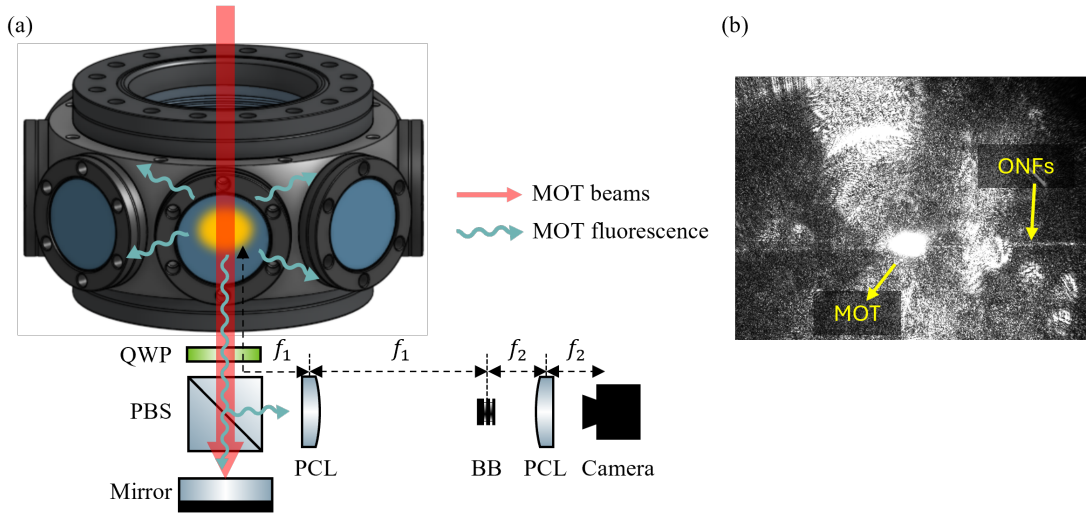

Figure 2.20: (a) Schematics of MOT fluorescence imaging from the bottom. The collimated and polarized MOT beams pass through the PBS and retro reflected. The MOT fluorescence is uncollimated and unpolarized, thus half of the power is reflected at the PBS, which is imaged via 4f imaging scheme. (b) A typical bottom-view image where the MOT and ONFs are aligned vertically.

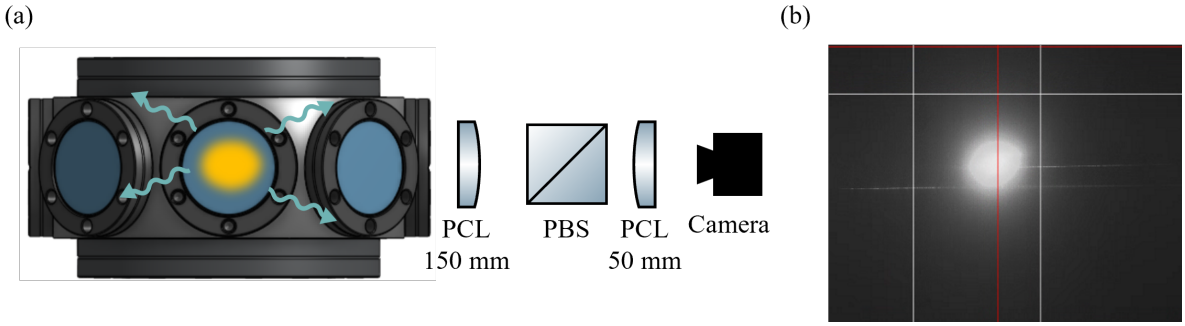

Figure 2.21: (a) Schematics of MOT fluorescence imaging from the side. A PCL of focal length 150 mm is placed at the focal point from the MOT center. Then the MOT is imaged by a second PCL of focal length 50 mm and onto the CCD camera. The PBS is placed between the two PCLs for polarization alignment of the guided beam. (b) A typical side-view image where the MOT and the upper ONF are overlapped vertically. The red and white lines are indicators in the camera program.

tion. This is used to align the polarization of the guided beam. We focus the fluorescent light with a 50 mm PCL onto a CCD camera (PointGrey FL2G-50S5C-C), with a magnification of 3.

2.5.2 Absorption Imaging

For absorption imaging, a collimated probe beam, which is large enough to cover the MOT, is sent from the direction opposite to the side-view imaging setup. The side-view imaging system images the intensity profile at the MOT position, effectively capturing the shadow cast by the atoms in the probe beam. For normalization, images are taken at three different time points: 1) with atoms present, 2) after the atoms have been dissipated away, and 3) with the probe beam off (background). The atomic absorption profile is then calculated using these three images.

Imaging atoms via their attenuation of light provides a direct measurement of the OD of the atomic cloud. In addition, since absorption imaging uses collimated probe light, it achieves unity collection efficiency and does not require a large collection angle, unlike fluorescence imaging.

2.6 Photon Counting System

Single-photon counting modules (SPCMs) and time-tagging electronics are used to measure photons emitted by the atoms into the ONF guided modes. Two SPCMs (Excelitas SPCM-780-13-FC and SPCM-AQRH-15-FC) are employed for photon detection. Since SPCMs operate at the single-photon level, they must be protected from exposure to excessive photon flux. To prevent saturation or damage from unknown source of light, strong frequency filtering is applied using two sequential VBGs. The VBGs are tuned to the ^{85}Rb D_2 transition and reflect only a narrow frequency band of $\approx$ 50 pm, centered around Bragg condition. The combined reflectivity

of the two VBGs for resonant light is $\approx 95\%$. Off-resonant frequency components do not reach the SPCMs.

The electrical signals from the SPCMs are sent to a time-tagging electronics (PicoQuant, PicoHarp 300). We record the arrival time of each photon with a bin time of 0.512 ns. Since the SPCMs output TTL signals while the PicoHarp accepts NIM signals, electrical attenuators and inverting circuits are used.

For simultaneous measurement from both SPCMs, we use a four-channel detector router (PicoQuant, PHR 800) designed to interface with the PicoHarp 300. It accepts up to four input channels, assigns time tags to each photon detection event, and sends the timing information for each channel to the PicoHarp 300.

2.7 Experimental Control and Measurement Program

A custom-written Python program is used to control and operate the experiments. It primarily interfaces with National Instruments PCI boards (NI PCI-6733 and PCIe-6353) and direct digital synthesizers (DDSs) (Novatech 409B). The analog and digital I/O channels of the PCI boards are used to switch and modulate various systems, including AOMs, APDs, and digital delay generators (Standard Research Systems DG645) The DDS outputs are sent directly to RF amplifiers, where the amplified signals drive the AOMs.

The program features a graphical interface for creating experimental sequences. Each sequence line supports two operation modes: constant and ramp. Based on this information on the modes, the clock signal is generated, inspired by the pseudoclock architecture in LabScript [159]. The devices are all clocked by a third device, a pulse blaster, which only clocks when the data

needs to be updated.

The program supports rapid repetition of experimental shots on the microsecond timescale, suitable for quantum optics experiments. The repetition rate is currently limited by the DDS table mode, which has a minimum time step of 100 μs.

A recent major update integrated measurement systems into the program, including analog inputs from NI boards and image acquisition from PointGrey cameras. This enables automated parameter scans, allowing for fast data collection with minimal system drift and human-induced noise.

Chapter 3: Collective Vacuum-Induced Quantum Beats

3.1 Observation of Vacuum-Induced Quantum Beats in Forward Scattering

We first investigate the forward-scattered mode of an ensemble with random positions. In this direction, it is known that the ensemble exhibits superradiant mode [115, 116]. We observed that in the superradiant mode, the transitions involving multiple excited levels can be also collectively enhanced, exhibiting collective quantum beats.

Quantum beats arise from the interference between transitions involving multiple excited states sharing a common ground state [160]. This interference leads to a periodic modulation in the decay profile of the emitted field intensity, with the modulation frequency corresponding to the energy difference between the excited states. Quantum beats have been used in precision measurements to probe the energy structure in atoms [161, 162], molecules [163], semiconductors [164], and quantum dots [165, 166].

Quantum beats are typically associated with an initial superposition of excited states. However, Hegerfeldt and Plenio theoretically demonstrated that quantum beats may appear even without such an initial superposition [167, 168]. This counterintuitive result arises from second-order vacuum-induced coupling between the excited states via a common ground state, which transfer population into initially unoccupied levels. It is helpful to recall that spontaneous emission is a second-order process, where the vacuum takes an excitation from an atom and returns it to the

atom. Upon integration of all the vacuum field modes, the excitation in the atom is gradually lost to the vacuum, resulting in exponential decay. If other excited levels lie near the initially populated one, the vacuum can see those levels and return the excitation into them. This second-order process connects the excited levels during decay and gives rise to vacuum-induced quantum beats.

Altenmuller reinterpreted the vacuum-induced quantum beats phenomenon using the dressed state picture [169]. In the presence of atom-field interaction, the bare atomic and field states are no longer the eigenstates of the system. Instead, the bare atomic state is a superposition of dressed states, thus resulting in the beating of these eigenstates.

The amplitude of vacuum-induced quantum beats scales as $\sim \Gamma/\Delta\omega$, where Γ is the decay rate of the excited states and $\Delta\omega$ is the energy separation between them. Since one typically considers $\Gamma \ll \Delta\omega$ for a well-defined multi-level energy structure, vacuum-induced quantum beats have generally been too small to be observed.

We show that vacuum-induced coupling between the upper levels can be collectively enhanced in an ensemble of atoms that are symmetrically coupled to the vacuum [136]. As a result, the amplitude of the quantum beats can be enhanced proportionally to the number of atoms participating in the collective dynamics. In this chapter, we summarize the theoretical and experimental study of collective quantum beats without an initial superposition. For more detailed discussions, see [136], which is included in Appendix C.

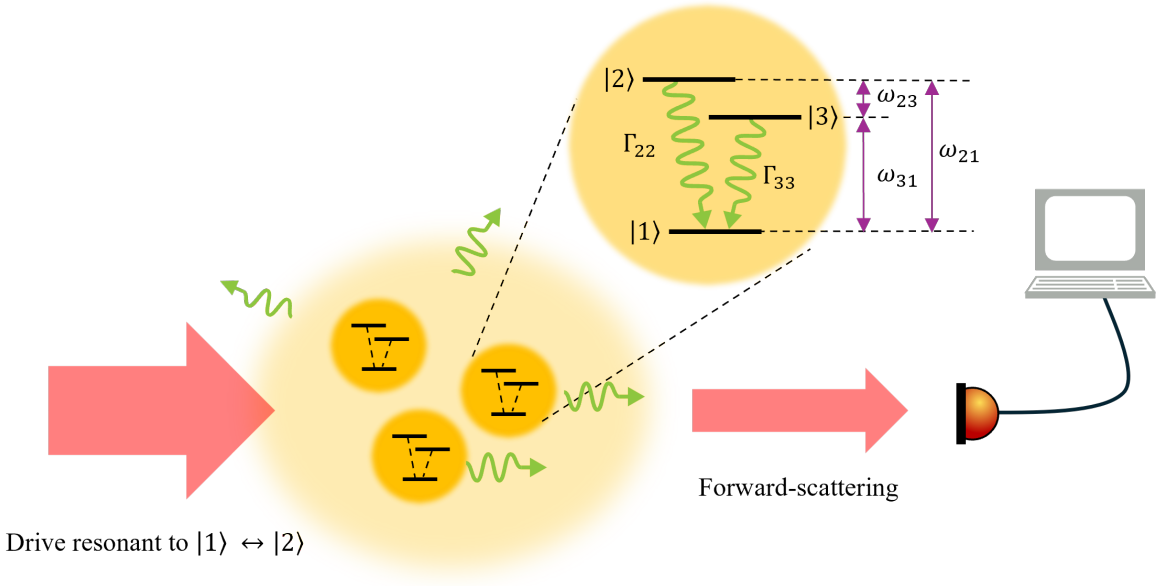

Figure 3.1: Schematics of the physical system and forward-scattering measurement for observation of collective vacuum-induced quantum beats.

3.1.1 Setup and Procedure

Figure 3.1 illustrates our system and measurement geometry for observing collective vacuum-induced quantum beats. We consider a three-level V-type level structure in the ^{85}Rb atom: $|1\rangle = \left|5^2S_{1/2}, F = 3\right\rangle$ is the ground state, and the two hyperfine states $|2\rangle = \left|5^2P_{3/2}, F' = 4\right\rangle$ and $|3\rangle = \left|5^2P_{3/2}, F' = 3\right\rangle$ serve as the excited states (see Fig. 1(b) in [136]). The decay rates from $|2\rangle$ and $|3\rangle$ to the ground state $|1\rangle$ are $\Gamma_{22} = 2\pi \times 6.1$ MHz and $\Gamma_{33} = (5/9)\Gamma_{22}$, respectively, where Γ_{33} is reduced considering the branching ratio [158]. The energy separation between the two excited states is $\omega_{23} = 2\pi \times 121$ MHz, and the transition wavelength between the ground and the excited states is $\lambda = 780$ nm.

We trapped a cloud of ^{85}Rb atoms and illuminated it with a long and weak drive beam resonant to the $|1\rangle \leftrightarrow |2\rangle$ transition. The drive intensity is $\sim 6 \times 10^8$ times smaller than the

saturation intensity, $I_s = 3.9$ mW/cm^2 [158]. Such a long and weak drive allows the system to reach a steady state in which most of the atomic population remains in the ground state $|1\rangle$, with a small fraction excited to $|2\rangle$. The population in $|3\rangle$ is negligible and can be ignored (see Supplemental Material in [136]).

We measured the forward-scattered mode with a small collection angle $\approx 6 \times 10^{-6}$ sr. In forward scattering, interference between atoms is ensured to be constructive regardless of their positions, as the phase differences in the atomic dipoles are exactly compensated by the photon propagation phase [115, 116].

3.1.2 Model

As we measure the forward scattered emission, we can capture the dynamics after the drive is turned off using a simple model in which N three-level V-type atoms are co-located at the origin. The Hamiltonian for such a system is

$$H = \sum_{m=1}^{N} \sum_{j=2,3} \hbar\omega_{j1} \hat{\sigma}^{+}_{m,j} \hat{\sigma}^{-}_{m,j} + \sum_{k,\mu} \hbar\omega_k \hat{a}^{\dagger}_{k,\mu} \hat{a}_{k,\mu} + \sum_{m=1}^{N} \sum_{j=2,3} \sum_{k,\mu} \hbar g_{m,j,k,\mu} \left(\hat{\sigma}^{+}_{m,j} \hat{a}_{k,\mu} + \hat{\sigma}^{-}_{m,j} \hat{a}^{\dagger}_{k,\mu} \right), \tag{3.1}$$

where $\hat{\sigma}^{+}_{m,j}$ and $\hat{\sigma}^{-}_{m,j}$ are the raising and lowering operators for the m-th atom and j-th level and $\hat{a}^{\dagger}_{k,\mu}$ and $\hat{a}_{k,\mu}$ are the creation and annihilation operator of the field mode with wave vector k and polarization μ. The atom-field coupling strength is $g_{m,j,k,\mu} \equiv \vec{d}^{m}_{j1} \cdot \vec{\varepsilon}_{k,\mu} \sqrt{\frac{\omega_k}{2\hbar\varepsilon_0 V}}$, where $\vec{\varepsilon}_{k,\mu}$ is the polarization unit vector of the field mode, ε_0 is the vacuum permittivity, and V is the vacuum mode volume. Each term in Eq. (3.1) corresponds to the atomic energy, EM field energy, and atom-light interaction energy, respectively. The atom-light interaction Hamiltonian

can take a single excitation from the N atom system and put it to the EM field modes and vice versa. Consequently, an excitation in the m-th atom and j-th level can couple to another atom and level via the second-order process mediated by the atom-light interaction. The vacuumm-induced coupling between $|j\rangle$ and $|l\rangle$ is quantified by the generalized decay rate

$$\Gamma_{jl} = \frac{d_{j1} \cdot d_{l1} \omega_{j1}^3}{3\pi\varepsilon_0 \hbar c^3}. \tag{3.2}$$

The vacuum-induced coupling between multiple atoms leads to collective decay, whose rate is enhanced in proportion to the number of atoms emitting cooperatively. In a realistic system, atoms may emit cooperatively only into certain field modes. Therefore, the collective decay rate can be written as $\Gamma_{jl}^{(N)} = (1 + fN)\Gamma_{jl}$, with f representing the fraction of emission modes that exhibit collective interference. In general, f depends on the geometry of the system, such as the shape of the atomic cloud and the detection mode.

Now imagine an initial state where all atoms share a single excitation in one of the excited levels, say $|2\rangle$, while the field modes are in the vacuum state $|\mathrm{vac}\rangle$:

$$|\Psi(0)\rangle = \frac{1}{\sqrt{N}} \sum_{m=1}^{N} \hat{\sigma}_{m,2}^{+} |11\cdots1\rangle |\mathrm{vac}\rangle . \tag{3.3}$$

In the regime where the upper levels are well resolved, i.e., $\Gamma_{jl}^{(N)} \ll \omega_{23}$, the atomic excitation amplitudes in $|2\rangle$ and $|3\rangle$ are

$$c_2(t) = \frac{1}{\sqrt{N}} \left[e^{-\Gamma_{22}^{(N)} t/2} e^{-i\omega_{21} t} - \left(\frac{\Gamma_{23}^{(N)}}{2\omega_{23}} \right)^2 \frac{\delta^*}{\delta} e^{-\Gamma_{33}^{(N)} t/2} e^{-i\omega_{31} t} \right], \tag{3.4a}$$

$$c_3(t) = -\frac{i\Gamma_{23}^{(N)}}{2\sqrt{N}\delta} \left[e^{-\Gamma_{22}^{(N)} t/2} e^{-i\omega_{21} t} - e^{-\Gamma_{33}^{(N)} t/2} e^{-i\omega_{31} t} \right], \tag{3.4b}$$

where $\delta = \sqrt{\omega_{23}^2 - \left(\Gamma_{\text{avg}}^{(N)}\right)^2 + 2i\omega_{23}\Gamma_{\text{d}}^{(N)}}$ with $\Gamma_{\text{avg}}^{(N)} = \frac{\Gamma_{33}^{(N)}+\Gamma_{22}^{(N)}}{2}$ and $\Gamma_{\text{d}} = \frac{\Gamma_{33}^{(N)}-\Gamma_{22}^{(N)}}{2}$. Note that the evolution of all atoms is identical, as both the initial state and the Hamiltonian are symmetric with respect to all atoms. As shown in Eq. (3.4a), most of the population in level $|2\rangle$ decays at a rate $\Gamma_{22}^{(N)}$, while the vacuum-induced coupling to level $|3\rangle$ enters as a perturbation. On the other hand, Eq. (3.4b) shows that the population in level $|3\rangle$ arises solely from the vacuum-induced coupling of the initial population in level $|2\rangle$ and scales as $|c_3(t)|^2 \sim \left(\frac{\Gamma_{23}^{(N)}}{\omega_{23}}\right)^2$.

The intensity of the light emitted from the atoms is

$$\frac{I(\tau)}{I_0} = e^{-\Gamma_{22}^{(N)}\tau} + \frac{\Gamma_{33}^{(N)}}{\Gamma_{22}^{(N)}}\left(\frac{\Gamma_{23}^{(N)}}{2\omega_{23}}\right)^2 e^{-\Gamma_{33}^{(N)}\tau} + \frac{\left(\Gamma_{23}^{(N)}\right)^2}{\omega_{23}\Gamma_{22}^{(N)}} e^{-\Gamma_{\text{avg}}^{(N)}\tau} \sin\left(\omega_{23}\tau + \arctan\frac{\Gamma_{22}^{(N)}}{\omega_{23}}\right), \tag{3.5}$$

where $I_0 = \frac{2d_{j1}d_{l1}\omega_{j1}^3\omega_{l1}^3}{3\pi\varepsilon_0 c^5}$. The first term is the decay of the initial excitation in level $|2\rangle$, the second term is the decay of the induced excitation in level $|3\rangle$, and the third term is the beating between the excitation in $|2\rangle$ and $|3\rangle$. The second term is negligible and can be omitted. Thus, we obtain the simplified model for the vacuum-induced beat dynamics seen in the intensity profile:

$$\frac{I(\tau)}{I_0} = e^{-\Gamma_{22}^{(N)}\tau} + I_b e^{-\Gamma_{\text{avg}}^{(N)}\tau} \sin(\omega_{23}\tau + \phi), \tag{3.6}$$

where the relative beat amplitude is

$$I_{\text{b}} \equiv \frac{\left(\Gamma_{23}^{(N)}\right)^2}{\omega_{23}\Gamma_{22}^{(N)}}, \tag{3.7}$$

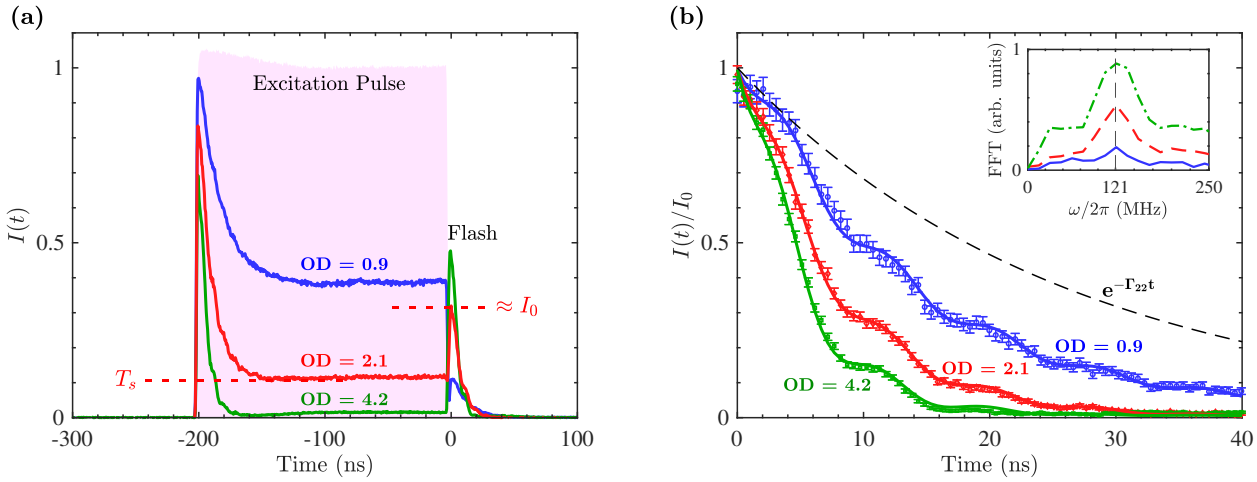

Figure 3.2: (a) Examples of the forward-scattered intensity normalized to the drive intensity for various ODs. As the drive field is abruptly turned off, the forward emission from atoms shows up. (b) The spontaneous decay profiles after the drive is turned off at time $t = 0$. The intensity of each curve is further normalized to the initial intensity (I_0). The single-atom decay profile $I(t) = e^{-\Gamma_{22}t}$ is drawn in black dashed line for comparison. The fast-Fourier transform (FFT) of the decay curves subtracted by the corresponding exponential fits are shown in the inset. Figures adapted from [136].

and the beat phase is

$$\phi = \arctan\left(\frac{\Gamma_{22}^{(N)}}{\omega_{23}}\right). \tag{3.8}$$

3.1.3 Result

The measured intensity profiles of the forward-scattering modes for different ODs are shown in Fig. 3.2. The OD is obtained from the steady-state transmission using the formula $\mathrm{OD} = -\ln \mathrm{T}$. The emission of atoms after the drive is turned off at time $t = 0$ is first fitted to an exponential function $e^{-\Gamma_{22}^{(N)}t}$, which shows linear dependence on the OD (see inset of Fig. 3.3 (a)). This confirms that we are seeing collective modes by measuring the forward-scattered emission.

On top of the decaying curve, we see a periodic modulation of intensity. The decaying curves are subtracted by the exponential fits and then Fourier-transformed (see inset of Fig. 3.2

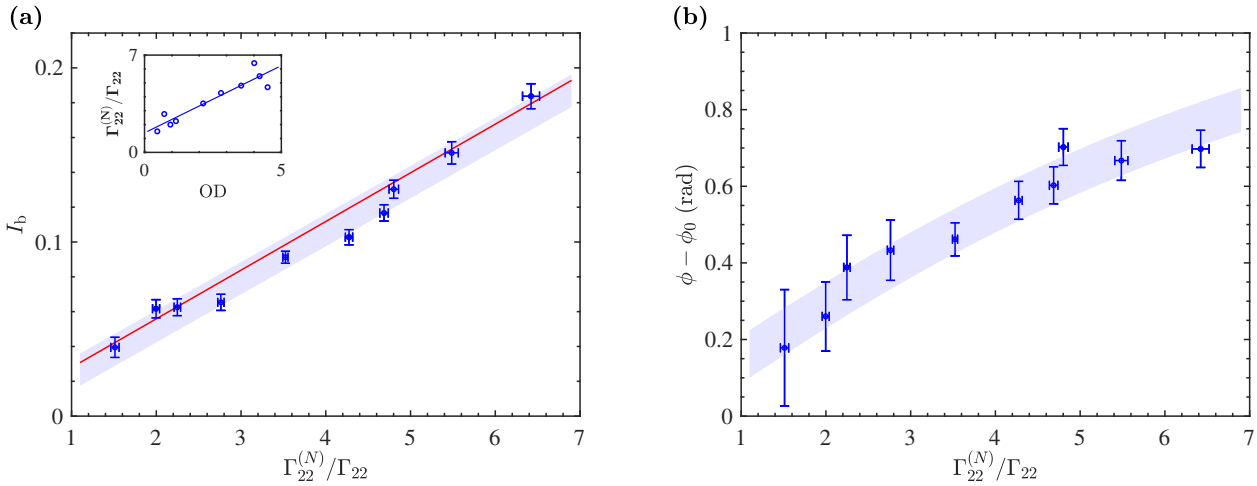

Figure 3.3: (a) The beat amplitude I_b and (b) the beat phase $\phi - \phi_0$ as a function of the collective enhancement factor $\Gamma_{22}^{(N)}/\Gamma_{22}$ for various ODs. The inset in (a) shows that the collective enhancement factor has linear dependence on the OD. Figures adapted from [136].

(b)), confirming that the modulation frequency corresponds to the energy separation between the excited levels. This signifies that we are seeing vacuum-induced quantum beats without initial superposition between upper levels.

Finally, the decay curve is fitted to Eq. (3.6) where we obtained the relative amplitude of the beating term and its phase, whose result is shown in Fig. 3.3. The beat amplitude is collectively enhanced, showing excellent agreement to the theory in Eq. (3.7). The phase of the beat is three times larger than expected value in Eq. (3.8). This might be due to the transient dynamics during the finite turn-off edge of the drive field (3.5 ns fall-time).

3.1.4 Discussion

We demonstrated collective quantum beats in the radiation of V-type atoms without an initial superposition of the upper levels, both theoretically and experimentally. The quantum beats without initial superposition show that the vacuum field can mediate population exchange between multiple atomic excited states. Although vacuum-induced coupling between hyperfine lev-

els is typically weak due to their large energy separation, the effect can be collectively enhanced by preparing an ensemble of atoms that couple to common EM field modes symmetrically. We measured forward scattering from a cloud of ^{85}Rb atoms driven by a weak and long excitation pulse. The spontaneous decay profile in the forward-scattered mode exhibits an enhanced decay rate increases linearly with OD, indicating the observation of supperadiant decay. The decay curve also shows periodic modulation at a frequency corresponding to the energy difference between the two upper hyperfine levels. The measured relative beat amplitude is proportional to the decay rate enhancement factor $\Gamma_{22}^{(N)}/\Gamma_{22}$, showing excellent agreement with our theoretical model without any free parameters. The observed beat phase also depends on the collective enhancement factor but is approximately three times larger than predicted. This discrepancy may arise from transient dynamics during the finite turn-off of the drive, suggesting the possibility that quantum beats could serve as a useful probe for characterizing non-equilibrium dynamics.

Our work demonstrates the rich interplay between two distinct quantum interference phenomena in spontaneous decay: collective dynamics in multi-atom systems [113] and quantum beats arising from multi-level systems [160]. Although these phenomena may seem unrelated, they can be described within a unified framework; multiple transitions, whether involving different atoms or different levels, can become coupled during the decay process. In the case of quantum beats, the key distinction lies in the energy differences between the transitions, which give rise to interference patterns manifesting as beating in the decay dynamics.

The study not only provides fundamental insight, but also applications in quantum technologies. For example, the vacuum-induced coupling between upper levels can provide transition pathways that can be engineered to make bright single-photon sources [170, 171]. The calculation we used can be applied to predict the collective dynamics of two quantum emitters

with energy level difference, which would be critical consideration in quantum computing using inhomogeneous emitters.

3.2 Collective Quantum Beats in Waveguide QED

Until now, the atoms have been assumed to be positioned at the same spatial point and to interact instantaneously. We now extend the study to include the effect of the photon propagation by considering the collective dynamics of V-type atoms via the waveguide. The waveguide enables long-range interaction between distant atoms as the photon does not suffer the $\sim 1/r^2$ power loss as in free space.

In analogy to the transition wavelength becoming the relevant length scale in determining the interference feature (super-/sub-radiance), we investigate the length scale that determines the interference involving multiple transitions of multiple atoms. Think of two photons emitted from an atom with slightly different transition frequencies, ω_{21} and ω_{31}, which are in phase when first emitted (see Fig. 2 in [153]). As the two photons travel along a waveguide, they gradually accumulate a phase difference, becoming perfectly out of phase at a distance $\pi v/\omega_{23}$. Thus, in determining the interference feature of multiple transitions, the "beat wavelength", $2\pi v/\omega_{23}$ becomes relevant. To give a sense of the relevant length scale, consider the example of the ^{85}Rb D_2 lines (Fig. 1(b) in [136]). The transition wavelengths for $|1\rangle \leftrightarrow |2\rangle$ and $|1\rangle \leftrightarrow |3\rangle$ are both around 780 nm. However, the beat wavelength between these two transitions is ≈ 2.5 m, a macroscopic length scale compared to the optical wavelength.

We first solve for the atomic and field dynamics where the physical systems for the quantum emitters and the waveguide are left general. For the numerical simulation, we use parameters

typical of superconducting qubit systems. We first investigate the Markovian regime, in which the atoms are delocalized but still interact instantaneously. This happens when the time delay between the atoms is smaller than the atomic relaxation timescale. Then we extend the system to the non-Markovian regime. The atomic separation becomes comparable to the relaxation time scale, introducing memory effects. In this limit, each atom interacts with the photon emitted by the other atom in the past. This section summarizes the work presented in [153], which is included in Appendix C, and also provides additional information not contained in the original publication.

Note that this theoretical study investigates scattering into modes other than the forward-scattered mode; specifically, it considers the case where the drive field illuminates the atoms perpendicularly, enabling the exploration of photon propagation effects.

3.2.1 Model

Consider two V-type emitters A and B coupled to a waveguide and positioned at x_A and x_B, as illustrated in Fig. 3.4. The ground state is denoted as $|1\rangle$ and the two excited states are $|2\rangle$ and $|3\rangle$. The transition frequency between $|1\rangle$ and $|2\rangle$ ($|3\rangle$) is ω_{21} (ω_{31}), and the energy difference between the two excited states is $\omega_{23} = \omega_{21} - \omega_{31}$. The excited states $|2\rangle$ and $|3\rangle$ decay to the ground state with rates Γ_{22} and Γ_{33}, respectively.

The Hamiltonian for the system is the same as Eq. (3.1), except that now the interaction Hamiltonian carries the phase term $e^{\pm ikx_m}$:

$$H_{AF} = -\sum_{m=A,B}\sum_{j=2,3}\sum_{k=-\infty}^{\infty}\sum_{\mu}\hbar g_{m,j,k,\mu}\left(\hat{\sigma}^{+}_{m,j}\hat{a}_{k,\mu}e^{ikx_m} + \hat{\sigma}^{-}_{m,j}\hat{a}^{\dagger}_{k,\mu}e^{-ikx_m}\right). \tag{3.9}$$

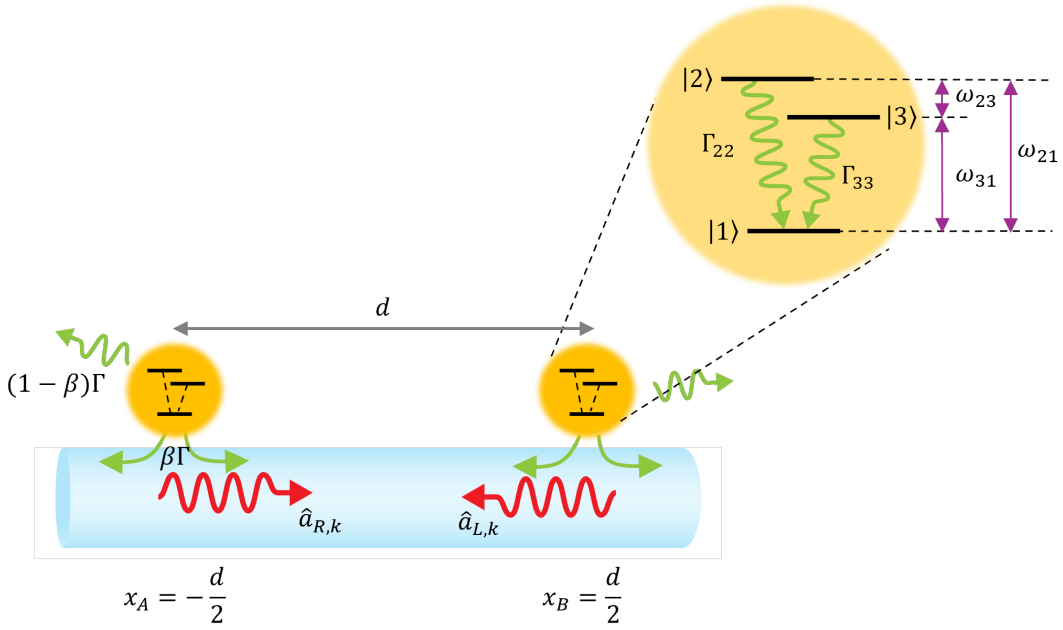

Figure 3.4: Schematics of the two V-type emitters coupled to a waveguide.

Note that k is now restricted in one-dimensional space. The phase terms reflect how atoms at different positions pick up different phases of the k-th Em field mode, leading to distance-dependent interference. Note that the previous model in Eq. (3.1) did not include such phase factors, as it assumed the atoms were co-located.

We solve the dynamics for two special initial states, where the atoms share a single excitation in state $|2\rangle$, either symmetrically or antisymmetrically:

$$\left|\Psi^{(+)}(0)\right\rangle = \frac{1}{\sqrt{2}}\Big(\,|2\rangle_A\,|1\rangle_B + |1\rangle_A\,|2\rangle_B\,\Big), \tag{3.10a}$$

$$\left|\Psi^{(-)}(0)\right\rangle = \frac{1}{\sqrt{2}}\Big(\,|2\rangle_A\,|1\rangle_B - |1\rangle_A\,|2\rangle_B\,\Big). \tag{3.10b}$$

Once we have the dynamics of the two initial states in Eq. (3.10), we can obtain the time-evolved state of a general initial state $|\Psi(0)\rangle = a\,|2\rangle_A\,|1\rangle_B + b\,|1\rangle_A\,|2\rangle_B + c\,|3\rangle_A\,|1\rangle_B + d\,|1\rangle_A\,|3\rangle_B$ from the superposition principle and the symmetry of the problem upon the exchange of variable

$|2\rangle \leftrightarrow |3\rangle$.

The time-evolved state remains in the single-excitation manifold:

$$\left|\Psi^{(+)}(t)\right\rangle = c_2^{(+)}(t)\left(|2\rangle_A|1\rangle_B + |1\rangle_A|2\rangle_B\right) + c_3^{(+)}(t)\left(|3\rangle_A|1\rangle_B + |1\rangle_A|3\rangle_B\right), \tag{3.11a}$$

$$\left|\Psi^{(-)}(t)\right\rangle = c_2^{(-)}(t)\left(|2\rangle_A|1\rangle_B - |1\rangle_A|2\rangle_B\right) + c_3^{(-)}(t)\left(|3\rangle_A|1\rangle_B - |1\rangle_A|3\rangle_B\right). \tag{3.11b}$$

Note that the symmetry of the atomic correlation in the initial state is maintained throughout the dynamics as the interaction Hamiltonian in Eq. (3.9) preserves the symmetry.

The atomic excitation amplitudes at time t for symmetric and antisymmetric initial states are expressed as a superposition of collective decay modes [1]:

$$c_2^{(\pm)}(t) = \sum_{n=-\infty}^{\infty} \alpha_n^{(\pm)} e^{s_n^{(\pm)} t}, \tag{3.12a}$$

$$c_3^{(\pm)}(t) = \sum_{n=-\infty}^{\infty} \beta_n^{(\pm)} e^{s_n^{(\pm)} t}. \tag{3.12b}$$

Here, $s_n^{(\pm)}$ is the generalized decay rate of the n-th decay mode, and $\alpha_n^{(\pm)}$ and $\beta_n^{(\pm)}$ are the corresponding coefficients of the decay modes for the dynamics of level $|2\rangle$ and $|3\rangle$, respectively. The generalized collective decay rate $s_n^{(\pm)}$ is the n-th pole of the propagator

$$G^{(\pm)}(s) \equiv \left(s + i\omega_{31} + \frac{\Gamma_{33}}{2} \pm \beta\frac{\Gamma_{33}}{2}e^{-\frac{d}{v}s}\right)\left(s + i\omega_{21} + \frac{\Gamma_{22}}{2} \pm \beta\frac{\Gamma_{22}}{2}e^{-\frac{d}{v}s}\right) - \frac{\Gamma_{23}\Gamma_{32}}{4}\left(1 \pm \beta e^{-\frac{d}{v}s}\right)^2. \tag{3.13}$$

[1] Note that here we define the atomic excitation amplitudes in Schrödinger picture, whereas in [153], we were defining things in the interaction picture. We later found that the Schrödinger picture yields a more symmetric form of the equations for $|2\rangle$ and $|3\rangle$. For example, The propagator in Eq. (3.13) shows symmetry upon change of variables: $|2\rangle \leftrightarrow |3\rangle$.

The coefficients of n-th decay mode are

$$\alpha_n^{(\pm)} = \lim_{s\to s_n}(s-s_n)\cdot\frac{1}{\sqrt{2}}\frac{s+i\omega_{31}+\frac{\Gamma_{33}}{2}\pm\beta\frac{\Gamma_{33}}{2}e^{-ds/v}}{G^{(\pm)(s)}}, \tag{3.14a}$$

$$\beta_n^{(\pm)} = -\lim_{s\to s_n}(s-s_n)\cdot\frac{1}{\sqrt{2}}\frac{\frac{\Gamma_{32}}{2}\pm\beta\frac{\Gamma_{32}}{2}e^{-ds/v}}{G^{(\pm)(s)}}. \tag{3.14b}$$

Note the symmetry of the problem under the exchange $|2\rangle \leftrightarrow |3\rangle$, except for the coefficients in Eq. (3.14), which are determined by the initial state. Since our initial state involves excitation only in $|2\rangle$, this symmetry is broken.

We now calculate the intensity of the light emitted by the two atoms. The intensity is evaluated by the expression $I(x,t) = \frac{\epsilon_0 c}{2}\langle\psi(t)|\hat{E}^\dagger(x,t)\hat{E}(x,t)|\psi(t)\rangle$, with the electric field operator defined as $\hat{E}(x,t) = \int_0^\infty \mathrm{d}k\mathcal{E}_k\hat{a}_k e^{ikx}e^{-i\omega_k t}$. Thus, the scattered light intensity is expressed as atomic amplitudes with appropriate time delay:

$$\frac{I(x,t)}{I_0} = \left|\sum_{j=2,3}\sum_{m=A,B}\frac{g_j}{g_2}\left\{\underbrace{c_{m,j}\left(t-\frac{x-x_m}{v}\right)\left[\Theta\left(t-\frac{x-x_m}{v}\right)-\Theta\left(-\frac{x-x_m}{v}\right)\right]}_{\text{Right light cone for atom } m \text{ at frequency } \omega_{j1}}\right.\right.$$
$$\left.\left.+\underbrace{c_{m,j}\left(t+\frac{x-x_m}{v}\right)\left[\Theta\left(t+\frac{x-x_m}{v}\right)-\Theta\left(\frac{x-x_m}{v}\right)\right]}_{\text{Left light cone for atom } m \text{ at frequency } \omega_{j1}}\right\}\right|^2. \tag{3.15}$$

Each term represents the light cone emitted by each atom, spreading in space-time with speed v while preserving causality. The rich interference pattern involving emission from two separated atoms and two excited levels can be seen in the intensity profile.

Decay rate of level 3 (Γ_{33}/Γ_{22})	1
Energy separation of level 2 and 3 (ω_{23}/Γ_{22})	50
Resonant frequency of level 2 (ω_{21}/Γ_{22})	10^4
Coherence length ($L_c \cdot \Gamma_{22}/v$)	1
Beat wavelength ($\lambda_{\text{beat}} \cdot \Gamma_{22}/v$)	$4\pi \times 10^{-2}$
Transition wavelength ($\lambda_{21} \cdot \Gamma_{22}/v$)	$2\pi \times 10^{-4}$

Table 3.1: Summary of parameters used in numerical simulation of quantum beats in waveguide QED, based on typical values in a superconducting circuit setup. The frequencies are in the units of Γ_{22}, and the lengths are in the units of v/Γ_{22}. Table adapted from [153].

3.2.2 Markovian limit

We numerically simulate the intensity profile in Eq. (3.15) using parameters in typical superconducting circuit systems [59, 172], as shown in Table 3.1. We first present the result in the Markovian limit, where the time delay between the two emitters is much shorter than the atomic relaxation time scale, i.e., $d/v \ll 1/\Gamma$. To ensure this condition, we chose the atomic separations between $0.5\lambda_{\text{beat}}$ and λ_{beat}, which are about ten times shorter than the coherence length.

Figure 3.5 shows the numerical simulation of the atomic and intensity profile of symmetric (blue solid lines) and antisymmetric (red dashed lines) initial states for the atomic separations being λ_{beat} and $0.5\lambda_{\text{beat}}$, assuming perfect coupling efficiency ($\beta = 1$). Figure 3.6 illustrates the poles and their coefficients in the dynamics of $|2\rangle$ and $|3\rangle$.

Level 2 Dynamics

The population in level $|2\rangle$ (Fig. 3.5 (a-b)) exhibits collective decay rate that is either enhanced ("superradiance", symmetric state) or suppressed ("subradiance", antisymmetric state) upon the arrival of the photon emitted by the other atom. The dynamics of level $|2\rangle$ resemble

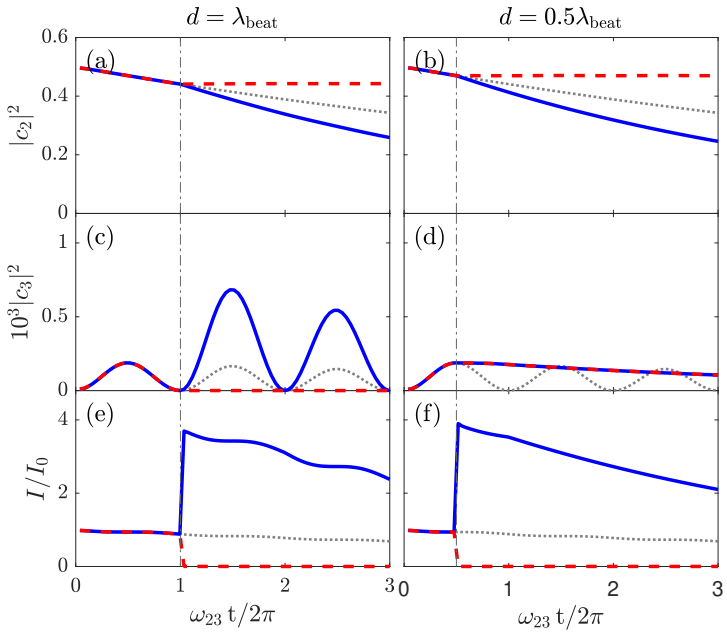

Figure 3.5: Atomic and field dynamics of two three-level V-type atoms coupled to a waveguide in the Markovian regime for perfect coupling efficiency ($\beta = 1$): (a-b) population in $|2\rangle$, (c-d) population in $|3\rangle$, and (e-f) intensity measured outside the system ($x \to x_B^+$, for interatomic separation (a,c,e) $d = \lambda_{\text{beat}}$ and (b,d,f) $d = 0.5\lambda_{\text{beat}}$. In all cases, the interatomic separation d is set to integer multiples of λ_{21}, and the symmetry of the problem is controlled by choosing the initial state to be either symmetric (blue solid lines) or antisymmetric (red dashed lines). The vertical dash-dotted lines indicate the time at which a photon emitted by one atom reaches the other. For comparison, the dynamics of a single atom are plotted as dotted lines. Figures adapted from [153].

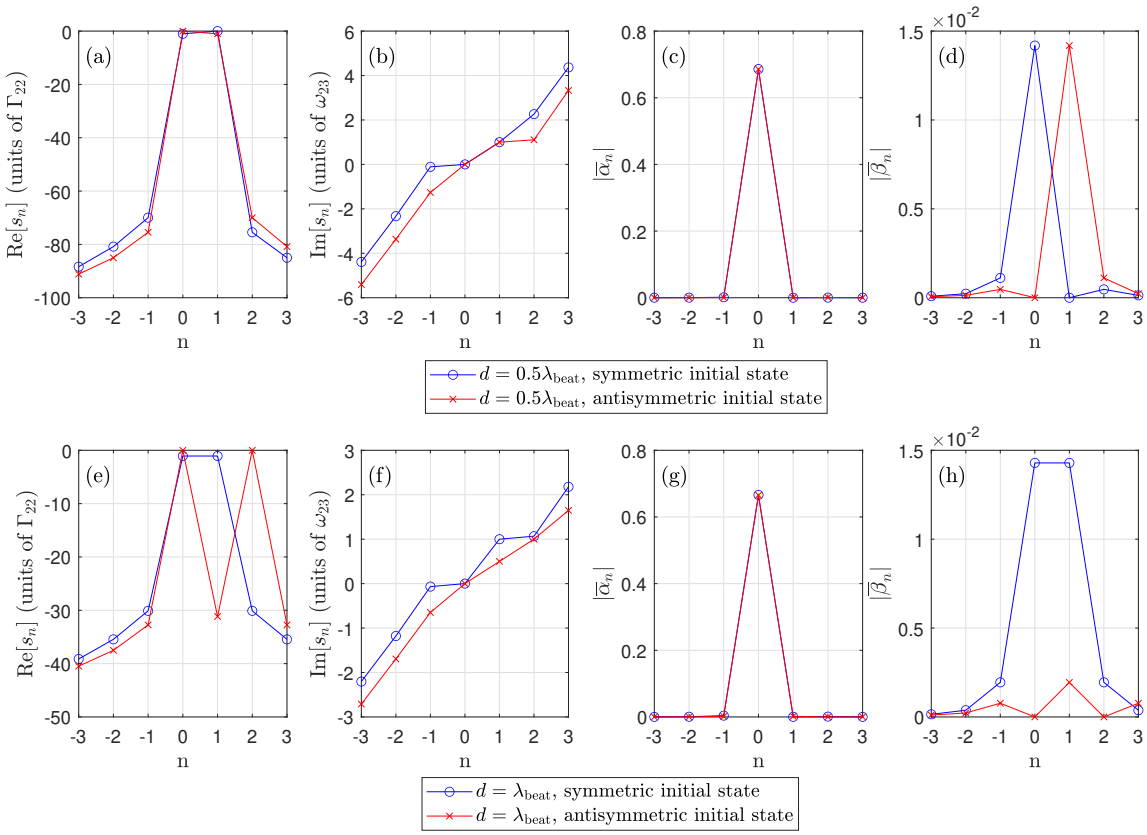

Figure 3.6: Poles of the collective dynamics for (a-d) $d = 0.5\lambda_{\text{beat}}$ and (e-h) $d = \lambda_{\text{beat}}$, with symmetric (blue) and antisymmetric (red) initial states. Each pole represents the collective decay mode with (a,e) real part indicating the decay rate and (b,f) the imaginary part energy level. The coefficient of the poles for (c,g) $|2\rangle$ and (d,h) $|3\rangle$ dynamics are shown. Figure adapted from [153].

that of an two-level system, and shows negligible dependence on the interatomic distance relative to λ_{beat}. This is because the coupling to level $|3\rangle$ enters only as a second-order perturbation effect.

Level 3 Dynamics

The population in level $|3\rangle$ (Fig. 3.5 (c-d)) signifies the collective vacuum-induced coupling, which is the dominant term when there is no initial excitation in level $|3\rangle$. When the interatomic distance is $d = \lambda_{\mathrm{beat}}$, the vacuum-induced coupling is fully enhanced (symmetric state) or fully suppressed (antisymmetric state). However, when the interatomic distance is $d = 0.5\lambda_{\mathrm{beat}}$, the vacuum-induced coupling is fully suppressed due to the destructive interference involving the two atoms, regardless of the initial symmetry of the atoms. The two photons with frequencies ω_{21} and ω_{31} are exactly out of phase when they travel a distance $0.5\lambda_{\mathrm{beat}}$.

Field Dynamics

As a result, the intensity profile (Fig. 3.5 (e-f)) shows a composite effect. First, the intensity is collectively enhanced in its size and decay rates when the two atoms are in the symmetric initial state, whereas it is fully suppressed when the atoms are antisymmetric initial state. It follows the level $|2\rangle$ dynamics as it is the leading term. Secondly, the collective quantum beats enters as a second order perturbation, which shows dependence on the interatomic separation with respect to λ_{beat}. Looking at the superradiant decay curves (solid blue lines), the quantum beats are collectively enhanced (suppressed) when the interatomic distance is integer (half-integer) multiples of λ_{beat}.

The limit $d \to 0$ with the symmetric initial state qualitatively agrees with our previous investigation using ^{85}Rb atoms described in Sec. 3.1. In that experiment, the atomic cloud size

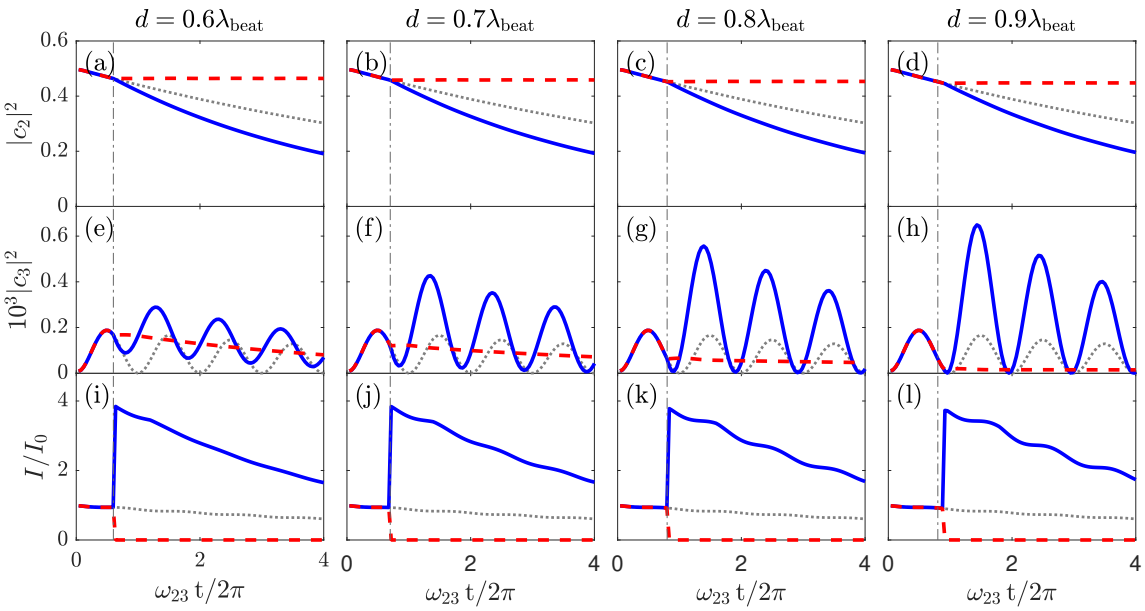

Figure 3.7: Span of distances in a Markovian regime: (a-d) level 2, (e-h) level 3, and (i-l) intensity dynamics for distances $0.6\lambda_{\text{beat}}$, $0.7\lambda_{\text{beat}}$, $0.8\lambda_{\text{beat}}$, and $0.9\lambda_{\text{beat}}$. The blue solid lines are for the case of symmetric initial state, and red dashed lines are for the antisymmetric initial state.

(~ 2 mm) was much smaller than the beat wavelength (~ 2.5 m). Consequently, the two photons of slightly different frequencies remained effectively in phase across the entire ensemble. Thus, the approximation of treating atoms as co-located could be justified.

Distance span between $d = 0.5\lambda_{\text{beat}}$ and $d = \lambda_{\text{beat}}$

Figure 3.7 shows the span of atomic and field dynamics in between $d = 0.5\lambda_{\text{beat}}$ and $d = \lambda_{\text{beat}}$. The $|2\rangle$ dynamics does not depend much on the atomic separation on the scale much less than v/Γ. The dynamics of $|3\rangle$ shows the interference of vacuum-induced coupling involving two atoms. For antisymmetric initial state (red dashed lines), the vacuum-induced coupling ceases as soon as the photon from one atom arrives to the other atom. In comparison, for symmetric case, we see transition from fully suppressed to fully enhanced vacuum-induced coupling as the distance is varied from $d = 0.5\lambda_{\text{beat}}$ to $d = \lambda_{\text{beat}}$. As a result, the intensity

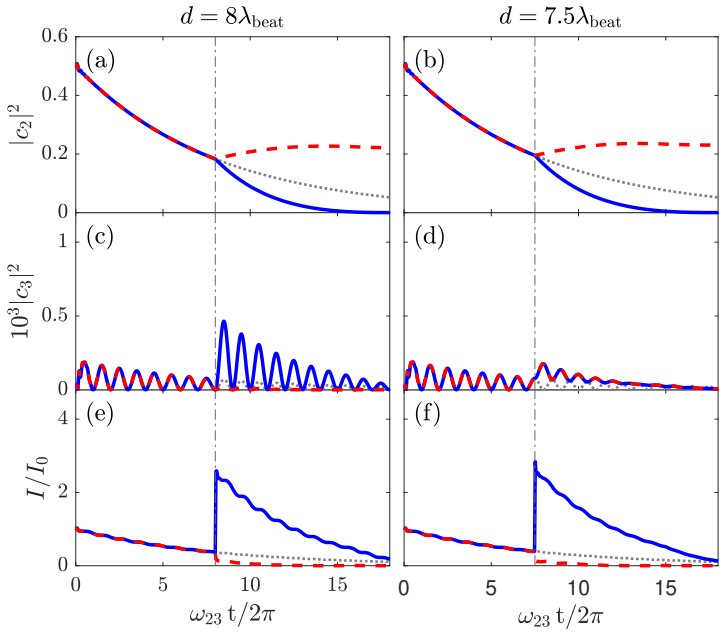

Figure 3.8: Atomic and field dynamics of two three-level V-type atoms coupled to a waveguide in the non-Markovian regime for perfect coupling efficiency ($\beta = 1$): (a-b) population in $|2\rangle$, (c-d) population in $|3\rangle$, and (e-f) intensity measured outside the system ($x \to x_B^+$, for interatomic separation (a,c,e) $d = 8\lambda_{\rm beat}$ and (b,d,f) $d = 7.5\lambda_{\rm beat}$. In all cases, the interatomic separation d is set to integer multiples of λ_{21}, and the symmetry of the problem is controlled by choosing the initial state to be either symmetric (blue solid lines) or antisymmetric (red dashed lines). The vertical dash-dotted lines indicate the time at which a photon emitted by one atom reaches the other. For comparison, the dynamics of a single atom are plotted as dotted lines. Figures adapted from [153].

profile shows transition from collectively suppressed quantum beats to the collectively enhanced quantum beats from $d = 0.5\lambda_{\rm beat}$ to $d = \lambda_{\rm beat}$.

3.2.3 Non-Markovian limit

We now consider the non-Markovian case, where the atoms are now separated by a time delay comparable to the atomic relaxation time scale ($d \gtrsim v/\Gamma$). In this regime, the atoms have significantly decayed by the time the photon emitted by the other atom arrives. Therefore, the photon-mediated interaction can no longer be treated as instantaneous, and a coherent time-

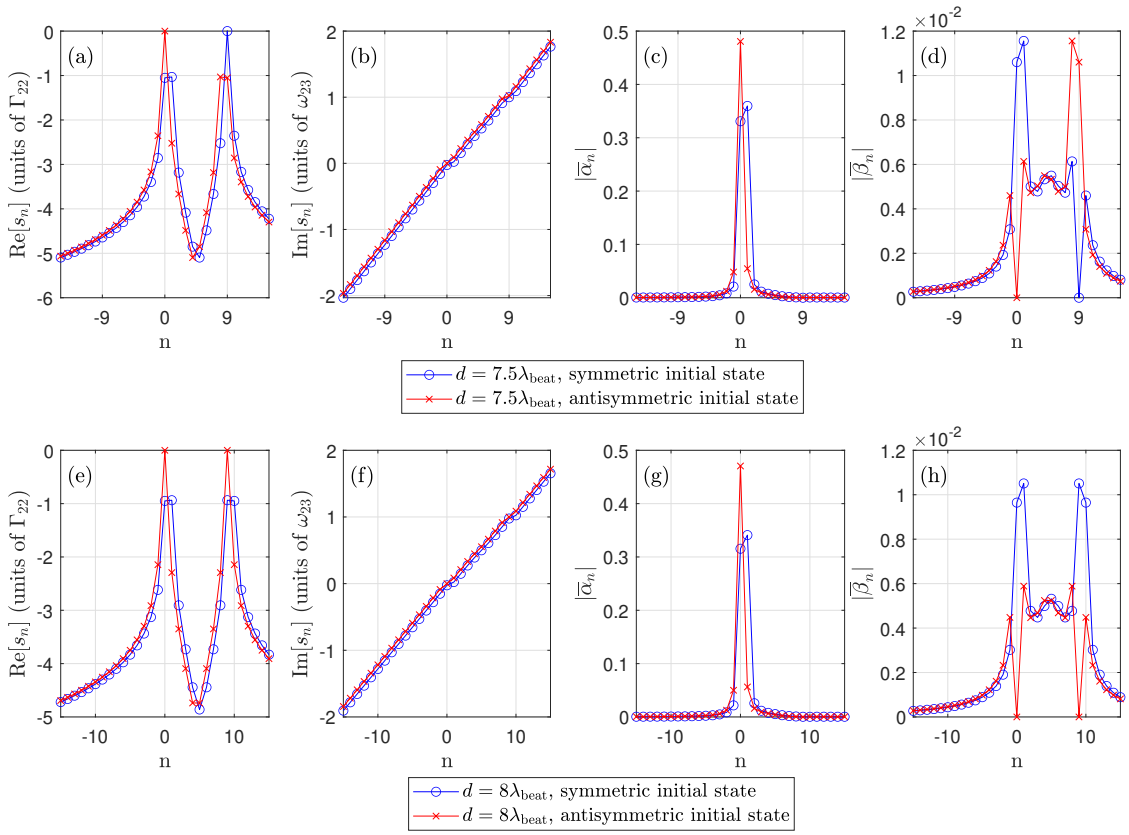

Figure 3.9: Poles of the collective dynamics for (a-d) $d = 7.5\lambda_{\text{beat}}$ and (e-h) $d = 8\lambda_{\text{beat}}$, with symmetric (blue) and antisymmetric (red) initial states. Each pole represents the collective decay mode with (a,e) real part indicating the decay rate and (b,f) the imaginary part energy level. The coefficient of the poles for (c,g) $|2\rangle$ and (d,h) $|3\rangle$ dynamics are shown. Figure adapted from [153].

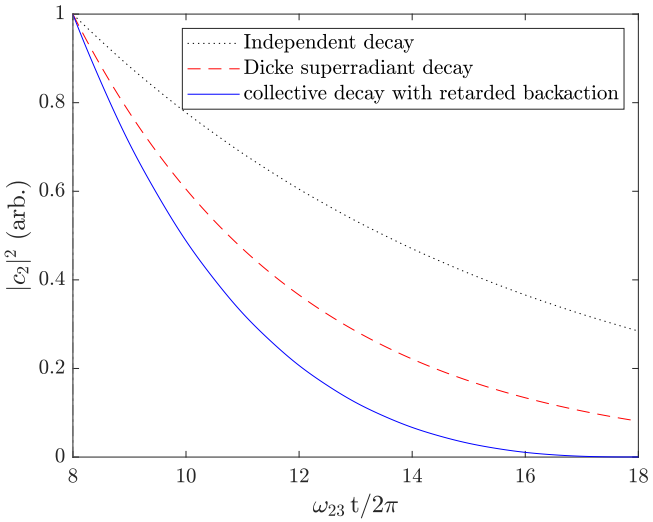

Figure 3.10: The dynamics of level $|2\rangle$ population for three different models: independent decay ($d = \infty$, dotted black), superradiant decay in Markovian regime ($d = 0$, dashed red), and faster-than-superradiant decay in non-Markovian regime ($d = 8\lambda_{\text{beat}}$, solid blue). The curves are rescaled to 1 at $t = 8\lambda_{\text{beat}}/v$ for comparison. Figures adapted from [153].

delayed feedback effect must be taken into account [66–68]. The atomic separations are varied between $7.5\lambda_{\text{beat}}$ and $8\lambda_{\text{beat}}$, which are comparable to the coherence length.

Figure 3.8 shows the numerical simulation of the atomic and field dynamics of symmetric (blue solid lines) and antisymmetric (red dashed lines) initial states for the atomic separations being $8\lambda_{\text{beat}}$ and $7.5\lambda_{\text{beat}}$, assuming perfect coupling efficiency ($\beta = 1$). Figure 3.9 illustrates the poles and their coefficients in the dynamics of $|2\rangle$ and $|3\rangle$.

Level 2 Dynamics

The level $|2\rangle$ dynamics as seen in Fig. 3.8 (a-b) manifests non-Markovian two-level system dynamics; the atom decays independently until it sees the photon that has been emitted by the other atom, and exhibit deviation from exponential decay thereafter. For a symmetric initial state, the atoms decay faster than the usual superradiant decay [66–68]. Figure 3.10 shows a

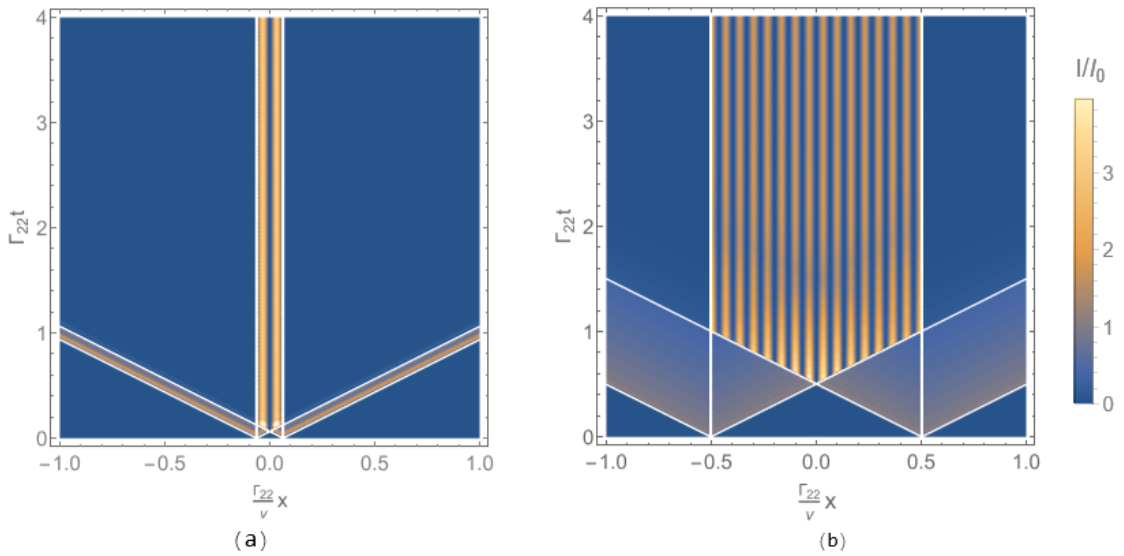

Figure 3.11: Intensity dynamics for an initially antisymmetric state of the two atoms as a function of detector position x and time. (a) For a small separation ($d = \lambda_{\text{beat}}$), the excitation stays mostly in the atoms, whereas (b) for a larger separation comparable to the coherence length ($d = 8\lambda_{\text{beat}}$), the bound state has a significant contribution from the photonic excitation amplitude, as observed from the standing wave formed in the region between the two atoms.

comparison of the population dynamics in $|2\rangle$, for independent decay (dotted black line), superradiant decay as in Markovian regime (dashed red line), and the faster-than-superradiant decay in non-Markovian regime(blue solid line). The time-delayed feedback accelerates the decay even beyond the Dicke superradiant decay.

For an antisymmetric initial state, the atoms form atom-photon bound states in the continuum (BIC) [69, 70, 173]. Such atom-photon bound states arise from the destructive interference between an atomic dipole and the fields emitted by the other atom, resulting in the field being reflected by the atoms and thus trapped between them. Note that, in the non-Markovian regime, this bound state comprises a large photonic excitation amplitude, unlike the subradiant state in the Markovian regime. This can be observed from Fig. 3.11, as well as the atom-photon bound state solution for a delocalized two-level system in Eq. (9) in [70], which we rewrite here for

convenience:

$$|\psi_b\rangle = \varepsilon_b \left[\hat{\sigma}_{\pm}^{+} - i\sqrt{\frac{\Gamma_{22}}{4v}} \int_{-d/2}^{d/2} \mathrm{d}x \left(e^{ik_0(x+d/2)}\hat{a}_R^{\dagger}(x) - e^{-ik_0(x+d/2)}\hat{a}_L^{\dagger}(x)\right)\right] |1\rangle_A |1\rangle_B |\{0\}\rangle \,, \tag{3.16}$$

where $|\varepsilon_b|^2 = 1/(1 + \frac{\Gamma_{22}d}{4v})$, $k_0 = \omega_{21}/v$, $\hat{\sigma}_{\pm}^{+} = (\hat{\sigma}_A^{+} \pm \hat{\sigma}_B^{+})/\sqrt{2}$ is the raising operator for the symmetric and antisymmetric collective state, $\hat{a}_{R(L)}^{\dagger}(x)$ is the real-space creation operator for the resonant right-(left-)going field modes at x. As d increases, the field component in the atom-photon bound state becomes more pronounced.

Level 3 Dynamics

The collective vacuum-induced coupling is seen in the dynamics of $|3\rangle$ (see Fig. 3.8 (c-d)). When the interatomic separation is $d = 8\lambda_{\mathrm{beat}}$ (Fig. 3.8 (c)), two different transitions of two different atoms are in phase. The symmetric state (solid blue line) shows collective enhancement of vacuum-induced coupling beyond the Markovian scaling that is proportional to the number of emitters. This can be explained by the significant contribution of collective decay modes near resonance (see blue dots in Fig. 3.9 (f) and (h)) arising from the delayed feedback effect. For the antisymmetric state (red dashed line), the vacuum-induced coupling is moderately suppressed. This is because of the contribution of collective modes near the resonance, which are not as fully suppressed as the resonant modes (see red dots in Fig. 3.9 (f) and (h)).

On the other hand, for the case $d = 7.5\lambda_{\mathrm{beat}}$, the collective vacuum-induced coupling is moderately suppressed regardless of the symmetry of the initial state. For a non-Markovian case, there are collective modes with frequencies close to the resonance, which significantly contribute

to the dynamics (see Fig. 3.9 (b) and (d)). Although the photons of the two transition frequencies become out of phase as they travel between the atoms, there are still collective decay channels they can couple to, and vacuum-induced coupling is not fully suppressed.

Field Dynamics

The field dynamics as shown in Fig. 3.8 (e-f)) exhibits a memory effect upon the arrival of the photon emitted by the other atom. For a symmetric initial state (blue solid lines), the intensity is enhanced in its size and decay rate, beyond collective enhancement in the Markovian regime. This is coined as superduperradiance [67, 68]. On the other hand, the radiation from atoms in an antisymmetric initial state exhibits destructive interference upon arrival of the time-delayed feedback. This suggests that the photon bounces back and forth between the atoms, forming a BIC [70].

We focus on the intensity profile of emission from symmetrically correlated atoms for the analysis of collective quantum beats. (solid blue lines in Fig. 3.8 (e-f)). When the atoms are separated by integer multiples of λ_{beat}, they exhibit quantum beats whose size is enhanced beyond the Markovian limit. On the other hand, for the case where the atoms are separated by half-integer multiples of λ_{beat}, the quantum beats are moderately suppressed; although the two transitions are destructively interfering at this propagation distance, there are other decay modes near the resonance that provide unsuppressed decay channels.

Distance span between $d = 7.5\lambda_{\mathrm{beat}}$ and $d = 8\lambda_{\mathrm{beat}}$

Figure 3.12 shows the atomic and field dynamics in between $d = 7.5\lambda_{\mathrm{beat}}$ and $d = 8\lambda_{\mathrm{beat}}$. In the level 3 dynamics (e-h), the vacuum-induced coupling shows a transition to fully enhanced

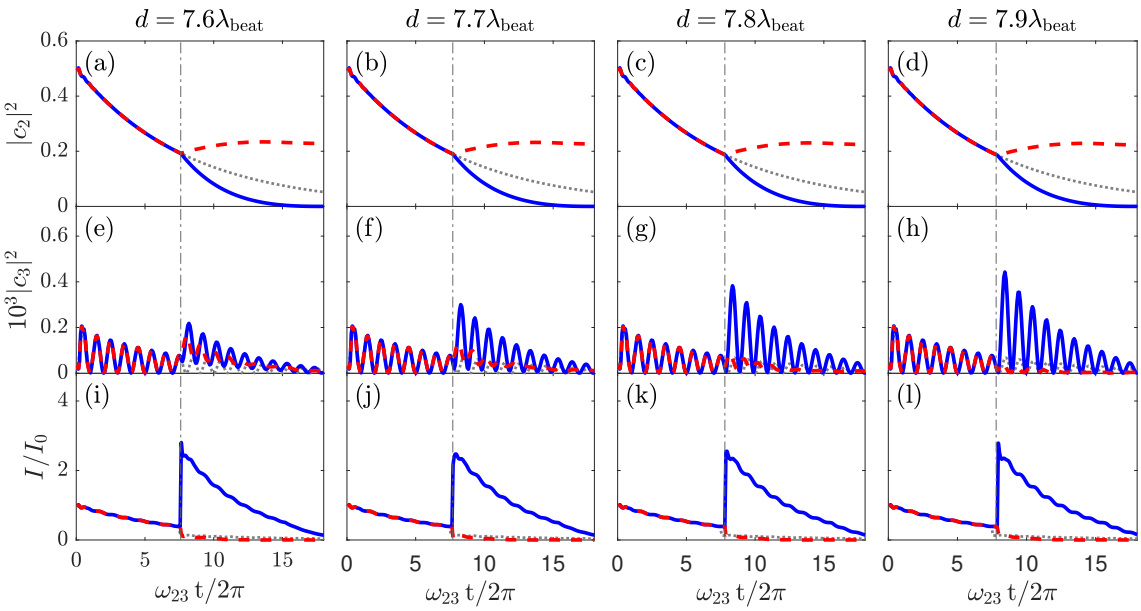

Figure 3.12: Span of distances in a non-Markovian regime: (a-d) level 2, (e-h) level 3, and (i-l) intensity dynamics for distances $7.6\lambda_{\text{beat}}$, $7.7\lambda_{\text{beat}}$, $7.8\lambda_{\text{beat}}$, and $7.9\lambda_{\text{beat}}$. The blue solid lines are for the case of a symmetric initial state, and the red dashed lines are for the antisymmetric initial state.

and suppressed cases as the separation of atoms is varied from $d = 7.5\lambda_{\text{beat}}$ to $d = 8\lambda_{\text{beat}}$.

3.2.4 Discussion

We theoretically studied collective vacuum-induced quantum beats, manifested in the spontaneous emission of two separated atoms coupled to a waveguide. We showed that atomic separation relative to the characteristic length scale $\lambda_{\text{beat}} = 2\pi v/\omega_{23}$ determines the interference between two different transitions in the distant atoms. As photons at frequencies ω_{21} and ω_{31} propagate, they accumulate a relative phase with a spatial period of λ_{beat}. When the atoms are separated by $\lambda_{\text{beat}}/2$, the two frequency components become out of phase. Consequently, if one transition becomes superradiant at this separation, the other must be subradiant, leading to suppression of the beating. In contrast, when the atoms are separated by λ_{beat}, the two frequency

components become in phase and exhibit collectively enhanced quantum beats.

We numerically calculated the atomic and field dynamics of spontaneous emission from two distant V-type emitters in a waveguide QED setup. In the Markovian regime, quantum beats are either enhanced proportionally with the number of atoms or completely suppresed, depending on the initial atomic state. As the atomic separation becomes comparable to the atomic relaxation timescale, the system enters the non-Markovian regime. In this regime, additional collective decay modes emerge near the resonant transitions, providing new decay channels that the traveling field modes can couple to. This leads to qualitatively different dynamics: quantum beats may become super-enhanced beyond the Markovian enhancement factor for symmetric initial states, or only moderately suppressed for antisymmetric states.

Our work offers valuable insights into delay effects in systems involving multi-level atoms. In particular, we demonstrated how collective decay modes interplay with atomic transition resonances. Our work offers a theoretical foundation for modeling long-range interactions between inhomogeneous emitters with multiple transition frequencies.

Chapter 4: Photon Correlations from Atomic Scattering in front of a Mirror

We now move on to investigate long-range interactions between atoms via ONF guided modes, as manifested in their radiative emission. Previously, Solano et al. demonstrated the collective decay of two atomic clouds separated by $\approx 300\,\mu$m, mediated by ONF guided modes [55]. Building on this experiment, we designed a new experiment aimed at observing the collective decay of a delocalized system interacting via an optical fiber, where the photon propagation time between the subsystems is comparable to the atomic relaxation time scale. In this setup, a cloud of ^{85}Rb atoms is coupled to an ONF and interacts with its mirror image formed by a distant mirror at the end of a long optical delay line (see Fig. 4.1).

We measure the intensity correlation function of the light scattered from the atomic cloud in this half cavity. Due to the low coupling efficiency of atoms to the ONF modes, we expect

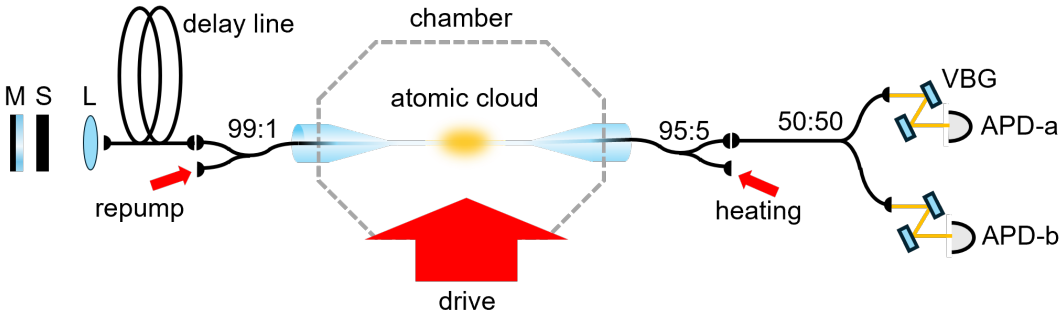

Figure 4.1: Schematic of the experimental setup for measuring the intensity correlation of light scattered from atoms in a half-cavity. M: mirror, S: shutter, L: lens, 99:1, 95:5, 50:50: beam splitters with given splitting ratio, VBG: volume Bragg grating, APD: avalanche photodiode.

correlation measurement will provide a clearer signature of non-Markovian dynamics than direct intensity measurements, as the intensity correlation function is conditioned on emission into the guided modes. The intensity correlation function of a single atom in front of a distant mirror has been theoretically studied [150] and experimentally demonstrated using a trapped ion in front of a mirror [174]. Depending on the emitter's position relative to the mirror, whether at a node, antinode, or slope of the standing wave in the half-cavity, the scattered light exhibits distinct behavior in its correlated photon counts. We aim to extend this study to (1) a waveguide QED platform, which offers greater scalability in delay length and atom number, and (2) a many-atom system, to explore the interplay between collective effects within a single ensemble and the non-Markovian dynamics.

On the other hand, a distinct yet equally relevant phenomenon that may arise in this setup is interference in the scattering from independent emitters coupled to a single EM field mode [175–180]. In the presence of multiple atoms, the photon statistics of the scattered light no longer exhibit the clean antibunching characteristic of single-atom scattering [3]. Instead, the system undergoes a transition from quasi-antibunching to bunching as the number of atoms increases [175, 176, 179, 180]. This transition arises from the increased probability that two atoms can be excited simultaneously and emit photons at the same time. Notably, the correlation between oppositely emitted photons remains antibunching regardless of the number of scatterers due to the underlying phase-matching condition [177, 178].

In this chapter, we present a theoretical framework for modeling a system comprising an atomic ensemble coupled to a waveguide and placed in front of a mirror, along with an experimental investigation using ^{85}Rb atoms interfaced with an ONF. The theory explores two distinct regimes: one dominated by time-delayed feedback (strong-coupling regime), and the other by

the external driving (weak-coupling regime). Analysis of our experimental data suggests that atoms coupled to an ONF interact only weakly via the guided modes. This implies that atomic ordering is required to achieve collectively enhanced cooperativity and exhibit strong atom-atom interaction via the ONF guided modes.

This chapter includes preliminary results from an ongoing project. The interpretations presented here are subject to revisions as the research progresses.

4.1 Model: Atomic Cloud in Front of a Mirror

We consider a system of N two-level atoms coupled to an ONF with coupling efficiency β. The atomic transition frequency is ω_0 and the decay rate is Γ. The atoms are driven by a laser of frequency ω_D propagating perpendicularly to the ONF. The j-th atom ($j = 1, 2, \cdots, N$) is placed at $z = z_j$ and a mirror is placed at $z = 0$, along the ONF. Without loss of generality, we can assume that both detectors are positioned at the same longitudinal location $z = z_d$ along the ONF, outside the half-cavity ($z_d > z_j,\ (j = 1, 2 \cdots, N)$).

The length scales relevant to this problem have the following relations. First, the size of the atomic ensemble is much smaller than the coherence length of the emitted photons, i.e., $|z_j - z_l| \ll v/\Gamma$ with v being the speed of light in the waveguide. This places the collective effects within a single ensemble in the Markovian regime. Secondly, the characteristic time delay between the atomic ensemble and its mirror image, τ_D, is comparable to the atomic relaxation time scale, $1/\Gamma$. The characteristic time delay is defined as $\tau_D \equiv 2z_0/v$, where $z_0 = \sum_{j=1}^{N} z_j/N$ is the average atomic position with respect to the mirror. As a result, the collective dynamics of the ensemble and its image lie in the non-Markovian regime. It is convenient to define the

dimensionless parameter $\eta = \tau_D \Gamma$, which is the normalized characteristic time delay with respect to the atomic relaxation time. Note that $\eta \gtrsim 1$ indicates that the system enters non-Markovian regime.

4.1.1 Hamiltonians

The electric field operator of the guided mode can be written as the sum of the positive and negative frequency components:

$$\hat{\mathbf{E}}(z) = \hat{\mathbf{E}}^{(+)}(z) + \hat{\mathbf{E}}^{(-)}(z). \tag{4.1}$$

The positive frequency component is given by

$$\hat{\mathbf{E}}^{(+)}(z) = i \int_0^\infty \mathrm{d}k \boldsymbol{\alpha}_k \sin(kz) \hat{a}_k, \tag{4.2}$$

where $\boldsymbol{\alpha}_k$ is the mode amplitude and $\hat{a}_k$ is the annihilation operator for the k-th guided mode. The negative frequency component $\hat{\mathbf{E}}^{(-)}(z)$ is the Hermitian conjugate of the positive frequency component $\hat{\mathbf{E}}^{(+)}(z)$. Note that the mode profile forms a standing wave structure due to the presence of the mirror at $z = 0$.

The total Hamiltonian is

$$H = H_0 + H_{\mathrm{D}} \tag{4.3}$$

where H_0 is the total Hamiltonian of the system of atoms and the guided field modes, and H_{D} is

the drive Hamiltonian. H_0 is

$$H_0 = H_{\mathrm{A}} + H_{\mathrm{F}} + H_{\mathrm{AF}}, \tag{4.4}$$

where H_{A} is the atomic Hamiltonian, H_{F} is the Hamiltonian of the electric field in the guided mode, and H_{AF} describes the interaction between the atoms and the guided mode. Note that we omitted the free-space field modes for simplicity; their effect is accounted phenomenologically through the coupling efficiency β. Each Hamiltonian reads

$$H_{\mathrm{A}} = \sum_{j=1}^{N} \hbar\omega_0 \hat{\sigma}_j^+ \hat{\sigma}_j^-, \tag{4.5a}$$

$$H_{\mathrm{F}} = \sum_k \hbar\omega_k \hat{a}_k^\dagger \hat{a}_k, \tag{4.5b}$$

$$H_{\mathrm{AF}} = i\sum_{j=1}^{N} \int_0^\infty \mathrm{d}k \, (\mathbf{d}_j \cdot \boldsymbol{\alpha}_k) \sin(kz_j) \left(\hat{\sigma}_j^- \hat{a}_k^\dagger - \hat{\sigma}_j^+ \hat{a}_k \right), \tag{4.5c}$$

$$H_{\mathrm{D}} = -\hbar\frac{\Omega}{2} \sum_{j=1}^{N} \left(e^{i\omega_D t} \hat{\sigma}_j^- + e^{-i\omega_D t} \hat{\sigma}_j^+ \right), \tag{4.5d}$$

where $\hbar$ is the reduced Planck constant, $\hat{\sigma}_j^+$, and $\hat{\sigma}_j^-$ are the raising and lowering operators for the j-th atom, ω_k is the frequency of the k-th guided mode, $\mathbf{d}_j$ is the dipole moment of the j-th atom, and Ω is the Rabi frequency of the drive field.

4.1.2 Electric Field Operator in Heisenberg Picture

To calculate the correlation functions of the electric field operator, it is convenient to work in the Heisenberg picture. Since our primary interest lies in how excitations transfer between the atoms and the guided modes, we neglect the drive Hamiltonian for now. The guided field

operator in the Heisenberg picture is thus

$$\hat{a}_k(t) \equiv e^{iH_0 t/\hbar} \hat{a}_k e^{-iH_0 t/\hbar} \tag{4.6}$$

The guided mode field operator follows the equation of motion:

$$\begin{aligned}
\frac{\mathrm{d}\hat{a}_k(t)}{\mathrm{d}t} &= \frac{i}{\hbar} \left[H_0, \hat{a}_k(t)\right], \\
&= \frac{i}{\hbar} e^{iH_0 t/\hbar} \left[H_0, \hat{a}_k\right] e^{-iH_0 t/\hbar}, \\
&= -i\omega_k \hat{a}_k(t) + \sum_{j=1}^{N} \frac{\mathbf{d}_j \cdot \boldsymbol{\alpha}_k}{\hbar} \sin(kz_j) \hat{\sigma}_j^-(t).
\end{aligned} \tag{4.7}$$

Under the transformation

$$\begin{aligned}
\hat{\tilde{a}}_k(t) &= \hat{a}_k(t) e^{i\omega_k t}, \\
\hat{\tilde{\sigma}}_j^-(t) &= \hat{\sigma}_j^- e^{i\omega_0 t},
\end{aligned} \tag{4.8a}$$

we get a simpler form of the equation of motion:

$$\frac{\mathrm{d}\hat{\tilde{a}}_k(t)}{\mathrm{d}t} = \sum_{j=1}^{N} \frac{\mathbf{d}_j \cdot \boldsymbol{\alpha}_k}{\hbar} \sin(kz_j) \hat{\tilde{\sigma}}_j^-(t) e^{i(\omega_k - \omega_0)t}. \tag{4.9}$$

Formally integrating Eq. (4.9), we get the annihilation operator of the guided field mode at time t

$$\hat{\tilde{a}}_k(t) = \hat{\tilde{a}}_k(0) + \sum_{j=1}^{N} \frac{\mathbf{d}_j \cdot \boldsymbol{\alpha}_k}{\hbar} \sin(kz_j) \int_0^t \mathrm{d}t' e^{i(\omega_k - \omega_0)t'} \hat{\tilde{\sigma}}_j^-(t'). \tag{4.10}$$

Thus, the electric field operator in guided mode is

$$\hat{\mathbf{E}}^{(+)}(z,t) = \hat{\mathbf{N}}^{(+)}(z,t) + \sum_{j=1}^{N} \hat{\mathbf{E}}_j^{(+)}(z,t), \tag{4.11}$$

where $\hat{\mathbf{N}}(z,t)$ is the noise field and $\hat{\mathbf{E}}_j(z,t)$ is the field scattered by the j-th atom:

$$\hat{\mathbf{N}}^{(+)}(z,t) = i\int_0^\infty \mathrm{d}k\boldsymbol{\alpha}_k \sin(kz) e^{-i\omega_k t}\hat{\tilde{a}}_k(0), \tag{4.12a}$$

$$\hat{\mathbf{E}}_j^{(+)}(z,t) = i\int_0^\infty \mathrm{d}k\boldsymbol{\alpha}_k \sin(kz) e^{-i\omega_k t}\frac{\mathbf{d}_j\cdot\boldsymbol{\alpha}_k}{\hbar}\sin(kz_j)\int_0^t \mathrm{d}t' e^{i(\omega_k-\omega_0)t'}\hat{\tilde{\sigma}}_j^-(t'). \tag{4.12b}$$

Assuming a flat spectral density of the guided modes ($\boldsymbol{\alpha} = \boldsymbol{\alpha}_k$) and identical and aligned atomic dipoles ($\mathbf{d} = \mathbf{d}_j$), we can simplify the integration in Eq. (4.12b).

$$\begin{aligned}\hat{\mathbf{E}}_j^{(+)}(z,t) = \mathbf{E}_0\Bigg[&\hat{\tilde{\sigma}}_j^-\left(t-\left|\frac{z-z_j}{v}\right|\right)e^{-i\omega_0\left(t-\left|\frac{z-z_j}{v}\right|\right)}\Theta\left(t-\left|\frac{z-z_j}{v}\right|\right)\\ &-\hat{\tilde{\sigma}}_j^-\left(t-\left|\frac{z+z_j}{v}\right|\right)e^{-i\omega_0\left(t-\left|\frac{z+z_j}{v}\right|\right)}\Theta\left(t-\left|\frac{z+z_j}{v}\right|\right)\Bigg],\end{aligned} \tag{4.13}$$

where $\mathbf{E}_0 = i\frac{\pi(\mathbf{d}\cdot\boldsymbol{\alpha})\boldsymbol{\alpha}}{4\hbar}$. The first term is the field emitted by the real atom, and the second term is the field emitted by the image atom.

We consider a realistic system in which losses due to free-space emission and imperfect mirror reflectivity are taken into account. The overall amplitude of the electric field operator is scaled by the coupling efficiency β, to account for emission into non-guided modes, while the reflection term is multiplied by the mirror reflection coefficient r. We interchangeably use the mirror reflectivity $R = |r|^2$ in this chapter. The electric field operator, including these loss

channels, is given by

$$\hat{\mathbf{E}}_j^{(+)}(z,t) = \beta \mathbf{E}_0 \left[\hat{\tilde{\sigma}}_j^- \left(t - \left| \frac{z - z_j}{v} \right| \right) e^{-i\omega_0 \left(t - \left| \frac{z-z_j}{v} \right| \right)} \Theta \left(t - \left| \frac{z - z_j}{v} \right| \right) \right.$$
$$\left. - r \hat{\tilde{\sigma}}_j^- \left(t - \left| \frac{z + z_j}{v} \right| \right) e^{-i\omega_0 \left(t - \left| \frac{z+z_j}{v} \right| \right)} \Theta \left(t - \left| \frac{z + z_j}{v} \right| \right) \right]. \tag{4.14}$$

4.1.3 Correlation Functions of Radiation Fields

The intensity correlation function of the radiation emitted from the atoms in the half-cavity is

$$G_N^{(2)}(\tau) = \lim_{t \to \infty} \sum_{j,l,m,n=1}^{N} \left\langle \hat{E}_j^{(-)}(z_d,t) \hat{E}_l^{(-)}(z_d,t+\tau) \hat{E}_m^{(+)}(z_d,t+\tau) \hat{E}_n^{(+)}(z_d,t) \right\rangle, \tag{4.15}$$

where we have neglected the noise field, assuming it is much weaker than the fields scattered by the atoms. Plugging in Eq. (4.14) into Eq. (4.15), the intensity correlation function can be expressed in terms of atomic operators' correlation functions as follows:

$$\frac{G_N^{(2)}(\tau)}{|\beta E_0|^4} = \lim_{t \to \infty} \sum_{j,l,m,n=1}^{N} \left\langle \left[\hat{\tilde{\sigma}}_j^+ \left(t - \frac{z_d - z_j}{v} \right) e^{i\omega_0 \frac{z_j}{v}} - r \hat{\tilde{\sigma}}_j^+ \left(t - \frac{z_d + z_j}{v} \right) e^{-i\omega_0 \frac{z_j}{v}} \right] \right.$$
$$\left[\hat{\tilde{\sigma}}_l^+ \left(t + \tau - \frac{z_d - z_l}{v} \right) e^{i\omega_0 \frac{z_l}{v}} - r \hat{\tilde{\sigma}}_l^+ \left(t + \tau - \frac{z_d + z_l}{v} \right) e^{-i\omega_0 \frac{z_l}{v}} \right]$$
$$\left[\hat{\tilde{\sigma}}_m^- \left(t + \tau - \frac{z_d - z_m}{v} \right) e^{-i\omega_0 \frac{z_m}{v}} - r \hat{\tilde{\sigma}}_m^- \left(t + \tau - \frac{z_d + z_m}{v} \right) e^{i\omega_0 \frac{z_m}{v}} \right]$$
$$\left. \left[\hat{\tilde{\sigma}}_n^- \left(t - \frac{z_d - z_n}{v} \right) e^{-i\omega_0 \frac{z_n}{v}} - r \hat{\tilde{\sigma}}_n^- \left(t - \frac{z_d + z_n}{v} \right) e^{i\omega_0 \frac{z_n}{v}} \right] \right\rangle. \tag{4.16}$$

The steady-state intensity of light scattered by N atoms outside the half-cavity is

$$I_N = \lim_{t\to\infty} \sum_{j,l=1}^{N} \left\langle \hat{E}_j^{(-)}(z_d,t)\hat{E}_l^{(+)}(z_d,t) \right\rangle . \tag{4.17}$$

Expressing Eq. (4.36) in terms of atomic operators, we get

$$\begin{aligned}\frac{I_N}{|\beta E_0|^2} = \lim_{t\to\infty} \sum_{j,l=1}^{N} \Bigg\langle & \left[\hat{\tilde{\sigma}}_j^{+} \left(t - \frac{z_d - z_j}{v} \right) e^{i\omega_0 \frac{z_j}{v}} - r\hat{\tilde{\sigma}}_j^{+} \left(t - \frac{z_d + z_j}{v} \right) e^{-i\omega_0 \frac{z_j}{v}} \right] \\ & \left[\hat{\tilde{\sigma}}_l^{-} \left(t - \frac{z_d - z_l}{v} \right) e^{-i\omega_0 \frac{z_l}{v}} - r\hat{\tilde{\sigma}}_l^{-} \left(t - \frac{z_d + z_l}{v} \right) e^{i\omega_0 \frac{z_l}{v}} \right] \Bigg\rangle . \end{aligned} \tag{4.18}$$

Now, both the intensity correlation function (Eq. (4.16)) and the intensity (Eq. (4.18)) of the scattered light are expressed in terms of atomic operators and are governed by the atomic dynamics. The atoms interact with two types of EM fields: the drive laser illuminating the atoms from the side, and the photons emitted by the atoms and reflected back onto them. The competition between these two fields can be characterized by the ratio of the drive strength ($\sim \Omega$) to the feedback strength due to the interaction with the returning photons ($\sim \beta^2\Gamma$).

4.2 Strong Coupling Regime ($\beta^2\Gamma \gtrsim \Omega$)

In the regime where the coupling efficiency is large and the drive is weak ($\beta^2\Gamma \gtrsim \Omega$), the atomic internal dynamics is primarily determined by the returning photons, resulting in a time-delayed feedback effect. We first solve for the atomic dynamics considering the time-delayed back action without the drive field, and then include the external drive as a perturbation.

4.2.1 Free Dynamics

We first solve for the dynamics of the atoms and guided field modes under H_0, the undriven part of the Hamiltonian. We consider the initial state of atoms that are symmetrically excited:

$$|\psi(0)\rangle = |+\rangle = \frac{1}{\sqrt{N}} \sum_{j=1}^{N} \hat{\sigma}_j^+ |G, \{0\}_k\rangle \,, \tag{4.19}$$

where $|G\rangle = |g, g, \cdots, g\rangle$ is the state where all atoms are in the ground states, and $|\{0\}_k\rangle$ is the state where there is no photon in the guided modes. We only consider the symmetric state as our initial state because the perpendicular illumination of the drive prepares the atoms in the symmetric superposition state.

We move to the interaction picture with respect to $H_{\mathrm{A}} + H_{\mathrm{F}}$. The atom-field interaction Hamiltonian in the interaction picture is

$$\tilde{H}_{\mathrm{AF}} = i \sum_{j=1}^{N} \int_0^\infty \mathrm{d}k \, (\mathbf{d}_j \cdot \boldsymbol{\alpha}_k) \sin(kz_j) \left(\hat{\sigma}_j^- \hat{a}_k^\dagger e^{i(\omega_k - \omega_0)t} - \hat{\sigma}_j^+ \hat{a}_k e^{(-i(\omega_k - \omega_0)t} \right). \tag{4.20}$$

The system evolution under $\tilde{H}_{\mathrm{AF}}$ keeps the system in the single excitation manifold. Thus, the time-evolved ansatz can be written as

$$|\psi(t)\rangle = \left[\sum_{j=1}^{N} \tilde{c}_j(t) \hat{\sigma}^+ + \sum_k \tilde{c}_k(t) \hat{a}^\dagger \right] |G, \{0\}_k\rangle \,, \tag{4.21}$$

where $\tilde{c}_j(t)$ is the excitation amplitude for the j-th atom and $\tilde{c}_k(t)$ is the amplitude for the k-th guided mode in the interaction picture. Writing the Schrodinger equation and removing the field

degrees of freedom, we get the differential equation for the atomic dynamics:

$$\begin{aligned}\partial_t \tilde{c}_j(t) = &-\frac{\Gamma}{2}\tilde{c}_j(t)\Theta(t) \\ &- \beta\frac{\Gamma}{2}\sum_{l\neq j}\tilde{c}_l\left(t-\left|\frac{z_j-z_l}{v_p}\right|\right)e^{i\omega_0\left|\frac{z_j-z_l}{v}\right|}\Theta\left(t-\left|\frac{z_j-z_l}{v_p}\right|\right) \\ &+ r\beta\frac{\Gamma}{2}\sum_{l}\tilde{c}_l\left(t-\left|\frac{z_j+z_l}{v_p}\right|\right)e^{i\omega_0\left|\frac{z_j+z_l}{v}\right|}\Theta\left(t-\left|\frac{z_j+z_l}{v_p}\right|\right).\end{aligned} \tag{4.22}$$

The first term represents free evolution, the second term describes interactions between different atoms within the ensemble, and the third term accounts for the back-action of past emissions reflected back onto the atoms. Given specific atomic positions, one can calculate the atomic excitation amplitude $c_j(t)$ numerically by integrating Eq. (4.22). Note that $\tilde{c}_j(t)$ is defined in the interaction picture, thus it varies at a timescale $\sim 1/\Gamma$. As the timescale for a photon to travel within the atomic ensemble is much smaller than the atomic decay time scale ($|(z_j - z_l)/v| \ll 1/\Gamma$), we can re-write Eq. 4.22 using $\tilde{c}_l\left(t-\left|\frac{z_j-z_l}{v}\right|\right) \simeq \tilde{c}_l\left(t\right)$ and $\tilde{c}_l\left(t-\left|\frac{z_j+z_l}{v}\right|\right) \simeq \tilde{c}_l\left(t-\tau_D\right)$:

$$\begin{aligned}\tilde{c}_j(t+\Delta t) = &\tilde{c}_j(t) - \Delta t\,\frac{\Gamma}{2}\left[\tilde{c}_j(t) + \beta\sum_{l\neq j}\tilde{c}_l\left(t\right)e^{i\omega_0\left|\frac{z_j-z_l}{v}\right|}\right]\Theta\left(t\right) \\ &+ \Delta t\,\frac{M\beta\Gamma}{2}\sum_{l}\tilde{c}_l\left(t-\frac{2z_0}{v}\right)e^{i\omega_0\left|\frac{z_j+z_l}{v}\right|}\Theta\left(t-\frac{2z_0}{v}\right),\end{aligned} \tag{4.23}$$

for numerical simulation. Note that the numerical integration time step is required to satisfy $\Delta t \ll 1/\Gamma$, but it can be much larger than the actual system evolution time scale $\sim 1/\omega_0$. This is the benefit of working in the interaction picture where the fast-rotating phases are removed.

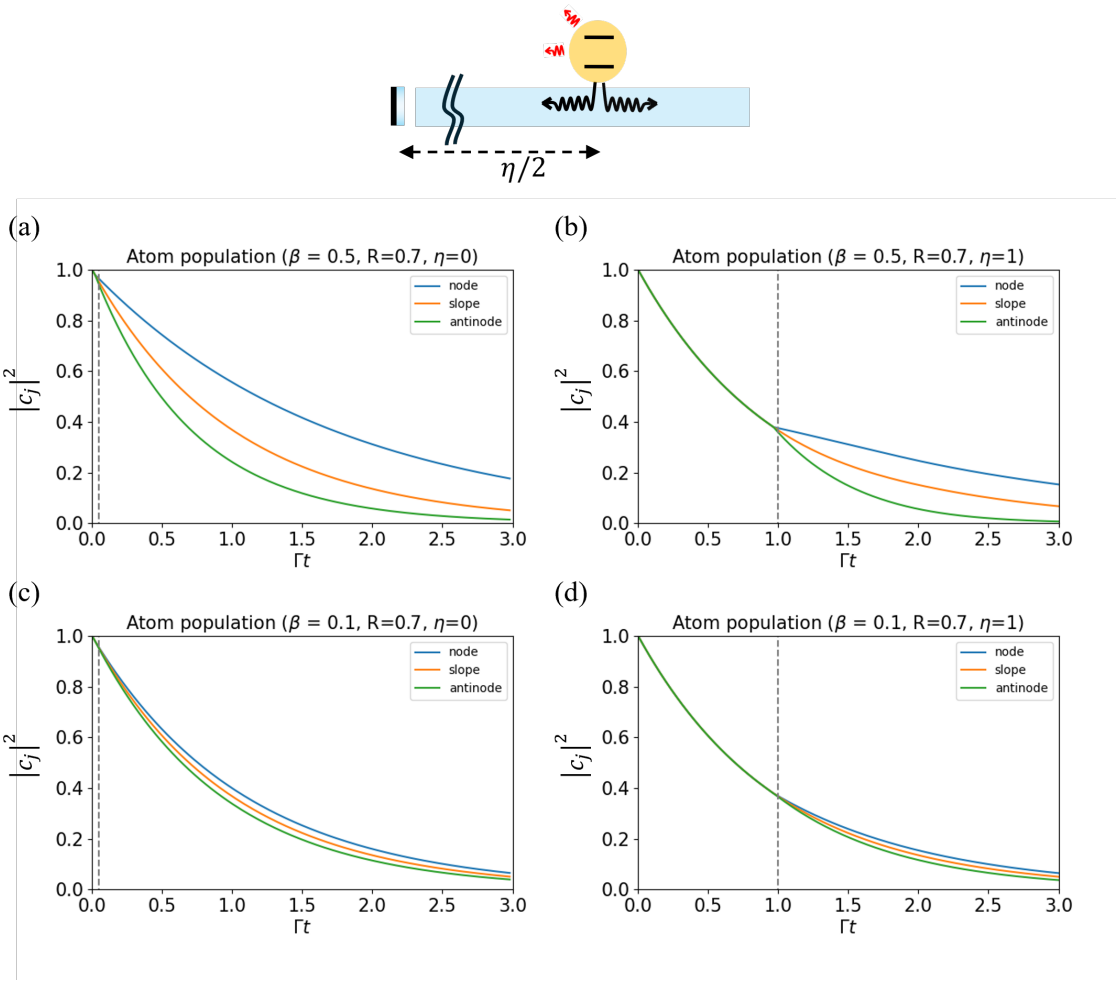

Figure 4.2: Examples of free dynamics of a single excited atom in front of a mirror at node (blue, $\omega_0\tau_D = 2n\pi$), slope (orange, $\omega_0\tau_D = (2n+1/2)\pi$), and antinode (green, $\omega_0\tau_D = (2n+1)\pi$, for time delays (a,c) $\eta = 0$ and (b,d) $\eta = 1$. The coupling efficiency is simulated for (a-b) $\beta = 0.5$, which corresponds to a cooperativity of 1, and (c-d) $\beta = 0.1$, typical of ONF-based systems. The mirror reflectivity is $R = 0.7$. Vertical dashed lines indicate the delay time η.

For the single atom case, Eq. (4.22) reduces to

$$\partial_t \tilde{c}_j(t) = -\frac{\Gamma}{2}\tilde{c}_j(t)\Theta(t) + r\beta\frac{\Gamma}{2}\tilde{c}_j\left(t - \left|\frac{2z_j}{v_p}\right|\right) e^{i\omega_0\left|\frac{2z_j}{v}\right|}\Theta\left(t - \left|\frac{2z_j}{v_p}\right|\right), \tag{4.24}$$

which agrees well with the result in [150]. Examples of the dynamics of single excited atoms are shown in Fig. 4.2, for time delays $\eta = 0, 1$ and coupling efficiencies $\beta = 0.1, 0.5$. When the delay is small, the atom exhibits superradiant decay at the antinode and subradiant decay at the node. The degree of collective enhancement and suppression of the decay rate depends on the coupling efficiency. In the non-Markovian regime ($\eta = 1$), the atoms show delayed feedback behavior, where the decay is either faster than superradiant at the antinode [67,68], or form a BIC at the node [67, 69].

To investigate the interplay between collective effects within a single ensemble and long-range interactions with its mirror image, we compare the decay dynamics of various atomic ensemble configurations, including single- and many-atom decays with various coupling efficiencies, as shown in Fig. 4.3. We simulate three scenarios:

1. **single-atom decay with $\beta = 0.1$ (solid blue):** A single atom decays independently with rate Γ until its past emission arrives at $t = \tau_D$. The impact of the time-delayed feedback is governed by the cooperativity $C = \beta/(1-\beta) = 1/9$.

2. **multi-atom ($N = 9$, ordered array with lattice constant λ_0) decay with $\beta = 0.1$ (dashed orange):** An ordered array cooperatively couples to the guided mode and has an enhanced decay rate $\Gamma^{(N)} = (1 - \beta + N\beta)\Gamma$ (see Appendix B for derivation), which is $1.8\,\Gamma$ for this case. Although the single-atom cooperativity is small, the total cooperativity

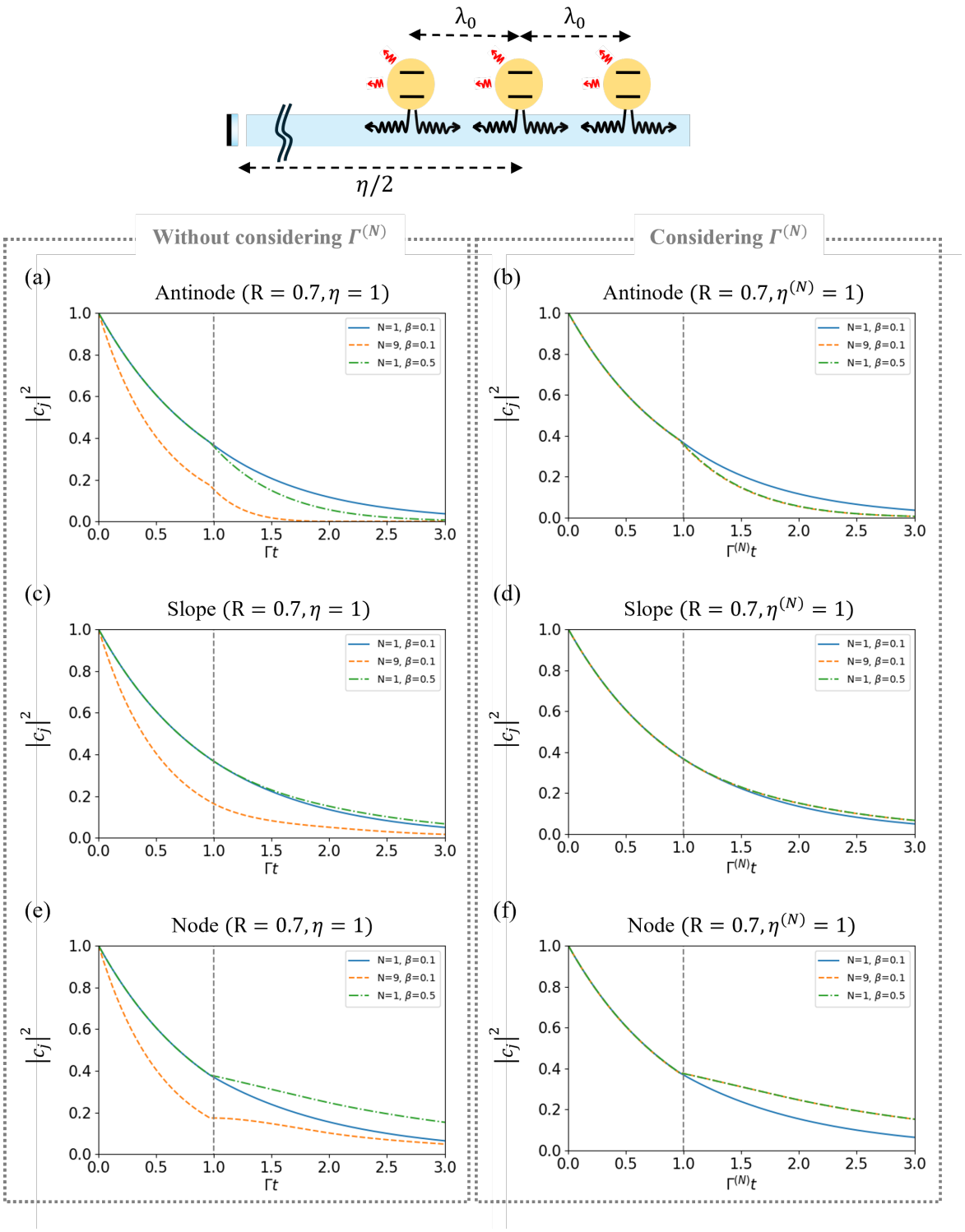

Figure 4.3: Comparison of free dynamics of single and multiple excited atoms in front of a mirror, for (a) $N = 1$, $\beta = 0.1$ (solid blue), (b) $N = 9$, $\beta = 0.1$ (dashed orange), and (c) $N = 1$, $\beta = 0.5$ (dash-dotted green). The latter two cases have the same total cooperativity, $C = 1$. Vertical dashed lines indicate the delay time η between the atomic array and its mirror image.

is collectively enhanced to reach the strong interaction regime: $C = N\beta/(1-\beta) = 1$.

3. **single atom decay with $\beta = 0.5$ (dash-dotted green):** Although it has higher coupling efficiency than in the first case ($N = 1, \beta = 0.1$), the decay rates for the two cases are the same. Thus, the atom decays with rate Γ before $t = \tau_D$. However, as the cooperativity is larger ($C = 1$), the effects of time-delayed feedback are more pronounced than in the first case.

Figure 4.3 (a, c, e) shows the case where the atoms are placed at $\eta = 1$. The atoms show either faster-than-superradiant decay when they are at antinodes and BIC when they are at nodes. However, the many-atom decay ($N = 9$, dashed orange) always shows a larger single-ensemble decay rate, and it is hard to compare. Furthermore, it is not only hard to analyze, but also the atoms feel an effectively larger η as their effective decay rate is increased. Although the distance between the atomic ensemble and the mirror is fixed, the array with a larger number of atoms decays faster, and thus, the feedback has an impact on a more delayed time compared to the atomic relaxation time scale.

Figure 4.3 (b, d, e) shows the case where the delay $\eta^{(N)} = 2z_0\Gamma^{(N)}/v$ reflects the collective decay rate in the atomic ensemble. The time axis is also renormalized to $\Gamma^{(N)}t$ for each curve. We observe that the second and the third situations, which have the same cooperativity, agree with each other. Thus, one can regard an atomic array with a lattice constant commensurate with the transition wavelength as a single superatom that has both the enhanced decay rate and cooperativity.

4.2.2 Driven Dynamics

Now we consider the driven dynamics perturbatively. The driven time-evolved state is expressed as the sum of perturbative terms:

$$\left|\psi^{(\mathrm{D})}(t)\right\rangle \simeq \left|\psi_0^{(\mathrm{D})}(t)\right\rangle + \left|\psi_1^{(\mathrm{D})}(t)\right\rangle + \cdots , \tag{4.25}$$

where each term represents 0-th and 1-st, and higher order perturbation terms. The 0-th and 1-st order terms are

$$\left|\psi_0^{(\mathrm{D})}(t)\right\rangle = e^{-iH_0 t/\hbar}\left|\psi(0)\right\rangle , \tag{4.26a}$$

$$\left|\psi_1^{(\mathrm{D})}(t)\right\rangle = -\frac{i}{\hbar}\int_0^t \mathrm{d}t' e^{-iH_0(t-t')/\hbar} H_D(t') e^{-iH_0 t'/\hbar}\left|\psi(0)\right\rangle . \tag{4.26b}$$

The 0-th order term corresponds to the state that has never interacted with the drive, while the 1-st order term represents the state that has interacted with the drive once. Note that the drive Hamiltonian changes the number of excitations in the system, whereas the rest of the Hamiltonian conserves it.

Now we assume an initial state where atoms are in the ground state and the field is in the vacuum, i.e., $|\psi(0)\rangle = |G, \{0\}_k\rangle$. Then, the zeroth-order term $\left|\psi_0^{(D)}(t)\right\rangle$ remains in the zero-excitation manifold. Putting in the drive Hamiltonian as defined in Eq. 4.5d, we can write the first order term $\left|\psi_1^{(D)}(t)\right\rangle$ as

$$\left|\psi_1^{(\mathrm{D})}(t)\right\rangle = \frac{i\sqrt{N}\Omega}{2}\int_0^t \mathrm{d}t' e^{-i\omega_D t'} e^{-iH_0(t-t')/\hbar}\left|+, \{0\}_k\right\rangle , \tag{4.27}$$

where $|+\rangle = \frac{1}{\sqrt{N}} \sum_{j=1}^{N} \hat{\sigma}_j^+ |G\rangle$ is the symmetrically excited atomic state. Note that the drive excites the atom to the symmetric state because it is driving perpendicularly from the side; all the atoms see the same phase of the drive field.

Then the driven excitation amplitude can be expressed in terms of the undriven excitation amplitude which can be obtained by numerically integrating Eq. (4.22).

$$\left|\psi_1^{(\mathrm{D})}(t)\right\rangle = \sum_{j=1}^{N} \tilde{c}_j^{(\mathrm{D})}(t) e^{-i\omega_D t} \left|j, \{0\}_k\right\rangle, \tag{4.28}$$

where $|j\rangle = \hat{\sigma}_j^+ |G\rangle$ is the state where j-th atom is excited. The driven atomic excitation amplitude is

$$\tilde{c}_j^{(D)}(t) = \frac{i\sqrt{N}\Omega}{2} \int_0^t \mathrm{d}t' e^{i(\omega_D - \omega_0)t'} \tilde{c}_j(t'). \tag{4.29}$$

Note that $\tilde{c}_j^{(D)}(t)$ is defined in the rotating frame of the drive field, whereas $\tilde{c}_j(t)$ is in the interaction picture with respect to $H_A + H_F$.

The examples of driven dynamics of a single atom in the presence of a mirror are shown in Fig. 4.4. When the atom is placed right in front of a mirror (Fig. 4.4 (a,c)), the driven dynamics show subradiant and superradiant behaviors depending on the atomic position. When the atom is at a node, it forms a subradiant state with its mirror image. This forms trapped light in between the atom and the mirror, and thus, the atomic excitation is higher in the steady state. On the other hand, when the atom is at antinode, it forms a superradiant state. Thus, the excitation is favorably scattered outside the half-cavity, leading to a smaller steady-state population in the atomic state. When the atom and its mirror image are distanced far apart (Fig. 4.4 (b,d)), they

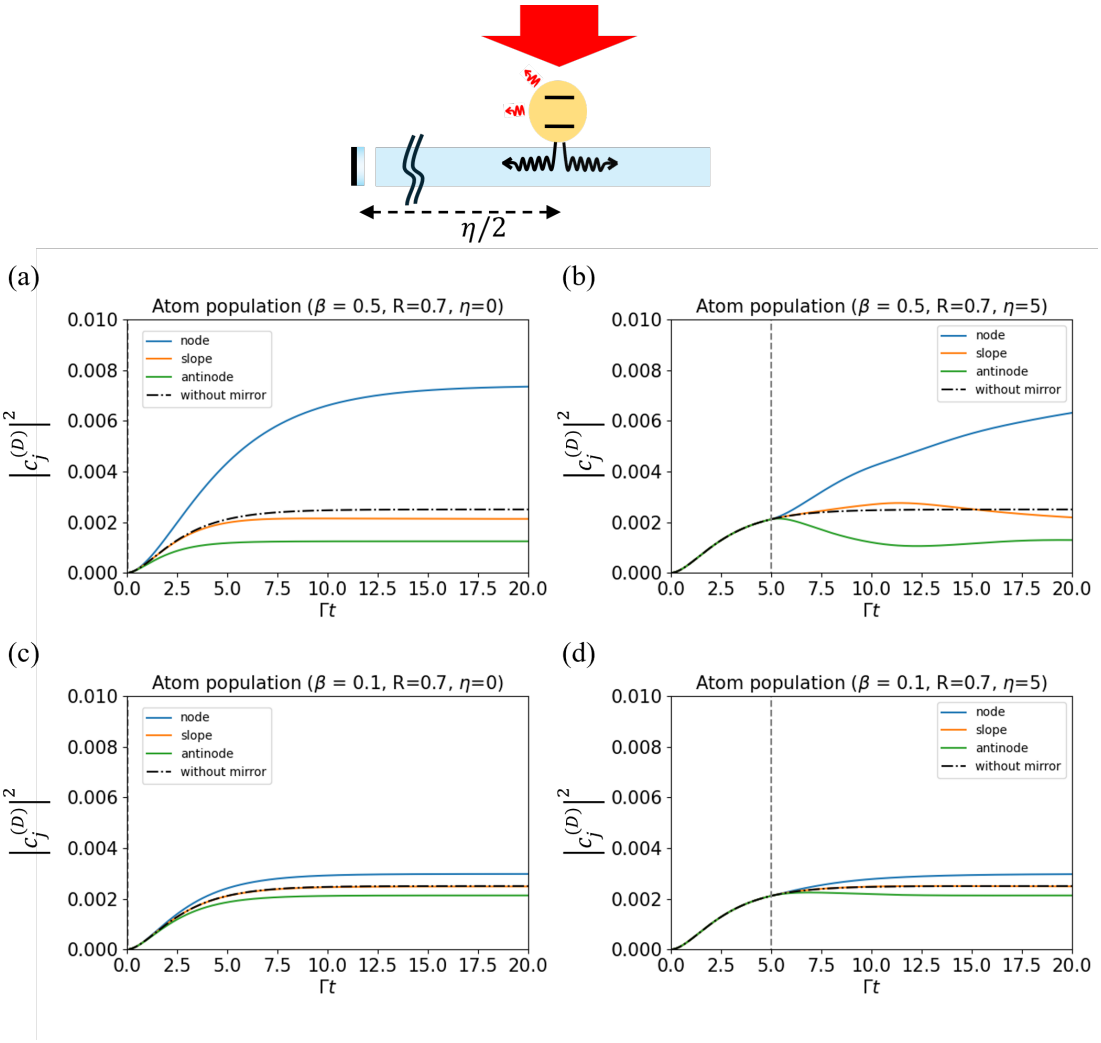

Figure 4.4: Examples of driven dynamics of a single atom placed in front of a mirror at node (blue, $\omega_0\tau_D = 2n\pi$), slope (orange, $\omega_0\tau_D = (2n+1/2)\pi$), and antinode (green, $\omega_0\tau_D = (2n+1)\pi$ of the standing wave $\sin(\omega_0 z/v)$, for time delays (a,c) $\eta = 0$ and (b,d) $\eta = 5$. For comparison, The coupling efficiency is simulated for (a-b) $\beta = 0.5$, which makes cooperativity to 1, and (c-d) $\beta = 0.1$, which is typical in ONF-based systems. The mirror reflectivity is $R = 0.7$, Rabi frequency of the drive is $\Omega = 0.05\Gamma$, and the drive detuning is zero. Vertical dashed lines indicate the time delay between the atom and its mirror image.

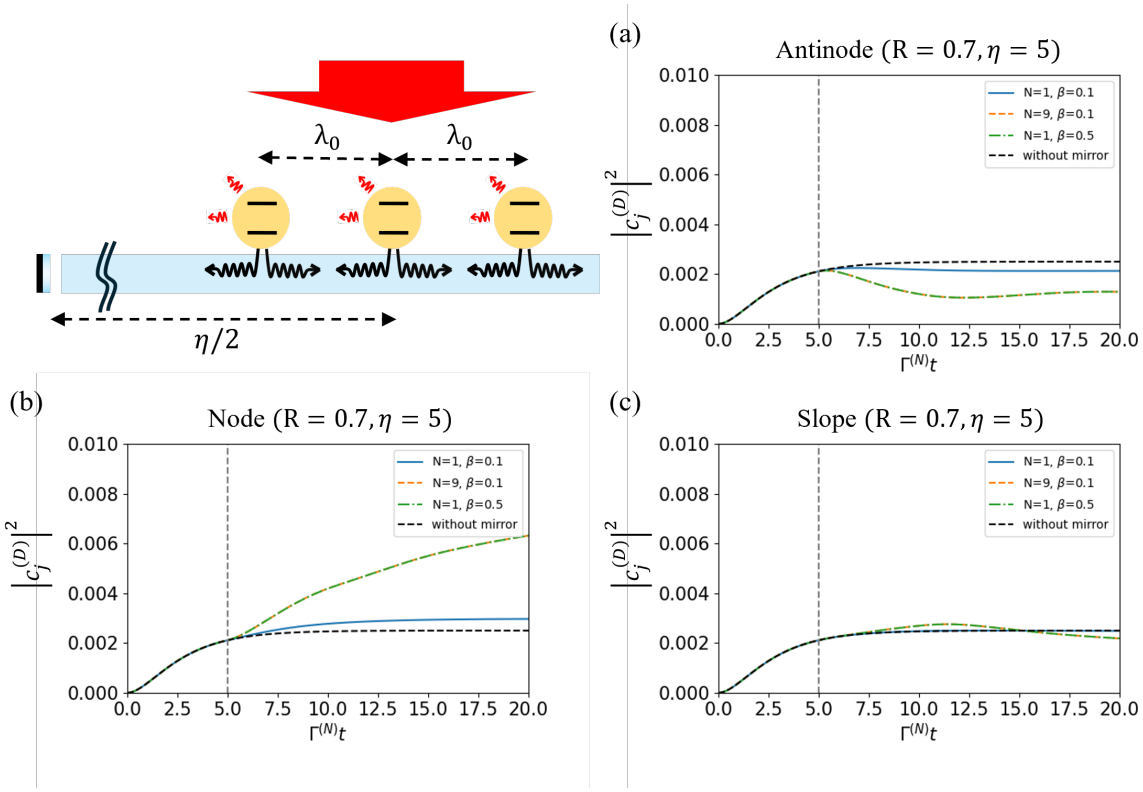

Figure 4.5: Comparison of driven dynamics of atoms in front of a mirror with various atomic configurations: $N = 1$, $\beta = 0.1$ (solid blue), $N = 9$, $\beta = 0.1$ (dashed orange), and $N = 1$, $\beta = 0.5$ (dash-dotted green), and a single atom in free space. The delay time is $\eta = 5$, mirror reflectivity is $R = 0.7$, Rabi frequency of the drive is $\Omega = 0.05\Gamma$, and the drive detuning is zero. The vertical dashed lines indicate the time delay between the atom and its mirror image.

exhibit coherent time-delayed feedback effects. When the atom is at a node, it forms a BIC, and thus, the excitation is trapped between the half-cavity and the atom. Compared to the Markovian case, the BIC state has appreciable amplitudes of photonic component [69], and thus, it has more capacity to store an excitation coming from the external drive. This can be seen in the atomic population which increases beyond the Markovian limit (in the simulation, the atomic population did not reach the steady state and keep increasing). When the atom is at an antinode, it exhibits a sudden increase of radiation outside the half-cavity, which is shown as the sudden decrease of atomic population as the coherent delayed feedback comes to the system. This effect is mitigated when the coupling efficiency becomes small.

The multi-atom dynamics in comparison with the single-atom dynamics is shown in Fig. 4.5, where the simulation parameter for the atomic configuration is the same as in Fig. 4.3. The time is scaled as $\Gamma^{(N)}t$, where $\Gamma^{(N)} = (1 - \beta + N\beta)\Gamma$ is the collective decay rate. The atom-mirror distance and the Rabi frequency are also adjusted to reflect the collective enhancement of the system's relaxation rate. For a single atom with coupling efficiency $\beta = 0.1$, the effect of the time-delayed feedback is small and shows a small deviation from the free space case. This small coupling efficiency can be overcome by having multiple atoms. The overall time-delayed dynamics only depends on the cooperativity, given that the delays and drive strength are normalized to the collective decay rate within the ensemble.

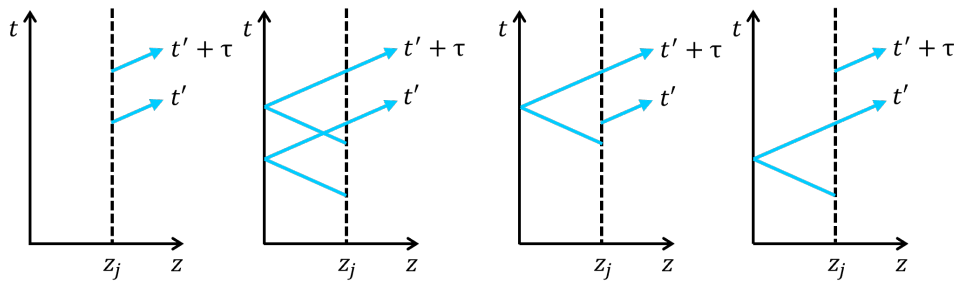

Figure 4.6: Four scenarios for photon click at time $t = t'$ and $t = t' + \tau$ which interfere in the correlated measurement.

4.2.3 Correlation Functions

The second-order correlation function in Eq. (4.16) can be written as a square of the amplitude of the final state vector:

$$\frac{G_N^{(2)}(\tau)}{|\beta E_0|^4} = \lim_{t\to\infty} \left|\left| \sum_{j,l=1}^{N} T \left[\hat{\tilde{\sigma}}_j^- \left(t + \tau - \frac{z_d - z_j}{v} \right) e^{-i\omega_0 \frac{z_j}{v}} - r \hat{\tilde{\sigma}}_j^- \left(t + \tau - \frac{z_d + z_j}{v} \right) e^{i\omega_0 \frac{z_j}{v}} \right] \right.$$
$$\left. \left[\hat{\tilde{\sigma}}_l^- \left(t - \frac{z_d - z_l}{v} \right) e^{-i\omega_0 \frac{z_l}{v}} - r \hat{\tilde{\sigma}}_l^- \left(t - \frac{z_d + z_l}{v} \right) e^{i\omega_0 \frac{z_l}{v}} \right] |\psi(0)\rangle \right|\right|^2 . \quad (4.30)$$

where T is the time ordering operator. Thus, we have

$$\begin{aligned}\frac{G_N^{(2)}(\tau)}{|\beta E_0|^4} = \lim_{t\to\infty} \Bigg| \sum_{j,l=1}^{N} \Bigg[& \tilde{c}_j^{(D)}\left(\tau + \frac{z_j - z_l}{v}\right) \tilde{c}_l^{(D)}\left(t - \frac{z_d - z_l}{v}\right) e^{-i\omega_D \frac{z_j+z_l}{v}} \\ & + r^2 \tilde{c}_j^{(D)}\left(\tau - \frac{z_j - z_l}{v}\right) \tilde{c}_l^{(D)}\left(t - \frac{z_d + z_l}{v}\right) e^{i\omega_D \frac{z_j+z_l}{v}} \\ & - r\tilde{c}_j^{(D)}\left(\tau + \frac{z_j + z_l}{v}\right) \tilde{c}_l^{(D)}\left(t - \frac{z_d + z_l}{v}\right) e^{-i\omega_D \frac{z_j-z_l}{v}} \\ & - r\tilde{c}_j^{(D)}\left(\tau - \frac{z_j + z_l}{v}\right) \tilde{c}_l^{(D)}\left(t - \frac{z_d - z_l}{v}\right) \Theta\left(\tau - \frac{z_j + z_l}{v}\right) e^{i\omega_D \frac{z_j-z_l}{v}} \\ & - r\tilde{c}_l^{(D)}\left(\frac{z_j + z_l}{v} - \tau\right) \tilde{c}_j^{(D)}\left(t + \tau - \frac{z_d + z_j}{v}\right) \Theta\left(\frac{z_j + z_l}{v} - \tau\right) e^{i\omega_D \frac{z_j-z_l}{v}} \Bigg] \Bigg|^2 . \end{aligned} \tag{4.31}$$

Each term represents the four interfering scenarios of emission from real atoms and image atoms clicking the start and stop counts (see Fig. 4.6). Note that Eq. (4.31) agrees with Eq. 29 in [150] for the single atom case.

Examples of the second-order correlation function of light scattered by multiple atoms are shown in Fig. 4.7. For this simulation, we used real parameters from ^{85}Rb atoms with time delay of 98 ns which corresponds to $\eta \approx 3.8$, coupling efficiency $\beta = 0.1$, Rabi frequency $\Omega = 0.05 \times \Gamma_0$ where Γ_0 is the natural linewidth of the D_2 transition, and mirror reflectivity $R = r^2 = 0.7$. Fig. 4.7 (a-c) shows the second-order correlation function $G_N^{(2)}$ of light scattered by an array of atoms placed in front of a mirror where the atoms are at nodes ($\omega_D \tau_d = 2n\pi$), antinodes ($\omega_D \tau_d = (2n+1)\pi$), and slope ($\omega_D \tau_d = (2n+1/2)\pi$), for varying number of atoms $N = 1, \cdots, 5$. Here, the atom-mirror distance and Rabi frequency are all fixed throughout the simulation without renormalization with respect to the collectively enhanced decay rate. This is because we are more interested in simulating real parameters and comparing the model with

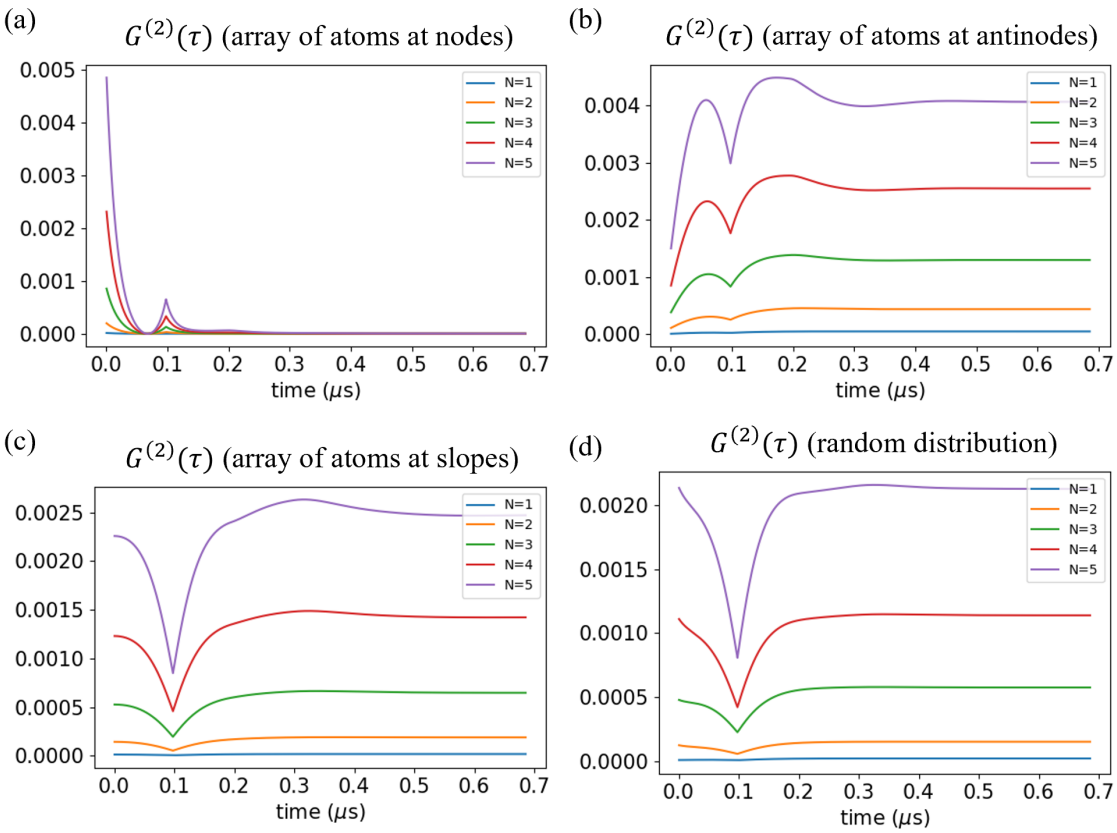

Figure 4.7: Second-order correlation function of scattering from (a-c) arrays of atoms of which lattice constant is commensurate to the drive wavelength and positioned at (a) nodes, (b) antinodes, (c) slopes in the half-cavity, and (d) an ensemble of atoms (averaged over 50 random distributions, which is checked to be converging). The number of atoms is varied between $N = 1, \cdots, 5$. The delay between the atoms and their mirror images is $\eta = 3.77$, coupling efficiency is $\beta = 0.1$, mirror reflectivity is $r^2 = 0.7$, Rabi frequency is $\Omega = 0.05\Gamma_0$, and the drive detuning is zero.

the experimental observations. Fig. 4.7 (a) shows that the scattering of atoms at nodes shows strong bunching at the coincidence count and local bunching at the delay corresponding to the atom-image distance. This shows that the BIC formed by delayed interaction of atoms exhibits a strong bunching effect when it leaks out of the cavity formed by the atom. Overall, the probability of observing photon pairs with large separation ($G^{(2)}(\tau \to \infty)$) is suppressed. Fig. 4.7 (b) shows atoms at antinodes, where antibunching at $\tau = 0$ and $\tau = \tau_D$ is observed. We observe that the faster-than-superradiant radiation [68] is strongly antibunched. Fig. 4.7 (C) shows atoms at the slope, which exhibit the strongest correlation at $\tau = \tau_D$. Fig. 4.7 (d) shows an average of 50 random distributions of atoms. We checked that 50 is a sufficient number to show converged dynamics. Regardless of the number of atoms, bunching at $\tau = 0$ and antibunching at $\tau = \tau_D$ are consistently showing, and these effects become more distinct as the number of atoms increases. These features can be understood by considering the probability of photon scattering outside the half-cavity. An atom at a node forms a cavity with its mirror image. It tends to emit strongly bunched photons, while photon pairs with finite separations are significantly suppressed. As the atomic position shifts toward antinodes, these effects transition to antibunched photons at both $\tau = 0$ and $\tau = \tau_D$, accompanied by an overall increase in photon count. Consequently, the atoms at the nodes predominantly contribute to the strongly bunched scattering at $\tau = 0$, whereas atoms located away from the nodes dominate at $\tau \gtrsim \tau_D$.

Overall, both for the ordered and randomly distributed atoms, the increase in the number of atoms results in a sharper structure in $G^{(2)}(\tau)$. In particular, the features in the correlation function become more pronounced when multiple atoms form a commensurate array, enabling cooperative radiation into the waveguide. This observation is consistent with the earlier analysis on atomic dynamics, which showed that a commensurate atomic array behaves as a single

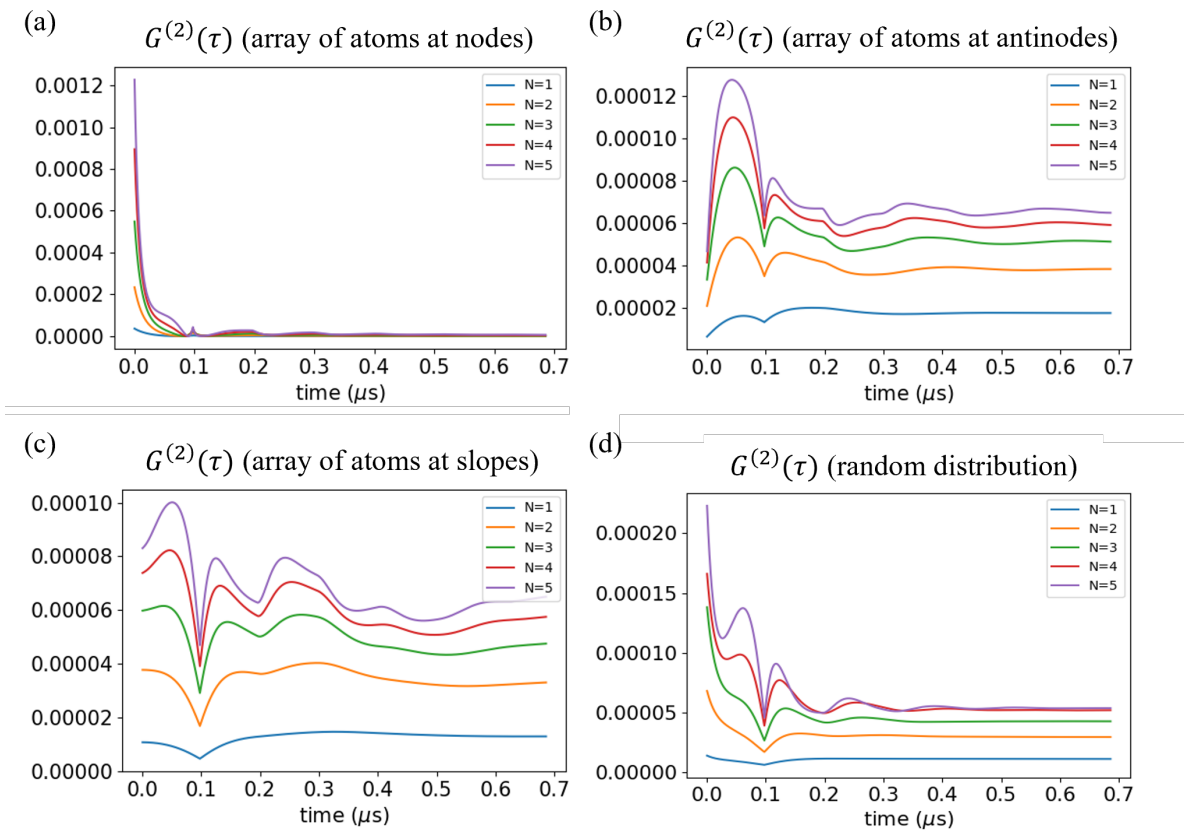

Figure 4.8: Second-order correlation function of scattering from (a-c) arrays of atoms of which lattice constant is commensurate to the drive wavelength and positioned at (a) nodes, (b) antinodes, and (c) slopes in the half-cavity, and (d) an ensemble of atoms (averaged over 50 random distributions, which is checked to be converging). Parameters are the same with Fig. 4.7 except that the coupling efficiency is $\beta = 0.5$.

superatom with enhanced decay rate and cooperativity.

The second-order correlation functions with higher coupling efficiencies are shown in Fig. 4.8. Overall, the features discussed for lower coupling efficiency in Fig. 4.7 consistently appear but are more pronounced.

4.3 Weak Coupling Regime ($\beta^2\Gamma \lesssim \Omega$)

4.3.1 Correlation Functions

Now, in the opposite limit where the external drive is stronger than the back-action of the radiated photons, the atoms behave like independent emitters. This implies that atoms are randomly distributed, as ordering would collectively enhance the coupling and thus increase the coupling efficiency, which may result in a strong coupling regime. Thus, we limit our scope to randomly distributed atoms in this regime.

In this regime, we can assume that the electric fields scattered from different atoms are not correlated as they do not see each other. Thus, we can separate the expectation value of fields scattered from different atoms, i.e., $\langle \hat{E}_j^{(-)} \hat{E}_l^{(+)} \rangle = \langle \hat{E}_j^{(-)} \rangle \langle \hat{E}_l^{(+)} \rangle$. Also, we ignore terms involving rapidly rotating phases such as $e^{i\omega_0 z_j/v}$, as the contribution of such terms is negligible due to the random positioning of the atoms. Thus, the intensity correlation function includes only the one- and two-atom contributions [175, 178].

Each term contributing to the intensity correlation function of the N-atom scattering is

- Single-atom contribution ($j = l = m = n$):

$$\sum_{j=1}^{N} \Big[\left(1 + r^4\right) \langle \hat{\tilde{\sigma}}_j^+(t') \hat{\tilde{\sigma}}_j^+(t'+\tau) \hat{\tilde{\sigma}}_j^-(t'+\tau) \hat{\tilde{\sigma}}_j^-(t') \rangle$$
$$+ r^2 \langle \hat{\tilde{\sigma}}_j^+(t') \hat{\tilde{\sigma}}_j^+(t'+\tau-\tau_d) \hat{\tilde{\sigma}}_j^-(t'+\tau-\tau_d) \hat{\tilde{\sigma}}_j^-(t') \rangle$$
$$+ r^2 \langle \hat{\tilde{\sigma}}_j^+(t') \hat{\tilde{\sigma}}_j^+(t'+\tau+\tau_d) \hat{\tilde{\sigma}}_j^-(t'+\tau+\tau_d) \hat{\tilde{\sigma}}_j^-(t') \rangle$$
$$+ 2r^2 \mathrm{Re} \langle \hat{\tilde{\sigma}}_j^+(t') \hat{\tilde{\sigma}}_j^+(t'+\tau-\tau_d) \hat{\tilde{\sigma}}_j^-(t'+\tau) \hat{\tilde{\sigma}}_j^-(t'-\tau_d) \rangle \Big], \tag{4.32}$$

where t' is a steady-state time point that is larger than any characteristic timescale of the atom and field dynamics. Note that $\hat{\tilde{\sigma}}_j^-(t)$ varies slowly with a timescale of $\sim 1/\Gamma$, since the fast rotating part $e^{-i\omega_0 t}$ has been factored out. In writing Eq. (4.32), the rapidly oscillating terms are neglected as they are averaged out when summed over the atomic ensembles. The first term represents the case where the start and stop photons are from the same ensemble - either from the real or image ensemble. The second term is the case where the start photon is from the real ensemble and the stop photon is from the image ensemble, and the third term is vice versa. The fourth term is the cross terms of the photons emitted by the real and image ensembles.

- Two-atom contribution ($j = l \neq m = n$):

$$\begin{aligned}\sum_{j\neq m} r^2 \Big[&\langle \hat{\tilde{\sigma}}_j^+(t')\hat{\tilde{\sigma}}_j^+(t'+\tau-\tau_d)\rangle \langle \hat{\tilde{\sigma}}_m^-(t'+\tau-\tau_d)\hat{\tilde{\sigma}}_m^-(t')\rangle \\ &+ \langle \hat{\tilde{\sigma}}_j^+(t')\hat{\tilde{\sigma}}_j^+(t'+\tau+\tau_d)\rangle \langle \hat{\tilde{\sigma}}_m^-(t'+\tau+\tau_d)\hat{\tilde{\sigma}}_m^-(t')\rangle \\ &+ 2\mathrm{Re}\ \langle \hat{\tilde{\sigma}}_j^+(t')\hat{\tilde{\sigma}}_j^+(t'+\tau-\tau_d)\rangle \langle \hat{\tilde{\sigma}}_m^-(t'+\tau)\hat{\tilde{\sigma}}_m^-(t'-\tau_d)\rangle \Big], \end{aligned} \tag{4.33}$$

This corresponds to the case where single scattering involves two atoms: the j-th atom absorbs a photon, and the m-th atom emits the photon. Such processes have been discussed in analogy to the four-wave-mixing process involving spontaneous radiation in two atoms [177].

- Two-atom contribution ($j = m \neq l = n$):

$$\sum_{j\neq l}\Big[\left(1+r^4\right)\langle\hat{\tilde{\sigma}}_j^+(t')\hat{\tilde{\sigma}}_j^-(t'+\tau)\rangle\langle\hat{\tilde{\sigma}}_l^+(t'+\tau)\hat{\tilde{\sigma}}_l^-(t')\rangle + 2r^2\mathrm{Re}\,\langle\hat{\tilde{\sigma}}_j^+(t')\hat{\tilde{\sigma}}_j^-(t'+\tau)\rangle\langle\hat{\tilde{\sigma}}_l^+(t'+\tau-\tau_d)\hat{\tilde{\sigma}}_l^-(t'-\tau_d)\rangle\Big], \tag{4.34}$$

This corresponds to the case where the two photon-clicks are coming from the combination of first-order correlation functions involving two atoms. These first-order correlation functions are responsible for the bunching effect in two-atom scattering.

- Two-atom contribution ($j = n \neq l = m$):

$$\sum_{j\neq l}\Big[\left(1+r^4\right)\langle\hat{\tilde{\sigma}}_j^+(t')\hat{\tilde{\sigma}}_j^-(t')\rangle\langle\hat{\tilde{\sigma}}_l^+(t'+\tau)\hat{\tilde{\sigma}}_l^-(t'+\tau)\rangle + r^2\langle\hat{\tilde{\sigma}}_j^+(t')\hat{\tilde{\sigma}}_j^-(t')\rangle\langle\hat{\tilde{\sigma}}_l^+(t'+\tau-\tau_d)\hat{\tilde{\sigma}}_l^-(t'+\tau-\tau_d)\rangle + r^2\langle\hat{\tilde{\sigma}}_j^+(t')\hat{\tilde{\sigma}}_j^-(t')\rangle\langle\hat{\tilde{\sigma}}_l^+(t'+\tau+\tau_d)\hat{\tilde{\sigma}}_l^-(t'+\tau+\tau_d)\rangle\Big]. \tag{4.35}$$

This case represents the scenario where each photon is emitted by two different atoms, contributing to the uncorrelated counts.

Similarly, the intensity of the scattered light in Eq. (4.18) only has single-atom contributions:

$$I_N = \lim_{t\to\infty}\sum_{j=1}^{N}\left\langle\hat{E}_j^{(-)}(z_d,t)\hat{E}_l^{(+)}(z_d,t)\right\rangle. \tag{4.36}$$

Expressing Eq. (4.36) in terms of atomic operators, we get

$$I_N = |\beta E_0|^2 \sum_{j=1}^{N} \left(1 + r^2\right) \langle \hat{\tilde{\sigma}}_j^+(t') \hat{\tilde{\sigma}}_j^-(t') \rangle \,. \tag{4.37}$$

The terms in the intensity correlation function and the intensity function are expressed in terms of single atom correlation functions. Since the atoms are independently scattering, we can use textbook formulae for the atomic correlation functions. The single-atom correlation functions are defined as:

$$g_A^{(1)}(\tau) \equiv \frac{\langle \hat{\tilde{\sigma}}^+(t) \hat{\tilde{\sigma}}^-(t+\tau) \rangle}{\langle \hat{\tilde{\sigma}}^+(t) \hat{\tilde{\sigma}}^-(t) \rangle}, \tag{4.38a}$$

$$g_A^{(1')}(\tau) \equiv \frac{\langle \hat{\tilde{\sigma}}^+(t) \hat{\tilde{\sigma}}^+(t+\tau) \rangle}{\langle \hat{\tilde{\sigma}}^+(t) \hat{\tilde{\sigma}}^-(t) \rangle}, \tag{4.38b}$$

$$g_A^{(2)}(\tau) \equiv \frac{\langle \hat{\tilde{\sigma}}^+(t) \hat{\tilde{\sigma}}^+(t+\tau) \hat{\tilde{\sigma}}^-(t+\tau) \hat{\tilde{\sigma}}^-(t) \rangle}{\langle \hat{\tilde{\sigma}}^+(t) \hat{\tilde{\sigma}}^-(t) \rangle^2}, \tag{4.38c}$$

$$I \equiv \langle \hat{\tilde{\sigma}}^+(t) \hat{\tilde{\sigma}}^-(t) \rangle \,, \tag{4.38d}$$

where t is a sufficiently large time when the system reaches a steady state. The form of single-atom correlation functions can be found in [181] and [178]. For a strong drive ($\Omega > \Gamma/4$), the single atom correlation functions are

$$g_A^{(1)}(\tau) = \frac{\Gamma^2}{2\Omega^2 + \Gamma^2} + \frac{1}{2} e^{-\frac{\Gamma}{2}\tau} + e^{-\frac{3}{4}\Gamma\tau} \left(P \cos \kappa\tau + Q \sin \kappa\tau\right), \tag{4.39a}$$

$$g_A^{(1')}(\tau) = -\frac{\Gamma^2}{2\Omega^2 + \Gamma^2} + \frac{1}{2} e^{-\frac{\Gamma}{2}\tau} - e^{-\frac{3}{4}\Gamma\tau} \left(P \cos \kappa\tau + Q \sin \kappa\tau\right), \tag{4.39b}$$

$$g_A^{(2)}(\tau) = 1 - e^{-\frac{3}{4}\Gamma\tau} \left[\cos \kappa\tau + \frac{3\Gamma}{4\kappa} \sin \kappa\tau\right], \tag{4.39c}$$

where ω is the drive frequency, $\kappa = \sqrt{\Omega^2 - \Gamma^2/16}$, $P = (2\Omega^2 - \Gamma^2)/(2\Omega^2 + \Gamma^2)/2$, and $Q = \Gamma(10\Omega^2 - \Gamma^2)/(8\kappa)/(2\Omega^2 + \Gamma^2)$. For a weak drive ($\Omega < \Gamma/4$), the single atom correlation functions are

$$g_A^{(1)}(\tau) = \frac{\Gamma^2}{2\Omega^2 + \Gamma^2} + \frac{1}{2}e^{-\frac{\Gamma}{2}\tau} + e^{-\frac{3}{4}\Gamma\tau}\left(P\cosh\tilde{\kappa}\tau + \tilde{Q}\sinh\tilde{\kappa}\tau\right) \tag{4.40a}$$

$$g_A^{(1')}(\tau) = -\frac{\Gamma^2}{2\Omega^2 + \Gamma^2} + \frac{1}{2}e^{-\frac{\Gamma}{2}\tau} - e^{-\frac{3}{4}\Gamma\tau}\left(P\cosh\tilde{\kappa}\tau + \tilde{Q}\sinh\tilde{\kappa}\tau\right) \tag{4.40b}$$

$$g_A^{(2)}(\tau) = 1 - e^{-\frac{3}{4}\Gamma\tau}\left[\cosh\tilde{\kappa}\tau + \frac{3\Gamma}{4\tilde{\kappa}}\sinh\tilde{\kappa}\tau\right], \tag{4.40c}$$

where $\tilde{\kappa} = \sqrt{\Gamma^2/16 - \Omega^2}$ and $\tilde{Q} = \Gamma(10\Omega^2 - \Gamma^2)/(8\tilde{\kappa})/(2\Omega^2 + \Gamma^2)$.

The single- and two-atom contributions in the intensity correlation function (Eqs. 4.32, 4.33, 4.34, 4.35) can then be expressed in terms of the free space single-atom correlation functions. Thus, the intensity correlation function reads

$$\begin{aligned}\frac{G_N^{(2)}(\tau)}{|\beta E_0|^4 I^2} =& N(N-1)\left[r^2\left|g_A^{(1')}(\tau-\tau_d) + g_A^{(1')}(\tau+\tau_d)\right|^2 + (1+r^2)^2\left(\left|g_A^{(1)}(\tau)\right|^2 + 1\right)\right] \\ &+ N\left[(1+r^4)g_A^{(2)}(\tau) + r^2\left(g_A^{(2)}(\tau-\tau_d) + g_A^{(2)}(\tau+\tau_d)\right)\right].\end{aligned} \tag{4.41}$$

The first term is the two-atom contribution, which scales as $N(N-1)$, and the second term is the single-atom contribution, which scales as N. Note that we ignored the four-time correlation function in the last term of Eq. (4.32), as it is highly unlikely that a single atom is excited at $t = t - \tau_d, t + \tau - \tau_d, t, t + \tau$.

Similarly, the intensity of the light scattered by N atoms is

$$I_N = |\beta E_0|^2 N \left(1 + r^2\right) I. \tag{4.42}$$

4.3.2 Same- and Opposite-Direction Correlation Functions

Eq. (4.41) can be understood as a simple summation of same-direction and opposite-direction correlation functions of N-atom scattering. The same-direction and opposite-direction correlation functions can be easily obtained by truncating terms in Eq. (4.16):

$$\frac{G_N^{(2)(\text{same})}(\tau)}{|\beta E_0|^4} = \lim_{t\to\infty} \sum_{j,l,m,n=1}^{N} \left\langle \hat{\tilde{\sigma}}_j^+ \left(t - \left|\frac{z_d - z_j}{v}\right|\right) \hat{\tilde{\sigma}}_l^+ \left(t + \tau - \left|\frac{z_d - z_l}{v}\right|\right) \right.$$
$$\left. \hat{\tilde{\sigma}}_m^- \left(t + \tau - \left|\frac{z_d - z_m}{v}\right|\right) \hat{\tilde{\sigma}}_n^- \left(t - \left|\frac{z_d - z_n}{v}\right|\right) \right\rangle e^{i\omega_0 \frac{z_j + z_l - z_m - z_n}{v}} \tag{4.43a}$$

$$\frac{G_N^{(2)(\text{opp})}(\tau)}{|\beta E_0|^4} = \lim_{t\to\infty} \sum_{j,l,m,n=1}^{N} r^2 \left\langle \hat{\tilde{\sigma}}_j^+ \left(t - \left|\frac{z_d + z_j}{v}\right|\right) \hat{\tilde{\sigma}}_l^+ \left(t + \tau - \left|\frac{z_d - z_l}{v}\right|\right) \right.$$
$$\left. \hat{\tilde{\sigma}}_m^- \left(t + \tau - \left|\frac{z_d - z_m}{v}\right|\right) \hat{\tilde{\sigma}}_n^- \left(t - \left|\frac{z_d + z_n}{v}\right|\right) \right\rangle e^{i\omega_0 \frac{-z_j + z_l - z_m + z_n}{v}}. \tag{4.43b}$$

In the opposite-correlation function (Eq. (4.43b)), the reflectivity r^2 now represents the imbalance in the power transmission efficiency in the two detection modes.

Assuming a random distribution of atoms, we get the same- and opposite-direction corre-

lation functions

$$\frac{G_N^{(2)(\text{same})}(\tau)}{|\beta E_0|^4 I^2} = N(N-1)\left(\left|g_A^{(1)}(\tau)\right|^2 + 1\right) + N g_A^{(2)}(\tau) \tag{4.44a}$$

$$\frac{G_N^{(2)(\text{opp})}(\tau)}{|\beta E_0|^4 I^2} = N(N-1)\left(r^2\left|g_A^{(1')}(\tau)\right|^2 + 1\right) + N r^2 g_A^{(2)}(\tau) \tag{4.44b}$$

Therefore, the correlation of scattering in front of a mirror (Eq. (4.41)) can be regarded as a simple sum of same- and opposite-direction correlations (Eq. (4.44a) and (4.44b)), with appropriate time shifts in the opposite correlations. As a result, the intensity correlation function of independent emitters in front of a mirror exhibits a nontrivial structure at $t = \tau_D$, despite the absence of atomic correlations.

4.3.3 Transit Time Effect and Atom Number Fluctuation

To compute the averaged intensity correlation function in a fluctuating system, it is convenient to count the number of photon pairs separated by a delay τ for each configuration. We follow [175] to calculate the number of photon pairs emitted from a finite-temperature atomic cloud.

Let's say two detectors measures the output of a 50-50 beam splitter. The detector "a" measures the start pulse and the detector "b" measures the stop pulse. The number of photon pairs in the field scattered by N-atom system that are separated by τ within the detector time

window $\Delta\tau$ is [175]:

$$\langle n_N(\tau)\rangle = \Lambda_N \Delta\tau \frac{\alpha_b S_b G_N^{(2)}(\tau)}{I_N}, \tag{4.45}$$

where Λ_N is the number of the accepted start pulses in the course of the experiment, and α_b and S_b are the efficiency and the area of detector b, respectively. Since the number of the start clicks Λ_N is proportional to the intensity at the detector I_N, the overall number of photon pairs separated by τ is proportional to the second order correlation function $G_N^{(2)}$.

In a real experiment with neutral atoms interfaced with an ONF, the atoms fly around the ONF. Thus, the number of atoms involved in the dynamics and the coupling efficiency of each atom varies over time. Such atom number fluctuation and transit time effect have been considered theoretically in [175, 176] and the model has been verified experimentally in atoms moving in and out of cavity or ONF region [179, 180]. We re-state the model for the intensity correlation function of light emitted by moving atoms, for a more general scenario which includes the case of atoms in front of a mirror.

Atom Number Fluctuation

We first consider the atom number fluctuation. When there is an N fixed number of atoms in the system, the number of photon pairs that are separated by τ is given by Eq. (4.45). Now considering the fluctuating number of atoms in the system, the number of photon pairs separated

by τ is the summation of all possible $\langle n_N(\tau)\rangle$:

$$\begin{aligned}\langle n(\tau)\rangle &= \sum_{N=0}^{\infty} \langle n_N(\tau)\rangle \\ &= \Lambda\Delta\tau \sum_{N=0}^{\infty} p_c(N) \frac{\alpha_b S_b G_N^{(2)}(\tau)}{I_N},\end{aligned} \tag{4.46}$$

where Λ is the total number of accepted start pulses and $p_c(N)$ is the conditional probability that there are N atoms in the system when there is a start pulse.

For independent emitters, one can connect this conditional probability to the atom number distribution $p(N)$ following argument in [175]. Let us say that the mean counting rate of the fluorescent light is R_a at detector a. Also, let $P(N, \text{start})\Delta t$ be the joint probability that there are N atoms in the system and that a start pulse occurs at time t within Δt. The conditional probability $p_c(N)$ is then obtained by dividing the joint probability $P(N, \text{start})\Delta t$ by the probability that a start pulse occurs within Δt, which is $R_a \Delta t$:

$$p_c(N) = \frac{P(N, \text{start})\Delta t}{R_a \Delta t}. \tag{4.47}$$

The joint probability $P(N, \text{start})\Delta t$ consists of mutually exclusive possibilities; there may be N atoms and the start pulse may be caused by emission of the first atom ($p(N)\alpha_a S_a \eta \langle I\rangle \Delta t$), etc, where η is the geometric factor that may reduce or increase the number of photon counts and $\langle I\rangle$ is the single-atom fluorescent light intensity in one direction. Also, the mean counting rate is connected to the mean intensity as $R_a = \alpha_a S_a \langle N\rangle \eta \langle I\rangle$. Thus,

$$p_c(N) = p(N) \times \frac{N}{\langle N\rangle}. \tag{4.48}$$

This enables us to use the atom number distribution function to describe the number of photon pairs separated by τ in a fluctuating system:

$$\langle n(\tau)\rangle = \Lambda\Delta\tau \sum_{N=0}^{\infty} p(N)\frac{N}{\langle N\rangle}\frac{\alpha_b S_b G_N^{(2)}(\tau)}{I_N}. \tag{4.49}$$

Plugging in Eq. (4.41) and (4.42), we have the number of photon pairs separated by τ in the scattering from atoms in front of a mirror:

$$\begin{aligned}\langle n(\tau)\rangle =&\Lambda\Delta\tau\alpha_b S_b \sum_{N=0}^{\infty}\frac{p(N)}{\langle N\rangle} I\left|\beta E_0\right|^2 \\ &\times\left\{N(N-1)\left[\frac{r^2}{(1+r^2)}\left|g_A^{(1')}(\tau-\tau_d)+g_A^{(1')}(\tau+\tau_d)\right|^2+(1+r^2)\left(\left|g_A^{(1)}(\tau)\right|^2+1\right)\right]\right. \\ &\left.+N\left[\frac{(1+r^4)}{(1+r^2)}g_A^{(2)}(\tau)+\frac{r^2}{(1+r^2)}\left(g_A^{(2)}(\tau-\tau_d)+g_A^{(2)}(\tau+\tau_d)\right)\right]\right\}.\end{aligned} \tag{4.50}$$

Assuming the Poisson distribution of the number of atoms, the summation over atomic ensembles results in

$$\begin{aligned}\langle n(\tau)\rangle =&\Lambda\Delta\tau\alpha_b S_b I\left|\beta E_0\right|^2 \\ &\times\left\{\langle N\rangle\left[\frac{r^2}{(1+r^2)}\left|g_A^{(1')}(\tau-\tau_d)+g_A^{(1')}(\tau+\tau_d)\right|^2+(1+r^2)\left(\left|g_A^{(1)}(\tau)\right|^2+1\right)\right]\right. \\ &\left.+\left[\frac{(1+r^4)}{(1+r^2)}g_A^{(2)}(\tau)+\frac{r^2}{(1+r^2)}\left(g_A^{(2)}(\tau-\tau_d)+g_A^{(2)}(\tau+\tau_d)\right)\right]\right\}.\end{aligned} \tag{4.51}$$

Transit Time Effect

The atomic motion not only results in the atom number fluctuation but also in the varying

coupling efficiency. If a photon was emitted from an atom at time t, the probability of having a second photon count from the same atom at time $t+\tau$ is reduced due to the atomic motion. This reduction is captured by the transit time function $f(\tau)$.

For atoms traveling around an ONF, the transit time function is known to have form [180]

$$f(\tau) = A\frac{e^{-2(|\tau|/\tau_0+qr_0)}}{(|\tau|/\tau_0+qr_0)}, \tag{4.52}$$

where A is the normalization coefficient which makes $f(\tau=0)=1$, τ_0 is the characteristic time an atom takes to exit from guided mode, q is the radial decay parameter of the guided mode (see Appendix A.1 for guided mode profile), and r_0 is the nanofiber radius.

The transit-time function $f(\tau)$ has to be multiplied whenever the correlation involves a single atom at different times. Thus, the single atom correlation functions defined in Eq. (4.53) are replaced with

$$g_A^{(1)}(\tau) \to f(\tau)g_A^{(1)}(\tau), \tag{4.53a}$$

$$g_A^{(1')}(\tau) \to f(\tau)g_A^{(1')}(\tau), \tag{4.53b}$$

$$g_A^{(2)}(\tau) \to f(\tau)g_A^{(2)}(\tau). \tag{4.53c}$$

Considering the transit time effect, the number of photon pairs separated by time τ (Eq. (4.51))

becomes

$$\begin{aligned}\langle n(\tau)\rangle =&\Lambda\Delta\tau\alpha_b S_b I\left|\beta E_0\right|^2\left\{\langle N\rangle\left(1+r^2\right)\left(1+\left|f(\tau)g_A^{(1)}(\tau)\right|^2\right)\right.\\&+\langle N\rangle\frac{r^2}{(1+r^2)}\left|f(\tau-\tau_d)g_A^{(1')}(\tau-\tau_d)+f(\tau+\tau_d)g_A^{(1')}(\tau+\tau_d)\right|^2\\&\left.+\frac{(1+r^4)}{(1+r^2)}f(\tau)g_A^{(2)}(\tau)+\frac{r^2}{(1+r^2)}\left(f(\tau-\tau_d)g_A^{(2)}(\tau-\tau_d)+f(\tau+\tau_d)g_A^{(2)}(\tau+\tau_d)\right)\right\}.\end{aligned} \tag{4.54}$$

Normalizing to the uncorrelated counts, i.e., $\langle n(\tau\to\infty)\rangle$, we get the normalized intensity correlation function (note that $f(\tau\to\infty)=0$):

$$\begin{aligned}g^{(2)}(\tau)=1+&\left|f(\tau)g_A^{(1)}(\tau)\right|^2+\frac{r^2}{\left(1+r^2\right)^2}\left|f(\tau-\tau_d)g_A^{(1')}(\tau-\tau_d)+f(\tau+\tau_d)g_A^{(1')}(\tau+\tau_d)\right|^2\\&+\frac{1}{\langle N\rangle}\left\{\frac{(1+r^4)}{\left(1+r^2\right)^2}f(\tau)g_A^{(2)}(\tau)+\frac{r^2}{\left(1+r^2\right)^2}\left(f(\tau-\tau_d)g_A^{(2)}(\tau-\tau_d)+f(\tau+\tau_d)g_A^{(2)}(\tau+\tau_d)\right)\right\}\end{aligned} \tag{4.55}$$

Similarly, the same-direction and opposite-direction correlation function of scattered light from finite temperature atom is obtained from Eq. (4.44):

$$g_N^{(2)(\text{same})}(\tau)=1+\left|f(\tau)g_A^{(1)}(\tau)\right|^2+f(\tau)g_A^{(2)}(\tau)/\langle N\rangle \tag{4.56a}$$

$$g_N^{(2)(\text{opp})}(\tau)=1+r^2\left|f(\tau)g_A^{(1')}(\tau)\right|^2+f(\tau)g_A^{(2)}(\tau)/\langle N\rangle \tag{4.56b}$$

The above equations match with the previously derived equations for same- and opposite-direction correlation functions in multi-atom systems [175, 176, 178–180].

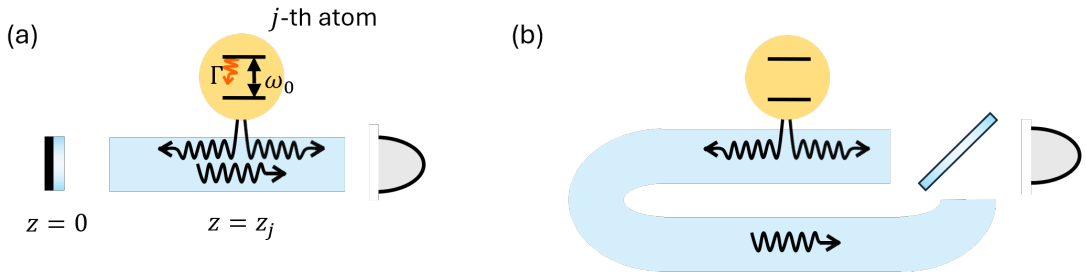

Figure 4.9: Simplified schematics of measurement setup for (a) with-mirror correlation function where the reflected photon goes through the atoms and may interact again, and (b) bypass delay correlation function where the returning photon does not interact with the atoms and combined with the directly emitted light at a beam splitter. For simplicity, only one detector is drawn.

4.4 Experiment

Figure 4.1 shows the schematics of our experiment. A cloud of ^{85}Rb atoms is trapped by MOT and overlapped with an ONF. The $1/e^2$ size of the MOT is $\approx$ 15 mm, and the temperature of the cloud is around the Doppler temperature of $\sim$125 μK. We consider the ground state $|g\rangle = \left|5^2S_{1/2}, F = 3\right\rangle$ and the excited state $|e\rangle = \left|5^2P_{3/2}, F' = 4\right\rangle$ as our two-level system. The atoms are resonantly driven from the side and emit into the fiber mode. A mirror is placed at one end of the fiber with an intervening delay line, and detectors measure the correlation counts at the other end of the fiber. The repump beam passes through the fiber and repumps only the atoms that are coupled to the ONF mode. It is injected through the 1% port of a fiber beam splitter from the mirror side. Since the repump power critically affects the number of atoms, we avoid directing it toward the mirror. The heating beam passes through the fiber via the 5% port of a fiber beam splitter from the detector side. The heating will have a reflection when the mirror is present, but the change in heating power is less critical as the heating beam is turned off during the measurement.

The major measurement geometry is shown in Fig. 4.9. We measure the correlation func-

tion of light scattered outside the half-cavity as shown in Fig. 4.9 (a). We also measure the correlation function of the same setup, but with the returning photon routed to a delay line that bypasses the atomic cloud, as illustrated in Fig. 4.9 (b). The comparison of the two measurements tests the effect of the delayed interaction of the atomic ensemble and its mirror ensemble.

We took the waiting-time distribution, i.e., a click at one of the detectors triggers the histogram, and a click at the other detector stops the histogram. We checked that the waiting-time distribution shows a similar structure to the true intensity correlation function, except that it shows global decay. We can thus reconstruct the pseudo-intensity correlation function by fitting the decaying curve of waiting time distribution far outside the relevant physical time scales, i.e., 2.5 μs. Then, we divide the data with the fitting to compensate for the global decay due to the artifact of the waiting-time-distribution measurement.

Then we fit $\tau > 500$ ns to obtain the transit time envelope. At time scales much larger than the atomic internal dynamics or delay time between the atom and the mirror, we can approximate the single atom correlation functions to $g_A^{(1)}(\tau \to \infty) = 0$, $g_A^{(1')}(\tau \to \infty) = 0$, and $g_A^{(2)}(\tau \to \infty) = 1$. Furthermore, the transit time envelope has a decaying timescale much larger than the delay times in our setup; thus, it can be approximated as $f(\tau \pm \tau_d) \approx f(\tau)$. Then, Eq. (4.55) becomes

$$g^{(2)}(\tau) = 1 + \frac{f(\tau)}{\langle N \rangle}. \tag{4.57}$$

Note that this transit time fitting formula is the same for the same- and opposite-direction correlation functions, as can be seen from Eq. (4.56). We use the transit time function form for ONF modes defined in Eq. (4.52). From this fitting, we get the average number of atoms $\langle N \rangle$ and the

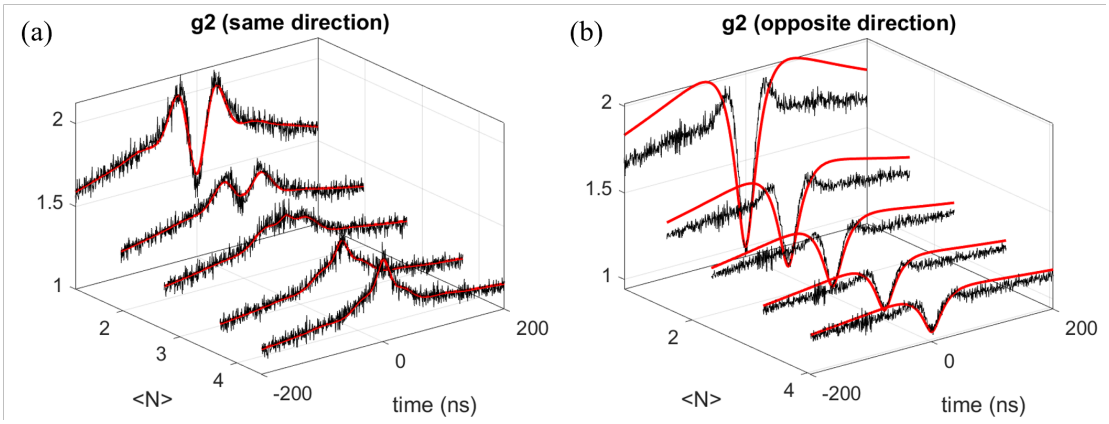

Figure 4.10: Intensity correlation functions of photons scattered into the (a) same and (b) opposite direction in the ONF guided modes. The correlation measurement was taken for varying the average number of atoms. The red solid lines are fits obtained using Eq. (4.56).

transit time constant τ_0.

4.5 Results

Fig 4.10 shows the intensity correlation function of scattered radiation into the same and opposite direction in the ONF guided modes for various average atom numbers. Both same- and opposite-direction emission correlation data fit well with the theoretical prediction in Eq. (4.56), shown as red solid lines. The emission in the same direction shows an antibunching-like feature when the average number of atoms is low. This is because of the single-atom contribution dominating the dynamics, as it is highly unlikely to have multiple atoms. As the average number of atoms increases, the coincidence count shows a transition to a bunching peak. The multi-atom scattering process becomes dominant, where two atoms can scatter photons simultaneously. This behavior has been well studied in [175, 176, 179, 180, 182]. On the other hand, the correlated counts of oppositely emitted photons show strong antibunching regardless of the average number of atoms. This is due to the phase-matching condition in the emission to the

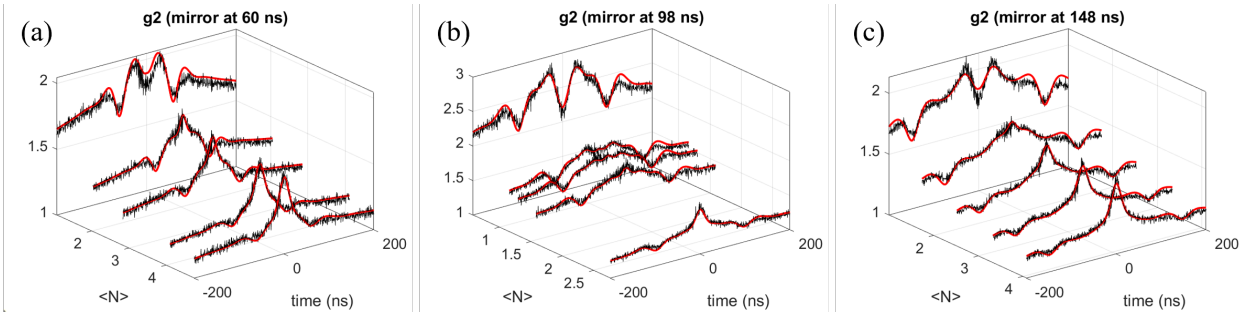

Figure 4.11: Intensity correlation functions of photons scattered from atoms in front of a mirror, for time delay (a) 60 ns, (b) 98 ns, and (c) 148 ns. The correlation measurement was taken for varying average number of atoms.

opposite direction. The two atom contribution of kind $\langle\hat{\sigma}^+(t)\hat{\sigma}^-(t+\tau)\rangle$ has a fast rotating term and thus averaged out over random atomic distribution. However, the two atom contribution of kind $\langle\hat{\sigma}^+(t)\hat{\sigma}^+(t+\tau)\rangle$ survives, which shows antibunching as well. It has been interpreted using analogy to four-wave-mixing in [177], where two photons are mixed at two atoms.

Figure 4.11 shows typical data taken for the atomic ensemble in front of a mirror, where the delay time between the atomic ensemble and the mirror ensemble is varied among 60 ns, 98 ns, and 148 ns, all of which are much larger than the atomic relaxation time scale (26 ns). For all three cases, the coincidence count at $\tau = 0$ shows an antibunching-to-bunching transition as the average number of atoms in the system increases, whereas it shows the robust antibunching at the delay that corresponds to the atom-image distance. Such behavior qualitatively matches the correlation function of the independent emission. If it were the strongly correlated emission, then it would've shown bunching at the null delay, as discussed in Sec. 4.2.3. The red graphs show the fitting to the weak-coupling g2 formula in Eq. (4.55), with Γ and Ω as free parameters. It shows exceptional agreement with the theory, where the fitted value of Γ is $\approx\ 1.6\Gamma_0$ and $\Omega\ \approx\ 2.3\Gamma_0$ where $\Gamma_0 = 2\pi \times 6$ MHz is the natural linewidth of the ^{85}Rb D_2 line.

To experimentally confirm that the interaction between the returning photons and the atomic

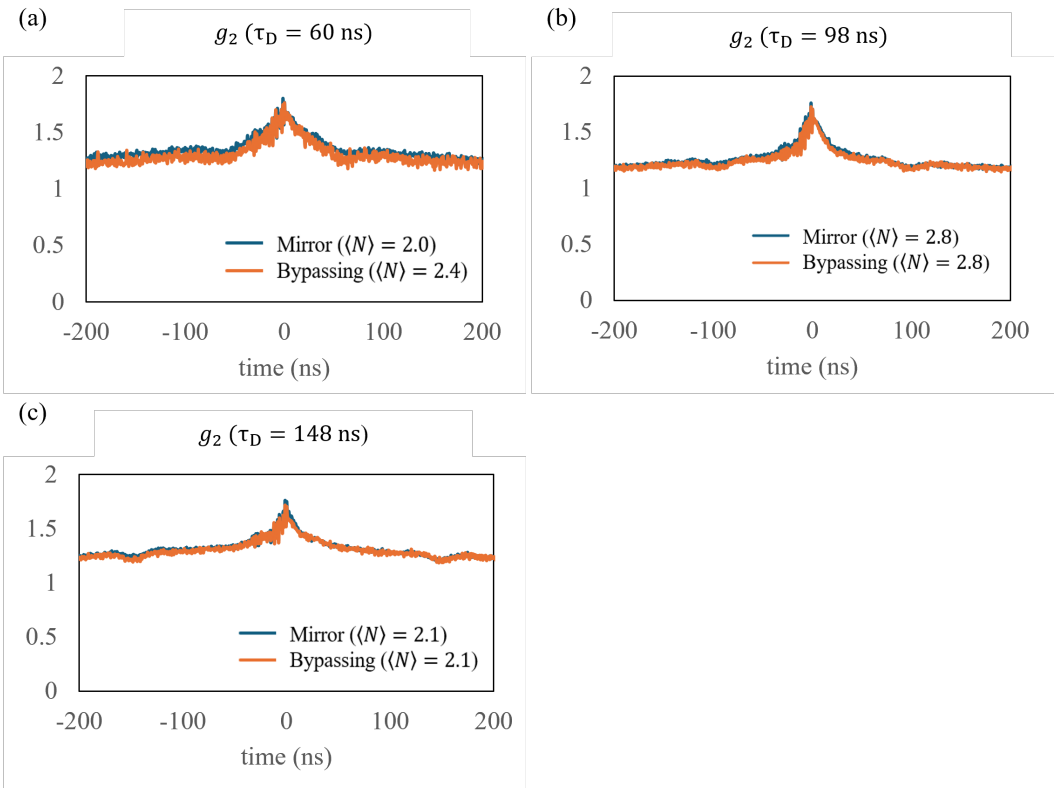

Figure 4.12: Comparison of mirror case as in Fig. 4.9 (b) and the bypassing delay case as in Fig. 4.9 (c) for three different delay times. Each case has a similar average number of atoms for direct comparison.

cloud is negligible, we measured the case where the reflected photon is sent to a bypassing delay line. The comparison of the mirror case and the bypassing delay case is shown in Fig. 4.12, for three different delay times. The two cases show negligible differences, implying that the interaction of the atomic ensemble via ONF guided mode is minimal.

4.6 Discussion

We investigated the driven-dissipative dynamics of ^{85}Rb atoms coupled to an ONF and put in front of a distant mirror. We investigated the scattering properties in terms of the intensity correlation function. The time delay between the atomic cloud and its mirror image is larger than the atomic relaxation timescale, possibly placing the system in the non-Markovian regime.

Our theoretical framework models the driven-dissipative dynamics of multiple atoms in front of a mirror, in a waveguide QED setup. The theory investigates two regimes: i) the time-delayed feedback due to the emission in the past dominates the atomic dynamics, and ii) the continuous external drive governs the atomic dynamics. The first case is studied for a single atom in free space, both theoretically [150] and experimentally [174]. Our model gives a more general picture, including the effect of multiple atoms cooperatively emitting and coupling to a waveguide. We demonstrated that, in this strong-coupling regime, the collective decay of a single ensemble rescales the problem, and cooperativity determines the delayed-feedback dynamics in atomic population and the intensity correlation of the emitted field. We investigated non-Markovian dynamics of atomic ensembles, where a single ensemble may exhibit collective effects. The atomic relaxation time scale depends on these collective effects. As non-Markovian criteria are defined with respect to the system relaxation time scale, one should rescale the non-

Markovian parameter (i.e., η for our case) with respect to the collectively modified relaxation time scale. On the other hand, the cooperativity determines how strongly the atoms interact via the guided mode. Thus, it determines both the collectively enhanced decay rate in a single ensemble and the interaction of an ensemble with its mirror image.

In the second regime of weak coupling and strong drive, we derived an intensity correlation function involving radiation from independent emitters, which involves one- and two-atom processes. The derived expression can be understood as a combination of the intensity correlation functions of photons emitted to the same- and opposite-direction in the EM field modes [175–177, 179, 180, 182].

We experimentally measured the correlation function of photons scattered by atoms coupled to ONF guided modes and placed in front of a mirror. The measured data could be explained by the weak coupling theory, where the drive determines the atomic internal dynamics and atoms independently scatter photons into the guided modes. It demonstrates a rich multi-emitter interference effect featured in the intensity correlation function of the scattered light [175–177, 179, 180, 182]. The strength of time-delayed interaction is qualitatively investigated by comparing the two cases, where the reflected photons either pass through or bypass the atomic cloud. The two cases showed negligible difference, indicating minimal effects of time-delayed interaction of the atomic cloud and its emission in the past.

We originally began this project based on [55], where atomic interaction via ONF guided modes has been demonstrated. However, the observed collective enhancement was within 10% due to low coupling efficiency. In this experiment, we introduced additional loss channels by taking the fiber outside the chamber, which include fiber splicing, butt coupler, and mirror losses. Furthermore, non-Markovian dynamics of two distant emitters involve complicated dynamics

even for a well-defined atomic position, making it even harder to analyze mixed signals of enhanced and suppressed decay rates due to random atomic positions.

Our work discusses the interference in the scattering from a multi-emitter system put in front of a mirror, where comparison of two light fields, that is, the past emission into the waveguide coming back to the system ($\sim \beta^2\Gamma$) and the continuous external drive ($\sim \Omega$), leads to distinct features in the intensity correlation function of the scattered light. Our discussion offers insight into the interplay between the collective effects and cooperativity in waveguide QED systems. Our work suggests the need for an ordered array commensurate with the resonant wavelength, interfaced with an ONF, for future studies of strong photon-mediated interactions in this all-fiber system.

Chapter 5: A Tunable-Spacing Atomic Array Coupled to an ONF

5.1 Introduction

Phase ordering of atoms is essential for enhancing collective cooperativity in waveguide QED systems. When atoms are spaced by integer multiples of the resonant wavelength, their interaction via the waveguide leads to collectively enhanced decay into the guided mode [33]. This phase alignment is especially important for neutral atoms coupled to an ONF, where the individual coupling efficiency is low (typically <10%) but thousands of atoms can be interfaced [71–75]. A commensurate atomic array thus provides an effective way to enhance cooperativity in ONF-based systems.

There have been two major approaches to building an ordered array of atoms around an ONF: i) guided optical lattices [81, 82, 183], and ii) optical tweezer arrays projected onto the ONF [28, 184]. In the first method, red- and blue-detuned trap beams are guided through the fiber. They have different evanescent decay lengths, forming a potential minimum around a few hundred nanometers from the fiber surface. By counter-propagating one of the trap beams, an evanescent optical lattice is formed. While this approach is power-efficient and supports thousands of uniform trapping sites, its lattice-constant tunability is limited. Moreover, because the dipole-trap beams are far-detuned from the atomic resonance, it cannot produce a commensurate array. On the other hand, interfacing optical tweezer arrays with an ONF offers excellent

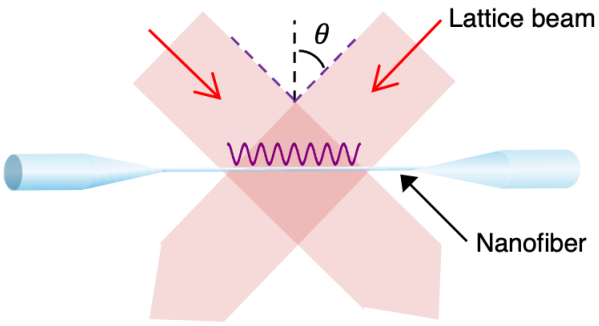

Figure 5.1: Diagram of optical accordion lattice interfaced with an ONF. Figure adapted from [154].

tunability in lattice spacing. A proof-of-principle demonstration has shown that a single atom can be trapped in a tweezer spot and coupled to the ONF guided modes [184]. While extending this method to multiple sites is still technically demanding, it holds significant promises for fiber-integrated quantum information processing [28].

We demonstrate a novel approach for creating an atomic array coupled to an ONF using an optical accordion lattice. In this method, two trap beams intersect at the ONF with an angle 2θ (see Fig. 5.1), which determines the lattice constant via

$$d = \frac{\lambda_T}{2\sin\theta}, \tag{5.1}$$

where λ_T is the wavelength of the trap beams. This approach offers tunable lattice spacing by interfacing free-space trap beams with the ONF, and scalability, as the interference of the two beams naturally creates thousands of lattice sites.

In this chapter, we describe the optical setup for making the accordion lattice, its integration with the ONF, and the procedure for loading atoms into the lattice sites. The preliminary data on trapped atoms is presented.

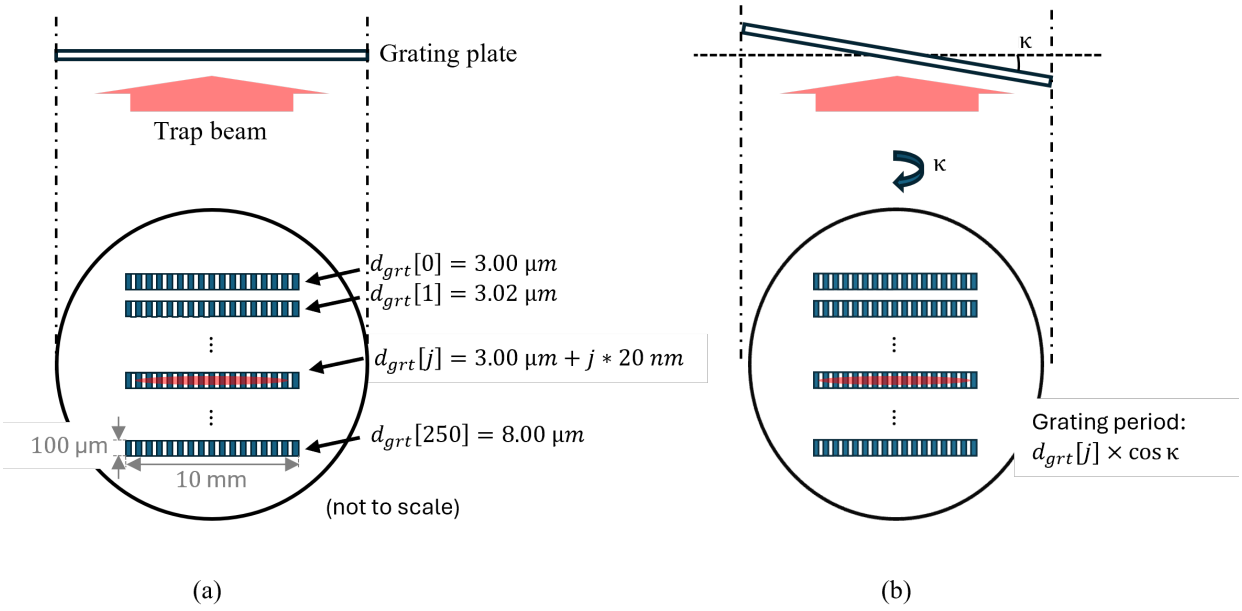

Figure 5.2: (a) Grating plate composed of stacked binary phase transmission gratings with varying grating periods. (b) The effective grating period can be tuned by rotating the plate by a small angle κ. For both cases, top views are provided for clarity.

5.2 Optical Setup and Test

In this section, we summarize our proposal and experimental demonstration of an optical setup for creating an optical accordion lattice using phase transmission gratings. A detailed discussion can be found in [154], which is included at Appendix C. A binary phase transmission grating is used to split the trapping beam into two spatial modes. The binary phase grating is composed of alternating equal-length regions with 0 and π phase shifts. It directs approximately 80% of the incoming optical power into the first-order diffraction modes. These gratings are fabricated in a cleanroom at DEVCOM Army Research Laboratory using the electron beam lithography technique (Raith EBPG5200 Plus), which provides precision better than 5 nm.

The first-order diffracted beams are made parallel by the first aspheric lens, re-focused by the second aspheric lens, and overlapped at the ONF to form an optical lattice (see Fig. 2(a)

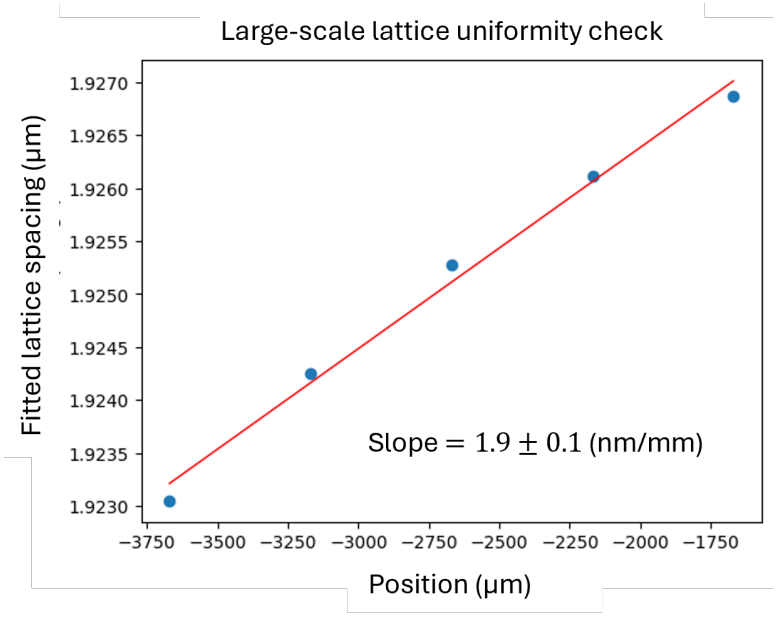

Figure 5.3: Large-scale lattice uniformity test—lattice constant fitted across different sections.

in [154]). The zeroth- and higher-order diffraction modes are spatially filtered out at the Fourier plane. The setup can also be viewed as a $4f$ imaging system that projects the grating structure onto the ONF plane, with DC filtering implemented in the Fourier plane. As a result, the quality of the resulting optical lattice directly inherits the sub-wavelength precision of the grating structure. The practical limitations to the lattice quality are set primarily by the numerical aperture (NA) of the aspheric lenses and the alignment accuracy. Furthermore, this configuration enables flexible lattice design, including non-uniform lattice spacings.

To create a quasi one-dimensional optical lattice, the trap beam is focused in one direction using a cylindrical lens positioned upstream. The grating plate is placed at the focal point of the cylindrical lens. This lens compresses the beam profile along one axis while leaving the orthogonal direction unchanged, resulting in a beam waist at the grating plate of $\approx$ 3.8 mm $\times$ 20 μm. At the ONF plane, the beam waist is reduced to $\approx$ 1.5 mm $\times$ 8 μm. The aspect ratio of roughly 190:1 enable efficient concentration of trap power around the ONF. Notably, the

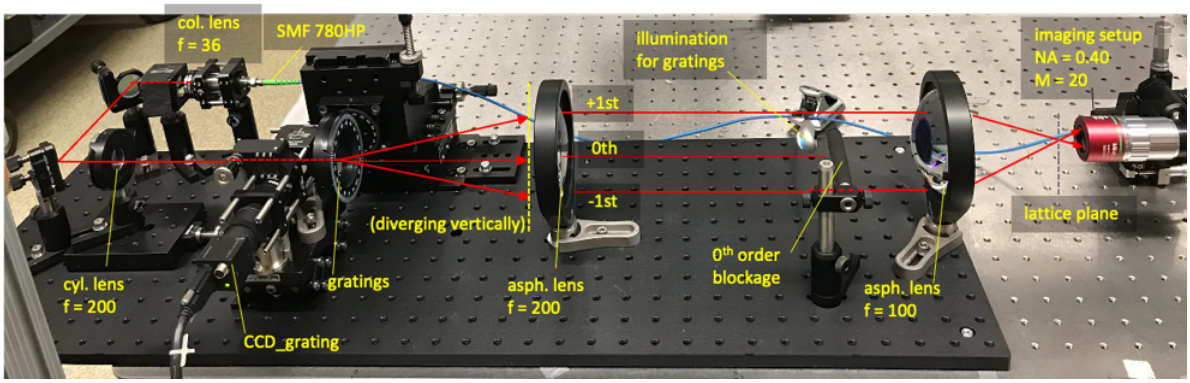

Figure 5.4: Optical setup for the accordion lattice generation using binary phase transmission grating.

transverse beam waist of 8 μm is still much larger than the ONF diameter of 480, so aligning the optical setup to the ONF is not too difficult.

The lattice constant is tuned by changing the grating period. The grating plate contains a stack of 251 quasi one-dimensional gratings with grating constants ranging from 3.0 μm to 8.0 μm in 20 nm steps, as illustrated in Fig. 5.2 (a). Each grating has a width of 10 mm and a height of 100 μm, fully enclosing the beam profile. By translating the grating plate vertically, the lattice constant at the ONF plane can be adjusted from 0.8 μm to 2.0 μm in 5 nm steps (see Fig. 4(a) in [154]). Fine tuning is achieved by rotating the grating plate with a small angle κ, as shown in Fig. 5.2 (b). This rotation effectively reduces the grating period by a factor of $\cos\kappa$. Consequently, within an angular tuning range of ≈ 100 mrad, the entire lattice spacing range can be covered (see Fig. 4(b) in [154]).

The optical setup was built on rails mounted on an optical breadboard, as shown in Fig. 5.4. We checked the quality of the optical lattice by imaging its intensity profile using a microscope objective lens (Mitutoyo P Plan 100x) and a CCD camera (PointGrey FL2G-50S5C-C). Within a 50 μm imaging window, the interference fringe contrast exceed 0.98 (see Fig. 3 in [154]). The large-scale uniformity has been checked by translating the imaging setup to capture different

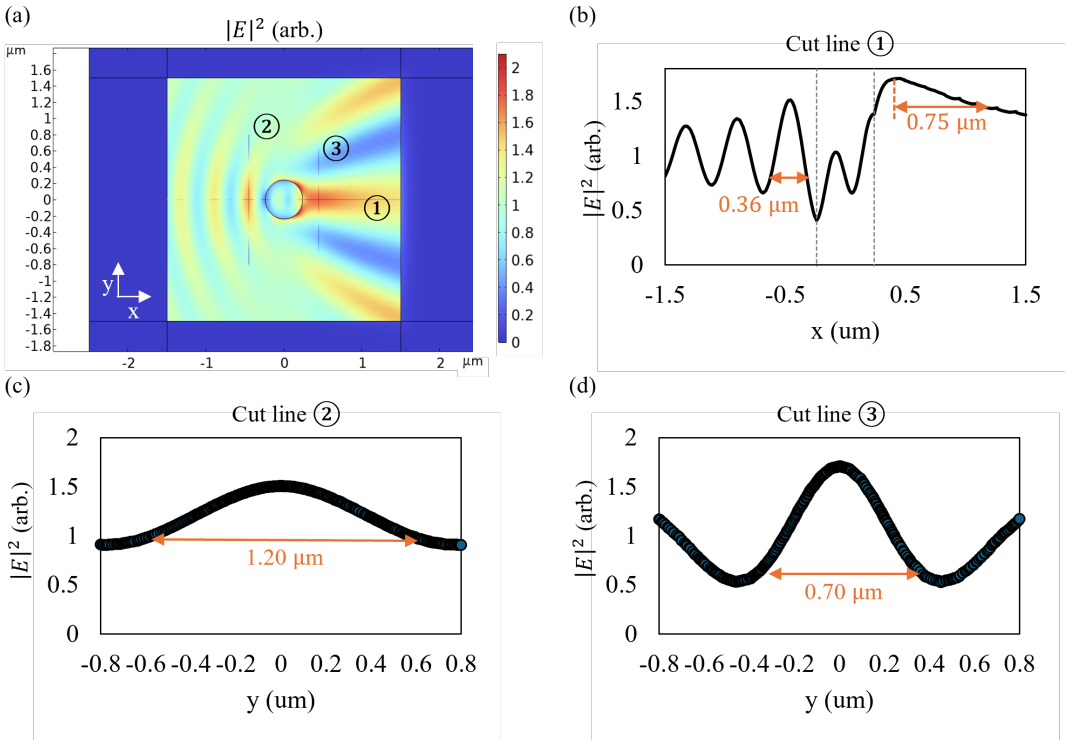

Figure 5.5: COMSOL simulation of light scattering from the ONF surface. (a) 2D simulation showing a 780 nm beam with a waist 10 μm incident from the left onto an ONF of radius 240 nm. (b) Intensity profile along cut line 1, which crosses the center of the ONF; the dashed gray lines mark the ONF surfaces. (c) Intensity profile along cut line 2, taken through the first standing wave peak in the y-direction. (d) Intensity profile along cut line 3, which intersects the trap position located at the focal point behind the ONF surface.

regions of the lattice and fitting each segment to extract the lattice constant as a function of position. We observed an overall variation of 2.05(7) nm/mm change in lattice constant, which is sufficiently uniform for quantum optics experiments.

5.3 Interfacing an Optical Lattice with an ONF

5.3.1 Simulation

We now interface the optical lattice with the ONF. Figure 5.5 shows a COMSOL simulation of an ONF with a radius 240 nm illuminated perpendicularly from the left by a trapping beam with

Trap site	$1/e^2$ radius	U_0 (arb.)	U_1 (arb.)
In front of the ONF			
x-direction	0.18 μm	0.85	0.66
y-direction	0.60 μm	0.60	0.91
Behind the ONF			
x-direction (long tail)	0.75 μm	0.31	1.4
y-direction	0.35 μm	1.18	0.53

Table 5.1: Geometrical parameters of the trap sites formed in front of and behind the ONF (see Fig. 5.5).

780 nm wavelength and 10 μm waist. The incident light reflects off the ONF surface, forming a standing-wave pattern in front of the fiber, while the beam is focused behind the ONF. These two regions - one in front of and one behind the ONF - form trap sites with tightly confined intensity profiles and close proximity to the fiber surface. The front trap site is located 210 nm from the ONF surface, and the back site is 206 nm away. These positions correspond to a calculated coupling efficiency of $\approx$0.7%. Atoms trapped in these sites can thus be interrogated through the ONF guided modes.

The transverse trap potential can be modeled with a Gaussian function:

$$U(x) = U_0 \exp\left(-\frac{2x^2}{w_0^2}\right) + U_1, \tag{5.2}$$

where w_0 is the $1/e^2$ beam radius, U_0 is the trap depth, and U_1 is an offset potential. The trap geometries for the sites in front of and behind the ONF are summarized in Table 5.1. The trap site behind the ONF is notably anharmonic in the x-direction, with a long tail extending $\approx$ 0.75 μm.

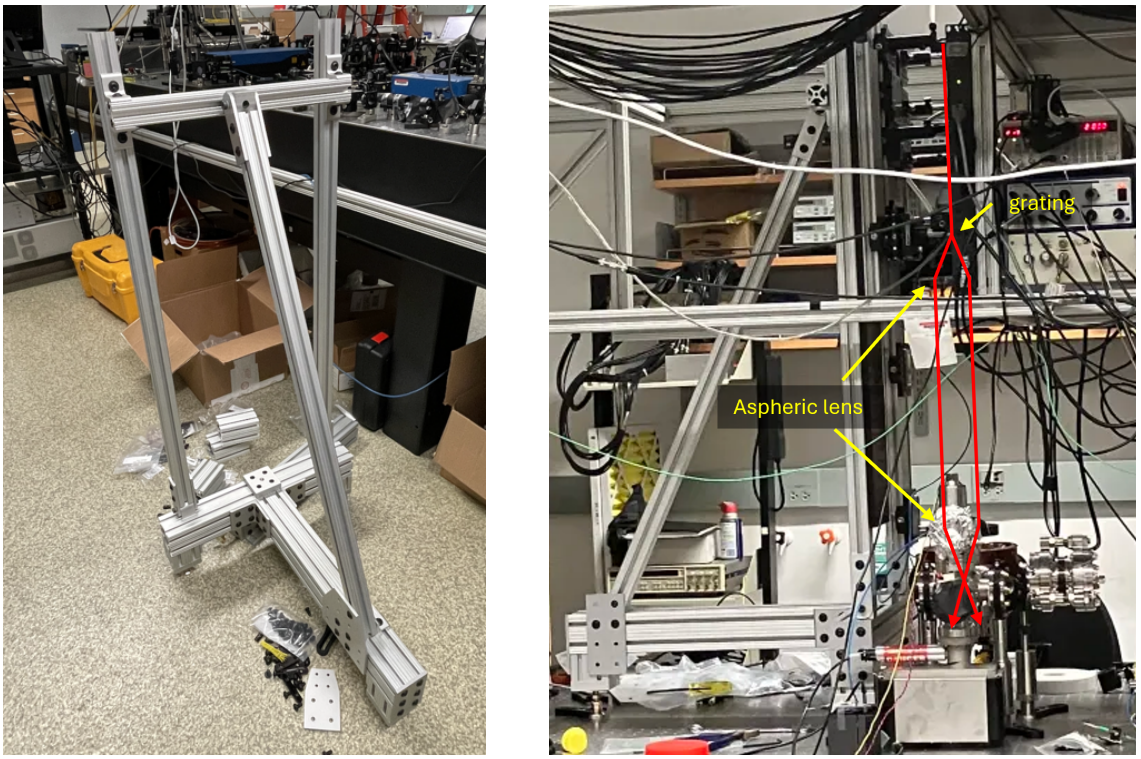

(a) (b)

Figure 5.6: (a) 80/20 system for interfacing optical setup on a breadboard to the chamber. (b) The optical setup for the accordion lattice is put on top of the vacuum chamber. Parts of the beam path are drawn with red arrows.

5.3.2 Alignment

The optical setup (Fig. 5.4) is mounted vertically above our existing chamber, supported by an 80/20 frame as shown in Fig. 5.6. The 80/20 frame has three legs with adjustable height and one rod that supports the breadboard from the back. It is important to ensure that the rear leg remains firmly pressed against the optical table either by securing it with a screw or holding it manually, as the center of mass can be beyond the frame, posing a risk of tipping. We made sure to hold the rear leg securely whenever we loosened and moved it around.

The alignment was checked by looking at the CCD camera that images the reflection from the grating plate (see 'CCD_grating' in Fig. 5.4). Recall that the optical lattice is created by

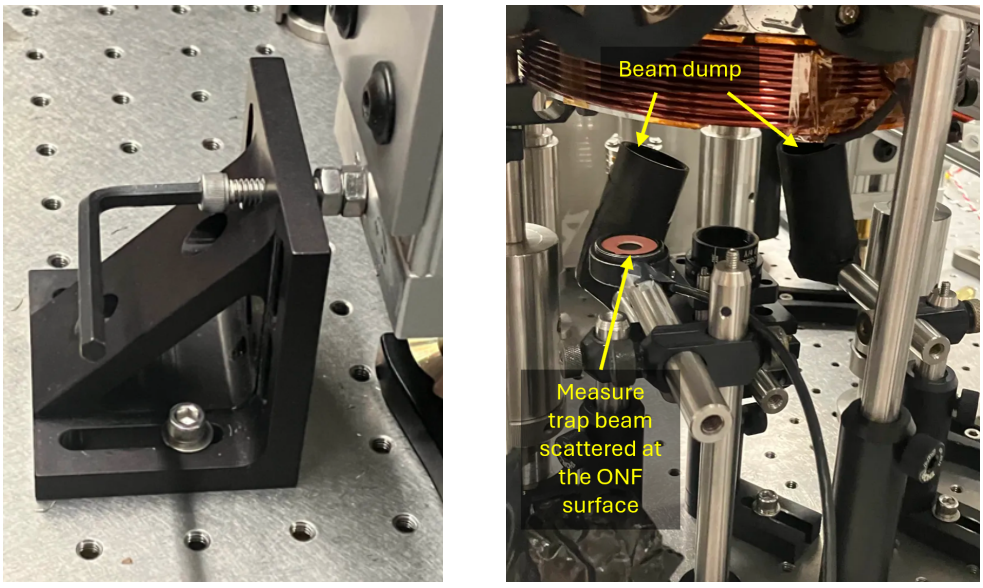

(a) (b)

Figure 5.7: Fine alignment of the lattice setup to the ONF is performed by (a) applying pressure to the 80/20 frame using sets of screws and nuts, and (b) monitoring the trap light scattered from the ONF surface.

$4f$-imaging the grating structure onto the ONF. Conversely, this also means that the ONF is $4f$-imaged onto the grating plate, which is then imaged by the CCD camera. Thus, the CCD captures both the grating structure and the ONF. By bringing the ONF into sharp focus on the CCD, we ensure that the optical lattice is properly aligned with the ONF. The alignment of the entire optical setup on the breadboard relative to the ONF was achieved by translating the entire 80/20 system and adjusting the height of its supporting legs.

For daily fine-tuning of the alignment, we applied slight pressure to the 80/20 frame using sets of screws and nuts, as shown in Fig. 5.7 (a). As a reference signal, the trap beam scattered off the ONF surface is measured, as in Fig. 5.7 (b). The trap beam scatters from the fiber surface, forming a long parabolic-like shape. With $\approx$ 400 mW trap beam power delivered to the lattice setup, the typical scattered power was $\approx$ 100 μW.

Furthermore, we observed that a small fraction of the lattice beam is scattered into the ONF

while preserving its original polarization. This scattered photon count also provides a useful signal for aligning the optical lattice with the ONF. With approximately 80 mW of power delivered to the optical lattice setup, we observed photon count rates on the order of 10^6 counts per second on the APD, measured without any heavy attenuation or filter in the fiber. In addition, this light scattered into the ONF serves as a reference for aligning the polarization analysis setup, enabling precise determination of the polarizations of other beams (e.g., probe or heating beams) at the ONF.

We cross-checked that maximizing the free-space scattered light also maximizes the photon counts coupled into the fiber, confirming that both signals provide consistent and reliable reference for aligning the lattice beams to the ONF.

5.4 Loading Atoms

5.4.1 Polarization Gradient Cooling (PGC)

The dipole trap beam is red-detuned by 125 GHz from the ^{85}Rb D_2 transition, providing a conservative trapping potential with minimal photon scattering [185]. The effective transfer of atoms into the dipole trap requires the atomic ensemble to be cooled to a temperature lower than the trap depth while the trap potential is in effect. A common rule of thumb is that the atomic temperature should be about one-tenth of the trap depth. Since our optical lattice provides a trap depth $\approx$ 400 mK, which is comparable to the Doppler temperature of ^{85}Rb D_2 line (145 μK [158]), additional sub-Doppler cooling is necessary after the MOT stage.

We use polarization gradient cooling (PGC) to cool the atomic cloud to $\approx$ 20 μK. PGC utilizes polarization gradients on the scale of the resonant wavelength, formed by the standing wave

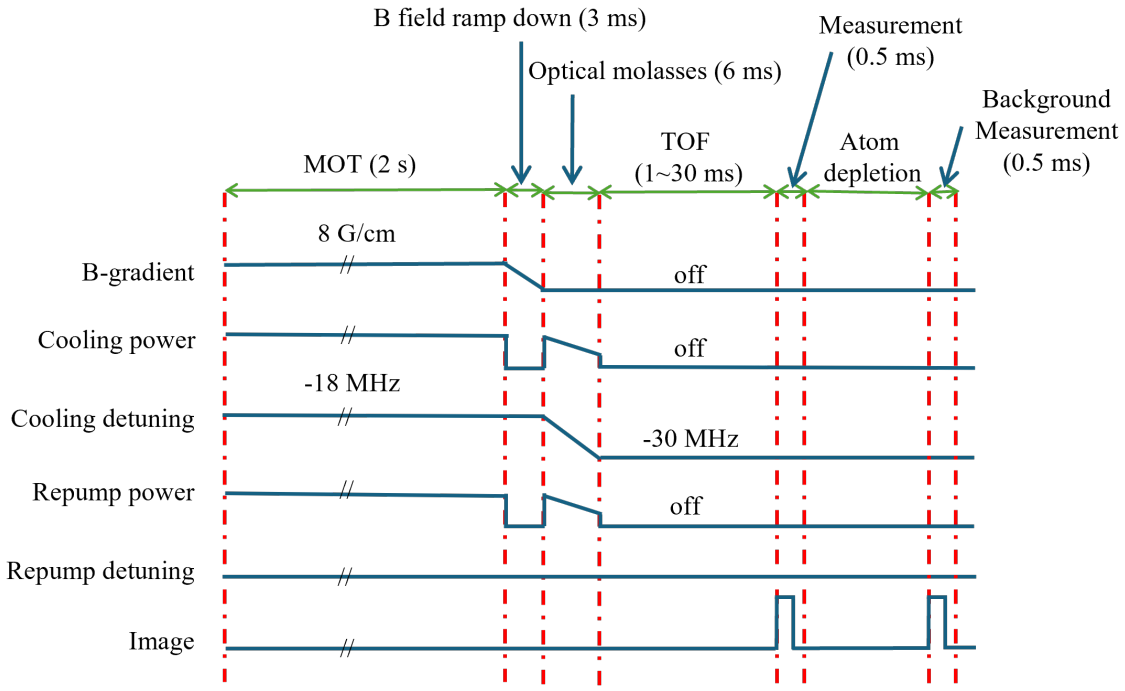

Figure 5.8: Experimental sequence for loading atoms into the optical lattice and measuring OD of the trapped ensemble. The trap beam is on all the time.

structure of the cooling beams [186, 187]. The general PGC sequence used in the experiments is illustrated in Fig. 5.8. After MOT collection, the magnetic field is ramped down with cooling beams turned off. Therefore, atoms do not feel any forces and remain in their initial position. The coils are ramped to a final value that cancels the ambient magnetic field. Once the magnetic field ramping is complete, the cooling and repump beams are turned on and ramped in power and detuning. As this molasses stage only slows down without confining them spatially, the final position of the cooled atoms remains unchanged. As a result, the position of the atomic cloud after PGC is determined solely by the initial MOT position, which is adjusted to overlap with the ONF and lattice. The lattice beam is on throughout the sequence, so that the cooled atoms can be transferred into the trap sites during the molasses phase.

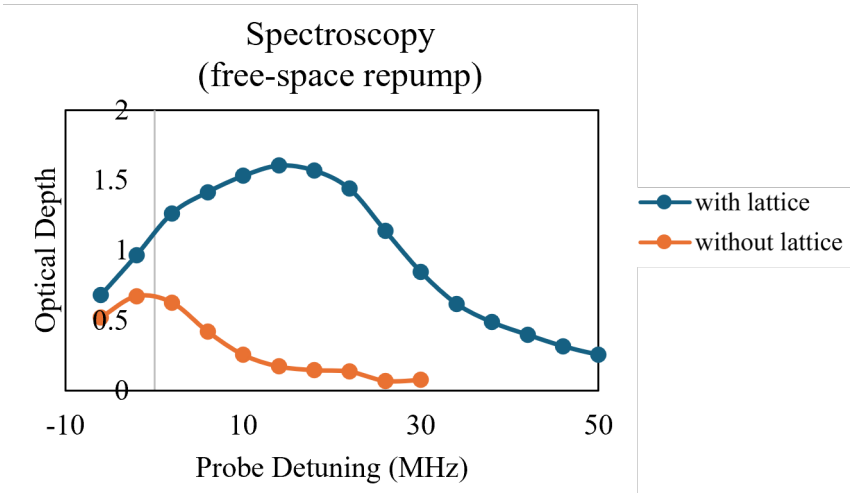

Figure 5.9: Example of OD measurement as a function of probe detuning. The blue data were taken with the lattice beam on throughout the entire sequence, while the orange data were taken with the lattice beam turned off. The TOF was 10 ms, and a free-space repump covering the atomic cloud was applied during the probing stage.

5.4.2 Transmission (OD) Measurement

We measure transmission through the ONF guided mode to diagnose atoms trapped within the lattice sites. Figure 5.9 shows a typical OD measurement as a function of probe detuning. During the measurement, a free-space repump beam is illuminated from the side to maintain the atomic population in the cycling transition. Comparing the cases where the lattice is turned on and off provides insight into the trapped atom population.

- **AC Stark shift:** When the lattice is on, the atomic resonance shifts by ≈ 20 MHz to the blue, due to the AC Stark shift experienced by atoms spatially overlapped with the dipole trap light. This does not necessarily refer to "trapped" atoms, but free atoms may pass through the optical lattice and become frequency-shifted.

- **Inhomogeneous broadening:** Also, a significant inhomogeneous broadening is observed in the presence of the lattice. This broadening likely arises from two main sources: i)

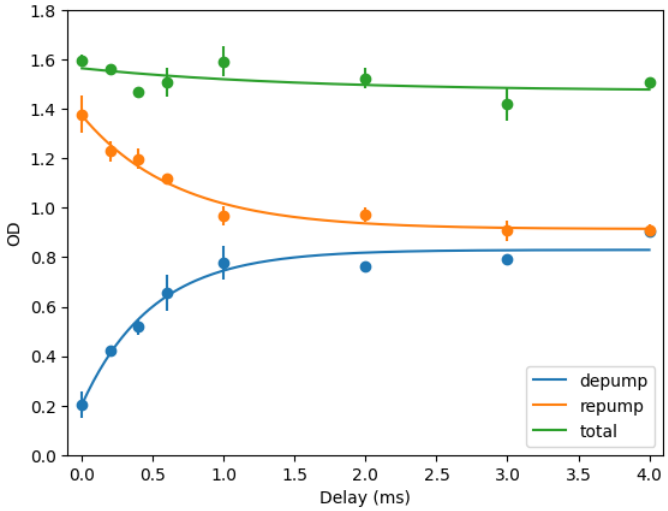

Figure 5.10: The OD of atoms in the ground state $F = 3$ is measured through the ONF guided modes over a 0.2 ms probe duration, following varying delay times after a 1 ms depump (blue) or repump (orange) pulse. The green data points correspond to measurements where the repump beam remains on during the probing. The total TOF is fixed at 10 ms across all cases.

the longitudinal intensity variation of the trapping beam, which has a Gaussian envelope along the ONF axis, and ii) differential AC Stark shifts are different for different Zeeman sublevels.

- **Contribution of untrapped atoms:** The OD remains relatively high even when the lattice beam is turned off. This is because the MOT dissipation timescale is comparable to the trap lifetime, which makes it difficult to distinguish between trapped and untrapped atoms. This implies that, even in the presence of the lattice, a substantial number of free atoms may linger near the ONF, experience an AC Stark shift despite not being trapped, and contribute to the measured OD.

In addition, we observed a depolarization effect in the atomic ground state manifold caused by scattering of the trap beam, as shown in Fig. 5.10. After the atoms are loaded into the lattice, a 10 ms time-of-flight (TOF) period is applied, followed by a 0.2 ms measurement stage. During

the TOF, either the depump (blue) or repump (orange) beam is illuminated to the atoms perpendicularly to the ONF for 1 ms. The time delay between the pump and the measurement is varied from 0 to 4 ms. The effects of both the repump and depump beams diminish on a time scale of $\approx$ 1 ms, which is attributed to the trap beam's scattering. The total OD (green) is measured with the repump beam kept on during the probing. Thus, atoms should be continuously repumped during the measurement stage to counteract depolarization caused by trap beam scattering. However, a brute-force free-space repumping can also affect untrapped atoms that happen to be near the ONF, making it difficult to distinguish between trapped and free atoms.

The following subsections explain how we addressed the issues discussed above.

5.4.3 Selective Probe of Trapped Atoms

We devised two measurement schemes to selectively probe only the trapped atoms. The first scheme utilizes the microscopic time scale over which untrapped atoms move in and out of the ONF field of view, using optical pumping to separate trapped and untrapped atoms into different ground states. Figure 5.11 illustrates the sequence (a-b) and typical spectroscopy data (c) of this scheme. The atomic cloud is depumped just before the measurement stage. During the measurement window, trains of chopped repump and probe pulses are sent through the ONF. The fiber-coupled repump beam selectively repumps atoms near the fiber, regardless of whether they are trapped or free. Untrapped, repumped atoms quickly drift away from the ONF within a few μs, while newly arriving free atoms remain depumped. A delay of 4 μs between the repump and probe pulses ensures that the probe primarily interrogates trapped atoms. The advantage of this method is that it enables selective probing of trapped atoms even when the entire atomic

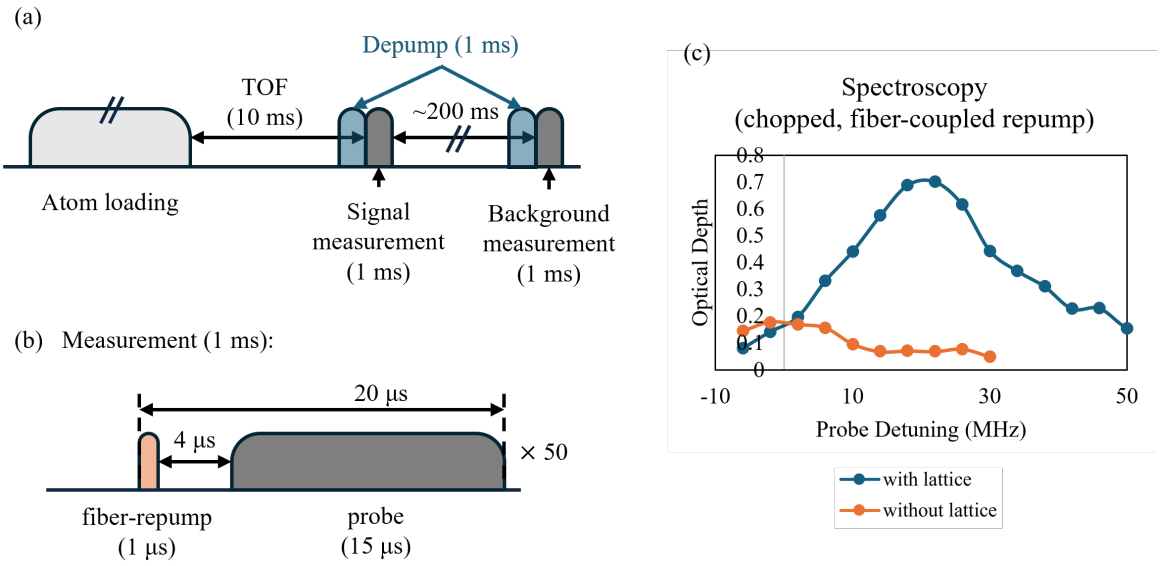

Figure 5.11: Chopped repump and probe scheme - (a) Experimental sequence for measuring the OD of trapped atoms. After TOF, a depump beam is illuminated on the atomic cloud prior to the measurement stage. (b) The measurement stage consists of trains of chopped fiber-repump and probe pulses, separated by 4 μs. This delay allows untrapped atoms to move out of the vicinity of the ONF, ensuring that the probe interacts only with the trapped atoms. Repetition of the sequence keeps the trapped atoms repumped, mitigating depolarization effects caused by scattering from the trap beam. (c) Typical spectroscopy data with the lattice on (blue) and off (orange).

cloud is still present around ONF, allowing measurements with short TOFs. However, because the scheme relies on the statistical motion of free atoms, there is a possibility that slowly moving untrapped atoms contribute to the signal.

The second scheme physically removes untrapped atoms by applying a push-out beam to clear the atomic cloud from the vicinity of the ONF. During TOF, the atomic cloud is first accelerated by resonant beams for 3 ms and then translated away for an additional 4 ms. As shown in Fig. 5.12, this method enables excellent separation of trapped and untrapped atoms in the OD measurement. However, it requires a minimum TOF $\sim$ 7 ms.

We used both schemes interchangeably throughout the experiment.

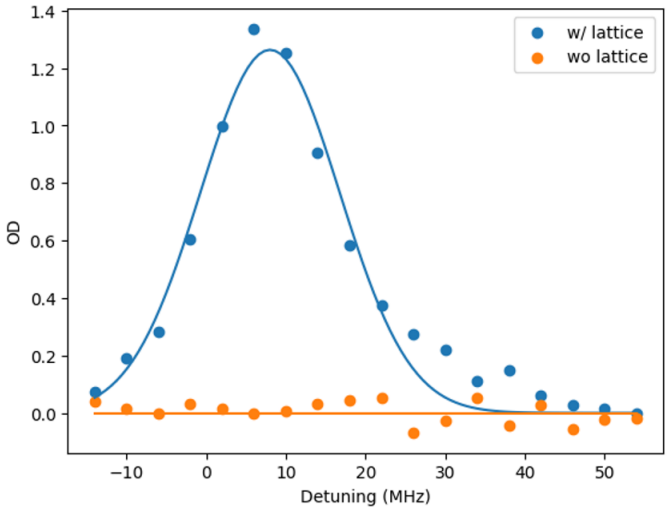

Figure 5.12: OD spectrum with (blue) and without (orange) the trap beam, taken after a 7 ms TOF, during which push-out beams remove the atomic cloud.

5.4.4 Mitigating Inhomogeneous Light Shifts

To minimize the broadening of trap depth due to the Gaussian intensity profile of the lattice along the ONF, we masked the lattice beam so that the atoms are trapped only in the central region of the optical lattice, where the intensity profile is flatter. Figure 5.13 (a) shows the mask, which blocks all but the central 2 mm of the lattice beam. The mask is placed directly on top of the grating plate. To safely dissipate the high-power trap beam blocked by the mask, black aluminum tape (Thorlabs T205-2.0) is applied. Figure 5.13 (b) shows a side-view fluorescence image, demonstrating the sharp edges of the masked trap beams. Figure 5.13 (c) presents the OD spectra with (orange) and without (blue) the lattice beam. These data were taken using the chopped repump and probe scheme. The spectrum in the presence of the lattice shows that a higher fraction of atoms experience large AC Stark shifts and a reduced population near zero shift, indicating that atoms are in the central, more intense region. However, this method does not completely eliminate inhomogeneous broadening, since even atoms at the same trap potential

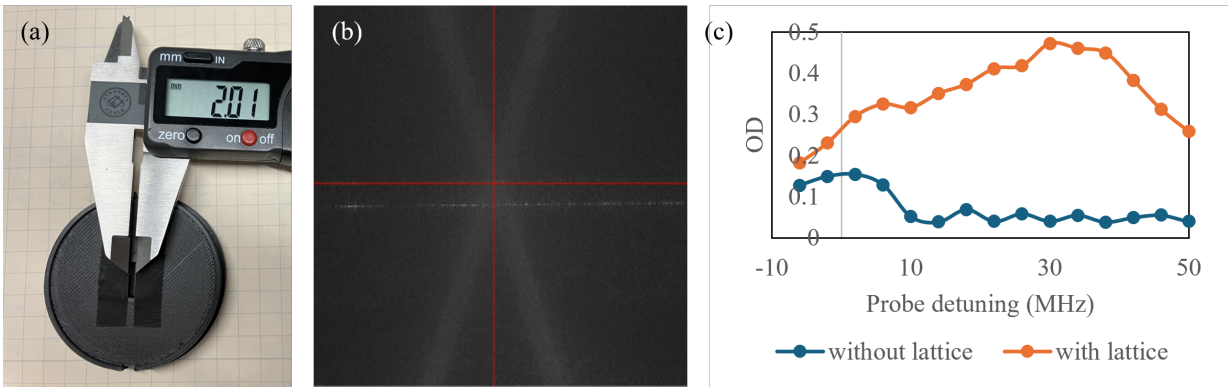

Figure 5.13: (a) Mask with 2 mm width window, which will be placed on top of the grating plate. (b) Side view of the trap beams with the mask. The red lines indicate the position of the upper ONF and the center of the MOT and the trap. The trap beam profile exhibits a sharp edge. (c) OD spectroscopy after placing the mask, with the lattice on (orange) and off (blue).

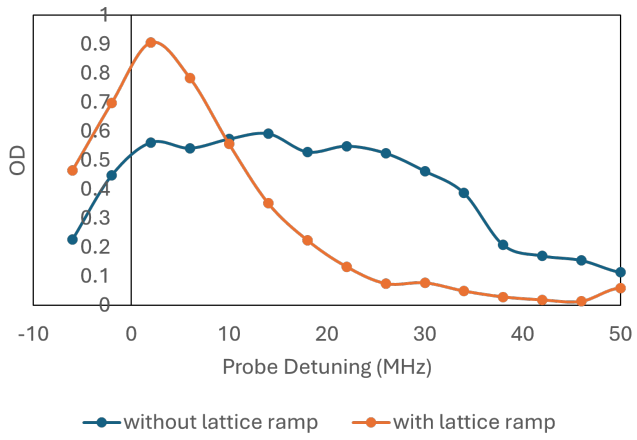

Figure 5.14: OD spectroscopy taken after 8 ms of TOF, with the lattice power either held constant (blue) or ramped down 0.4 ms before the measurement (orange).

experience different transition frequencies depending on their Zeeman sublevels.

Although optical pumping could be used to eliminate the spread in Zeeman sublevels, we adopted a simpler approach. The overall AC Stark shift was reduced by ramping down the trap beam power just before the measurement. As shown in Fig. 5.14, ramping down the lattice power reduces both the average light shift and its inhomogeneous broadening. As a result, the atomic population becomes more localized in frequency space, allowing a single probe frequency to interact with a larger number of atoms.

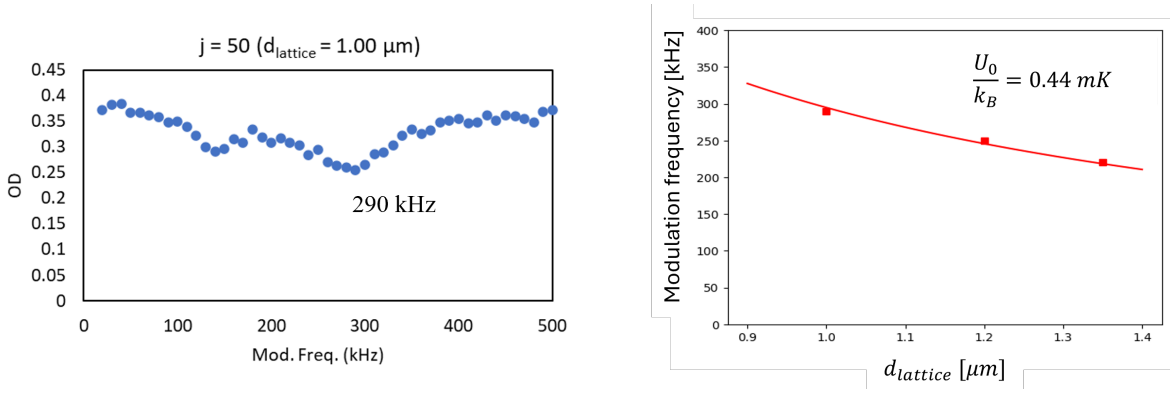

(a) (b)

Figure 5.15: Parametric heating measurement: (a) OD as a function of the modulation frequency for a lattice constant of d_{lat}=1 μm. A resonance peak appears at 290 kHz, around twice the trap frequency in the longitudinal direction. (b) Resonance modulation frequencies measured for varying lattice constants d_{lat}. The data are fit to extract the trap depth in the longitudinal direction, yielding a value of 0.44 mK.

5.5 Trap Geometry

We have confirmed that the atoms are indeed trapped within the periodic structure of the optical lattice by observing changes in the trap frequency corresponding to variations in the lattice constant. Assuming a lattice constant d_{lat} and a trap depth U_0, the potential near each lattice site can be approximated as a harmonic potential:

$$U(z) = U_0 \sin^2\left(\frac{\pi z}{d_{\mathrm{lat}}}\right) \simeq U_0 \left(\frac{\pi}{d_{\mathrm{lat}}}\right)^2 z^2 = \frac{1}{2} m\omega^2 z^2, \tag{5.3}$$

where m is the atomic mass and ω is the angular trap frequency. The trap frequency is thus

$$f = \frac{\omega}{2\pi} = \frac{1}{d_{\mathrm{lat}}}\sqrt{\frac{U_0}{2m}}. \tag{5.4}$$

From the measured AC Stark shift of ≈ 20 MHz in the atomic transition, we attribute half of this shift to the ground state shift. This corresponds to a trap depth of $U_0 \approx 0.5$ mK. For a lattice constant of $d_{\mathrm{lat}} = 1\,\mu$m, this yields trap frequency of ≈ 155 kHz.

We use parametric heating to measure the trap frequencies of trapped atoms. The trap beam power is periodically modulated $\approx 10\%$ in its power using an AOM. Figure 5.15 (a) shows the OD as a function of the modulation frequency for a lattice constant of d_{lat} = 1 μm. We observe a clear heating resonance near twice the trap frequency, $2f$. A smaller heating resonance near f was also observed, but further investigation revealed that this was due to the overdrive of the modulation. The dip at f disappeared when we reduced the modulation amplitude, confirming that it was not intrinsic to trap geometry. Figure 5.15 (b) shows the trap frequencies measured for lattice constants of 1.00 μm, 1.20 μm, and 1.35 μm, and their fitting to Eq. (5.4). From the fitting, the trap depth of 0.44 mK is obtained. This measurement confirms that the atoms are indeed trapped in the tunable-spacing optical lattice.

5.6 Number of Trapped Atoms

We measure the number of trapped atoms using the saturation behavior of atomic scattering. A resonant probe beam is sent through the ONF with varying power. The scattering rate of a single two-level atom follows the standard saturation model [158]

$$R = \left(\frac{\Gamma}{2}\right) \frac{I/I_{\mathrm{sat}}}{1 + 4(\Delta/\Gamma)^2 + (I/I_{\mathrm{sat}})}, \tag{5.5}$$

where I_{sat} is the saturation intensity and $\Delta = 0$ for resonant probing. As seen in Eq. (5.5), the scattering rate saturates to a maximum value of $\Gamma/2$ per atom at high probe intensity. For N

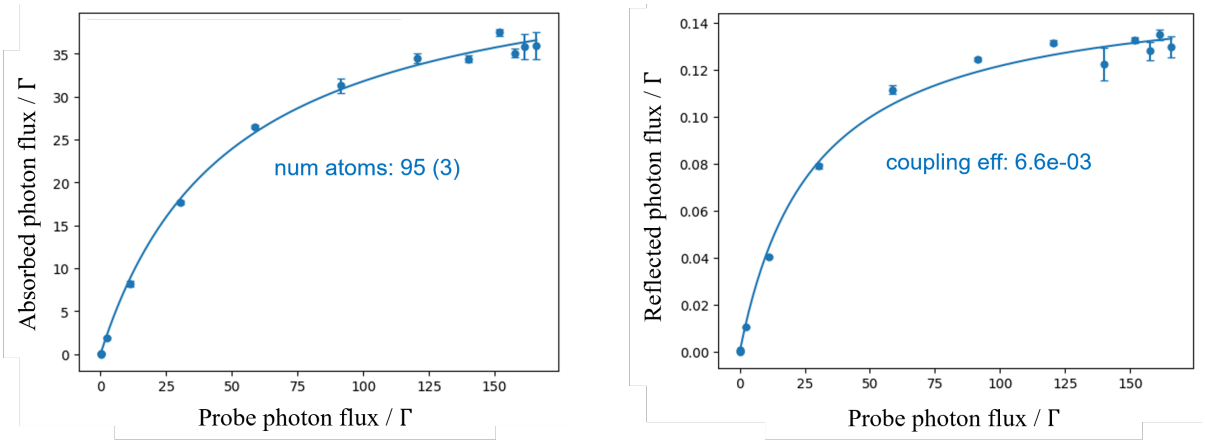

(a) (b)

Figure 5.16: Saturation measurement in the (a) transmitted and (b) reflected photon flux with varying probe photon flux. The measurement uses push-out scheme with TOF of 7 ms. From the transmission data, the number of atoms is extracted to be 95 (3). The coupling efficiency from reflection data is found to be $\approx 0.66\%$, which is in good agreement with the theoretical prediction.

atoms, the total scattering rate scales as $N\Gamma/2$ in the saturated regime. Thus, by measuring the scattered photon flux as a function of the probe photon flux, we can extract the number of atoms. The scattered photon flux is obtained from the difference in photon counts with and without atoms. The raw counts measured at the APD are converted into the actual photon flux at the ONF by accounting for losses from fiber coupling and detection inefficiency. Figure 5.16 (a) shows the measured scattered photon flux as a function of probe photon flux, fitted to Eq. (5.5). The measurement was performed after a 7 ms TOF, during which the atomic cloud was removed using pushout beams. From the fit, we extract the number of trapped atoms 95(3). This corresponds to a filling factor $\approx 2.5\%$ assuming a 2-mm-long lattice with a 1 μm spacing.

The coupling efficiency can be obtained from the reflection measurement. The reflected photon flux divided by the scattered photon flux provides a direct estimate of $\beta/2$. The measured coupling efficiency is 0.66%, in good agreement with the theoretical prediction of 0.7%.

5.7 Discussion

We presented a novel optical setup for creating a tunable-spacing one-dimensional optical lattice around an ONF and a proof-of-principle demonstration of trapping atoms in these lattice sites.

We first demonstrated the qualities of the optical lattice created by this method. Our setup uses stacks of quasi-one-dimensional binary phase transmission gratings to create variable-spacing optical lattices. The grating structure is $4f$-imaged onto the ONF, allowing for the creation of thousands of lattice sites. The gratings are fabricated using the electron-beam lithography technique, which offers precision below 5 nm, well below optical wavelengths. Thus, the generated optical lattice showed excellent uniformity and precision over the entire 2 mm length. The overall lattice constant exhibited a 0.2% chirp over the entire 2 mm lattice region, which is attributed to imperfect alignment and lens aberrations. The power balance between the two first-order diffracted beams is excellent, resulting in high contrast (>0.98) in the lattice. We demonstrated continuous tuning of the lattice constant over large range (0.8 μm to 2.0 μm), by shifting between different gratings having different periods and rotating the grating plate with a small angle. This tuning range can be flexibly adjusted, with the NA of the aspheric lenses being the primary limiting factor.

The proof-of-principle demonstration of trapping atoms in this lattice has been performed with the optical setup installed outside the chamber using 80/20 frame. The atoms are trapped at two localized spots in the transverse plane, each distanced $\approx$ 200 nm from the ONF surface.

Preliminary data indicate that $\sim$ 100 atoms are trapped within the tunable-spacing lattice sites and coupled to the ONF guided modes with a coupling efficiency $\sim$ 0.66%. Further charac-

terization and improvement are left to future work: The trap geometry can be fully characterized, including distinguishing atoms trapped in front of and behind the ONF; the number of trapped atoms can be increased by optimizing the MOT parameters and the loading sequence; the inhomogeneous broadening can ultimately be mitigated by opticaly pumping the atoms into a maximally stretched Zeeman sublevel.

The final chapter presents a new method of creating a tunable-spacing atomic array coupled to an ONF. While existing methods, such as guided optical lattice [81, 82, 183] or tweezer array interfaced to an ONF [28, 184], offer distinct advantages, our setup accesses a new parameter regime that enables both one-dimensional tunability and scalability.

In this chapter, we demonstrated a new method of interfacing an atomic array with an ONF, which offers both lattice tunability and scalability. The tunable array enables the realization of various geometries, including commensurate configurations that exhibit collectively enhanced coupling to the guided mode. This facilitates high-cooperativity atom-fiber systems, providing a platform for exploring collective quantum optics phenomena in waveguide QED setups. Additionally, it presents a promising route toward scaling up neutral atom–based quantum computers by connecting mid-sized systems through optical fiber networks.

Chapter 6: Conclusion and Outlook

We have investigated the collective dynamics of ^{85}Rb atoms coupled to an ONF. In particular, the effects of atomic spatial distribution and photon propagation effects on the one-dimensional collective dynamics have been studied.

We have first investigated collective dynamics in V-type multilevel systems, considering two hyperfine states $|F' = 4\rangle$ and $|F' = 3\rangle$ in the ^{85}Rb D_2 transition [136]. The forward-scattered mode is measured, ensuring the atoms are superradiantly emitting. We have experimentally demonstrated that vacuum-mediated coupling between the two well-separated hyperfine excited levels (120 MHz apart) can be collectively enhanced. As a result, collective quantum beats are observed even when only one of the excited states is initially populated. While such vacuum-induced coupling is a second-order process and has a small effect, we could collectively enhance it.

We theoretically extended the system to a waveguide QED setup and studied the effect of photon propagation between the atoms [153]. We showed that the relevant length scale in determining collective quantum beats involving two distant atoms is the beat wavelength λ_{beat}. It determines the period of relative phase shifts between two EM field modes corresponding to two resonant transitions. As a result, the quantum beats are collectively enhanced (suppressed) when the emitters are separated by an integer (half-integer) multiple of λ_{beat}. In the non-Markovian

regime, the scattering from distant atoms forms a cavity-like system, leading to additional collective decay modes near resonance. This alters the dynamics of the collective quantum beats; the beat size is enhanced beyond the Markovian limit for symmetric systems and only moderately suppressed for antisymmetric systems. Our work on the collective dynamics of V-type multilevel systems can have applications in quantum technologies, such as bright single-photon sources [170, 171] or the analysis of collective dynamics in inhomogeneous emitters.

We also experimentally studied the possible long-distance interaction of atoms via the ONF guided mode. A ^{85}Rb atomic cloud is overlapped with an ONF and put in front of a mirror, where the delay time between the atomic ensemble and its mirror image is comparable to the atomic relaxation time scale. We developed a unified model describing the intensity correlation function of light scattered from atoms in front of a mirror for strong and weak coupling regimes. In a strong coupling regime, the dynamics exhibit rich interplay between the collective effects within the single ensemble and the delayed interaction between multiple ensembles. We showed that when the dynamics are normalized to the collectively enhanced decay rate, it is the cooperativity that determines the interaction between multiple ensembles. In a weak coupling regime, we demonstrated the interference effects of scattering from multiple independent emitters, shown in the intensity correlation function. Intensity correlation measurement indicates that our physical system resides in a weak coupling regime, where time-delayed feedback is negligible. While the observed multi-emitter interference itself is interesting, our study suggests that long-range interaction in ONF-based systems would require the ordering of atoms commensurate to the transition wavelength.

The final chapter presents a new method of creating a tunable-spacing atomic array coupled to an ONF. While existing methods, such as guided optical lattice [81, 82, 183] or tweezer array

interfaced to an ONF [28, 184], offer distinct advantages, our setup accesses a new parameter regime that enables both one-dimensional tunability and scalability. Our setup generates a high-quality optical lattice–with trap sites ~ 1000, contrast > 0.98, power efficiency to trap beams $\sim 80\%$, and uniformity of $\sim 0.2\%$ chirp over the entire 2 mm range–, suitable for quantum optics and computation research [154]. A proof-of-principle demonstration of trapping ~ 100 atoms in the lattice and interfacing them to ONF is presented. This number can be further increased by optimizing the initial MOT and loading parameters. We envision this novel setup as a step toward integrating a neutral atom system into an optical fiber network with high cooperativity, which will be essential for distributed quantum computation, quantum networks, and studying the fundamental physics of collective quantum optics.

Appendix A: ONF Guided Mode Profile

Conventional optical fibers guide light through a total internal reflection at the core-cladding boundary. Both the core and the cladding are made from silica, but the refractive index of the core is slightly increased by doping with materials such as Germanium and Aluminum, and the refractive index of the cladding can be decreased by doping with materials such as Fluorine. For a typical single-mode optical fiber, the diameters of the core and the clad are 5 μm and 125 μm, respectively. Such geometry makes a weakly guided mode profile, which can be approximated by the linear modes LP_{01}.

An ONF is pulled from the conventional optical fiber to the level where the diameter becomes subwavelength. Because the ONF is pulled so thin, the core of the original fiber vanishes, and the clad silica now serves as the core for the ONF. The surrounding vacuum serves as the cladding. Thus, ONF is different from conventional fibers in two senses: its subwavelength diameter and the high contrast in the refractive indices of the core (silica) and the clad (vacuum). Such properties make ONF host the fundamental mode HE_{11} that cannot be approximated as the linear mode LP_{01} as in conventional optical fibers. Furthermore, significant power of the light is guided outside the fiber. Therefore, the atoms residing near the ONF surface can be mode-overlapped with the guided mode and emit into the fiber.

In this appendix, we present the calculation of the fundamental HE_{11} mode of the step-

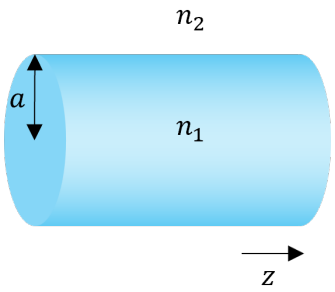

Figure A.1: A step-index fiber of radius a is aligned along z-axis, with a core refractive index n_1 and cladding refractive index n_2.

index fiber and the numerical calculation for an example ONF geometry.

A.1 Mode Profile of a Propagating EM Wave in a Step-Index Fiber

We consider a step-index fiber placed along the z-axis as shown in Fig. A.1. The refractive index is n_1 for $r < a$, and n_2 for $r > a$, where $n_1 > n_2$ is assumed so that the light can be guided by total internal reflection. The guided modes of a step-index fiber can be obtained by solving the Maxwell equations in cylindrical coordinates [155, 156, 188–191]. The Maxwell equation for electric and magnetic field vectors $\vec{E}$ and $\vec{H}$ in source-free space is

$$\vec{\nabla} \cdot \vec{E} = 0, \tag{A.1a}$$

$$\vec{\nabla} \cdot \vec{H} = 0, \tag{A.1b}$$

$$\vec{\nabla} \times \vec{E} = -\mu \frac{\partial \vec{H}}{\partial t}, \tag{A.1c}$$

$$\vec{\nabla} \times \vec{H} = \varepsilon \frac{\partial \vec{E}}{\partial t}, \tag{A.1d}$$

where μ and ε are the permeability and permittivity, respectively.

We consider an EM wave propagating along the waveguide:

$$\begin{bmatrix} \vec{E}(r,\phi,z,t) \\ \vec{H}(r,\phi,z,t) \end{bmatrix} = \begin{bmatrix} \vec{E}(r,\phi) \\ \vec{H}(r,\phi) \end{bmatrix} e^{i(\omega t - \beta z)}. \tag{A.2}$$

Here, ω is the angular frequency and β is the propagation constant of the propagating light.

Using the ansatz in Eq. (A.2), the Maxwell curl equations in Eqs. (A.1c) and (A.1d) can be written as

$$\frac{1}{r}\frac{\partial}{\partial\phi}E_z + i\beta E_\phi = -i\omega\mu H_r, \tag{A.3a}$$

$$-i\beta E_r - \frac{\partial}{\partial r}E_z = -i\omega\mu H_\phi, \tag{A.3b}$$

$$\frac{1}{r}\frac{\partial}{\partial r}(rE_\phi) - \frac{1}{r}\frac{\partial}{\partial\phi}E_r = -i\omega\mu H_z, \tag{A.3c}$$

$$\frac{1}{r}\frac{\partial}{\partial\phi}H_z + i\beta H_\phi = i\omega\varepsilon E_r, \tag{A.3d}$$

$$-i\beta H_r - \frac{\partial}{\partial r}H_z = i\omega\varepsilon E_\phi, \tag{A.3e}$$

$$\frac{1}{r}\frac{\partial}{\partial r}(rH_\phi) - \frac{1}{r}\frac{\partial}{\partial\phi}H_r = i\omega\varepsilon E_z. \tag{A.3f}$$

Rearranging Eqs. (A.3a), (A.3b), (A.3d), and (A.3e), we can express the transverse field profiles

(E_r, E_ϕ, H_r, and H_ϕ) in terms of E_z and H_z:

$$E_r = \frac{i\beta}{\beta^2 - \mu\varepsilon\omega^2}\left(\frac{\partial}{\partial r}E_z + \frac{\mu\omega}{\beta}\frac{\partial}{r\partial\phi}H_z\right), \tag{A.4a}$$

$$E_\phi = \frac{i\beta}{\beta^2 - \mu\varepsilon\omega^2}\left(\frac{\partial}{r\partial\phi}E_z - \frac{\mu\omega}{\beta}\frac{\partial}{\partial r}H_z\right), \tag{A.4b}$$

$$H_r = \frac{i\beta}{\beta^2 - \mu\varepsilon\omega^2}\left(\frac{\partial}{\partial r}H_z - \frac{\varepsilon\omega}{\beta}\frac{\partial}{r\partial\phi}E_z\right), \tag{A.4c}$$

$$H_\phi = \frac{i\beta}{\beta^2 - \mu\varepsilon\omega^2}\left(\frac{\partial}{r\partial\phi}H_z + \frac{\varepsilon\omega}{\beta}\frac{\partial}{\partial r}E_z\right). \tag{A.4d}$$

The longitudinal field components E_z and H_z can be obtained from the wave equation, which is derived from Eqs. (A.1) and (A.2):

$$\left(\nabla^2 + k^2\right)\begin{bmatrix}\vec{E}\\ \vec{H}\end{bmatrix} = 0, \tag{A.5}$$

where $k^2 = \mu\varepsilon\omega^2 = n^2\omega^2/c^2 = n^2k_0^2$ with n being the refractive index at the position of interest and k_0 being the angular wavenumber in free space. The z-component of the wave equation is

$$\left(\frac{\partial^2}{\partial r^2} + \frac{1}{r}\frac{\partial}{\partial r} + \frac{1}{r^2}\frac{\partial^2}{\partial\phi^2} + (k^2 - \beta^2)\right)\begin{bmatrix}E_z(r,\phi)\\ H_z(r,\phi)\end{bmatrix} = 0 \tag{A.6}$$

The differential equation is separable, and the solution takes the form

$$\begin{bmatrix}E_z(r,\phi)\\ H_z(r,\phi)\end{bmatrix} = \psi(r)e^{\pm il\phi}, \quad (l = 0, 1, 2, 3, \cdots) \tag{A.7}$$

where radial part satisfies

$$\frac{\partial^2\psi}{\partial r^2} + \frac{1}{r}\frac{\partial\psi}{\partial r} + (k^2 - \beta^2 - \frac{l^2}{r^2})\psi = 0. \tag{A.8}$$

The solutions are the Bessel functions of order l.

$$\psi(r) = \begin{cases} c_1 J_l(hr) + c_2 Y_l(hr), & \text{if } k^2 - \beta^2 > 0 \\ c_1 I_l(qr) + c_2 K_l(qr), & \text{if } k^2 - \beta^2 < 0 \end{cases} \tag{A.9}$$

where $h = \sqrt{k^2 - \beta^2}$, $q = \sqrt{\beta^2 - k^2}$, J_l and Y_l are Bessel functions of the first and second kind or order l, respectively, and I_l and K_l are the modified Bessel functions of the first and second kind of order l, respectively.

For lossless guiding of the field, the propagation constant β should be within the range

$$n_2\omega/c \leq \beta \leq n_1\omega/c \tag{A.10}$$

Thus, in Eq. (A.9), $r < a$ corresponds to the case $k^2 - \beta^2 > 0$ and $r > a$ to the case $k^2 - \beta^2 < 0$. Furthermore, $Y_l(hr)$ is singular at $r = 0$ and $I_l(qr)$ diverges as $r \to \infty$, and thus they are not

physical. The z-component of the electric and magnetic fields are thus

Core ($r < a$):

$$E_z = AJ_l(hr)e^{i(\omega t \pm l\phi - \beta z)}, \tag{A.11a}$$

$$H_z = BJ_l(hr)e^{i(\omega t \pm l\phi - \beta z)}, \tag{A.11b}$$

Clad ($r > a$):

$$E_z = CK_l(qr)e^{i(\omega t \pm l\phi - \beta z)}, \tag{A.11c}$$

$$H_z = DK_l(qr)e^{i(\omega t \pm l\phi - \beta z)}, \tag{A.11d}$$

where $h = \sqrt{n_1^2 k_0^2 - \beta^2}$, $q = \sqrt{\beta^2 - n_2^2 k_0^2}$ characterizes the field inside and outside the fiber, and the coefficients A, B, C, and D are determined by the boundary conditions.

Using Eqs. (A.4) and (A.11), we obtain all the components of the electric and magnetic

field vectors:

Core ($r < a$):

$$E_r = -\frac{i\beta}{h^2}\left(AhJ_l'(hr) \pm \frac{i\mu\omega l}{\beta r}BJ_l(hr)\right)e^{i(\omega t \pm l\phi - \beta z)}, \tag{A.12a}$$

$$E_\phi = -\frac{i\beta}{h^2}\left(\pm\frac{il}{r}AJ_l(hr) - \frac{\mu\omega}{\beta}BhJ_l'(hr)\right)e^{i(\omega t \pm l\phi - \beta z)}, \tag{A.12b}$$

$$E_z = AJ_l(hr)e^{i(\omega t \pm l\phi - \beta z)}, \tag{A.12c}$$

$$H_r = -\frac{i\beta}{h^2}\left(BhJ_l'(hr) \mp \frac{i\varepsilon_1\omega l}{\beta r}AJ_l(hr)\right)e^{i(\omega t \pm l\phi - \beta z)}, \tag{A.12d}$$

$$H_\phi = -\frac{i\beta}{h^2}\left(\pm\frac{il}{r}BJ_l(hr) + \frac{\varepsilon_1\omega}{\beta}AhJ_l'(hr)\right)e^{i(\omega t \pm l\phi - \beta z)}, \tag{A.12e}$$

$$H_z = BJ_l(hr)e^{i(\omega t \pm l\phi - \beta z)}, \tag{A.12f}$$

Clad ($r > a$):

$$E_r = \frac{i\beta}{q^2}\left(CqK_l'(qr) \pm \frac{i\mu\omega l}{\beta r}DK_l(qr)\right)e^{i(\omega t \pm l\phi - \beta z)}, \tag{A.12g}$$

$$E_\phi = \frac{i\beta}{q^2}\left(\pm\frac{il}{r}CK_l(qr) - \frac{\mu\omega}{\beta}DqK_l'(qr)\right)e^{i(\omega t \pm l\phi - \beta z)}, \tag{A.12h}$$

$$E_z = CK_l(qr)e^{i(\omega t \pm l\phi - \beta z)}, \tag{A.12i}$$

$$H_r = \frac{i\beta}{q^2}\left(DqK_l'(qr) \mp \frac{i\varepsilon_2\omega l}{\beta r}CK_l(qr)\right)e^{i(\omega t \pm l\phi - \beta z)}, \tag{A.12j}$$

$$H_\phi = \frac{i\beta}{q^2}\left(\pm\frac{il}{r}DK_l(qr) + \frac{\varepsilon_2\omega}{\beta}CqK_l'(qr)\right)e^{i(\omega t \pm l\phi - \beta z)}, \tag{A.12k}$$

$$H_z = DK_l(qr)e^{i(\omega t \pm l\phi - \beta z)}, \tag{A.12l}$$

where $\varepsilon_1 = \varepsilon_0 n_1^2$ and $\varepsilon_2 = \varepsilon_0 n_2^2$ are the permittivity at the core and the clad, respectively, and $J_l'(hr) = dJ_l(hr)/d(hr)$ and $K_l'(qr) = dK_l(qr)/d(qr)$.

The four coefficients A, B, C, and D can be determined from the boundary condition, that

is, E_ϕ, E_z, H_ϕ, and H_z should be continuous at $R = a$:

$$\pm \frac{il}{h^2 a} J_l(ha) A - \frac{\mu\omega}{h\beta} J_l'(ha) B \pm \frac{il}{q^2 a} K_l(qa) C - \frac{\mu\omega}{q\beta} K_l'(qa) D = 0, \tag{A.13a}$$

$$J_l(ha) A - K_l(qa) C = 0, \tag{A.13b}$$

$$\frac{\varepsilon_1\omega}{h\beta} J_l'(ha) A \pm \frac{il}{h^2 a} J_l(ha) B + \frac{\varepsilon_2\omega}{q\beta} K_l'(qa) C \pm \frac{il}{q^2 a} K_l(qa) D = 0, \tag{A.13c}$$

$$J_l(ha) B - K_l(qa) D = 0. \tag{A.13d}$$

We have nonzero solutions for A, B, C, and D, when the determinant of the above coupled equations is zero:

$$\left(\frac{J_l'(ha)}{haJ_l(ha)} + \frac{K_l'(qa)}{qaK_l(qa)}\right)\left(\frac{n_1^2 J_l'(ha)}{haJ_l(ha)} + \frac{n_2^2 K_l'(qa)}{qaK_l(qa)}\right) = l^2\left[\left(\frac{1}{ha}\right)^2 + \left(\frac{1}{qa}\right)^2\right]^2 \left(\frac{\beta}{k_0}\right)^2, \tag{A.14}$$

where $k_0 = \sqrt{\varepsilon_0\mu_0}\omega = \omega/c$ is the wave vector of the propagating EM wave in the vacuum. From the above transcendental equation, we can solve for the propagation constant β. Let us express Eq. (A.14) in the form of a quadratic equation of $J_l'(ha)/(haJ_l(ha))$:

$$n_1^2\left(\frac{J_l'(ha)}{haJ_l(ha)}\right)^2 + (n_1^2 + n_2^2)\left(\frac{K_l'(qa)}{qaK_l(qa)}\right)\left(\frac{J_l'(ha)}{haJ_l(ha)}\right) + n_2^2\left(\frac{K_l'(qa)}{qaK_l(qa)}\right)^2 - l^2\left[\left(\frac{1}{ha}\right)^2 + \left(\frac{1}{qa}\right)^2\right]^2\left(\frac{\beta}{k_0}\right)^2 = 0. \tag{A.15}$$

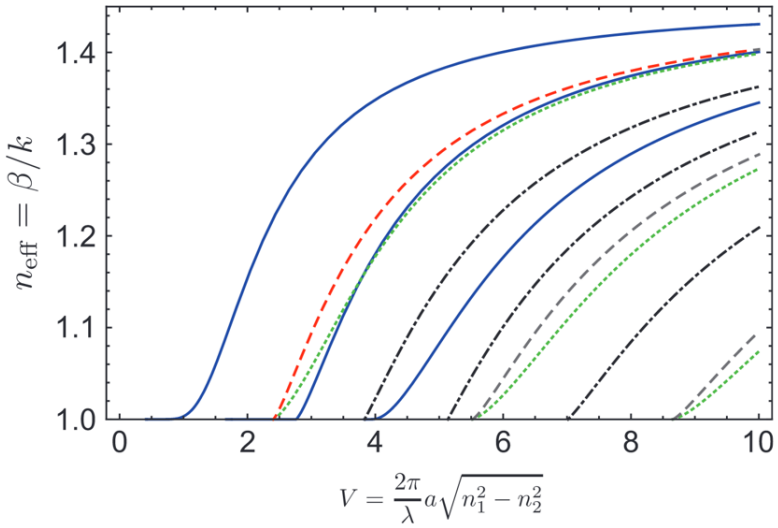

Figure A.2: Solutions $n_{\text{eff}} = \beta/0$ to Eq. (A.20) for various V-numbers. Each color represents the modes HE (solid blue), EH (dashed-dotted black, TE (dashed red), and TM (dotted green) modes. Figure adapted from [73].

The solution has the form

$$\frac{J_l'(ha)}{haJ_l(ha)} = -\frac{n_1^2 + n_2^2}{2n_1^2}\left(\frac{K_l'(qa)}{qaK_l(qa)}\right) \pm \left\{\left(\frac{n_1^2 - n_2^2}{2n_1^2}\frac{K_l'(qa)}{qaK_l(qa)}\right)^2 + \frac{l^2\beta^2}{n_1^2 k_0^2}\left[\left(\frac{1}{ha}\right)^2 + \left(\frac{1}{qa}\right)^2\right]^2\right\}^{1/2}, \tag{A.16}$$

where the $\pm$ solutions correspond to the EH and HE modes, respectively. In determining the propagation constant β, it is convenient to define a parameter called V-number:

$$V = k_0\sqrt{n_1^2 - n_2^2}\, a = \frac{2\pi}{\lambda}\sqrt{n_1^2 - n_2^2}\, a, \tag{A.17}$$

which scales the fiber geometry (radius a and NA$= \sqrt{n_1^2 - n_2^2}$) with respect to the wavelength of the guided light. Figure A.2 shows the solutions $n_{\text{eff}} = \beta/k_0$ to Eq. (A.20). Below $V = 2.405$, only the HE_{11} mode can propagate through the waveguide.

When β is found, the coefficients B, C, and D are expressed in terms of A:

$$\frac{B}{A} = \pm\frac{il\beta}{\mu\omega}\left[\left(\frac{1}{ha}\right)^2 + \left(\frac{1}{qa}\right)^2\right]\left[\frac{J_l'(ha)}{haJ_l(ha)} + \frac{K_l'(qa)}{qaK_l(qa)}\right]^{-1}, \tag{A.18a}$$

$$\frac{C}{A} = \frac{J_l(ha)}{K_l(qa)}, \tag{A.18b}$$

$$\frac{D}{A} = \pm\frac{il\beta}{\mu\omega}\frac{J_l(ha)}{K_l(qa)}\left[\left(\frac{1}{ha}\right)^2 + \left(\frac{1}{qa}\right)^2\right]\left[\frac{J_l'(ha)}{haJ_l(ha)} + \frac{K_l'(qa)}{qaK_l(qa)}\right]^{-1}. \tag{A.18c}$$

The coefficient A is determined by the normalization condition [77]:

$$\int_0^{2\pi} \mathrm{d}\phi \int_0^{\infty} n(r)\left|\vec{E}(r,\phi)\right|^2 r\mathrm{d}r = 1. \tag{A.19}$$

A.2 Mode Profile of a Subwavelength Waveguide with Vacuum-clad

Now we consider a subwavelength-diameter waveguide that hosts only a single mode HE_{11}. The transcendental equation in Eq. (A.20) is now [189]

$$\begin{aligned}\frac{J_0(ha)}{haJ_1(ha)} = &-\frac{n_1^2+n_2^2}{2n_1^2}\left(\frac{K_1'(qa)}{qaK_1(qa)}\right) + \frac{1}{h^2a^2} \\ &\pm\left\{\left(\frac{n_1^2-n_2^2}{2n_1^2}\frac{K_1'(qa)}{qaK_1(qa)}\right)^2 + \frac{\beta^2}{n_1^2k_0^2}\left[\left(\frac{1}{ha}\right)^2 + \left(\frac{1}{qa}\right)^2\right]^2\right\}^{1/2},\end{aligned} \tag{A.20}$$

where we employed the property $J_l'(x) = J_{l-1}(x) - J_l(x)/x$.

The numerical simulation of the guided mode profile for circularly polarized HE_{11} modes ($l = \pm 1$ in Eq.(A.12)) and for quasi-linearly polarized modes (obtained by summing the circular polarization components) using the experimental parameters is shown in Fig.A.3. Note that, due to the strong guiding in a subwavelength vacuum-clad fiber, the longitudinal field compo-

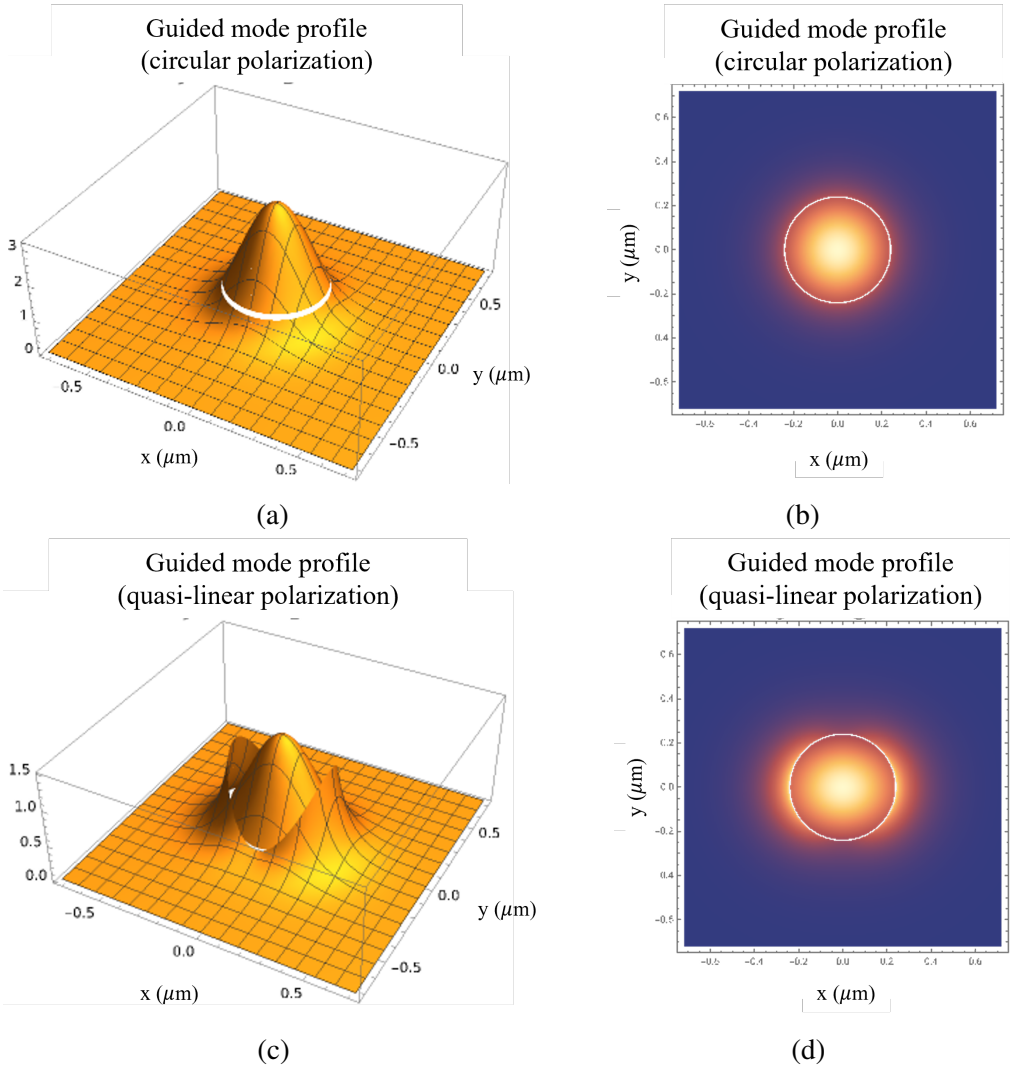

Figure A.3: Guided mode profile of (a-b) circular and (c-d) quasi-linear polarization. The fiber radius is 240 nm, wavelength of the propagating light is 780 nm, effective refractive index n_{eff}=1.1622.

nent E_z is non-negligible and the mode cannot be approximated by the linearly polarized LP_{01} mode [189].

Appendix B: Collective Modes of Dilute Atomic Systems in Waveguide QED

We formulate the collective decay modes of atoms coupled to a waveguide where the atom-atom interaction is only mediated via the guided mode (dilute atomic ensemble regime) [33, 56, 110, 130]. In this formulation, we remain in the Markovian regime. Thus, the interaction between atoms takes over distances comparable to or larger than the transition wavelength, yet it happens instantaneously before the atoms decay away. Specifically, we discuss the collective modes of randomly distributed atoms and an ordered array of atoms.

Consider a system of N two-level atoms positioned along a waveguide at $z = z_1, z_2, \cdots, z_N$ and coupled to the guided mode. The free Hamiltonian for the emitter and the guided field modes is

$$H_0 = \sum_{j=1}^{N} \hbar\omega_0 \hat{\sigma}_j^+ \hat{\sigma}_j^- + \sum_k \hbar\omega_k \hat{a}_k^\dagger \hat{a}_k, \tag{B.1}$$

where $\hbar$ is the reduced Planck constant, ω_0 is the atomic transition frequency, and ω_k is the frequency of the k-th field mode. The operators $\hat{\sigma}_j^+$ and $\hat{\sigma}_j^-$ are the raising and lowering operators for the j-th atom, and $\hat{a}_k^\dagger$ and $\hat{a}_k$ are the creation and annihilation operators for the k-th field mode. Note that we ignored the polarization modes of the field here.

The emitters and the field modes are coupled by dipole interaction. The atom-field interac-

tion Hamiltonian is [2]

$$H_{\mathrm{AF}} = \sum_{j=1}^{N} \sum_{k} \hbar g_{j,k} \left(\hat{\sigma}_j^{+} \hat{a}_k e^{ikz_j} + \hat{a}_k^{\dagger} \hat{\sigma}_j^{-} e^{-ikz_j} \right), \tag{B.2}$$

under rotating wave approximation, which leaves the terms that preserve the number of excitations in the atom + field system. The interaction strength between the j-th atom and the k-th mode $g_{j,k}$ is defined as

$$g_{j,k} = -\frac{d_j \cdot \mathcal{E}_k}{\hbar}, \tag{B.3}$$

where d_j is the transition dipole matrix of j-th atom and $\mathcal{E}_k$ is the field amplitude of k-th field mode. As we are interested in the interaction between the atoms and the field modes, we move to the interaction picture with respect to the free Hamiltonian H_0. The interaction Hamiltonian in the interaction picture is

$$\tilde{H}_{\mathrm{AF}} = \sum_{j=1}^{N} \sum_{k} \hbar g_{j,k} \left(\hat{\sigma}_j^{+} \hat{a}_k e^{ikz_j} e^{-i(\omega_k - \omega_0)t} + \hat{a}_k^{\dagger} \hat{\sigma}_j^{-} e^{-ikz_j} e^{i(\omega_k - \omega_0)t} \right). \tag{B.4}$$

For consistency, we will use tilde signs for the operators and states in the interaction picture with respect to the free Hamiltonian H_0 in this dissertation.

We consider the time evolution of single excitation in the atom + field system. Note that the total Hamiltonian $H_0 + H_{\mathrm{AF}}$ preserves the number of excitations. Thus, we can write single

excitation ansatz for our time-evolved state:

$$\left|\tilde{\psi}(t)\right\rangle = \left[\sum_{j=1}^{N} \tilde{c}_j(t)\hat{\sigma}^{+} + \sum_{k} \tilde{c}_k(t)\hat{a}^{\dagger}\right] |G, \{0\}_k\rangle \,, \tag{B.5}$$

where $|G\rangle = |g, g, \cdots, g\rangle$ denotes the state where all the atoms are in the ground state, and $|\{0\}_k\rangle$ represents the vacuum state. $\tilde{c}_j(t)$ is the j-th atom excitation amplitude at time t, and $\tilde{c}_k(t)$ is the k-th field mode's excitation amplitude, both in the interaction picture.

The Schrödinger equation leads to the coupled differential equation for the atomic and field amplitudes:

$$\partial_t \tilde{c}_j(t) = -i \sum_{k} g_{j,k} e^{ikz_j} e^{-i(\omega_k - \omega_0)t} \tilde{c}_k(t), \tag{B.6a}$$

$$\partial_t \tilde{c}_k(t) = -i \sum_{j=1}^{N} g_{j,k} e^{-ikz_j} e^{i(\omega_k - \omega_0)t} \tilde{c}_j(t). \tag{B.6b}$$

The Eq. (B.6a) represents the case where the j-th atom absorbs a photon, and Eq. (B.6b) the case where the atoms (coherently) emit a photon in a k-th mode. Formally integrating (B.6b) and putting back into the (B.6a), we get the atomic differential equation:

$$\partial_t \tilde{c}_j(t) = -\sum_{l=1}^{N} \int_0^t \mathrm{d}t' \tilde{c}_l(t') e^{i\omega_0(t-t')} \sum_{k} g_{j,k} g_{l,k} e^{ik(z_j - z_l)} e^{i\omega_k(t'-t)}. \tag{B.7}$$

We assume a flat spectral density of the guided mode and parallel atomic dipoles, which leads to homogeneous atom-light interaction strength; $g_{j,k} = g_0$. Evaluating the integrations, we get the

equation of motion for the atomic dipoles:

$$\partial_t \tilde{c}_j(t) = -\frac{\Gamma}{2}\tilde{c}_j(t)\Theta(t) - \frac{\beta\Gamma}{2}\sum_{l\neq j}\tilde{c}_l\left(t - \left|\frac{z_j - z_l}{v_p}\right|\right)e^{i\omega_0\left|\frac{z_j-z_l}{v_p}\right|}\Theta\left(t - \left|\frac{z_j - z_l}{v_p}\right|\right), \tag{B.8}$$

where Γ is the total decay rate, $\beta = \Gamma_{1D}/\Gamma$ is the coupling efficiency of atom to the guided mode (where Γ_{1D} is the decay rate to the guided mode), and v_p is the phase velocity of the field in the waveguide. Although we did not explicitly consider the coupling of atoms to the mode outside the waveguide, we phenomenologically added the contribution of free space modes in obtaining Eq. (B.8) by adding free space coupling $(1-\beta)\Gamma/2$. In doing so, we assumed that the distinct atoms are far enough that they only interact via the guided mode.

We now use the assumption that the atoms are in the Markovian regime, i.e., the size of the atomic cloud is smaller than the atomic relaxation length scale ($|z_j - z_l| \ll v_p/\Gamma$). The interaction between atoms takes place instantaneously as it happens at a time scale ($|z_j - z_l|/v_p$) much smaller than the atomic relaxation time scale ($1/\Gamma$). In this limit, the atomic amplitudes on the right-hand side can be evaluated for the identical time points, i.e., $\tilde{c}_j\left(t - |z_j - z_l|/v_p\right) \simeq \tilde{c}_j\left(t\right)$. Note that the atomic amplitude is evaluated in the interaction picture and there is no fast-oscillating phase. The total system evolution can be written as

$$\partial_t \vec{c}(t) = -M\vec{c}(t) \tag{B.9}$$

where

$$\vec{c}(t) = \begin{pmatrix} \tilde{c}_1(t) \\ \tilde{c}_2(t) \\ \cdots \\ \tilde{c}_N(t) \end{pmatrix} \tag{B.10}$$

is the atomic amplitude vector and

$$M = \frac{\Gamma}{2} \begin{pmatrix} 1 & \beta\, e^{i\omega_0 \left|\frac{z_1 - z_2}{v_p}\right|} & \cdots & \beta\, e^{i\omega_0 \left|\frac{z_1 - z_N}{v_p}\right|} \\ \beta\, e^{i\omega_0 \left|\frac{z_1 - z_2}{v_p}\right|} & 1 & \cdots & \beta\, e^{i\omega_0 \left|\frac{z_2 - z_N}{v_p}\right|} \\ \vdots & \vdots & \ddots & \vdots \\ \beta\, e^{i\omega_0 \left|\frac{z_1 - z_N}{v_p}\right|} & \beta\, e^{i\omega_0 \left|\frac{z_2 - z_N}{v_p}\right|} & \cdots & 1 \end{pmatrix} \tag{B.11}$$

is the generalized decay rate matrix. The diagonal terms in M represent the atomic decay of its own, and the off-diagonal terms represent the interaction between atoms via guided mode. Due to this coupling between atoms, the atomic system decays rather collectively. The eigenstates of M are the collective modes, and the corresponding eigenvalues are the decay rates of the collective modes. Note that the eigenvalues can be complex numbers whose real values represent the decay rate of the mode and the imaginary values represent the energy of the mode.

For example, consider a special case where the atoms are symmetrically excited in the beginning

$$\tilde{c}_1(0) = \tilde{c}_2(0) = \cdots = \tilde{c}_N(0) = \frac{1}{\sqrt{N}}, \tag{B.12}$$

and the propagation phases between the atoms are zero

$$\omega_0 \frac{z_j - z_l}{v_p} = 2n\pi, \quad (n \in \mathbb{Z})\,. \tag{B.13}$$

We see that the symmetry in the atomic state is maintained during time evolution; $\tilde{c}_1(t) = \tilde{c}_2(t) = \cdots = \tilde{c}_N(t)$. Thus, we have

$$\partial_t \tilde{c}_1(t) = -\left(\frac{(1-\beta)\Gamma}{2} + N\frac{\beta\Gamma}{2}\right)\tilde{c}_1(t). \tag{B.14}$$

Thus, the decay into the guided mode is collectively enhanced (superradiance), proportional to the number of atoms. The antisymmetry, either in the initial state or the propagation phases, would introduce decay modes with suppressed rates.

B.1 Randomly Positioned Atoms

For the case when the emitters are randomly positioned, the collective modes are distributed within a range whose real values are bound by the theoretical lower limit ($(1-\beta)\Gamma$) and upper limit ($(1-\beta+N\beta)\Gamma$). The single-shot simulation of randomly distributed $N = 2$ and $N = 30$ atoms with coupling efficiency $\beta = 0.1$ is shown in Fig. B.1 (a) and (b). When there are only two atoms, there are equal amounts of collective decay modes with enhanced and suppressed decay rates. However, as the number of emitters increases, most collective modes exhibit suppressed decay rates, while only a few may have enhanced decay rates. This is because the enhancement of the decay rate requires the atoms to be aligned with respect to the transition wavelength, which becomes increasingly difficult as the number of atoms increases. The theoretical maximum decay

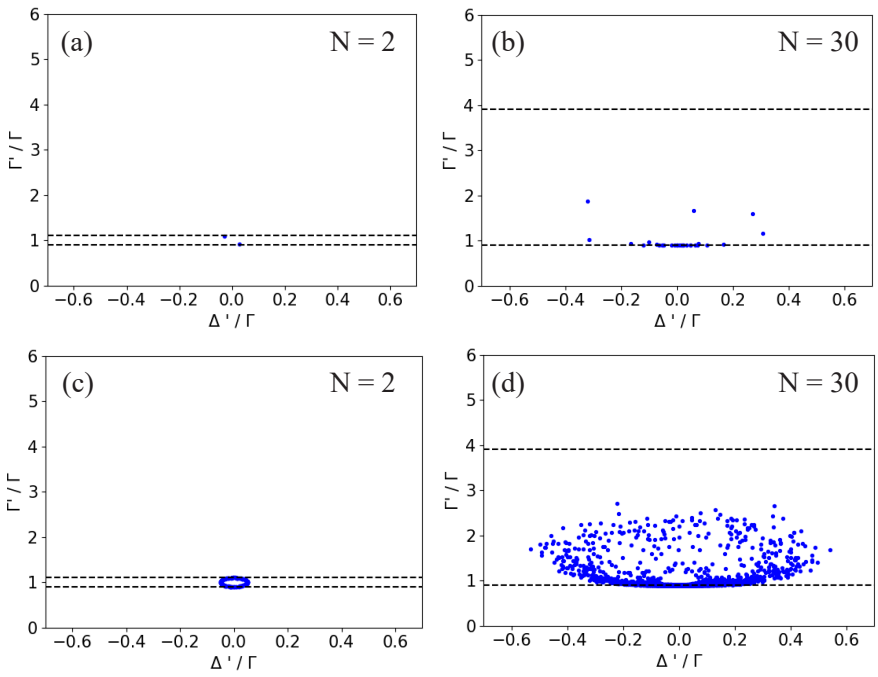

Figure B.1: Simulation of collective modes of randomly distributed atoms with coupling efficiency $\beta = 0.1$. Single-shot simulations for (a) N=2 and (b) N=30 atoms and 100 shots for (c) N=2 and (d) N=30 atoms are demonstrated. The theoretical lower and upper limits of the collective decay rates are drawn as dashed horizontal lines.

rate is $(1 - \beta + N\beta)\Gamma$, which corresponds to the case when the atoms are precisely aligned in integer multiples of the transition wavelength. The theoretical lower limit of the collective decay rate is $(1 - \beta)\Gamma$ and corresponds to the case when the emission of atoms into the guided mode is fully destructive. The simulation for 100 random distributions for each case is shown in Fig. B.1 (c) and (d). The collective modes are well bound by the theoretical limits. The range of detuning of the collective modes gets broader as the number of atoms increases.

B.2 Ordered Arrays of Atoms

Now we consider a special case where the atoms form a periodic array with lattice constant d [33, 56, 130]. We can see from the form of the collective evolution matrix M in Eq. (B.11) that

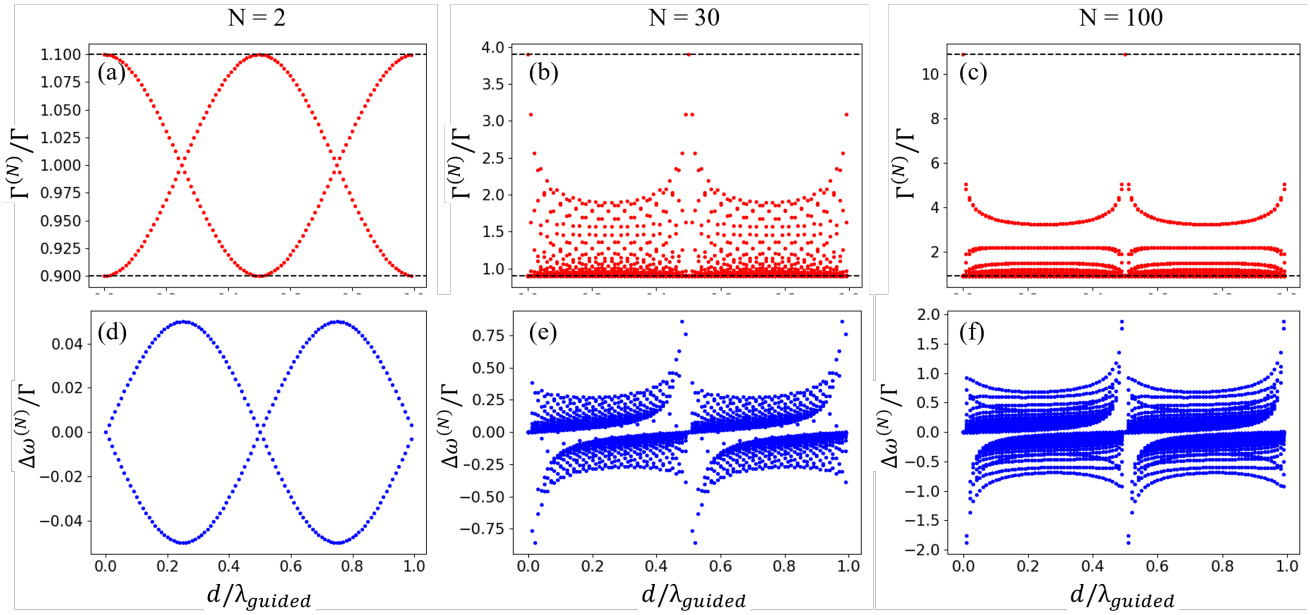

Figure B.2: Simulation of collective modes of periodically positioned atoms as a function of lattice constants d. (a-c) shows the collective decay rates and (d-f) shows the energy shifts of the collective modes. (a,d) for N=2, (b,e) for N=30, and (c,f) for N=100.

the exact lattice constant does not matter, but the lattice constant modulo the transition wavelength matters.

The collective mode's decay rate and energy shifts as a function of lattice constants between 0 to λ are shown in Fig. B.2, for number of atoms N=2, 30, and 100. The atom-atom interaction can be tuned from dissipative to dispersive interactions by tuning the lattice constant. When the lattice constant is an integer multiple of $\lambda/2$, the atom-atom interaction becomes purely dissipative. As a result, the pure superradiant and subradiant collective modes with zero energy shift open. For the lattice constants other than multiples of $\lambda/2$, the atoms interact with each other both dissipatively and dispersively, leading to collective modes with modified decay rates and energy shifts. For $N = 2$, the interaction can be purely dispersive when the separation between the atoms is $\lambda_{\text{guided}}/4$. In this case, there are no shifts in the decay rates; however, the two collective modes now have a maximum energy difference.

Appendix C: Relevant Publications

In this appendix, the publications produced during this dissertation work are presented. These include the observation of vacuum-induced collective quantum beats [136], a theoretical investigation of collective quantum beats in distant emitters [153], and the proposal and demonstration of an optical setup for making a tunable-spacing optical lattice coupled to an ONF [154].

Observation of Vacuum-Induced Collective Quantum Beats

Hyok Sang Han,[1] Ahreum Lee,[1] Kanupriya Sinha,[2,5,*] Fredrik K. Fatemi,[3,4] and S. L. Rolston[1,4,†]
[1]Joint Quantum Institute, University of Maryland and the National Institute of Standards and Technology, College Park, Maryland 20742, USA
[2]Department of Electrical and Computer Engineering, Princeton University, Princeton, New Jersey 08544, USA
[3]U.S. Army Research Laboratory, Adelphi, Maryland 20783, USA
[4]Quantum Technology Center, University of Maryland, College Park, Maryland 20742, USA
[5]School of Electrical, Computer and Energy Engineering, Arizona State University, Tempe, Arizona 85287, USA

(Received 1 March 2021; accepted 2 July 2021; published 13 August 2021)

We demonstrate collectively enhanced vacuum-induced quantum beat dynamics from a three-level V-type atomic system. Exciting a dilute atomic gas of magneto-optically trapped ^{85}Rb atoms with a weak drive resonant on one of the transitions, we observe the forward-scattered field after a sudden shut-off of the laser. The subsequent radiative dynamics, measured for various optical depths of the atomic cloud, exhibits superradiant decay rates, as well as collectively enhanced quantum beats. Our work is also the first experimental illustration of quantum beats arising from atoms initially prepared in a single excited level as a result of the vacuum-induced coupling between excited levels.

DOI: 10.1103/PhysRevLett.127.073604

Introduction.—Quantum beats are a well-studied phenomenon that refers to the interference between spontaneously emitted radiation from two or more excited levels, resulting in a periodic modulation of the radiated field intensity [1]. This has been a valuable spectroscopic tool to measure the energy difference between excited levels across many experimental platforms such as atoms [2,3], molecules [4], semiconductors [5], and quantum dots [6,7].

Although quantum beats have been extensively studied, here we demonstrate two new aspects: (i) quantum beats without an initial superposition of excited levels, and (ii) enhanced beat amplitudes due to collective emission of light [8,9]. In a typical quantum beat experiment, an excitation pulse with sufficient bandwidth to span the energy spacing between multiple excited atomic levels is used to create an initial coherent superposition. The beat signal amplitude is proportional to the coherence between the excited levels; and in the absence of an initial superposition, one might expect no quantum beats. This notion was challenged in [10,11], predicting that the vacuum electromagnetic field can create the required coherence between the excited atomic levels. However, experimental observation of such vacuum-induced quantum beats is challenging due to the competing requirements on the level structure: The excited level's separation needs to be large compared to the natural linewidth to enable the initialization of only one of the levels that, in turn, reduces the strength of the vacuum-induced coupling.

We experimentally address this using the well-separated ^{85}Rb $^5P_{3/2}$ $F' = 3$ and 4 hyperfine levels as our excited levels and using a long enough (200 ns) excitation pulse such that any coherence due to the turn-on edge decays away, leaving the atomic population in a single excited level. Detecting the forward-scattered mode [see Fig. 1(a)] allows us to observe the radiation from a timed-Dicke state [12–14]. We theoretically illustrate that for such a collective state, the quantum beat dynamics can be cooperatively

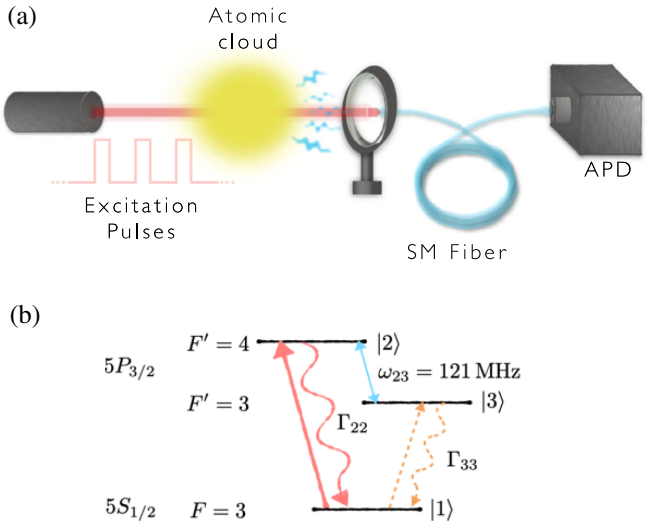

FIG. 1. (a) Experimental setup. Linearly polarized excitation beam containing train of pulses illuminates cold ^{85}Rb atomic cloud produced by MOT. Photons scattered by cloud in forward direction coupled into single-mode fiber, counted by avalanche photodiode, and histogrammed to obtain atomic radiative decay profile. (b) Relevant energy levels of ^{85}Rb atom. Excitation beam (780 nm) resonantly drives $|1\rangle \leftrightarrow |2\rangle$ transition. Γ_{22} and Γ_{33} are decay rates of excited levels $|2\rangle$ and $|3\rangle$, respectively, to ground level $|1\rangle$.

enhanced by the constructive interference between the transition processes in different atoms. The collective amplification of the forward-scattered beat signal allows us to observe vacuum-induced quantum beats and serves as an experimental proof of collective effects in quantum beats. Such collective enhancement may also be used to amplify small signals that are otherwise unobservable.

Model.—Let us consider a system of three-level V-type ^{85}Rb atoms, with the ground level $|1\rangle = |5S_{1/2}, F = 3\rangle$ and the two excited levels $|2\rangle = |5P_{3/2}, F' = 4\rangle$ and $|3\rangle = |5P_{3/2}, F' = 3\rangle$ [see Fig. 1(b)]. The frequency difference between the excited levels is $\omega_{23} = 2\pi \cdot 121$ MHz, and the optical transition wavelength between the ground and the excited levels is $\lambda = 780$ nm. We observe the forward scattering, where the phase factor of the field from propagation within the atomic cloud is exactly compensated for by the phases of the atomic dipoles initially induced by the drive [12]. The damping rate of atomic levels originating from second-order coupling between $|j\rangle$ and $|l\rangle$ is

$$\Gamma_{jl} = \frac{\vec{d}_{j1} \cdot \vec{d}_{l1} \omega_{j1}^3}{3\pi\varepsilon_0 \hbar c^3},$$

where $\vec{d}_{j1}$ and ω_{j1} are the transition dipole moments and the transition frequency between $|j\rangle$ and $|1\rangle$, respectively. Note that Γ_{23} represents the cross-damping rate between the excited states [11], whereas Γ_{22} and Γ_{33} describe the normal decay of the excited states. Assuming that all the transition dipole moments are real and parallel to each other, $\Gamma_{23} \approx \sqrt{\Gamma_{22}\Gamma_{33}}$. In our system, $\Gamma_{22} = 2\pi \cdot 6.1$ MHz is the single-atom decay rate of the $5P_{3/2}$ level and $\Gamma_{33} = (5/9)\Gamma_{22}$ because $|3\rangle$ decays to $|1\rangle$ only fractionally with the branching ratio of 5/9 [15].

The atoms are initialized in a symmetric state with a shared single excitation in $|2\rangle$. After a sudden turn-off of the drive field, the atomic ensemble starts to decay due to its interaction with the vacuum field modes, which couple the excited levels to reveal quantum beating. We analytically solve the atomic and field dynamics using the Wigner-Weisskopf theory in the experimental regime where the excited atomic levels are well separated from each other ($\Gamma_{jl}^{(N)} \ll \omega_{23}$) [16] to find the intensity of light emitted from the ensemble as (see Supplemental Material [17])

$$\frac{I(t)}{I_0} = e^{-\Gamma_{22}^{(N)} t} + I_b e^{-\Gamma_{\mathrm{avg}}^{(N)} t} \sin(\omega_{23} t + \phi), \tag{1}$$

where we have defined the total collective decay rate as $\Gamma_{jl}^{(N)} \equiv (1 + Nf)\Gamma_{jl}$, with f corresponding to the angular emission factor into the forward-scattered modes and N corresponding to the effective number of atoms emitting collectively [18]. We have assumed here that the atoms emit collectively in the forward direction as a result of the phase coherence due to the timed-Dicke state, whereas the emission in the remainder of the modes is independent. $\Gamma_{\mathrm{avg}}^{(N)} \equiv (\Gamma_{22}^{(N)} + \Gamma_{33}^{(N)})/2$ is the average decay rate of excited levels, the beat contrast is defined as

$$I_b = \frac{(\Gamma_{23}^{(N)})^2}{\omega_{23}\Gamma_{22}^{(N)}} \approx \frac{5}{9}\frac{\Gamma_{22}^{(N)}}{\omega_{23}}, \tag{2}$$

and the beat phase is defined as

$$\phi = \arctan\left(\frac{\Gamma_{22}^{(N)}}{\omega_{23}}\right). \tag{3}$$

The first term of Eq. (1) represents the collective decay from $|2\rangle$, with a cooperatively enhanced amplitude and decay rate relative to a single atom. The second term accounts for the small but non-negligible beat that decays away with an enhanced average rate of $\Gamma_{\mathrm{avg}}^{(N)}$. This result shows that vacuum-induced quantum beats in the absence of an initial superposition of excited atomic levels can exhibit collective effects, generalizing the single-atom quantum trajectory prediction in [11]. From Eq. (2), we observe that the collective nature of the quantum beat originates from the virtual coupling between the excited levels as indicated by the cross-damping term Γ_{23}.

Experiment.—Figure 1(a) shows the schematic of the experiment. A cold atomic cloud of $\sim 10^8$ ^{85}Rb atoms is produced by a magneto-optical trap (MOT) with Gaussian-shaped atomic density distribution having a $1/e$ diameter of ~ 2 mm. The ensemble satisfies the dilute regime, $\rho\lambda^3 \ll 1$, where ρ is the spatial atomic density, meaning that the separation between atoms is much larger than the photon wavelength. An excitation beam with a $1/e^2$ diameter of 1.6 mm is overlapped with the cloud whose transmitted light is collected by a single-mode (SM) fiber 0.6 m away in the forward direction.

For the observation of the spontaneous emission, the MOT lasers are turned off for 200 μs, during which atoms initialized in $|1\rangle$ are illuminated by a train of excitation pulses that resonantly drive the $|1\rangle \leftrightarrow |2\rangle$ transition. The peak intensity of the excitation beam is $\sim 6 \times 10^8$ times smaller than the saturation intensity of $I_s = 3.9$ mW/cm^2 of the transition [15], delivering less than one photon per pulse on average, and ensuring that the system is well within the single-excitation regime. Each excitation pulse is turned on (off) for 200 ns (800 ns) with > 30 dB extinction and a 3.5 ns fall time controlled by two fibered Mach-Zehnder intensity modulators (EOSPACE AZ-0K5-10-PFA-PFA-780) in series.

After the driving field is switched off, spontaneously emitted photons coupled to the SM fiber are counted by an avalanche photodiode and histogrammed by time tagging them with 0.5 ns resolution. By detecting only those

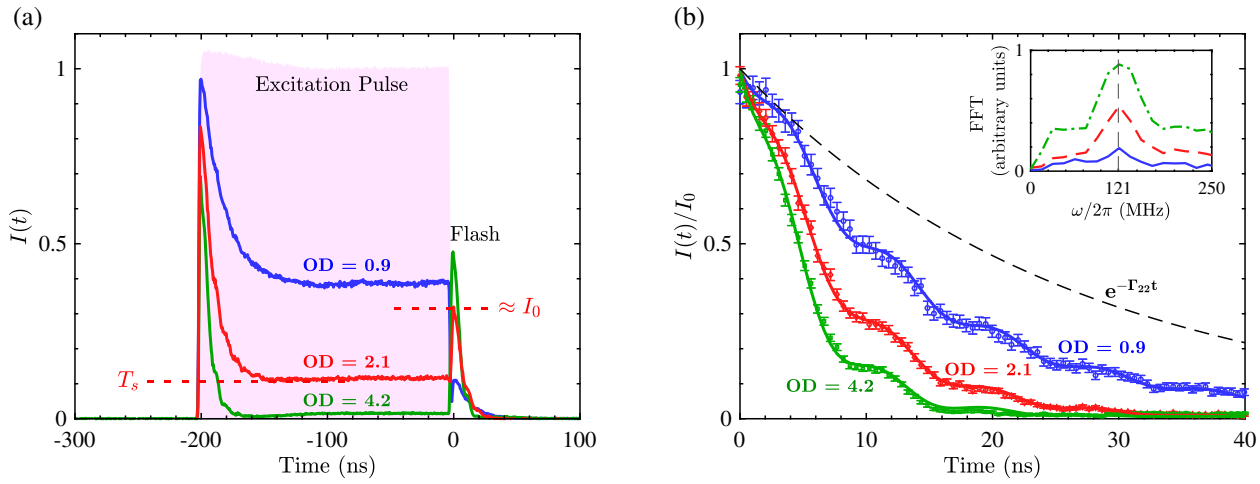

FIG. 2. (a) Examples of the histogrammed photon counts for various optical depths, representing forward-mode intensity, and normalized to that of excitation pulse. As excitation pulse is abruptly (within ≈3.5 ns) turned off, flash of photon emission occurs with peak intensity close to I_0. (b) Zoomed-in view of decay profiles after flash peak for analysis. Intensity of each curve further normalized to exponential decay amplitude I_0 [≈ flash peak size shown in Fig. 2(a)]. Error bars represent shot-noise limit of photon counts. Overlaid solid lines fit data using Eq. (1), whose results are displayed in Fig. 3 for entire OD range of experiment. Black dashed line represents single-atom decay curve $I(t) = e^{-\Gamma_{22}t}$ ($\Gamma_{22} = 2\pi \cdot 6.1$ MHz) without considering collective effects. In inset, absolute values of fast-Fourier transforms of beat signals for OD = 0.9 (solid blue), 2.1 (dashed red), and 4.2 (dash-dotted green line) show peaks at splitting between two excited levels (see Supplemental Material for detail [17]).

photons coupled to the SM fiber, we effectively filter out incoherent fluorescence, owing to the small collection solid angle ($\approx 6 \times 10^{-6}$ sr). The atomic velocity of $v \approx 120$ nm/μs corresponding to the Doppler temperature of $T_D \approx 150$ μK gives negligible motion compared to the optical wavelength (780 nm) within the timescale of the emission process ($1/\Gamma_{22}^{(N)} \leq 26$ ns). After the repetition of 200 pulses within 200 μs, the MOT lasers are turned back on to recover and maintain the atomic cloud for 1.8 ms before a new measurement cycle begins, repeating the whole sequence every 2 ms. For typical histogrammed data, we run the sequence continuously for 30 min, comprising 2×10^8 excitation pulses.

Examples of histogrammed photon counts are shown in Fig. 2(a), where $I(t)$ represents the intensity of the forward-scattered light normalized to the incident intensity. The atomic samples are almost transparent at the sharp switch-on edge of the excitation pulse due to its broad spectral components, but the transmission soon decays to a steady-state value T_s, which we use to calculate the optical depth (OD $= -\ln T_s$). We vary the OD of the MOT cloud between 0 and 5 by adjusting the injection current running through the rubidium dispensers (SAES Getters RB/NF/7/25) between 3.5 and 6.5 A to increase atomic background pressure. The steady-state transmission T_s results from the destructive interference between the driving field and the field coherently radiated (with π-phase shift) in the forward direction by the atomic dipoles. When the driving field is switched off, only the atomic radiation field remains in the forward direction, resulting in a sudden intensity jump ("flash"), which has been intensively investigated in previous studies [19–21]. The flash peak intensity, which is proportional to the OD before it saturates at OD ≈ 4, represents the intensity I_0 of the overall decay as in Eq. (1).

The decay profiles after the flash peak are magnified in Fig. 2(b) for detailed analysis. Each curve is normalized to the exponential decay amplitude I_0 [see Eq. (1)], and so the enhanced decay rates and the beat contrast for different ODs can be easily compared. For comparison, the single-atom decay curve of $I(t) = e^{-\Gamma_{22}t}$ with no collective enhancement is also shown (black dashed line). We first note that a higher OD results in an enhanced decay rate, demonstrating the collective nature of the emission process. The quantum beat signal is apparent as a sinusoidal modulation of the exponential decay. To verify the frequency of the observed beat signal, we first remove the exponential decay profile from the data and then fast-Fourier transform (FFT) the residual. The FFT results (see inset) confirm that the observed beat frequency is ω_{23}, as expected. This illustrates the occurrence of quantum beats in the absence of an initial superposition between the excited levels.

The solid curves overlaid with the experimental data in Fig. 2(b) represent the fitting of Eq. (1) with I_b, $\Gamma_{22}^{(N)}$, and ϕ as fitting parameters, showing excellent agreement between the analytical prediction and the observed emission dynamics. To preclude the possibility of exciting additional population in levels $|2\rangle$ and $|3\rangle$ due to the off-resonant Fourier components of the drive intensity, we numerically simulate the atomic dynamics via the optical Bloch equations (OBEs) by considering a realistic model for the laser dynamics with a 3.5 ns turn-on edge, a 200 ns drive, and a 3.5 ns turn-off edge (see Supplemental Material [17]). The emitted intensity curves calculated from the

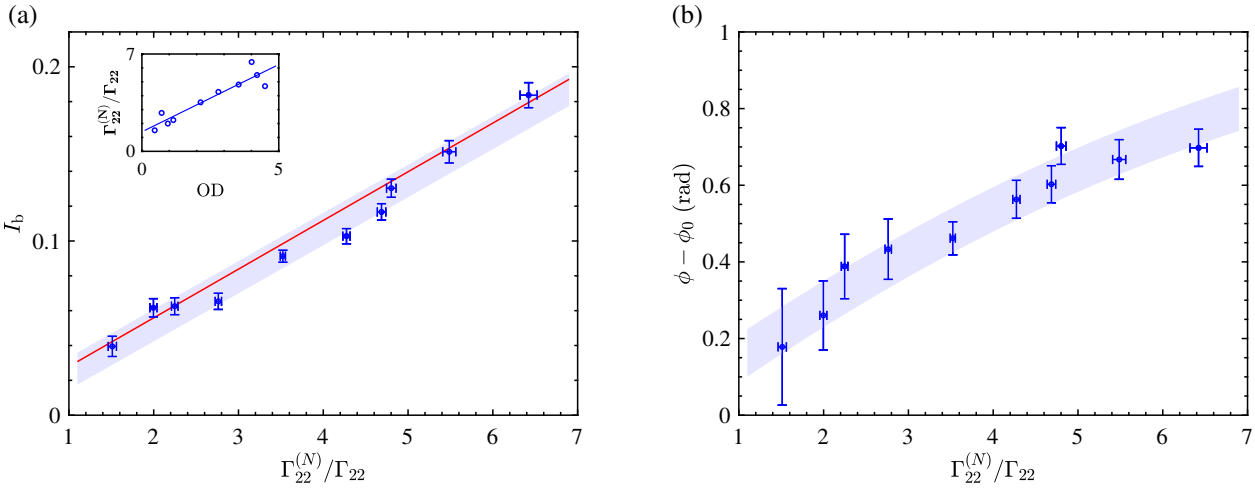

FIG. 3. (a) Beat contrast I_b plotted as function of $\Gamma_{22}^{(N)}/\Gamma_{22}$ for various ODs. Plotted error bars represent one-sigma confidence interval of fitting to modulated decay curves. Shaded region displays one-sigma confidence band of linear fit to data. Red solid line is theory curve plotting Eq. (2). Inset shows linear dependence of $\Gamma_{22}^{(N)}/\Gamma_{22}$ on OD. (b) Beat phase ϕ subtracted by common offset ϕ_0 presented. Shaded region represents one-sigma confidence band of fitting of Eq. (4) to data.

OBE dynamics are indistinguishable from the solid curves that represent the analytical Wigner-Weisskopf approach excluding the drive dynamics [Eq. (1)]. We therefore conclude that the off-resonant Fourier components associated with the turn-on and turn-off edges are sufficiently small that they do not cause an appreciable difference to the beat dynamics.

The data fitting of Eq. (1), the examples of which are presented in Fig. 2(b), is extended to the full experimental range of ODs between 0 and 5 as presented in Fig. 3. In the inset, the linear dependence of the enhancement factor $\Gamma_{22}^{(N)}/\Gamma_{22}$ on the OD displays the collective nature of the emission process, which is in agreement with the superradiant behavior [13,18,22–25]. The blue solid line fitting the data provides a linear relation $\Gamma_{22}^{(N)}/\Gamma_{22} = 1.0(1)\cdot\mathrm{OD} + 1.4(4)$, showing a qualitative agreement with the previous studies [26]. The beat contrast I_b is plotted as a function of $\Gamma_{22}^{(N)}/\Gamma_{22}$ in Fig. 3(a). The blue shaded region represents the one-sigma confidence band of the linear fit to the data, displaying the amplification of the quantum beat due to the increasing number of cooperative atoms. The red solid line plotting Eq. (2) is in good agreement with the data, confirming the validity of our model.

The measured beat phase ϕ is displayed in Fig. 3(b) and fit to

$$\phi = \arctan\left(\eta \cdot \frac{\Gamma_{22}^{(N)}}{\Gamma_{22}}\right) + \phi_0. \tag{4}$$

The fitted value of $\phi_0 = 0.17$ is presumably due to the transient intensity of the driving field during the switch-off time. From the fit, $\eta = 1.5(3) \times 10^{-1}$ is almost three times larger than its expected value of $\Gamma_{22}/\omega_{23} = 5.0 \times 10^{-2}$ [see Eq. (3)]. We note that nonequilibrium dynamics during the switch-off time can produce an additional OD-dependent phase delay, potentially resulting in a larger η value than expected, which is not captured by our current model. Such an additional phase can be used to characterize the nonequilibrium dynamics of emission during the transient time, the study of which is left to future work.

Discussion.—We have demonstrated collective quantum beats in a spontaneous emission process without an initial superposition of the excited levels in a three-level atomic system. The collective nature of the forward emission results in an enhanced coupling between the excited levels, which is manifested in cooperatively amplified quantum beats. We observe that the enhancement factor $\Gamma_{22}^{(N)}/\Gamma_{22}$ for the collective decay rate increases with the atomic OD. The beat contrast also scales with $\Gamma_{22}^{(N)}/\Gamma_{22}$, in agreement with our theoretical prediction. It signifies a combination of two different quantum interference phenomena featuring interplay between multilevel atomic structure and multiatom collective effects, which have been the focus of many theoretical studies [27–29].

The collective enhancement of quantum beats can be a valuable tool in precision spectroscopy by enhancing beat amplitudes in systems with small signals. It can also be utilized as a source of strongly correlated photons. For example, previous works have illustrated that a system of three-level V-type atoms in an interferometric setup, as in the case of a "quantum beat laser" [30,31], can exhibit strong correlations in the two-frequency emission [32,33]. It has been suggested as a means of generating or amplifying entanglement in the radiated field modes [34,35]. These proposed schemes rely on the coherence between the excited atomic levels, therefore requiring a strong classical drive to induce such coherences.

Vacuum-induced collective quantum beats can circumvent the need for a classical drive, thereby avoiding additional noise, while facilitating a collective signal enhancement.

Our study of collective quantum effects can be readily combined with waveguide optics to study interactions between distant atomic ensembles [36–42]. Recent studies have shown that such delocalized collective states can exhibit surprisingly rich non-Markovian dynamics [43–50]. A challenge in observing such exotic dynamics is that the quantum optical correlation between the multiple emitters is highly sensitive to the position of individual atoms, requiring subwavelength precision. Replacing the optical frequency by the beat radio frequency could allow one to bypass the strict requirements on controlling the atomic positions. An experimental investigation of collective effects in non-Markovian regimes with multilevel atomic ensembles coupled to optical nanofibers is within the scope of our future works [42].

The supporting data for this Letter are openly available from D. A. Steck's Alkali D Line Data suppository [15].

We thank Hyun Gyung Lee and Huan Q. Bui for technical support and fruitful discussions. We are also grateful to Pablo Solano and Jonathan Hoffman for helpful comments. This research is supported by the U.S. Army Research Laboratory's Maryland ARL Quantum Partnership (W911NF-19-2-0181) and the Joint Quantum Institute (70NANB16H168).

H. S. H. and A. L. contributed equally to this work.

*kanu@princeton.edu
†rolston@umd.edu

[1] E. T. Jaynes, in *Foundations of Radiation Theory and Quantum Electrodynamics*, edited by A. O. Barut (Springer US, Boston, MA, 1980), p. 37.
[2] S. Haroche, J. A. Paisner, and A. L. Schawlow, Phys. Rev. Lett. **30**, 948 (1973).
[3] C. G. Wade, N. Šibalić, J. Keaveney, C. S. Adams, and K. J. Weatherill, Phys. Rev. A **90**, 033424 (2014).
[4] E. Hack and J. R. Huber, Int. Rev. Phys. Chem. **10**, 287 (1991).
[5] H. Stolz, V. Langer, E. Schreiber, S. Permogorov, and W. von der Osten, Phys. Rev. Lett. **67**, 679 (1991).
[6] I. E. Kozin, V. G. Davydov, I. V. Ignatiev, A. V. Kavokin, K. V. Kavokin, G. Malpuech, H.-W. Ren, M. Sugisaki, S. Sugou, and Y. Masumoto, Phys. Rev. B **65**, 241312(R) (2002).
[7] J. Bylsma, P. Dey, J. Paul, S. Hoogland, E. H. Sargent, J. M. Luther, M. C. Beard, and D. Karaiskaj, Phys. Rev. B **86**, 125322 (2012).
[8] R. H. Dicke, Phys. Rev. **93**, 99 (1954).
[9] M. Gross and S. Haroche, Phys. Rep. **93**, 301 (1982).
[10] G. C. Hegerfeldt and M. B. Plenio, Phys. Rev. A **47**, 2186 (1993).
[11] G. C. Hegerfeldt and M. B. Plenio, Quantum Opt. **6**, 15 (1994).
[12] M. O. Scully, E. S. Fry, C. H. R. Ooi, and K. Wódkiewicz, Phys. Rev. Lett. **96**, 010501 (2006).
[13] T. Bienaimé, R. Bachelard, N. Piovella, and R. Kaiser, Fortschr. Phys. **61**, 377 (2013).
[14] S. L. Bromley, B. Zhu, M. Bishof, X. Zhang, T. Bothwell, J. Schachenmayer, T. L. Nicholson, R. Kaiser, S. F. Yelin, M. D. Lukin, A. M. Rey, and J. Ye, Nat. Commun. **7**, 11039 (2016).
[15] D. A. Streck, Data for "Rubidium 85D Line Data," Revision 2.2.1, Alkali D Line Data, http://steck.us/alkalidata (21 Nov. 2019).
[16] Although the vacuum-induced quantum beats are a second-order process, we note that the population in the excited level $|3\rangle$ depends on the relative strength of the cross-damping coefficient to the excited level separation, $|c_3(t)| \sim \Gamma_{23}/\omega_{23}$ (see Supplemental Material for details [17]), making the contribution non-negligible.
[17] See Supplemental Material at http://link.aps.org/supplemental/10.1103/PhysRevLett.127.073604 for derivation of the theoretical model and data analysis.
[18] M. O. Araújo, I. Krešić, R. Kaiser, and W. Guerin, Phys. Rev. Lett. **117**, 073002 (2016).
[19] M. Chalony, R. Pierrat, D. Delande, and D. Wilkowski, Phys. Rev. A **84**, 011401(R) (2011).
[20] C. C. Kwong, T. Yang, M. S. Pramod, K. Pandey, D. Delande, R. Pierrat, and D. Wilkowski, Phys. Rev. Lett. **113**, 223601 (2014).
[21] C. C. Kwong, T. Yang, D. Delande, R. Pierrat, and D. Wilkowski, Phys. Rev. Lett. **115**, 223601 (2015).
[22] T. Bienaimé, M. Petruzzo, D. Bigerni, N. Piovella, and R. Kaiser, J. Mod. Opt. **58**, 1942 (2011).
[23] T. Bienaimé, N. Piovella, and R. Kaiser, Phys. Rev. Lett. **108**, 123602 (2012).
[24] S. J. Roof, K. J. Kemp, M. D. Havey, and I. M. Sokolov, Phys. Rev. Lett. **117**, 073003 (2016).
[25] W. Guerin, M. T. Rouabah, and R. Kaiser, J. Mod. Opt. **64**, 895 (2017).
[26] See, for example, equation 4 in [18]. The previously predicted value (1/12) of the ratio between the collective decay rate enhancement and the OD is different from our measured value of 1.0(1). We remark that our experimental characteristics, such as the atomic density distribution or detection solid angle, may have caused a deviation from the analytical prediction [22].
[27] G. S. Agarwal, Phys. Rev. A **15**, 2380 (1977).
[28] G. S. Agarwal and A. K. Patnaik, Phys. Rev. A **63**, 043805 (2001).
[29] W. W. Chow, M. O. Scully, and J. O. Stoner, Phys. Rev. A **11**, 1380 (1975).
[30] M. O. Scully, Phys. Rev. Lett. **55**, 2802 (1985).
[31] M. O. Scully and M. S. Zubairy, Phys. Rev. A **35**, 752 (1987).
[32] M. Ohtsu and K. Y. Liou, Appl. Phys. Lett. **52**, 10 (1988).
[33] M. P. Winters, J. L. Hall, and P. E. Toschek, Phys. Rev. Lett. **65**, 3116 (1990).
[34] H. Xiong, M. O. Scully, and M. S. Zubairy, Phys. Rev. Lett. **94**, 023601 (2005).

[35] S. Qamar, F. Ghafoor, M. Hillery, and M. S. Zubairy, Phys. Rev. A **77**, 062308 (2008).
[36] D. E. Chang, V. Vuletić, and M. D. Lukin, Nat. Photonics **8**, 685 (2014).
[37] E. Vetsch, D. Reitz, G. Sagué, R. Schmidt, S. T. Dawkins, and A. Rauschenbeutel, Phys. Rev. Lett. **104**, 203603 (2010).
[38] A. Goban, K. S. Choi, D. J. Alton, D. Ding, C. Lacroûte, M. Pototschnig, T. Thiele, N. P. Stern, and H. J. Kimble, Phys. Rev. Lett. **109**, 033603 (2012).
[39] A. Goban, C.-L. Hung, J. D. Hood, S.-P. Yu, J. A. Muniz, O. Painter, and H. J. Kimble, Phys. Rev. Lett. **115**, 063601 (2015).
[40] S.-P. Yu, J. D. Hood, J. A. Muniz, M. J. Martin, R. Norte, C.-L. Hung, S. M. Meenehan, J. D. Cohen, O. Painter, and H. J. Kimble, Appl. Phys. Lett. **104**, 111103 (2014).
[41] A. Goban, C.-L. Hung, S.-P. Yu, J. D. Hood, J. A. Muniz, J. H. Lee, M. J. Martin, A. C. McClung, K. S. Choi, D. E. Chang, O. Painter, and H. J. Kimble, Nat. Commun. **5**, 3808 (2014).
[42] P. Solano, J. A. Grover, J. E. Hoffman, S. Ravets, F. K. Fatemi, L. A. Orozco, and S. L. Rolston, Adv. At. Mol. Opt. Phys. **66**, 439 (2017).
[43] H. Pichler and P. Zoller, Phys. Rev. Lett. **116**, 093601 (2016).
[44] F. Dinc, İ. Ercan, and A. M. Brańczyk, Quantum **3**, 213 (2019).
[45] F. Dinc and A. M. Brańczyk, Phys. Rev. Research **1**, 032042 (R) (2019).
[46] A. Carmele, N. Nemet, V. Canela, and S. Parkins, Phys. Rev. Research **2**, 013238 (2020).
[47] K. Sinha, P. Meystre, E. A. Goldschmidt, F. K. Fatemi, S. L. Rolston, and P. Solano, Phys. Rev. Lett. **124**, 043603 (2020).
[48] K. Sinha, P. Meystre, and P. Solano, in *Quantum Nanophotonic Materials, Devices, and Systems 2019*, edited by C. Soci, M. T. Sheldon, and M. Agio (11091, SPIE, Bellingham, 2019), p. 53.
[49] G. Calajó, Y.-L. L. Fang, H. U. Baranger, and F. Ciccarello, Phys. Rev. Lett. **122**, 073601 (2019).
[50] K. Sinha, A. González-Tudela, Y. Lu, and P. Solano, Phys. Rev. A **102**, 043718 (2020).

Supplemental Material for "Observation of vacuum-induced collective quantum beats"

Hyok Sang Han,[1] Ahreum Lee,[1] Kanupriya Sinha,[2,*] Fredrik K. Fatemi,[3,4] and S. L. Rolston[1,4,†]

[1] *Joint Quantum Institute, University of Maryland and the National Institute of Standards and Technology, College Park, Maryland 20742, USA*
[2] *Department of Electrical Engineering, Princeton University, Princeton, New Jersey 08544, USA*
[3] *U.S. Army Research Laboratory, Adelphi, Maryland 20783, USA*
[4] *Quantum Technology Center, University of Maryland, College Park, MD 20742, USA*

I. MODEL

We consider a collection of N three-level V-type atoms located at the same position. We label the ground state as $|1\rangle$ and the two excited states as $|2\rangle$ and $|3\rangle$, and the transition frequency from level j to i as ω_{ij}. A weak drive field which is resonantly tuned to ω_{21} prepares the atomic system in a timed-Dicke state. As the drive field is turned off, we detect the photons emitted from the cloud in the forward direction. In the experiment, the atomic cloud has a finite size, but for theoretical simplicity we can assume it to be point-like ensemble interacting each other through the vacuum field modes. This is because we are measuring the forward scattering, where any phases of emitted photons due to the atomic position distribution is exactly compensated by the phases initially imprinted on the atoms by the drive field [S1]. Additionally, the transitions $|1\rangle \leftrightarrow |2\rangle$ and $|1\rangle \leftrightarrow |3\rangle$ interact with the field effectively with the same phase considering that the atomic cloud size is much smaller compared to $2\pi c/\omega_{23}$. We note that while the forward-scattered field is collectively enhanced, the decay rate of the atoms arising from interaction with the rest of the modes is not cooperative [S2].

The atomic Hamiltonian H_A and the vacuum field Hamiltonian H_F are

$$\begin{aligned} H_A &= \sum_{m=1}^{N} \sum_{j=2,3} \hbar\omega_{j1} \hat{\sigma}^{+}_{m,j} \hat{\sigma}^{-}_{m,j}, \\ H_F &= \sum_{k} \hbar\omega_k \hat{a}^{\dagger}_k \hat{a}_k, \end{aligned} \tag{S1}$$

where $\hat{\sigma}^{\pm}_{m,j}$ is the raising/lowering operator acting on m^{th} atom and j^{th} level, $\hat{a}^{\dagger}_k$ and $\hat{a}_k$ are the field creation/annihilation operators of the corresponding frequency mode ω_k, and N refers to the effective number of atoms acting cooperatively in the forward direction.

First, we prepare the atomic system by a weak drive field. The atom-drive field interaction Hamiltonian is

$$H_{\text{AD}} = -\sum_{m=1}^{N} \sum_{j=2,3} \hbar\Omega^{m}_{j} \left(\hat{\sigma}^{+}_{m,j} e^{-i\omega_D t} + \hat{\sigma}^{-}_{m,j} e^{i\omega_D t} \right). \tag{S2}$$

Here, ω_D is the drive frequency and $\Omega^{m}_{j} \equiv \vec{d}^{m}_{j1} \cdot \vec{\epsilon_D} E_D$ is the Rabi frequency of j^{th} level, where $\vec{d}^{m}_{j1}$ is the dipole moment of $|j\rangle \leftrightarrow |1\rangle$ transition of m^{th} atom, $\vec{\epsilon}_D$ is the polarization unit vector of the drive field, and E_D is the electric field of the drive field. Given that the atomic ensemble is driven with the common field in our experiment, we will assume that the atomic dipoles are aligned with the drive and each other. We can thus omit the atomic labels to write Ω_j.

The interaction Hamiltonian describing the atom-vacuum field interaction, under the rotating wave approximation, is given as

$$H_{\text{AV}} = -\sum_{m=1}^{N} \sum_{j=2,3} \sum_{k} \hbar g_{m,j}(\omega_k) \left(\hat{\sigma}^{+}_{m,j} \hat{a}_k + \hat{\sigma}^{-}_{m,j} \hat{a}^{\dagger}_k \right). \tag{S3}$$

Here, the atom-field coupling strength $g_{m,j}(\omega_k) \equiv \vec{d}^{m}_{j1} \cdot \vec{\epsilon}_k \sqrt{\frac{\omega_k}{2\hbar\varepsilon_0 V}}$, where $\vec{\epsilon}_k$ is the polarization unit vector of the field mode, ε_0 is the vacuum permittivity, and V is the field mode volume. As justified previously, the atomic dipoles are aligned to each other and we write $g_j(\omega_k)$. Also, note that the sum over k only refers to the forward-scattered modes. The spontaneous emission arising from the rest of the modes is to be considered separately later.

* kanu@princeton.edu
† rolston@umd.edu

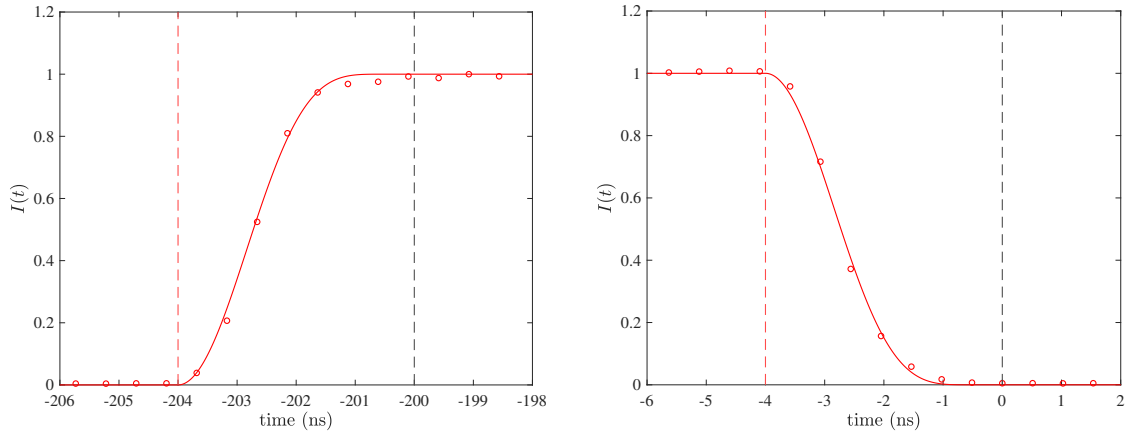

FIG. S1. The drive field intensity (red circles) at turn-on and turn-off edges simulated as a truncated $\cos^4\left(\frac{\pi}{2}\frac{t-t_0}{\tau}\right)$ function (red solid line). We assume the initial time for the turn-on and turn-off edges at $t_0 = -204\,\text{ns}$ and $t_0 = -4\,\text{ns}$, respectively, and the fall-time to be $\tau = 3.5\,\text{ns}$. While the intensity of the drive field turns off mostly within ≈ 3.5 ns, the data is analyzed after an additional 0.5-ns to further remove the residual drive intensity and the transient effect from our measurement, which sets $t = 0$ as shown in Fig. 2 (b).

II. DRIVEN DYNAMICS

We consider here the driven dynamics of the atoms. Moving to the rotating frame with respect to the drive frequency, and tracing out the vacuum field modes, we can write the following Born-Markov master equation for the atomic density matrix:

$$\frac{d\hat{\rho}_A}{dt} = -\frac{i}{\hbar}\left[\widehat{H}_A + \widehat{H}_{AD}, \hat{\rho}_A\right] - \sum_{m,n=1}^{N}\sum_{i,j=2,3}\frac{\Gamma^{(D)}_{ij,mn}}{2}\left[\hat{\rho}_A\widehat{\sigma}^{+}_{m,i}\widehat{\sigma}^{-}_{n,j} + \widehat{\sigma}^{+}_{m,i}\widehat{\sigma}^{-}_{n,j}\hat{\rho}_A - 2\widehat{\sigma}^{-}_{n,j}\hat{\rho}_A\widehat{\sigma}^{+}_{m,i}\right], \tag{S4}$$

where $\widehat{H}_A = -\sum_{m=1}^{N}\sum_{j=2,3}\hbar\Delta_j\widehat{\sigma}^{+}_{m,j}\widehat{\sigma}^{-}_{m,j}$ is the free atomic Hamiltonian and $\widehat{H}_{AD} = -\sum_{m=1}^{N}\sum_{j=2,3}\hbar\Omega^{m}_{j}\left(\widehat{\sigma}^{+}_{m,j} + \widehat{\sigma}^{-}_{m,j}\right)$ is the atom-drive interaction Hamiltonian in the rotating frame, with $\Delta_j \equiv \omega_{j1} - \omega_D$. The driven damping rates are defined as $\Gamma^{(D)}_{ij,mn} \equiv \frac{\vec{d}^{m}_{i1}\cdot\vec{d}^{n}_{j1}\omega_D^3}{3\pi\varepsilon_0\hbar c^3}$, with the indices i, j referring to the atomic levels, and m, n to different atoms.

Using the above master equation, one can obtain the following optical Bloch equations (OBEs) for the case of a

single atom:

$$\partial_t \rho_{33} = i\Omega_3(\rho_{13}-\rho_{31}) - \Gamma_{33}^{(D)}\rho_{33} - \frac{\Gamma_{23}^{(D)}}{2}\rho_{23} - \frac{\Gamma_{23}^{(D)}}{2}\rho_{32} \tag{S5a}$$

$$\partial_t \rho_{22} = i\Omega_2(\rho_{12}-\rho_{21}) - \Gamma_{22}^{(D)}\rho_{22} - \frac{\Gamma_{23}^{(D)}}{2}\rho_{23} - \frac{\Gamma_{23}^{(D)}}{2}\rho_{32} \tag{S5b}$$

$$\partial_t \rho_{11} = -i\Omega_3(\rho_{13}-\rho_{31}) - i\Omega_2(\rho_{12}-\rho_{21}) + \Gamma_{33}^{(D)}\rho_{33} + \Gamma_{22}^{(D)}\rho_{22} + \Gamma_{23}^{(D)}(\rho_{23}+\rho_{32}) \tag{S5c}$$

$$\partial_t \rho_{31} = -i\Omega_2\rho_{32} - i\Omega_3(\rho_{33}-\rho_{11}) - \left(\frac{\Gamma_{33}^{(D)}}{2} - i\Delta_3\right)\rho_{31} - \frac{\Gamma_{23}^{(D)}}{2}\rho_{21} \tag{S5d}$$

$$\partial_t \rho_{13} = i\Omega_2\rho_{23} + i\Omega_3(\rho_{33}-\rho_{11}) - \left(\frac{\Gamma_{33}^{(D)}}{2} + i\Delta_3\right)\rho_{13} - \frac{\Gamma_{23}^{(D)}}{2}\rho_{12} \tag{S5e}$$

$$\partial_t \rho_{21} = -i\Omega_3\rho_{23} - i\Omega_2(\rho_{22}-\rho_{11}) - \left(\frac{\Gamma_{22}^{(D)}}{2} - i\Delta_2\right)\rho_{21} - \frac{\Gamma_{23}^{(D)}}{2}\rho_{31} \tag{S5f}$$

$$\partial_t \rho_{12} = i\Omega_3\rho_{32} + i\Omega_2(\rho_{22}-\rho_{11}) - \left(\frac{\Gamma_{22}^{(D)}}{2} + i\Delta_2\right)\rho_{12} - \frac{\Gamma_{23}^{(D)}}{2}\rho_{13} \tag{S5g}$$

$$\partial_t \rho_{32} = -i\Omega_2\rho_{31} + i\Omega_3\rho_{12} - \left(\frac{\Gamma_{22}^{(D)}+\Gamma_{33}^{(D)}}{2} - i\omega_{23}\right)\rho_{32} - \frac{\Gamma_{23}^{(D)}}{2}(\rho_{22}+\rho_{33}) \tag{S5h}$$

$$\partial_t \rho_{23} = i\Omega_2\rho_{13} - i\Omega_3\rho_{21} - \left(\frac{\Gamma_{22}^{(D)}+\Gamma_{33}^{(D)}}{2} + i\omega_{23}\right)\rho_{23} - \frac{\Gamma_{23}^{(D)}}{2}(\rho_{22}+\rho_{33}), \tag{S5i}$$

where we have defined the single atom driven damping rate as $\Gamma_{ij}^{(D)} \equiv \frac{\vec{d}_{i1}\cdot\vec{d}_{j1}\omega_D^3}{3\pi\varepsilon_0\hbar c^3}$.

Numerically solving Eq. (S5a)–Eq. (S5i) along with the normalization condition $\rho_{33}+\rho_{22}+\rho_{11}=1$ gives us the steady state density matrix ρ_S for the atom. Substituting our experimental parameters, we get the populations: $\rho_{S,33}\approx 0$, $\rho_{S,22}\approx 10^{-10}$, and $\rho_{S,11}\approx 1$. The absolute value of the coherences are: $|\rho_{S,23}|\approx 0$, $|\rho_{S,21}|\approx 10^{-5}$, and $|\rho_{S,31}|\approx 0$. These estimates are made assuming the collective enhancement of the damping rate to be $\Gamma_{ij}^{(D)}(N)/\Gamma_{ij}^{(D)} \approx 1-10$ and the collective Rabi frequency to be $\Omega_j(N)\approx\sqrt{N}\Omega_j$. Thus we can conclude that the atomic ensemble is well within the single excitation regime in $|2\rangle$.

To preclude the possibility of exciting additional population in the levels $|2\rangle$ and $|3\rangle$ during laser turn-off due to off-resonant Fourier components, we numerically simulate the OBEs to find the atomic density matrix evolution, modeling the laser turn-off shape as a truncated $\cos^4$ function (see Fig. S1) and varying the Rabi frequency accordingly. Fig. S2 shows a comparison of the three different cases:

I. *OBE*: We simulate the atomic dynamics via the OBEs for (i) 3.5 ns laser turn-on edge, (ii) 200 ns laser drive, (iii) 3.5 ns laser turn-off edge, and (iv) 60 ns after laser turn-off, modeling the laser turn-on and turn-off with a truncated $\cos^4$ function as shown in Fig. S1. The atoms are assumed to be initially in the ground state before the drive is turned on.

II. *Wigner-Weisskopf (WW) approach*: We calculate the atomic density matrix dynamics analytically starting after the laser turn-off, and assuming an initial state to be a collective state with a shared single excitation in level $|2\rangle$ (see Section III for details).

III. *OBE, $\Gamma_{23}\to 0$*: This corresponds to the OBE dynamics with the drive and initial atomic state as in case I, except we ignore the vacuum-induced coupling between the excited levels, assuming $\Gamma_{23}\to 0$.

We see that the atomic dynamics for cases I and II behave similarly, illustrating that the approximate model of the dynamics excluding the drive turn-on and turn-off edges gives correct atomic dynamics up to an initial time displacement. This shows that the off-resonant Fourier components associated with the turn-on and turn-off edges are sufficiently small such that they do not cause an appreciable difference to the beat dynamics. On the other hand, we also observe that the atomic dynamics in the absence of vacuum-induced coupling (case III) differs from the other two cases, demonstrating that the vacuum-induced coupling is indeed responsible for the beat dynamics. This is explicit in the dynamics as shown in Fig. S2.

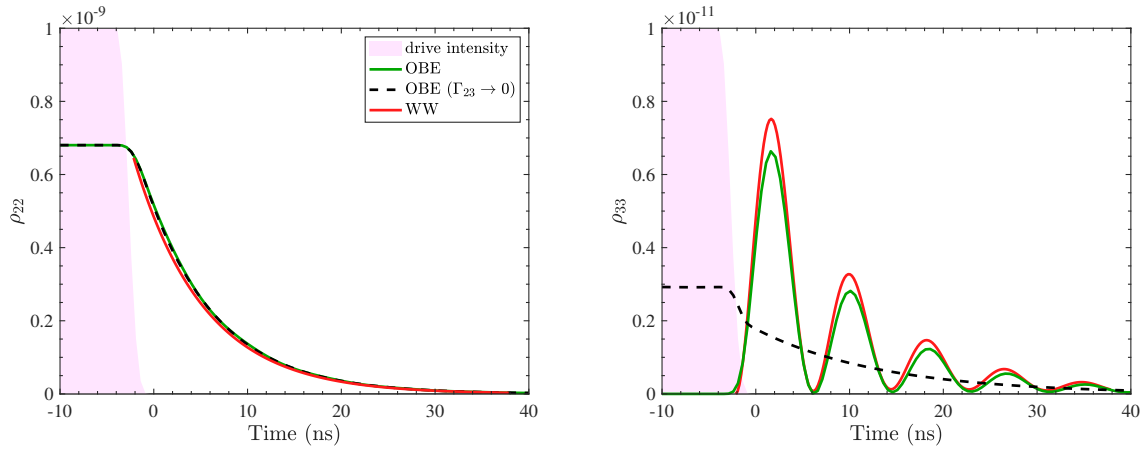

FIG. S2. Atomic populations (a) ρ_{22} and (b) ρ_{33} during and after the drive turn-off. Green solid curves correspond to the atomic dynamics obtained from the OBEs including the laser turn-on, the 200-ns drive and finite-time turn-off edge (case I). Red solid curves represent the analytical solution from the Wigner-Weisskopf (WW) approach where the system evolves without the drive (case II). The black dashed curves represent the dynamics obtained from the OBEs ignoring the vacuum-induced coupling between the excited levels ($\Gamma_{23} \to 0$) (case III). The horizontal axis for the red solid curves (case II) is adjusted with respect to the green solid (case I) so that the plots overlap in time.

III. QUANTUM BEAT DYNAMICS FROM WIGNER-WEISSKOPF THEORY

As the drive field is turned off, the system evolves with the atom-vacuum field interaction Hamiltonian. Moving to the interaction representation with respect to $H_A + H_F$, we get the interaction Hamiltonian in the interaction picture:

$$\tilde{H}_{\mathrm{AV}} = -\sum_{m=1}^{N}\sum_{j=2,3}\sum_{k}\hbar g_j(\omega_k)\left(\hat{\sigma}^{+}_{m,j}\hat{a}_k e^{i(\omega_{j1}-\omega_k)t} + \hat{\sigma}^{-}_{m,j}\hat{a}^{\dagger}_k e^{-i(\omega_{j1}-\omega_k)t}\right), \tag{S6}$$

Initially the system shares one excitation in $|2\rangle$ symmetrically, and the EM field is in the vaccum state such that

$$|\Psi(0)\rangle = \frac{1}{\sqrt{N}}\sum_{m=1}^{N}\hat{\sigma}^{+}_{m,2}\,|11\cdots1\rangle\,|\{0\}\rangle\,. \tag{S7}$$

As the system evolves due to the atom-vacuum field interaction, it remains in the single-excitation manifold of total atom + field Hilbert space, as one can see from the interaction Hamiltonian (Eq. (S6)):

$$|\Psi(t)\rangle = \left(\sum_{m=1}^{N}\sum_{j=2,3}c_{m,j}(t)\hat{\sigma}^{+}_{m,j} + \sum_{k}c_k(t)\hat{a}^{\dagger}_k\right)|11\cdots1\rangle\,|\{0\}\rangle\,. \tag{S8}$$

Now we solve the Schrödinger equation to find the time evolution of the atom + field system under the atom-field interaction using Eqs.(S8) and (S6) to obtain

$$\partial_t c_{m,j}(t) = i\sum_{k}g_j(\omega_k)e^{i(\omega_{j1}-\omega_k)t}c_{\omega_k}(t), \tag{S9a}$$

$$\partial_t c_{\omega_k}(t) = i\sum_{m=1}^{N}\sum_{j=2,3}g_j(\omega_k)e^{-i(\omega_{j1}-\omega_k)t}c_{m,j}(t). \tag{S9b}$$

Formally integrating Eq. (S9)(b) and plugging it in Eq. (S9)(a), we have

$$\partial_t c_{m,j}(t) = -\sum_{k}g_j(\omega_k)e^{i(\omega_{j1}-\omega_k)t}\int_0^t \mathrm{d}\tau\sum_{n=1}^{N}\sum_{l=2,3}g_l(\omega_k)e^{-i(\omega_{l1}-\omega_k)\tau}c_{n,l}(\tau). \tag{S10}$$

We observe that $c_{m,2}(t)$'s ($c_{m,3}(t)$'s) have the same initial conditions and the same evolution equation, thus we can justifiably define $c_2(t) \equiv c_{m,2}(t)$ ($c_3(t) \equiv c_{m,3}(t)$).

Assuming a flat spectral density of the field and making the Born-Markov approximation we get

$$\partial_t c_2(t) = -\frac{\Gamma_{22}^{(N)}}{2} c_2(t) - \frac{\Gamma_{23}^{(N)}}{2} e^{i\omega_{23}t} c_3(t), \tag{S11a}$$

$$\partial_t c_3(t) = -\frac{\Gamma_{33}^{(N)}}{2} c_3(t) - \frac{\Gamma_{32}^{(N)}}{2} e^{-i\omega_{23}t} c_2(t), \tag{S11b}$$

where we have defined $\Gamma_{jl}^{(N)} \equiv \Gamma_{jl} + Nf\Gamma_{jl}$, with $\Gamma_{jl} = \frac{\vec{d}_{j1}\cdot\vec{d}_{l1}\omega_{l1}^3}{3\pi\varepsilon_0\hbar c^3}$ as the generalized decay rate into the quasi-isotropic modes and $Nf\Gamma_{jl}$ as the collective decay rate in the forward direction [S2, S3]. The factor f represents the geometrical factor coming from restricting the emission to the forward scattered modes. We emphasize here that the emission into all the modes (not specifically the forward direction) denoted by Γ_{jl} is added phenomenologically and is not collective. Considering that the atomic dipole moments induced by the drive field are oriented along the polarization of the driving field, we can obtain $\Gamma_{23} = \sqrt{\Gamma_{22}\Gamma_{33}}$, which can be extended to $\Gamma_{23}^{(N)} = \sqrt{\Gamma_{22}^{(N)}\Gamma_{33}^{(N)}}$.

To solve the coupled differential equations, we take the Laplace transform of Eq. (S11)(a) and (b):

$$s\tilde{c}_2(s) = c_2(0) - \frac{\Gamma_{22}^{(N)}}{2}\tilde{c}_2(s) - \frac{\Gamma_{23}^{(N)}}{2}\tilde{c}_3(s - i\omega_{23}), \tag{S12a}$$

$$s\tilde{c}_3(s) = c_3(0) - \frac{\Gamma_{33}^{(N)}}{2}\tilde{c}_3(s) - \frac{\Gamma_{32}^{(N)}}{2}\tilde{c}_2(s + i\omega_{23}), \tag{S12b}$$

where we have defined $\tilde{c}_j(s) \equiv \int_0^\infty c_j(t)e^{-st}\mathrm{d}(t)$ as the Laplace transform of $c_j\,(t)$. Substituting the initial conditions, we obtain the Laplace coefficients as

$$\tilde{c}_2(s) = \frac{1}{\sqrt{N}} \frac{s + \frac{\Gamma_{33}^{(N)}}{2} - i\omega_{23}}{s^2 + (\Gamma_{\mathrm{avg}}^{(N)} - i\omega_{23})s - i\omega_{23}\frac{\Gamma_{22}^{(N)}}{2}}, \tag{S13a}$$

$$\tilde{c}_3(s) = -\frac{\Gamma_{32}^{(N)}}{2\sqrt{N}} \frac{1}{s^2 + (\Gamma_{\mathrm{avg}}^{(N)} + i\omega_{23})s + i\omega_{23}\frac{\Gamma_{33}^{(N)}}{2}}. \tag{S13b}$$

And the poles of the denominators are, respectively,

$$s_{\pm}^{(2)} = -\frac{\Gamma_{\mathrm{avg}}^{(N)}}{2} + \frac{i\omega_{23}}{2} \pm \frac{i\delta}{2}, \tag{S14a}$$

$$s_{\pm}^{(3)} = -\frac{\Gamma_{\mathrm{avg}}^{(N)}}{2} - \frac{i\omega_{23}}{2} \pm \frac{i\delta}{2}, \tag{S14b}$$

where we have defined $\Gamma_{\mathrm{avg}}^{(N)} = \frac{\Gamma_{33}^{(N)} + \Gamma_{22}^{(N)}}{2}$, $\Gamma_{\mathrm{d}} = \frac{\Gamma_{33}^{(N)} - \Gamma_{22}^{(N)}}{2}$, and $\delta = \sqrt{\omega_{23}^2 - \left(\Gamma_{\mathrm{avg}}^{(N)}\right)^2 + 2i\omega_{23}\Gamma_{\mathrm{d}}^{(N)}}$. The real part of the above roots corresponds to the collective decay rate of each of the excited states, while the imaginary part corresponds to the frequencies. The fact that δ is generally a complex number unless $\Gamma_{22} \neq \Gamma_{33}$ means that we will have modification to both the decay rate and the frequency. To see this more clearly, we can expand δ up to second order in $\Gamma_{jl}^{(N)}/\omega_{23}$, considering we are working in a spectroscopically well-separated regime ($\Gamma_{jl}^{(N)} \ll \omega_{23}$);

$$\delta \approx \omega_{23}\left[1 - \frac{1}{2}\left(\frac{\Gamma_{23}^{(N)}}{\omega_{23}}\right)^2\right] + i\Gamma_d^{(N)}\left[1 + \frac{1}{2}\left(\frac{\Gamma_{23}^{(N)}}{\omega_{23}}\right)^2\right], \tag{S15}$$

the above poles become

$$s_+^{(2)} = -\frac{\Gamma_{33}^{(N)}}{2}\left(1+\frac{\Gamma_{\rm d}^{(N)}\Gamma_{22}^{(N)}}{2\omega_{23}^2}\right)+i\omega_{23}\left[1-\left(\frac{\Gamma_{23}^{(N)}}{2\omega_{23}}\right)^2\right], \tag{S16a}$$

$$s_-^{(2)} = -\frac{\Gamma_{22}^{(N)}}{2}\left(1-\frac{\Gamma_{\rm d}^{(N)}\Gamma_{33}^{(N)}}{2\omega_{23}^2}\right)+i\omega_{23}\left(\frac{\Gamma_{23}^{(N)}}{2\omega_{23}}\right)^2, \tag{S16b}$$

$$s_+^{(3)} = -\frac{\Gamma_{33}^{(N)}}{2}\left(1+\frac{\Gamma_{\rm d}^{(N)}\Gamma_{22}^{(N)}}{2\omega_{23}^2}\right)-i\omega_{23}\left(\frac{\Gamma_{23}^{(N)}}{2\omega_{23}}\right)^2 \tag{S16c}$$

$$s_-^{(3)} = -\frac{\Gamma_{22}^{(N)}}{2}\left(1-\frac{\Gamma_{\rm d}^{(N)}\Gamma_{33}^{(N)}}{2\omega_{23}^2}\right)-i\omega_{23}\left[1-\left(\frac{\Gamma_{23}^{(N)}}{2\omega_{23}}\right)^2\right]. \tag{S16d}$$

The atomic state coefficients in time domain are

$$c_2(t) = \frac{1}{2\sqrt{N}\delta}e^{-\Gamma_{\rm avg}^{(N)}t/2}e^{i\omega_{23}t/2}\left[(-i\Gamma_d^{(N)}-\omega_{23}+\delta)e^{i\delta t/2}+(i\Gamma_d^{(N)}+\omega_{23}+\delta)e^{-i\delta t/2}\right], \tag{S17a}$$

$$c_3(t) = \frac{i\Gamma_{32}^{(N)}}{2\sqrt{N}\delta}e^{-\Gamma_{\rm avg}^{(N)}t/2}e^{-i\omega_{23}t/2}\left[e^{i\delta t/2}-e^{-i\delta t/2}\right]. \tag{S17b}$$

Again, expanding δ assuming $\Gamma_{jl}^{(N)} \ll \omega_{23}$, we get

$$c_2(t) = \frac{1}{\sqrt{N}}\left[e^{-\Gamma_{22}^{(N)}t/2}-\left(\frac{\Gamma_{23}^{(N)}}{2\omega_{23}}\right)^2\frac{\delta^*}{\delta}e^{-\Gamma_{33}^{(N)}t/2}e^{i\omega_{23}t}\right], \tag{S18a}$$

$$c_3(t) = -\frac{i\Gamma_{23}^{(N)}}{2\sqrt{N}\delta}\left[e^{-\Gamma_{22}^{(N)}t/2}e^{-i\omega_{23}t}-e^{-\Gamma_{33}^{(N)}t/2}\right]. \tag{S18b}$$

We note from the above that to lowest order in Γ_{23}/ω_{23} the population in level $|3\rangle$ scales roughly as $|c_3(t)|^2 \sim \left(\frac{\Gamma_{23}^{(N)}}{\omega_{23}}\right)^2$. Note that the collection of N atoms behaves like one "super-atom" which decays with a rate that is N-times that of an individual atom in the forward direction. We note that the system is not only superradiant with respect to the transition involving the initially excited level, but also with respect to other transitions as well as a result of the vacuum-induced coupling between the levels. Most population in $|2\rangle$ decays with the decay rate $\Gamma_{22}^{(N)}$, and small amount of it decays with $\Gamma_{33}^{(N)}$ and has corresponding level shift ω_{23}. In $|3\rangle$ are the equal amount of components decaying with $\Gamma_{22}^{(N)}$ (and level shifted $-\omega_{23}$) and $\Gamma_{33}^{(N)}$. The small but nonzero contribution of $|3\rangle$ makes beating of frequency about ω_{23}.

IV. FIELD INTENSITY

The light intensity at position x and time t (assuming the atom is at position $x=0$ and it starts to evolve at time $t=0$) is

$$I(x,t) = \frac{\epsilon_0 c}{2}\langle\Psi(t)|\hat{E}^\dagger(x,t)\hat{E}(x,t)|\Psi(t)\rangle, \tag{S19}$$

where the electric field operator is

$$\hat{E}(x,t) = \int_{-\infty}^{\infty} {\rm d}k\, E_k \hat{a}_k e^{ikx}e^{-i\omega_k t}. \tag{S20}$$

Plugging in the electric field operator and the single-excitation ansatz (Eq. (S8)), we obtain the intensity up to a constant factor:

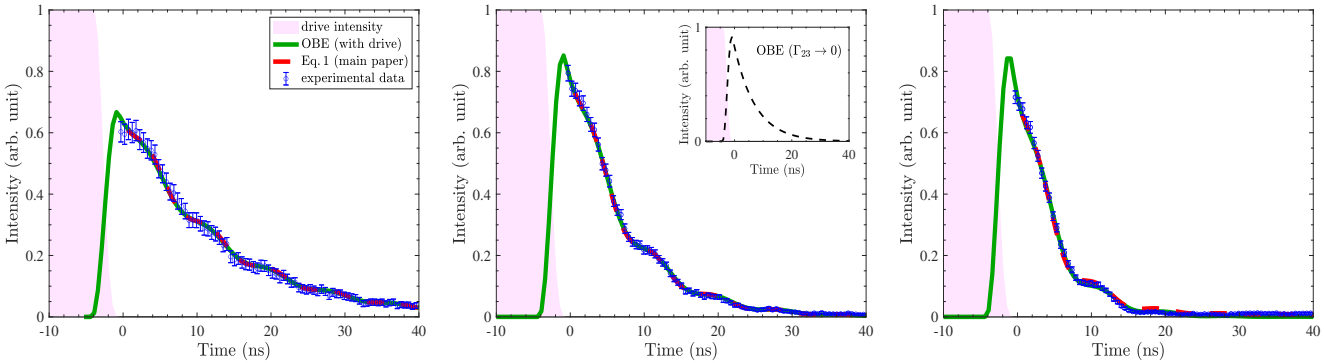

FIG. S3. Beat intensity dynamics for (a) OD = 0.9, (b) OD = 2.1, and (c) OD = 4.2, corresponding to the experimental data in Fig. 2(b) of main paper. The solid green curve denotes the dynamics obtained from the OBEs including the drive dynamics, the red dashed curve corresponds to analytical solution obtained from Wigner-Weisskopf approach (Eq. 1 of main paper), the blue circles represent the experimental data, and the pink region indicates the drive pulse. The inset in (b) further shows that if we ignore the vacuum-induced coupling in the OBE model ($\Gamma_{23} \to 0$), there are no beats, demonstrating that the vacuum-induced coupling is essential for obtaining the beat dynamics.

$$I(x,t) = I_0 N^2 \left| \sqrt{\Gamma_{22}} e^{-i\omega_{23}\tau} c_2(\tau) + \sqrt{\Gamma_{33}} c_3(\tau) \right|^2 \Theta(\tau), \tag{S21}$$

where $\tau = t - |x/v|$.

Substituting Eqs. (S17)(a) and (b) in the above and approximating δ in the regime $\Gamma_{jl}^{(N)} \ll \omega_{23}$, we get

$$\frac{I(\tau)}{I_0} = e^{-\Gamma_{22}^{(N)}\tau} + \frac{\Gamma_{33}^{(N)}}{\Gamma_{22}^{(N)}} \left(\frac{\Gamma_{23}^{(N)}}{2\omega_{23}} \right)^2 e^{-\Gamma_{33}^{(N)}\tau} + \frac{\left(\Gamma_{23}^{(N)}\right)^2}{\omega_{23}\Gamma_{22}^{(N)}} e^{-\Gamma_{\text{avg}}^{(N)}\tau} \sin(\omega_{23}\tau + \phi), \tag{S22}$$

where I_0 is a normalization factor which increases as the number of atom increases. Neglecting the small second term in the right hand side, we get the beat contrast:

$$I_{\text{b}} \equiv \frac{\left(\Gamma_{23}^{(N)}\right)^2}{\omega_{23}\Gamma_{22}^{(N)}}, \tag{S23}$$

and the beat phase ϕ:

$$\phi = \arctan\left(\frac{\Gamma_{22}^{(N)}}{\omega_{23}} \right). \tag{S24}$$

We see that even if there was no population in level 3 in the beginning, the vacuum field builds up a coherence between level 2 and level 3 to make a quantum beat. This is in line with the quantum trajectory calculation of single atom case [S4], where the individual decay rates are replaced with collective decay rates. We can verify that the collective effect manifests in the beat size and the beat phase.

The intensity profile from Eq. S22 for three different OD's used in the experiment are shown as red dashed lines in Fig. S3. With appropriate time adjustment the Eq. S22 matches well with the experimental data. For comparison, the OBE calculation considering the realistic laser dynamics (turn-on, drive for 200 ns, turn-off) is overlaid (green solid line). The OBE calculation assumes the atoms to be initially in the ground state before the laser is turned on, and the emitted intensity is obtained as $I(t) = -\frac{\text{d}}{\text{d}t}(\rho_{22} + \rho_{33})$. The inset of (b) shows the decay curve without vacuum-induced coupling ($\Gamma_{23} \to 0$), confirming that the observation of beat is indeed from the vacuum coupling of excited states.

V. PRECURSOR DYNAMICS

We analyze the precursor dynamics in Fig. S4. The atoms are initially in an uncorrelated state at the laser turn-on edge. The collective behavior builds up during the dynamics, as can be seen in Fig. S4, where the beat contrast versus OD is compared for precursor and flash dynamics. We observe from the slope of the two curves that the flash exhibits a larger collective enhancement compared to the precursor.

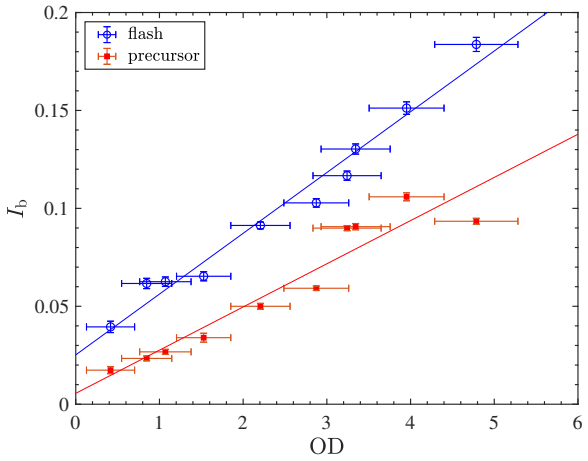

FIG. S4. The beat contrast as a function of the optical depth (OD) for the flash and precursor dynamics. Due to the systematic uncertainty (such as fluctuations in background photon counts) of the individual ODs measured at higher values (see inset of Fig. 3 (a) of main), the OD-axis in this figure was re-calibrated by the linear-fit of the OD and $\Gamma_{22}^{(N)}/\Gamma_{22}$ relation.

VI. DATA ANALYSIS IN FIG. 2 (B)

The modulated decay profiles of the flash after the peak are magnified in Fig. 2 (b). The purpose of the figure is to visually compare the decay rate and the beat contrast I_b, so we normalize each curve with the exponential decay amplitude such that the normalized intensity starts to decay from ≈ 1 at $t = 0$. In practice, we fit the $I(t)$ shown in Fig. 2 (a) after $t = 0$ using Eq. 1 to get I_0 for each curve, to get $I(t)/I_0$ curves as in Fig. 2 (b). Note that, more precisely, it is the fitting curve that decays from $I(t)/I_0 \approx 1$, not the experimental data. In fact, the plotted data tend to be lower than the fitting curves near $t = 0$, due to the effect of the transient behavior around the flash peak.

The inset displays the FFT of the beat signal shown in the main figure. We first subtract from $I(t)/I_0$ data the exponential decay profile the first term of the fitting function Eq. 1 as well as the dc offset. The residual, which is a sinusoidal oscillation with an exponentially decaying envelope, is the beat signal represented by the second term of Eq. 1. The FFT of the beat signal has the lower background at $\omega = 0$ due to the pre-removal of the exponential decay and the offset. The linewidth of each spectrum is limited by the finite lifetime of the beat signal, which corresponds to $\Gamma_{\text{avg}}^{(N)}$ as in Eq. 1.

[S1] M. O. Scully, E. S. Fry, C. H. R. Ooi, and K. Wódkiewicz, Phys. Rev. Lett. **96**, 010501 (2006).
[S2] T. Bienaimé, M. Petruzzo, D. Bigerni, N. Piovella, and R. Kaiser, Journal of Modern Optics **58**, 1942 (2011).
[S3] M. O. Araújo, I. Krešić, R. Kaiser, and W. Guerin, Phys. Rev. Lett. **117**, 073002 (2016).
[S4] G. C. Hegerfeldt and M. B. Plenio, Quantum Opt. **6**, 15 (1994).

Collective quantum beats from distant multilevel emitters

Ahreum Lee,[1,*] Hyok Sang Han,[1] Fredrik K. Fatemi,[2,3] S. L. Rolston,[1,3] and Kanu Sinha[4]

[1]*Joint Quantum Institute, University of Maryland and the National Institute of Standards and Technology, College Park, Maryland 20742, USA*

[2]*DEVCOM Army Research Laboratory, Adelphi, Maryland 20783, USA*

[3]*Quantum Technology Center, University of Maryland, College Park, Maryland 20742, USA*

[4]*School of Electrical, Computer and Energy Engineering, Arizona State University, Tempe, Arizona 85287, USA*

(Received 15 July 2022; accepted 16 December 2022; published 3 January 2023)

We analyze the dynamics of quantum beats in a system of two V-type three-level atoms coupled to a waveguide. We show that quantum beats can be collectively enhanced or suppressed, akin to Dicke super- and subradiance, depending on the interatomic separation and the initial correlations between the atoms. In particular, the interference properties of the collective beats are determined by the distance between the atoms modulo the beat wavelength. We study the collective atomic and field dynamics, illustrating a crossover from a Markovian to a non-Markovian regime as the atomic separation becomes sufficiently large to bring memory effects of the electromagnetic environment into consideration. In such a non-Markovian regime, collective quantum beats can be enhanced beyond the Markovian limit as a result of retardation effects. Our results demonstrate the rich interplay between multilevel and multiatom quantum interference effects arising in a system of distant quantum emitters.

DOI: 10.1103/PhysRevA.107.013701

I. INTRODUCTION

Quantum beats refer to the quantum interference effect in the radiation emitted from different excited levels in a multilevel atomic system [1]. Similar to the well-known phenomenon of collective atomic spontaneous emission [2], quantum beats can exhibit cooperative effects when considering the fluorescence from a collection of multilevel atoms as demonstrated theoretically [3] and experimentally [4]. Collective effects can thus be a tool for enhancing quantum beats, relevant to improving the sensitivity of precision time-resolved spectroscopy methods [5].

Collective atom-field interactions have been historically explored in systems where atoms are confined within small volumes compared to the resonant wavelengths [6–10]. However, waveguides allow for the realization of cooperative effects between distant emitters, which has been a subject of significant interest in recent theoretical and experimental works [11–22]. In such cases, the radiation emitted from a pair of emitters that are prepared in a symmetric initial state is super(sub)radiant for an interatomic separation that is a (half-)integer multiple of the resonant transition wavelength. Thus the atomic separation (d) modulo the resonant wavelength is crucial in determining the collective emission properties of a system. The interference can thus be engineered in ordered atomic arrays to exhibit strong collective phenomena creating nearly perfect mirrors [23–25] and facilitating quantum metrology [26,27] and quantum memory [13,28].

In this paper, we study the collective quantum beat dynamics of distant multilevel emitters coupled to a waveguide. In such a case, the collective dynamics involves multiple transition frequencies and exhibits even richer interference behavior. We find that at larger length scale the beat wavelength $\lambda_{\text{beat}} \equiv 2\pi v/\omega_{\text{beat}}$ (ω_{beat} being the beat frequency and v being the speed of light in the waveguide) becomes relevant in determining the phase relations between the radiation emitted from different transitions. For a pair of distant multilevel atoms that are prepared in a symmetric initial state with respect to one of the transitions, we show that the resulting quantum beats can be enhanced (suppressed) for an interatomic separation that is a (half-)integer multiple of the beat wavelength, similar to the dependence of Dicke super- and subradiance on the atomic separation modulo the resonant wavelength.

Furthermore, we investigate the regime where the interatomic separation becomes comparable to the coherence length defined as $L_c = v/\Gamma$, where Γ is the characteristic spontaneous emission rate for individual atoms. It has been shown that in such a case the system exhibits rich retardation-induced non-Markovian dynamics, with features such as collective spontaneous emission rates exceeding those of Dicke superradiance [29–32] and formation of highly delocalized atom-photon bound states [32–36]. Increasing the atomic separation to regimes where the retardation effects become relevant, we illustrate a crossover from a Markovian to a non-Markovian dynamics of collective quantum beats.

The paper is organized as follows. We present the model for the system of two V-type three level atoms coupled to a waveguide in Sec. II. Section III analyzes the collective quantum beat dynamics for the atomic and field degrees of freedom. In Sec. IV, we describe the distance dependence of collective quantum beat dynamics. We discuss the conclusions and outlook of the paper in Sec. V.

II. MODEL

We consider two three-level V-type atoms coupled through a one-dimensional waveguide, as shown in the schematic Fig. 1. The ground state is labeled as $|1\rangle$ and the two excited

*alee1206@umd.edu

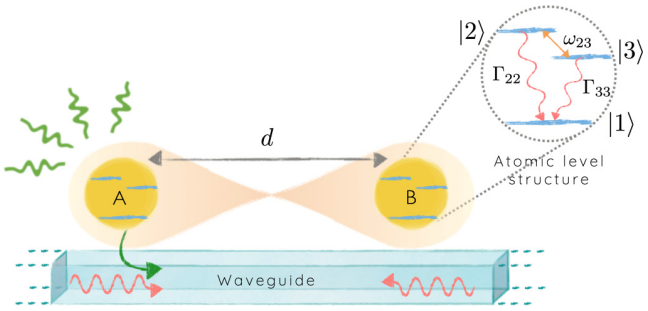

FIG. 1. Schematic representation of two three-level atoms, denoted by A and B, coupled to a waveguide. We consider that each atom has a V-type level structure, with the ground state denoted by $|1\rangle$ and the two excited states denoted by $|2\rangle$ and $|3\rangle$, with decay rates Γ_{22} and Γ_{33}, respectively. The detuning between levels $|2\rangle$ and $|3\rangle$ is ω_{23}. We consider different regimes of the interatomic separation d such that (1) $d \sim \lambda_{\text{beat}} \ll L_c$ and (2) $\lambda_{\text{beat}} \ll d \sim L_c$, with $\lambda_{\text{beat}} = 2\pi v/\omega_{23}$ as the beat wavelength and $L_c = v/\Gamma_{22}$ as the coherence length, with v as the speed of the EM field in the waveguide.

levels are $|2\rangle$ and $|3\rangle$. The frequency difference between levels i and j is denoted as ω_{ij}. The positions of the two atoms are denoted by $x_A = -d/2$ and $x_B = d/2$.

We can write the total Hamiltonian of the system as $H = H_0 + H_{AF}$, where H_0 is the free Hamiltonian and H_{AF} represents the atom-field interaction. The free Hamiltonian is defined as

$$H_0 = \sum_{m=A,B}\sum_{j=2,3}\hbar\omega_{j1}\hat{\sigma}^+_{m,j}\hat{\sigma}^-_{m,j} + \sum_k \hbar\omega_k\left[\hat{a}^\dagger_{R,k}\hat{a}_{R,k} + \hat{a}^\dagger_{L,k}\hat{a}_{L,k}\right]. \quad (1)$$

The first term corresponds to the atomic Hamiltonian where $\hat{\sigma}^\pm_{m,j}$ are the atomic raising and lowering operators acting on the jth level of atom m. The second term is the Hamiltonian for the electromagnetic (EM) field where the creation and annihilation operators $\hat{a}^{(\dagger)}_{R,k}$ and $\hat{a}^{(\dagger)}_{L,k}$ correspond to the right and left propagating field modes with frequency ω_k along the waveguide, respectively. Moving to the interaction picture with respect to H_0, the atom-field interaction Hamiltonian $\tilde{H}_{AF} \equiv e^{iH_0t/\hbar}H_{AF}\,e^{-iH_0t/\hbar}$ is given by

$$\tilde{H}_{AF} = -\sum_{m=A,B}\sum_{j=2,3}\sum_k \hbar g_{m,j}(\omega_k)\left\{\hat{\sigma}^+_{m,j}\left[\hat{a}_{R,k}e^{ikx_m} + \hat{a}_{L,k}e^{-ikx_m}\right]e^{i(\omega_{j1}-\omega_k)t} + \text{H.c.}\right\} \quad (2)$$

where we have employed the rotating-wave approximation. We remark that the waveguide enables the interaction between two distant atoms via a common set of guided modes, without the $\approx 1/r^3$ reduction of interaction strength as in free space. We further assume that the atom-field coupling strengths for the two atoms are equal such that $g_{A,j}(\omega_k) = g_{B,j}(\omega_k) \equiv g_j(\omega_k)$.

We consider a system where the two atoms initially share a single excitation in level 2 and the EM field is in the vacuum state:

$$|\Psi(0)\rangle = \left(\cos\theta|2\rangle_A|1\rangle_B + e^{i\phi}\sin\theta|1\rangle_A|2\rangle_B\right)\otimes|\{0\}\rangle. \quad (3)$$

We remark that even in the absence of an initial superposition of the levels 2 and 3 there is a second-order coupling between the excited levels due to the emission and absorption of virtual photons. Such a second-order coupling allows for the possibility of the initially unpopulated excited level $|3\rangle$ to emit simultaneously with level $|2\rangle$, resulting in vacuum-induced quantum beats [37], as was recently demonstrated experimentally in [4]. Furthermore, the above initial state readily extends to the more general initial state in the single excitation manifold where a single excitation is shared among any of the excited states and any of the two atoms.

Observing that the interaction Hamiltonian preserves the number of excitations in the atom-field system, we make the following ansatz for the time-evolved state:

$$|\Psi(t)\rangle = \left[\sum_{m=A,B}\sum_{j=2,3}c_{m,j}(t)\hat{\sigma}^+_{m,j} + \sum_k\left\{c_R(\omega_k,t)\hat{a}^\dagger_{R,k} + c_L(\omega_k,t)\hat{a}^\dagger_{L,k}\right\}\right]|1\rangle_A|1\rangle_B|\{0\}\rangle. \quad (4)$$

$c_{m,j}(t)$ denotes the excitation amplitude for the mth atom in the jth level and $c_{R(L)}(\omega_k,t)$ stands for the excitation amplitude for the right (left) propagating field mode of frequency ω_k.

III. COLLECTIVE QUANTUM BEAT DYNAMICS

A. Equations of motion

From the interaction Hamiltonian and the single-excitation ansatz for the total system state [Eqs. (2) and (4)], we obtain the equations of motion for the atomic and field excitation amplitudes as follows:

$$\partial_t c_{m,j}(t) = i\sum_k g_j(\omega_k)e^{i(\omega_{j1}-\omega_k)t} \times\left[c_R(\omega_k,t)e^{ikx_m} + c_L(\omega_k,t)e^{-ikx_m}\right], \quad (5)$$

$$\partial_t c_R(\omega_k,t) = i\sum_{m=A,B}\sum_{j=2,3}g_j(\omega_k)e^{-i(\omega_{j1}-\omega_k)t}c_{m,j}(t)e^{-ikx_m}, \quad (6)$$

$$\partial_t c_L(\omega_k,t) = i\sum_{m=A,B}\sum_{j=2,3}g_j(\omega_k)e^{-i(\omega_{j1}-\omega_k)t}c_{m,j}(t)e^{ikx_m}. \quad (7)$$

One can solve for the atomic dynamics by tracing out the field modes assuming a flat spectral density of the EM field such that $g_j(\omega_k) \approx g_j(\omega_{j1}) \equiv g_j$ to obtain

$$\partial_t c_{m,j}(t) = -\sum_{l=2,3}\frac{\Gamma_{jl}}{2}e^{i\omega_{jl}t}c_{m,l}(t) - \sum_{l=2,3}\frac{\eta\Gamma_{jl}}{2}e^{i\omega_{jl}t}e^{i\omega_{l1}\frac{d}{v}}c_{n,l}\left(t-\frac{d}{v}\right)\Theta\left(t-\frac{d}{v}\right), \quad (8)$$

where the atomic indices n and m are not equal and the generalized decay rate Γ_{jl} is defined as

$$\Gamma_{jl} = \frac{d_{j1}d_{l1}\omega^3_{jl}}{3\pi\epsilon_0\hbar v^3}, \quad (9)$$

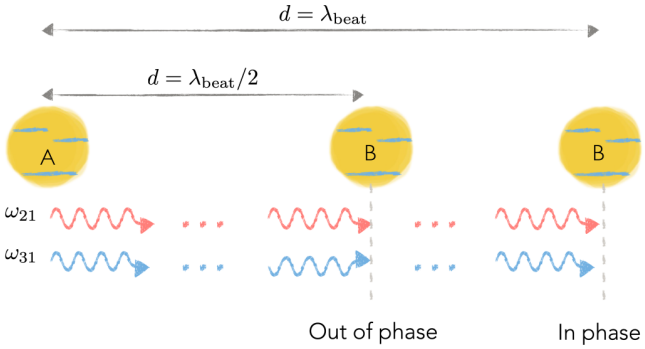

FIG. 2. Schematic representation of the interference between radiation emitted from different atomic transitions for propagation distances of $d = \lambda_{\text{beat}}/2$ and λ_{beat}. The two field modes at different frequencies are in phase right after being emitted and gradually become out of phase as they travel through the waveguide. For a propagation distance of half the beat wavelength, the two modes are exactly out of phase with each other; for a propagation distance equal to the beat wavelength, they become in phase again. Thus, the interatomic distance modulo the beat wavelength determines the interference properties of the radiation emitted from the two transitions.

assuming the transition dipole moments are parallel to each other. We remark that we phenomenologically added the coupling efficiency $\eta \equiv \Gamma_{1D}/\Gamma_{\text{tot}}$, where Γ_{1D} is the decay rate to the waveguide and Γ_{tot} is the total decay rate, in order to account for the decay to the other channels such as free space. The underlying assumption is that spatially separated atoms only interact via guided modes.

One can identify the various processes that contribute to the total collective quantum beat dynamics from Eq. (8) as follows: (1) individual atomic spontaneous emission, corresponding to the terms involving the same atom and same excited level ($n = m$, $j = l$); (2) individual atomic quantum beats, corresponding to the terms involving the same atom and different excited levels ($n = m$, $j \neq l$); (3) collective spontaneous emission, corresponding to the terms with different atoms and same excited levels ($n \neq m$, $j = l$); and (4) collective emission of quantum beats, represented by the interference terms between different atoms and different excited levels ($n \neq m$, $j \neq l$).

The collective atomic and field dynamics is obtained as a combination of the above four processes, exhibiting a rich interplay between different length scales. For example, for a symmetric initial state, (1) when d is a (half-)integer multiple of the transition wavelength λ_{j1}, the photons emitted by the two distant atoms from the respective transitions ($|j\rangle \leftrightarrow |1\rangle$) are in (out of) phase, and (2) when d is a (half-)integer multiple of the beat wavelength λ_{beat}, the two photons of wavelengths λ_{21} and λ_{31} become in (out of) phase at the position of the other atom, as illustrated in Fig. 2.

Furthermore, non-Markovian retardation effects become prominent as the atomic separation becomes comparable to the coherence length of the photons emitted from the atoms. The Markov approximation assumes that the bath correlations decay on a much faster timescale compared to the system relaxation, thus the system evolution only depends on its instantaneous state. In a regime where $d \gtrsim L_c$, the timescale over which the EM field interacts with the delocalized system ($\tau_B \sim d/v$) becomes comparable to the system relaxation timescale ($\tau_R \approx 1/\Gamma_{jj}$). Thus, as $d/v \gtrsim 1/\Gamma_{jj}$, or $\tau_B/\tau_R \gtrsim 1$, it becomes pertinent to include the retardation effects in the EM field mediating the interaction between the two atoms, making the system non-Markovian [32].

B. Atomic dynamics

An arbitrary initial state with a shared single excitation between the two atoms in level $|2\rangle$ [Eq. (3)] can be always decomposed into symmetric($|\psi_+\rangle$) and antisymmetric($|\psi_-\rangle$) states:

$$|\psi_\pm\rangle = \frac{1}{\sqrt{2}}(|2\rangle_A|1\rangle_B \pm |1\rangle_A|2\rangle_B). \tag{10}$$

Thus, we will limit our investigation to the initial states $|\psi_\pm\rangle$. For completeness, the description of a general initial-state case is given in Appendix A.

The time-evolved excitation amplitudes for the two atoms follow the symmetry of the initial state, such that

$$c_{A,j}^{(\pm)}(t) = \pm c_{B,j}^{(\pm)}(t), \tag{11}$$

where the superscripts $+(-)$ correspond to the (anti)symmetric initial states $|\psi_\pm\rangle$. Importantly, we note that the symmetry of the atomic state with respect to both the $|3\rangle \leftrightarrow |1\rangle$ and the $|2\rangle \leftrightarrow |1\rangle$ transitions is the same as the initial symmetry for the $|2\rangle \leftrightarrow |1\rangle$ transition throughout the dynamics.

To simplify the notation, we will drop the atomic labels m, i.e., $c_{A,j}^{(\pm)}(t) \equiv c_j^{(\pm)}(t)$, and focus on the evolution of atom A. From solving the coupled atomic dynamical equations of motion in Eq. (8) by taking a Laplace transform, one obtains the atomic dynamics as the sum of various modes (see Appendix A for details):

$$c_2^{(\pm)}(t) = \sum_{n=-\infty}^{\infty} \alpha_n^{(\pm)} e^{s_n^{(\pm)} t}, \tag{12}$$

$$c_3^{(\pm)}(t) = \sum_{n=-\infty}^{\infty} \beta_n^{(\pm)} e^{\left(s_n^{(\pm)} - i\omega_{23}\right) t}. \tag{13}$$

The coefficients $s_n^{(\pm)}$ and $s_n^{(\pm)} - i\omega_{23}$ denote the characteristic complex eigenfrequencies of the amplitude dynamics for the levels 2 and 3, respectively, and are defined as the poles of the propagator $G^{(\pm)}(s)$:

$$G^{(\pm)}(s) \equiv \Bigg[\left(s - i\omega_{23} + \frac{\Gamma_{33}}{2} \pm \eta\frac{\Gamma_{33}}{2} e^{i\phi_2} e^{-\frac{d}{v}s}\right) \times \left(s + \frac{\Gamma_{22}}{2} \pm \eta\frac{\Gamma_{22}}{2} e^{i\phi_2} e^{-\frac{d}{v}s}\right) - \frac{\Gamma_{23}\Gamma_{32}}{4}\left(1 \pm \eta e^{i\phi_2} e^{-\frac{d}{v}s}\right)^2\Bigg]^{-1}. \tag{14}$$

Here, $\phi_2 = \omega_{21} d/v$ is the propagation phases for the resonant transition frequency ω_{21}. In general, the propagator above has an infinite number of poles, and it is difficult to express the corresponding eigenfrequencies in a closed-form analytical solution. We therefore obtain $s_n^{(\pm)}$ numerically for

a finite number of poles of the propagator $G^{(\pm)}(s_n^{(\pm)})$ with $n \in \{-N, \ldots, N\}$.

The corresponding coefficients $\alpha_n^{(\pm)}$ and $\beta_n^{(\pm)}$ for the nth eigenfrequency are

$$\alpha_n^{(\pm)} = \frac{1}{\sqrt{2}} \lim_{s\to s_n} \frac{s - i\omega_{23} + \frac{\Gamma_{33}}{2} \pm \eta \frac{\Gamma_{33}}{2} e^{i\phi_2} e^{-\frac{d}{v}s}}{\partial_s \left\{[G^{(\pm)}(s)]^{-1}\right\}}, \tag{15}$$

$$\beta_n^{(\pm)} = -\frac{\Gamma_{32}}{2\sqrt{2}} \lim_{s\to s_n} \frac{\left(1 \pm \eta e^{i\phi_2} e^{-\frac{d}{v}s}\right)}{\partial_s \left\{[G^{(\pm)}(s)]^{-1}\right\}}. \tag{16}$$

In the limit where atoms are colocated, the eigenfrequencies given by the poles of the propagator [Eq. (14)] can be solved analytically, and the atomic dynamics corresponds to simple collective quantum beat dynamics without delay. We remark that when the atoms are colocated different atoms may interact via the free space as well as the guided field modes, thus the effective coupling efficiency for this specific case should be set to 1. Generally, when the atoms are close enough so that they may interact through the free space mode, the coupling efficiency should change accordingly. For the symmetric initial state, this yields two solutions: $s^{(+)} = \{-\frac{\Gamma_{22}+\Gamma_{33}}{2} + i\frac{\omega_{23}+\delta}{2}, -\frac{\Gamma_{22}+\Gamma_{33}}{2} + i\frac{\omega_{23}-\delta}{2}\}$ where $\delta = [\omega_{23}{}^2 - (\Gamma_{22} + \Gamma_{33})^2 - 2i\omega_{23}(\Gamma_{22} - \Gamma_{33})]^{\frac{1}{2}}$. In the regime where the excited levels are well separated ($\frac{\Gamma_{ij}}{\omega_{23}} \ll 1$), the atomic dynamics can be simplified as follows:

$$c_2^{(+)}(t) = \frac{1}{\sqrt{2}}\left[e^{-\Gamma_{22}t} - \left(\frac{\Gamma_{32}\Gamma_{23}}{\omega_{23}{}^2}\right)e^{-\Gamma_{33}t}e^{i\omega_{23}t}\right], \tag{17}$$

$$c_3^{(+)}(t) = \frac{i\Gamma_{32}}{\sqrt{2}\omega_{23}}\left[e^{-\Gamma_{33}t} - e^{-\Gamma_{22}t}e^{-i\omega_{23}t}\right]. \tag{18}$$

The dynamics of the amplitude of level 2 is dominated by the collective decay at a rate Γ_{22}, overlaid with a beating term with an amplitude $\Gamma_{32}\Gamma_{23}/\omega_{23}^2 \ll 1$. The initial population in level 3 being zero, the excitations in level 3 arise exclusively from a second-order vacuum-induced coupling between level 2 and level 3. Thus, the decay and the beat terms in $c_3(t)$ have the same amplitude.

For the antisymmetric initial state in the zero-distance case we obtain the complex eigenfrequencies as $s^{(-)} = \{0,\ i\omega_{23}\}$, without any real component or decay. Thus, the system remains in the subradiant state with no evolution of the corresponding atomic coefficients: $c_2^{(-)}(t) = \frac{1}{\sqrt{2}}$, $c_3^{(-)}(t) = 0$.

C. Field dynamics

While the atomic dynamics provides physical intuition, it cannot be measured directly in experiments. Instead, one measures the intensity of the light emitted from the system, which carries indirect information about the atomic dynamics. The intensity emitted by the atomic system is given by $I(x,t) = \frac{\epsilon_0 c}{2}\langle\psi(t)|\hat{E}^\dagger(x,t)\hat{E}(x,t)|\psi(t)\rangle$, with the electric-field operator defined as $\hat{E}(x,t) = \int_0^\infty dk \mathcal{E}_k[\hat{a}_{R,k}e^{ikx} + \hat{a}_{L,k}e^{-ikx}]e^{-i\omega_k t}$. This can be calculated explicitly as follows (see Appendix B for details):

$$I(x,t)/I_0 = \left|\sum_{j=2,3}\sum_{m=A,B}\frac{g_j}{g_2}\left\{\underbrace{c_{m,j}\left(t - \frac{x-x_m}{v}\right)e^{-i\omega_{j1}\left(t-\frac{x-x_m}{v}\right)}\left[\Theta\left(t - \frac{x-x_m}{v}\right) - \Theta\left(-\frac{x-x_m}{v}\right)\right]}_{\text{Right light cone for atom } m \text{ at frequency } \omega_{j1}}\right.\right.$$
$$\left.\left. + \underbrace{c_{m,j}\left(t + \frac{x-x_m}{v}\right)e^{-i\omega_{j1}\left(t+\frac{x-x_m}{v}\right)}\left[\Theta\left(t + \frac{x-x_m}{v}\right) - \Theta\left(\frac{x-x_m}{v}\right)\right]}_{\text{Left light cone for atom } m \text{ at frequency } \omega_{j1}}\right\}\right|^2. \tag{19}$$

The first and second terms in the above expression appear in terms of $t \pm (x - x_m)/v$, corresponding to the light cone emitted by atom m at frequency ω_{j1} towards right and left, respectively. Before the two light cones meet, the atoms are causally disconnected and emit independently. As each atom "sees" the other atom, the interference between the light cones at the two transition frequencies emitted by the two atoms leads to collective quantum beat dynamics.

The intensity measured outside the system ($x < x_A$ or $x > x_B$) can be expressed in a further simplified form by taking the limit $x \to x_B^+$ and making use of the system eigenfrequencies:

$$I(t)/I_0 = \left|\sum_n \left(\alpha_n^{(\pm)} + \frac{g_3}{g_2}\beta_n^{(\pm)}\right)\right.$$
$$\left.\times \left(\Theta(t) \pm e^{-s_n^{(\pm)}d/v}\Theta(t - d/v)\right)e^{s_n^{(\pm)}t}\right|^2. \tag{20}$$

From the above expression we note that quantum beats result from the interference of the modes with different frequencies, such that $\mathrm{Im}s_n^{(\pm)} \neq \mathrm{Im}s_m^{(\pm)}$. In particular, collective quantum beats originate from the interference between the fields emitted by the two atoms at different frequencies for $t > d/v$. The collective beat amplitude has a distance dependence as can be seen from the prefactor $e^{-s_n^{(\pm)}d/v}$, which corresponds to the difference in phase and amplitude for various field modes as they propagate between the two atoms.

In the limit of two coincident atoms ($d \to 0$), the intensity measured at $x \to x_B^+$ is

$$I(t)/I_0 = \left|c_{A2}(t) + \frac{g_3}{g_2}c_{A3}(t)e^{i\omega_{23}t}\right.$$
$$\left. + c_{B2}(t) + \frac{g_3}{g_2}c_{B3}(t)e^{i\omega_{23}t}\right|^2\Theta(t). \tag{21}$$

TABLE I. Summary of parameters used in calculations, based on typical values in a superconducting circuit setup. The frequencies are in the units of Γ_{22}, and the lengths are in units of v/Γ_{22}.

Decay rate of level 3 (Γ_{33}/Γ_{22})	1
Energy separation of level 2 and 3 (ω_{23}/Γ_{22})	50
Resonant frequency of level 2 (ω_{21}/Γ_{22})	10^4
Coherence length ($L_c \times \Gamma_{22}/v$)	1
Beat wavelength ($\lambda_{\text{beat}} \times \Gamma_{22}/v$)	$4\pi \times 10^{-2}$
Transition wavelength ($\lambda_{21} \times \Gamma_{22}/v$)	$2\pi \times 10^{-4}$

For the antisymmetric initial state where $c_{A2}(t) = -c_{B2}(t)$ and $c_{A3}(t) = -c_{B3}(t)$, the total emitted intensity vanishes, as expected for a Dicke subradiant state.

For a symmetric initial state where $c_{A2}(t) = c_{B2}(t)$ and $c_{A3}(t) = c_{B3}(t)$, the emitted intensity is four times that of a single three-level atom, corresponding to standard Dicke superradiance. Plugging in Eqs. (17) and (18) into Eq. (21), one gets

$$I(t)/I_0 = e^{-2\Gamma_{22}t} + \frac{\Gamma_{33}}{\Gamma_{22}}\left(\frac{\Gamma_{23}\Gamma_{32}}{{\omega_{23}}^2}\right)e^{-2\Gamma_{33}t} - 2\frac{\Gamma_{23}\Gamma_{32}}{\omega_{23}\Gamma_{22}}\sin(\omega_{23}t)e^{-(\Gamma_{22}+\Gamma_{33})t}, \quad (22)$$

using the relation ${g_j}^2 \propto \Gamma_{jj}$. The first two terms correspond to spontaneous emission from levels 2 and 3, and the third term represents quantum beats. The above expression is in agreement with the collective quantum beat dynamics from coincident atoms as previously obtained in [4].[1]

IV. DISTANCE DEPENDENCE OF COLLECTIVE QUANTUM BEAT DYNAMICS

We now present the system dynamics for a specific implementation of the model in a superconducting circuit setup as an example [21,38], with parameters described in Table I. As superconducting circuits allow for both a strong enough coupling between the emitters and field, as well as a precise control of emitter positions, the parameters can be preferentially chosen to best observe the collective quantum beat dynamics. For example, the ratio $\sim\Gamma_{23}/\omega_{23}$ can be sufficiently large so that the vacuum-induced coupling between the excited levels results in sizable quantum beats [Eq. (22)]. Unlike in the case of optical frequencies, the transition wavelengths being in the microwave regime enables a precise enough positioning of emitters such that one can realize the desired separations needed to observe various interference phenomena in collective quantum beats. Also, the ratio of the characteristic wavelengths (transition and beat wavelengths) to the coherence length, while being small, is still substantial enough compared to optical regimes to allow one to access both the Markovian and non-Markovian regimes of the system dynamics with a small variation of the emitter separation d. We note that, as long as the parameters are carefully chosen regarding the above requirements, the various interference properties of collective quantum beats should appear in any multilevel quantum system.

In particular we discuss the dependence of the collective system dynamics on atomic separation across two different regimes wherein (1) $d \ll L_c$ (Markovian regime) and (2) $d \gtrsim L_c$ (non-Markovian regime). In each of these regimes, we analyze the system dynamics for the symmetric and antisymmetric initial states of the two artificial atoms [Eq. (10)], considering interatomic separations of integer and half-integer multiples of the beat wavelength. For simplicity we assume that d is an integer multiple of λ_{21}. While the initial state determines the total collective spontaneous emission, the interatomic distance modulo the beat wavelength determines the interference properties of the collective quantum beats, as discussed in Sec. III A.

A. Markovian regime

We study the dynamics of atomic excitation probabilities and the field intensity for interatomic separations of $d = \{\lambda_{\text{beat}}, \lambda_{\text{beat}}/2\} \ll L_c$. We numerically calculate the poles of Eq. (14) for $|\text{Re}[s_n^{(j,\pm)}]| < 200\,\Gamma_{22}$ and $|\text{Im}[s_n^{(j,\pm)}]| < 200\,\omega_{23}$. Including sufficient high-frequency modes allows one to correctly capture the dynamics of the system for the timescales of interest (see Appendix C for details).

Figure 3 depicts the atomic and field dynamics for initial symmetric and antisymmetric states of the two atoms. We note that the onset of collective dynamics happens at $d = \lambda_{\text{beat}}$ or $\frac{1}{2}\lambda_{\text{beat}}$ depending on the interatomic separation as indicated by the vertical dash-dotted lines. Figures 3(a) and 3(b) illustrate the level 2 population dynamics which exhibits a super(sub)radiant decay for (anti)symmetric initial states. It can be seen from Eq. (17) that the amplitude of the beat term is smaller compared to that of the individual decay in level 2 dynamics by a factor of $\Gamma_{23}\Gamma_{32}/{\omega_{23}}^2 \ll 1$. Thus, we do not see any visible beats in the level 2 population curves.

More interestingly, Figs. 3(c) and 3(d) illustrate the collective quantum beat effect as seen in the level 3 population dynamics. We note that for an interatomic separation of $d = \lambda_{\text{beat}}$ there is a collective enhancement of the quantum beats for the symmetric initial state, and suppression for the antisymmetric initial state as denoted in Fig. 3(c). For this separation, the phase of the field modes mediating the interaction between the atoms is an even integer multiple of 2π such that $\omega_{21}d/v = 2n\pi$, $\omega_{31}d/v = 2m\pi$ ($\{n, m\} \in \mathbb{N}$). Furthermore, the total atomic state is (anti)symmetric with respect to the $|3\rangle \leftrightarrow |1\rangle$ transition for an initial (anti)symmetric state with respect to the $|2\rangle \leftrightarrow |1\rangle$ transition. Thus, we observe an enhancement or suppression of the quantum beats for an initial symmetric or antisymmetric state, respectively. More specifically, it can be seen that the amplitude of the first peak of the collective "superradiant" quantum beats (solid blue) is enhanced roughly by a factor of $\approx$4.1 in comparison with the

[1]While, strictly speaking, the experiment in [4] corresponds to a timed Dicke state of a finite-sized ensemble, it can be approximated well by a symmetric state of coincident atoms. Such an assumption is valid in the limit where the ensemble size ($\approx$2 mm) is much smaller compared to the beat wavelength ($\approx$2.5 m). We further remark that the dynamics of a timed Dicke state of atoms separated by a distance comparable to λ_{beat} is different from that of the symmetric state of coincident atoms because every $\frac{1}{2}\lambda_{\text{beat}}$ the photons of two different frequencies would be out of phase.

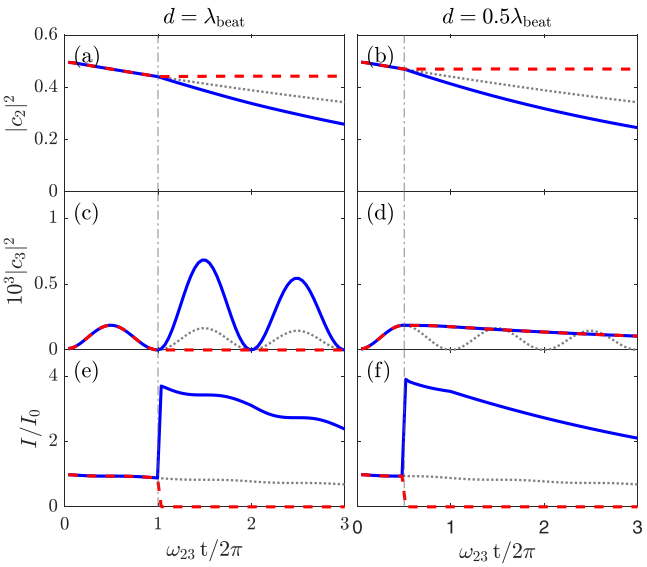

FIG. 3. Atom-field dynamics in the Markovian regime: (a), (b) level 2 dynamics, (c), (d) level 3 dynamics, and (e), (f) field dynamics measured at $x \to x_B^+$ for interatomic separations (a), (c), (e) $d = \lambda_{\text{beat}}$ and (b), (d), (f) $d = \frac{1}{2}\lambda_{\text{beat}}$. The solid blue curves are for the symmetric initial state, and the dashed red curves are for the antisymmetric initial state. The vertical dash-dotted lines indicate the times when the field emitted from one atom reaches the other atom. For comparison the single atom dynamics is drawn with the dotted gray lines. The level 3 population is scaled by a factor of 10^3 for clarity of illustration.

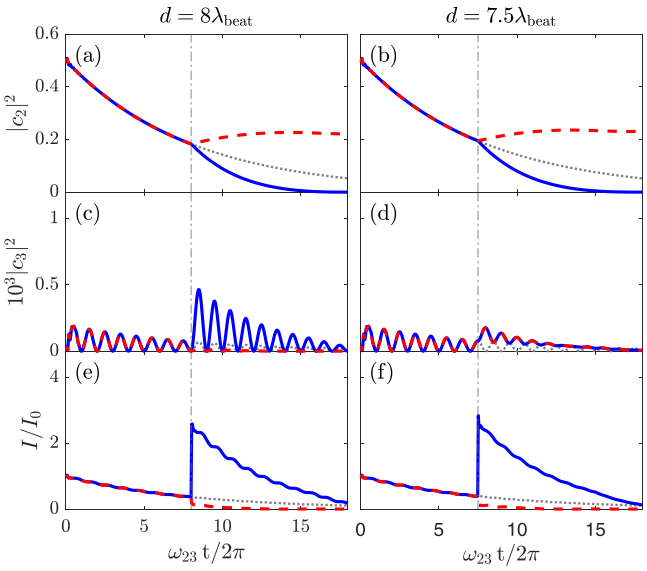

FIG. 4. Non-Markovian regime: (a), (b) level 2 dynamics, (c), (d) level 3 dynamics, and (e), (f) field dynamics measured at $x \to x_B^+$ for interatomic separations (a), (c), (e) $d = 8\lambda_{\text{beat}}$ and (b), (d), (f) $d = 7.5\lambda_{\text{beat}}$. The solid blue curves are for the symmetric initial state, and the dashed red curves are for the antisymmetric initial state. The vertical dashed-dotted lines indicate the times when the field emitted from one atom reaches the other atom. For comparison the single atom dynamics is drawn with the dotted gray lines. The level 3 population is scaled by a factor of 10^3.

independent emission case (dotted gray). In contrast, it can be seen in Fig. 3(d) that for a separation of $d = \lambda_{\text{beat}}/2$ the resulting beats are suppressed as a result of the destructive interference between the fields emitted from the two atoms at ω_{21} and ω_{31}, as illustrated in Fig. 2.

In Figs. 3(e) and 3(f), the intensity of the light measured outside the system is depicted. The radiated intensity, as given by Eq. (19), is governed by the interference between the atomic excitation amplitudes. For the (anti)symmetric initial state, the overall emission is superradiant (subradiant). For the case of superradiant emission, the size of the beat is enhanced (suppressed) for an atomic separation of $d = \lambda_{\text{beat}}$ ($d = \frac{1}{2}\lambda_{\text{beat}}$), in agreement with the collective atomic dynamics.

B. Non-Markovian regime

We now consider the case wherein the atomic separations are comparable to the coherence length of the emitted photons, with $d = 7.5\lambda_{\text{beat}} \approx 0.94L_c$ and $8\lambda_{\text{beat}} \approx L_c$. We note that for such large separations the retardation effects of the waveguide field become relevant, rendering the system dynamics non-Markovian. We calculate the dynamics numerically by obtaining the characteristic system frequencies as the poles of the propagator Eq. (14) within $|\text{Re}[s_n^{(j,\pm)}]| < 10\,\Gamma_{22}$ and $|\text{Im}[s_n^{(j,\pm)}]| < 10\,\omega_{23}$ (see Appendix C for details).

The atomic and field dynamics for this regime is shown in Fig. 4 for the initial symmetric and antisymmetric states. The level 2 dynamics for a symmetric initial state as denoted by the solid blue curves in Figs. 4(a) and 4(b) exhibits collective emission rates faster than standard Dicke superradiance, which is termed "superduperradiance" (see Appendix D for comparison of decay profiles of superduperradiance and Dicke superradiance), similar to the non-Markovian collective dynamics for a system of two two-level atoms [29,32,39]. Such an enhancement of the collective decay rate can be understood by considering the atomic collective emission in terms of a mutually stimulated emission process wherein each atomic dipole is stimulated by the field emitted by the other atom [31,40]. As each atom emits into the waveguide, there is a probability amplitude associated with the emitted field reaching the other atom—in the presence of delay this amplitude increases with the atomic separation, causing an enhancement in the instantaneous rate of collective emission beyond regular superradiance. For an antisymmetric initial state (dashed red curves), one can see the formation of delocalized atom-photon bound states in continuum in agreement with previous studies in delocalized two-level emitters [33,34]. Such atom-photon bound states arise as a result of the destructive interference between the atomic dipole and the fields emitted by each of the atoms, which causes the fields to be reflected as they interact with the atoms.

The effects of retardation on collective quantum beats are illustrated in the population dynamics of level 3 in Figs. 4(c) and 4(d). For an interatomic separation $d = 8\lambda_{\text{beat}}$ as seen in Fig. 4(c), we observe an enhancement of the quantum beats for a symmetric initial state and moderate suppression of beats for the antisymmetric initial state. Furthermore, comparing the first peak of the collective quantum beats (solid blue)

with that of the independent decay (dotted gray) shows an enhancement beyond the Markovian case by roughly a factor of ≈6.8. For a separation of $d = 7.5\lambda_{\text{beat}}$ as illustrated in Fig. 4(d), the population dynamics of level 3 for both the initial symmetric and antisymmetric cases exhibits beating in addition to an exponential decay.

The light intensity measured outside the system is depicted in Figs. 4(e) and 4(f). The symmetric initial state exhibits an overall exponential decay faster than Dicke superradiance, with an overlaid beating that is enhanced (suppressed) for a separation $d = 8\lambda_{\text{beat}}$ ($d = 7.5\lambda_{\text{beat}}$). The antisymmetric initial state shows a suppressed total emission outside the system, indicating that most of the light is trapped in between the atoms forming a delocalized atom-photon bound state. We note that the atom-photon bound state in this case has a larger photonic amplitude than in the Markovian case. However, there is a finite emission into the field modes from the otherwise subradiant state, indicating existence of additional modes in a non-Markovian regime that provide channels for the atomic excitations to decay away. Such modes have been previously investigated in the context of the steady-state atomic spectrum emitted from two distant two-level atoms [31].

V. DISCUSSION

In this paper we have demonstrated the distance-dependent dynamics of collective quantum beats, resulting from the interference between the radiation emitted from a collection of multilevel atoms coupled to a waveguide. Considering a system of two V-type three-level atoms interacting via a waveguide, we show that the coherent interference between the spontaneous emission from different excited levels of the two atoms results in a collective quantum beat phenomenon [4] (Sec. II). We find that the distance between the atoms modulo the beat wavelength (d/λ_{beat}) is critical in determining the interference properties of such collective quantum beats: the emitted fields at the two transition frequencies go from interfering constructively to interfering destructively for $d = n\lambda_{\text{beat}}$ to $(n + 1/2)\lambda_{\text{beat}}$ (Fig. 2). We obtain the collective dynamics of the total atom-field system by analyzing the system in terms of its characteristic complex eigenfrequencies determined by the poles of the system propagator (Sec. III). In the limit $d \to 0$ our results agree with the recent experimental investigations of vacuum-induced collective quantum beats from a small sample, which could be approximately considered as a system of coincident atoms [4]. A general analysis of the collective atomic and field dynamics as a function of the interatomic separation and the initial atomic states is presented in Sec. IV. We find that while the atomic separation modulo the transition wavelength in conjunction with the symmetry properties of the initial state governs the overall collective spontaneous emission the length scale λ_{beat} governs the collective nature of the quantum beats. We further investigate the non-Markovian dynamics of collective quantum beats in Sec. IV B. As the system size become comparable to the coherence length of the emitted photons ($d \sim v/\Gamma$), there can be significant retardation effects in the field mediating the interaction between the atoms, rendering the system dynamics non-Markovian. In such a regime, we find that the collective quantum beats can exhibit a non-Markovian enhancement beyond superradiant quantum beats arising in the Markovian regime, as illustrated in Fig. 4.

The results presented in this paper open directions for investigating and controlling radiation from multilevel atomic systems coupled to waveguides. Quantum beats are relevant to precision time-resolved spectroscopy measurements [5]; a collective enhancement of quantum beats can improve sensitivities of such measurements. It would be pertinent to extend the present model to a system of N atoms for characterizing the metrological advantage offered by the collective nature of quantum beats.

Furthermore, collections of quantum emitters coupled to waveguides are a paradigmatic system for implementation of quantum networks and long-distance quantum communication protocols. It has been shown that collective multilevel atomic systems offer a higher-dimensional entangled state space, enabling efficient quantum memories [41] and secure quantum communication [42–44]. Our analysis is relevant to such schemes, with a consideration of retardation effects, which can be significant in distributed quantum information processing.

ACKNOWLEDGMENTS

We thank Pablo Solano, Mohammad Hafezi, and Deniz Kurdak for helpful discussions. This research was supported by the Maryland ARL Quantum Partnership (Grant No. W911NF-19-2-0181) and Joint Quantum Institute (Grant No. 70NANB16H168).

APPENDIX A: ATOMIC DYNAMICS

We can solve the coupled atomic equations of motion [Eq. (8)] by using Laplace transformation. Defining Laplace-transformed coefficients, $\tilde{c}_{m,j}(s) \equiv \int_0^\infty c_{m,j}(t)e^{-st}dt$, Eq. (8) reads

$$\partial_t c_{m,j}(t) = -\sum_{l=2,3} \frac{\Gamma_{jl}}{2}\tilde{c}_{m,l}(s - i\omega_{jl}) - \sum_{l=2,3} \frac{\eta\Gamma_{jl}}{2} e^{-\frac{d}{v}(s-i\omega_{j1})}\tilde{c}_{n,l}(s - i\omega_{jl}), \tag{A1}$$

where $m \neq n$. Setting the initial-state condition [Eq. (3)], we get the coupled equations in Laplace space:

$$s\tilde{c}_{A2}(s) = \cos\theta - \frac{\Gamma_{22}}{2}\tilde{c}_{A2}(s) - \frac{\Gamma_{23}}{2}\tilde{c}_{A3}(s - i\omega_{23}) - \frac{\Gamma_{22}}{2}\eta e^{i\phi_2}e^{-\frac{d}{v}s}\tilde{c}_{B2}(s) - \frac{\Gamma_{23}}{2}\eta e^{i\phi_2}e^{-\frac{d}{v}s}\tilde{c}_{B3}(s - i\omega_{23}), \tag{A2a}$$

$$s\tilde{c}_{B2}(s) = e^{i\phi}\sin\theta - \frac{\Gamma_{22}}{2}\eta e^{i\phi_2}e^{-\frac{d}{v}s}\tilde{c}_{A2}(s) - \frac{\Gamma_{23}}{2}\eta e^{i\phi_2}e^{-\frac{d}{v}s}\tilde{c}_{A3}(s - i\omega_{23}) - \frac{\Gamma_{22}}{2}\tilde{c}_{B2}(s) - \frac{\Gamma_{23}}{2}\tilde{c}_{B3}(s - i\omega_{23}), \tag{A2b}$$

$$s\tilde{c}_{A3}(s) = -\frac{\Gamma_{32}}{2}\tilde{c}_{A2}(s+i\omega_{23}) - \frac{\Gamma_{33}}{2}\tilde{c}_{A3}(s) - \frac{\Gamma_{32}}{2}\eta e^{i\phi_3}e^{-\frac{d}{v}s}\tilde{c}_{B2}(s+i\omega_{23}) - \frac{\Gamma_{33}}{2}\eta e^{i\phi_3}e^{-\frac{d}{v}s}\tilde{c}_{B3}(s), \tag{A2c}$$

$$s\tilde{c}_{B3}(s) = -\frac{\Gamma_{32}}{2}\eta e^{i\phi_3}e^{-\frac{d}{v}s}\tilde{c}_{A2}(s+i\omega_{23}) - \frac{\Gamma_{33}}{2}\eta e^{i\phi_3}e^{-\frac{d}{v}s}\tilde{c}_{A3}(s) - \frac{\Gamma_{32}}{2}\tilde{c}_{B2}(s+i\omega_{23}) - \frac{\Gamma_{33}}{2}\tilde{c}_{B3}(s). \tag{A2d}$$

Here, $\phi_j = \omega_{j1}d/v$ is the general propagation phase for a photon of frequency ω_{j1}. First solving for $\tilde{c}_{A2}(s)$ and $\tilde{c}_{B2}(s)$, we get

$$\tilde{c}_{A2}(s) = \frac{\cos\theta\, A(s) - e^{i\phi}\sin\theta\, B(s)}{C(s)},$$
$$\tilde{c}_{B2}(s) = \frac{e^{i\phi}\sin\theta\, A(s) - \cos\theta\, B(s)}{C(s)}, \tag{A3}$$

where $A(s)$, $B(s)$, $C(s)$, and $D(s)$ are defined as

$$\begin{aligned}
A(s) &= \left(s - i\omega_{23} + \frac{\Gamma_{33}}{2}\right)\left[\left(s+\frac{\Gamma_{22}}{2}\right)\left(s - i\omega_{23} + \frac{\Gamma_{33}}{2}\right) - \frac{\Gamma_{23}\Gamma_{32}}{4}\right] \\
&\quad - \eta^2 e^{2i\phi_2}e^{-2\frac{d}{v}s}\left[\left(\frac{\Gamma_{33}}{2}\right)^2\left(s+\frac{\Gamma_{22}}{2}\right) + \frac{\Gamma_{23}\Gamma_{32}}{4}\left(s - i\omega_{23} - \frac{\Gamma_{33}}{2}\right)\right], \\
B(s) &= \eta e^{i\phi_2}e^{-\frac{d}{v}s}\left[\frac{\Gamma_{22}}{2}\left(s - i\omega_{23} + \frac{\Gamma_{33}}{2}\right)^2 - \frac{\Gamma_{23}\Gamma_{32}}{4}\left(2s - 2i\omega_{23} + \frac{\Gamma_{33}}{2}\right)\right] - \eta^3 e^{3i\phi_2}e^{-3\frac{d}{v}s}\frac{\Gamma_{33}}{2}\left[\frac{\Gamma_{22}\Gamma_{33}}{4} - \frac{\Gamma_{23}\Gamma_{32}}{4}\right], \\
C(s) &= \left[\left(s - i\omega_{23} + \frac{\Gamma_{33}}{2} + \frac{\Gamma_{33}}{2}\eta e^{i\phi_2}e^{-\frac{d}{v}s}\right)\left(s + \frac{\Gamma_{22}}{2} + \frac{\Gamma_{22}}{2}\eta e^{i\phi_2}e^{-\frac{d}{v}s}\right) - \frac{\Gamma_{23}\Gamma_{32}}{4}\left(1+\eta e^{i\phi_2}e^{-\frac{d}{v}s}\right)^2\right] \\
&\quad \times \left[\left(s - i\omega_{23} + \frac{\Gamma_{33}}{2} - \frac{\Gamma_{33}}{2}\eta e^{i\phi_2}e^{-\frac{d}{v}s}\right)\left(s + \frac{\Gamma_{22}}{2} - \frac{\Gamma_{22}}{2}\eta e^{i\phi_2}e^{-\frac{d}{v}s}\right) - \frac{\Gamma_{23}\Gamma_{32}}{4}\left(1-\eta e^{i\phi_2}e^{-\frac{d}{v}s}\right)^2\right].
\end{aligned} \tag{A4}$$

Then $\tilde{c}_{A3}(s)$ and $\tilde{c}_{B3}(s)$ are obtained in terms of $\tilde{c}_{A2}(s)$ and $\tilde{c}_{B2}(s)$:

$$\begin{aligned}
\tilde{c}_{A3}(s) &= -\frac{\Gamma_{32}}{2}\frac{\left(s + \frac{\Gamma_{33}}{2} - \frac{\Gamma_{33}}{2}\eta^2 e^{2i\phi_3}e^{-2\frac{d}{v}s}\right)\tilde{c}_{A2}(s+i\omega_{23}) + s\eta e^{i\phi_3}e^{-\frac{d}{v}s}\tilde{c}_{B2}(s+i\omega_{23})}{\left(s+\frac{\Gamma_{33}}{2}\right)^2 - \left(\frac{\Gamma_{33}}{2}\right)^2\eta^2 e^{2i\phi_3}e^{-2\frac{d}{v}s}}, \\
\tilde{c}_{B3}(s) &= -\frac{\Gamma_{32}}{2}\frac{s\eta e^{i\phi_3}e^{-\frac{d}{v}s}\tilde{c}_{A2}(s+i\omega_{23}) + \left(s + \frac{\Gamma_{33}}{2} - \frac{\Gamma_{33}}{2}\eta^2 e^{2i\phi_3}e^{-2\frac{d}{v}s}\right)\tilde{c}_{B2}(s+i\omega_{23})}{\left(s+\frac{\Gamma_{33}}{2}\right)^2 - \left(\frac{\Gamma_{33}}{2}\right)^2\eta^2 e^{2i\phi_3}e^{-2\frac{d}{v}s}}.
\end{aligned} \tag{A5}$$

We first numerically find the poles s_n of the denominators in Eqs. (A3) and (A5), with each pole representing a complex eigenfrequency of the system. The excitation amplitude $\tilde{c}(s)$ in Laplace space is expressed in terms of its modes:

$$\tilde{c}(s) = \sum_n \frac{w_n}{s - s_n}, \tag{A6}$$

where $w_n = \lim_{s\to s_n}(s - s_n)\tilde{c}(s)$.

In this paper we consider two specific initial states: a symmetric and antisymmetric superposition of a single excitation in level 2. For the symmetric initial state, i.e., $\theta = \pi/4$ and $\phi = 0$,

$$\tilde{c}_{A2}(s) = \tilde{c}_{B2}(s) = \frac{1}{\sqrt{2}}\frac{s - i\omega_{23} + \frac{\Gamma_{33}}{2} + \frac{\Gamma_{33}}{2}\eta e^{i\phi_2}e^{-\frac{d}{v}s}}{\left(s - i\omega_{23} + \frac{\Gamma_{33}}{2} + \frac{\Gamma_{33}}{2}\eta e^{i\phi_2}e^{-\frac{d}{v}s}\right)\left(s + \frac{\Gamma_{22}}{2} + \frac{\Gamma_{22}}{2}\eta e^{i\phi_2}e^{-\frac{d}{v}s}\right) - \frac{\Gamma_{23}\Gamma_{32}}{4}(1+\eta e^{i\phi_2}e^{-\frac{d}{v}s})^2}, \tag{A7}$$

$$\tilde{c}_{A3}(s) = \tilde{c}_{B3}(s) = -\frac{\Gamma_{32}}{2\sqrt{2}}\frac{1 + \eta e^{i\phi_3}e^{-\frac{d}{v}s}}{\left(s + \frac{\Gamma_{33}}{2} + \frac{\Gamma_{33}}{2}\eta e^{i\phi_3}e^{-\frac{d}{v}s}\right)\left(s + i\omega_{23} + \frac{\Gamma_{22}}{2} + \frac{\Gamma_{22}}{2}\eta e^{i\phi_3}e^{-\frac{d}{v}s}\right) - \frac{\Gamma_{23}\Gamma_{32}}{4}(1+\eta e^{i\phi_3}e^{-\frac{d}{v}s})^2}. \tag{A8}$$

Note that the denominators in Eqs. (A7) and (A8) are the same up to a constant shift of the Laplace variable $s \to s + i\omega_{23}$.

Similarly, for an antisymmetric initial state, i.e., $\theta = \pi/4$ and $\phi = \pi$,

$$\tilde{c}_{A2}(s) = -\tilde{c}_{B2}(s) = \frac{1}{\sqrt{2}}\frac{s - i\omega_{23} + \frac{\Gamma_{33}}{2} - \frac{\Gamma_{33}}{2}\eta e^{i\phi_2}e^{-\frac{d}{v}s}}{\left(s - i\omega_{23} + \frac{\Gamma_{33}}{2} - \frac{\Gamma_{33}}{2}\eta e^{i\phi_2}e^{-\frac{d}{v}s}\right)\left(s + \frac{\Gamma_{22}}{2} - \frac{\Gamma_{22}}{2}\eta e^{i\phi_2}e^{-\frac{d}{v}s}\right) - \frac{\Gamma_{23}\Gamma_{32}}{4}(1-\eta e^{i\phi_2}e^{-\frac{d}{v}s})^2}, \tag{A9}$$

$$\tilde{c}_{A3}(s) = -\tilde{c}_{B3}(s) = -\frac{\Gamma_{32}}{2\sqrt{2}}\frac{1 - \eta e^{i\phi_3}e^{-\frac{d}{v}s}}{\left(s + \frac{\Gamma_{33}}{2} - \frac{\Gamma_{33}}{2}\eta e^{i\phi_3}e^{-\frac{d}{v}s}\right)\left(s + i\omega_{23} + \frac{\Gamma_{22}}{2} - \frac{\Gamma_{22}}{2}\eta e^{i\phi_3}e^{-\frac{d}{v}s}\right) - \frac{\Gamma_{23}\Gamma_{32}}{4}(1-\eta e^{i\phi_3}e^{-\frac{d}{v}s})^2}. \tag{A10}$$

Similar to the symmetric case, the denominators on the right-hand sides of Eqs. (A9) and (A10) are the same up to a Laplace variable shift of $s \to s + i\omega_{23}$ as well.

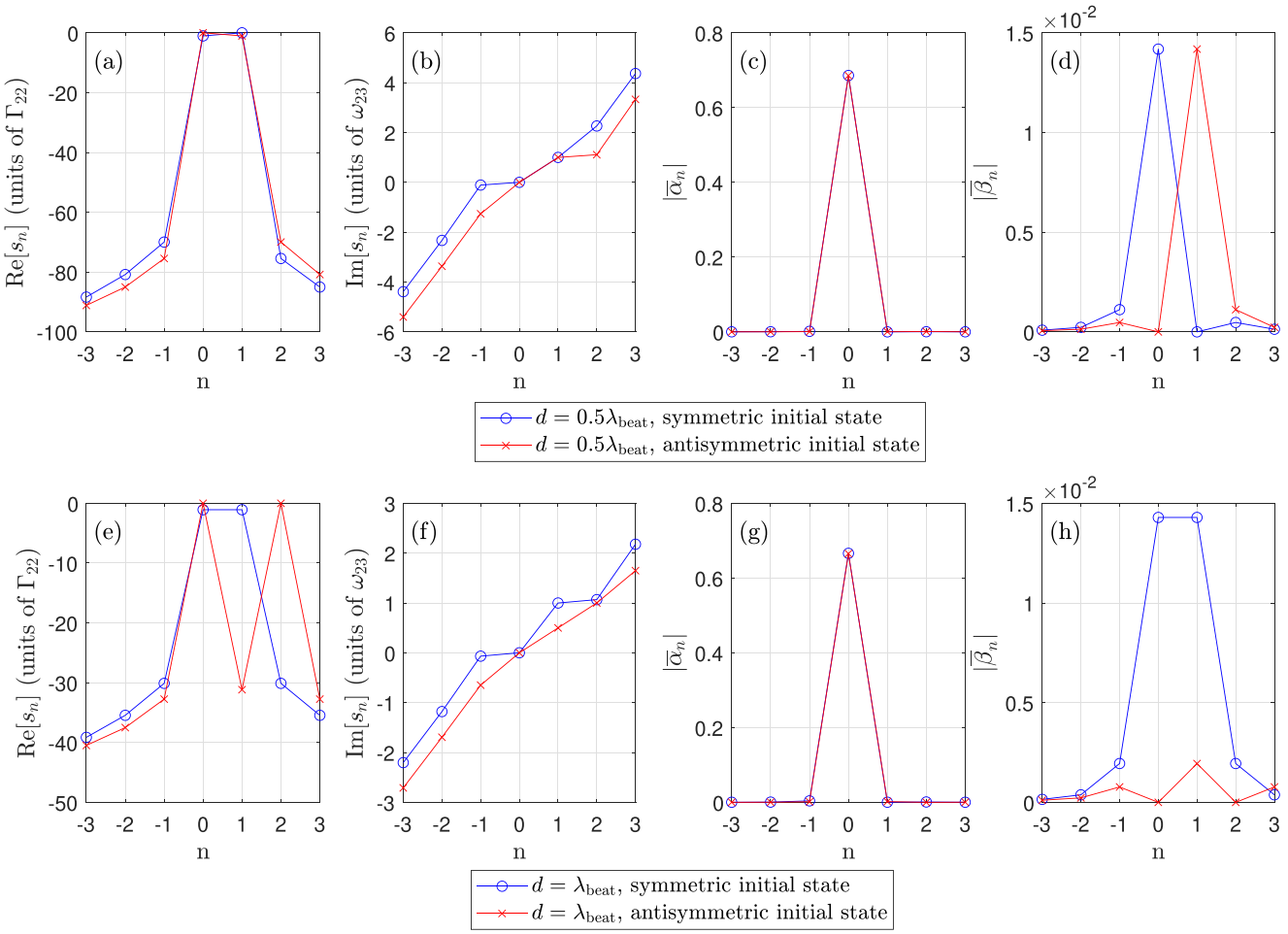

FIG. 5. Markovian regime: The poles and the corresponding coefficients for symmetric (blue circle) and antisymmetric (red x) initial states, for the separation of (a)–(d) $d = 0.5\,\lambda_{\text{beat}}$ and (e)–(h) $d = \lambda_{\text{beat}}$. (a), (e) The real part of the poles corresponds to the decay rate of each mode in units of Γ_{22} and (b), (f) the imaginary part corresponds to the frequency of the modes in units of ω_{23}. (c), (g) The coefficient $\overline{\alpha}_n$ shows the contribution of each pole to the level 2 dynamics and (d), (h) the coefficient $\overline{\beta}_n$ shows the contribution to the level 3 dynamics.

We remark that the dynamics of a general initial state in the single excitation manifold $|\Psi(0)\rangle = K_{2A}|2\rangle_A|1\rangle_B + K_{2B}|1\rangle_A|2\rangle_B + K_{3A}|3\rangle_A|1\rangle_B + K_{3B}|1\rangle_A|3\rangle_B$, with $|K_{2A}|^2 + |K_{2B}|^2 + |K_{3A}|^2 + |K_{3B}|^2 = 1$, can be obtained directly from our result. An initial excitation in $|3\rangle_A(|3\rangle_B)$ would follow the same dynamics as for the case of an initial excitation in $|2\rangle_A(|2\rangle_B)$, given by Eqs. (12) and (13), with the following substitutions:

$$\omega_{23} \leftrightarrow -\omega_{23},$$
$$\Gamma_{22} \leftrightarrow \Gamma_{33},$$
$$\Gamma_{23} \leftrightarrow \Gamma_{32}.$$

APPENDIX B: FIELD INTENSITY DYNAMICS

We consider the dynamics of the intensity radiated by the atoms as follows:

$$I(x,t) = \frac{\epsilon_0 c}{2}\langle\Psi(t)|\left[\int_0^\infty dk_1 \mathcal{E}^*_{k_1}\left\{\hat{a}^\dagger_{R,k_1}e^{-ik_1x} + \hat{a}^\dagger_{L,k_1}e^{ik_1x}\right\}e^{i\omega_1 t}\right]\left[\int_0^\infty dk_2 \mathcal{E}_{k_2}\left\{\hat{a}_{R,k_2}e^{ik_2x} + \hat{a}_{L,k_2}e^{-ik_2x}\right\}e^{-i\omega_2 t}\right]|\Psi(t)\rangle$$
$$= \frac{\epsilon_0 c|\mathcal{E}_0|^2}{2}\left|\int_0^\infty dk\left[c_R(\omega_k,t)e^{ikx} + c_L(\omega_k,t)e^{-ikx}\right]e^{-i\omega_k t}\right|^2, \tag{B1}$$

where we have assumed that $\mathcal{E}_k \approx \mathcal{E}_0$ to be constant near the atomic resonance frequency.

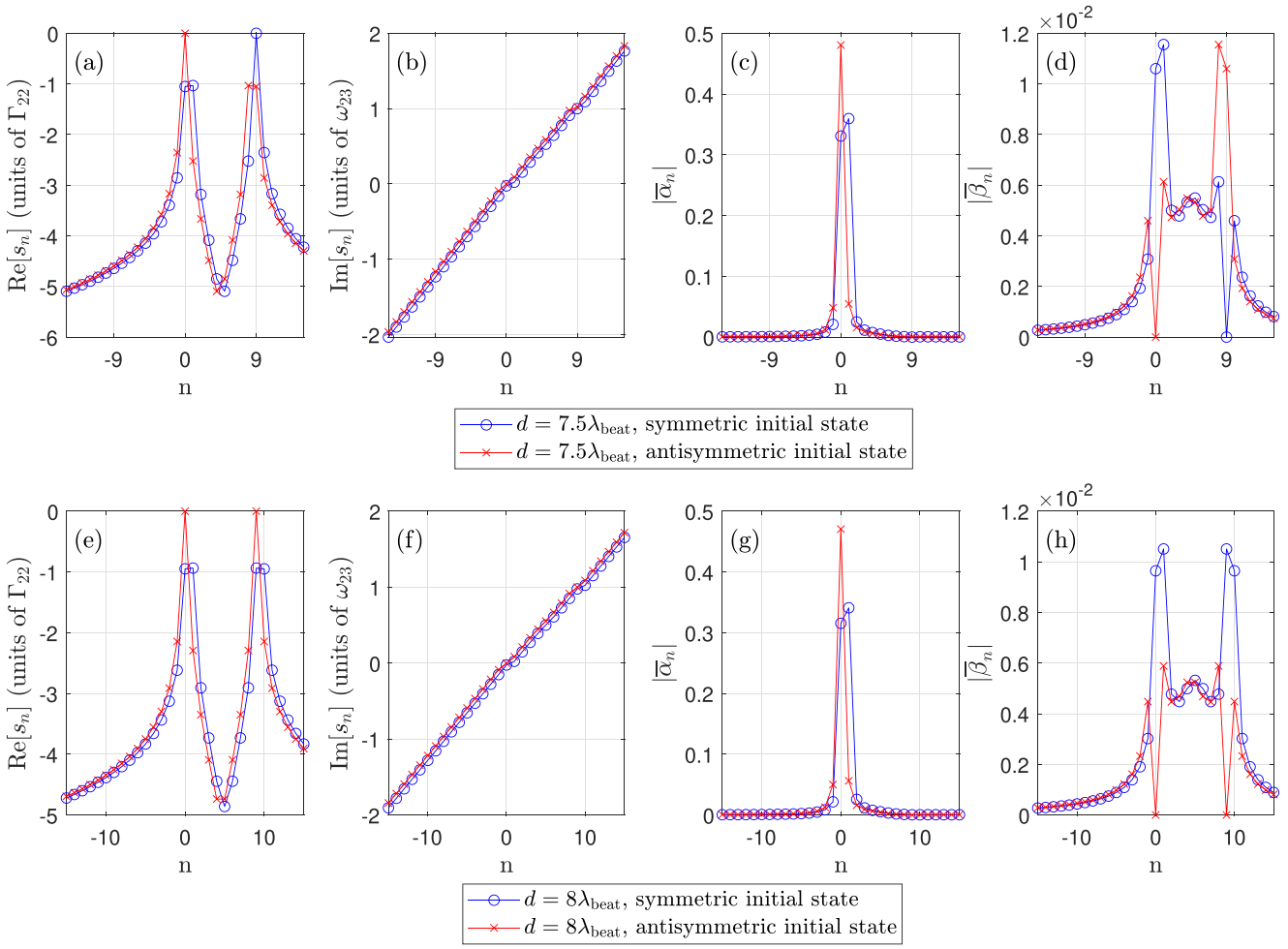

FIG. 6. Non-Markovian regime: The example of the poles and the corresponding coefficients for symmetric (blue circle) and antisymmetric (red x) initial states, for (a)–(d) $d = 7.5\,\lambda_{\text{beat}}$ and (e)–(h) $d = 8\lambda_{\text{beat}}$. (a), (e) The real part of the poles corresponds to the decay rate of each mode in units of Γ_{22} and (b), (f) the imaginary part corresponds to the frequency of the modes in units of ω_{23}. (c), (g) The coefficient $\overline{\alpha}_n$ shows the contribution of each pole to the level 2 dynamics and (d), (h) the coefficient $\overline{\beta}_n$ shows the contribution to the level 3 dynamics.

We can derive the excitation amplitudes of the field modes from Eq. (6) and (7) as follows:

$$c_R(\omega_k,t)=i\int_0^t d\tau \sum_{m=A,B}\sum_{j=2,3} g_j(\omega_k)e^{-i(\omega_{j1}-\omega_k)\tau}c_{m,j}(\tau)e^{-ikx_m}, \tag{B2}$$

$$c_L(\omega_k,t)=i\int_0^t d\tau \sum_{m=A,B}\sum_{j=2,3} g_j(\omega_k)e^{-i(\omega_{j1}-\omega_k)\tau}c_{m,j}(\tau)e^{ikx_m}. \tag{B3}$$

Then one can simplify the intensity expression [Eq. (B1)] in terms of the atomic coefficients as follows:

$$\begin{aligned} I(x,t)=\frac{\epsilon_0 c|\mathcal{E}_0|^2}{4\pi}\Bigg|\int d\omega e^{-i\omega t}\Bigg[\int_0^t d\tau \sum_{j=2,3} g_j\big\{&c_{Aj}(\tau)e^{i\omega(-x+x_A)/v}+c_{Bj}(\tau)e^{i\omega(-x+x_B)/v}\\ &+c_{Aj}(\tau)e^{-i\omega(-x+x_A)/v}\\ &+c_{Bj}(\tau)e^{-i\omega(-x+x_B)/v}\big\}e^{i(\omega-\omega_{j1})\tau}\Bigg]\Bigg|^2, \end{aligned} \tag{B4}$$

where we have used Eqs. (B2) and (B3) to determine the field excitation amplitudes in terms of those of the atoms. Performing first the integral over frequency and subsequently the integral over time leads to Eq. (19).

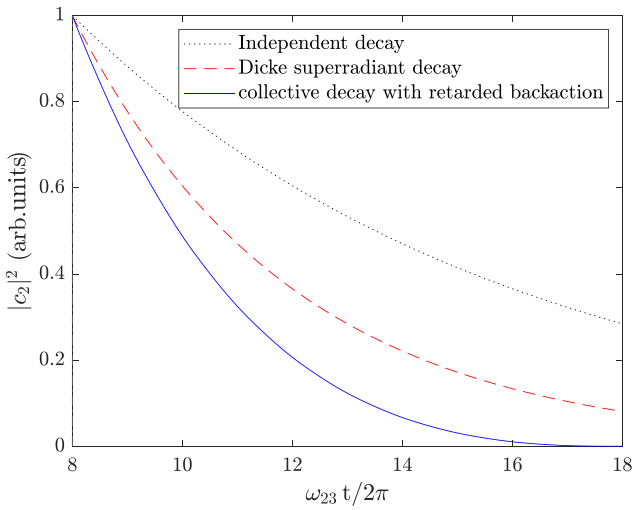

FIG. 7. The dynamics of the population in level 2 of the initial symmetric state of atoms for three scenarios: independent decay ($d = \infty$, dotted black), Dicke superradiance ($d = 0$, dashed red), and superduperradiance, i.e., the non-Markovian collective decay with retarded backaction ($d = 8\lambda_{\text{beat}}$, solid blue), each rescaled to 1 at $t = 8\lambda_{\text{beat}}/v$ for clear comparison.

APPENDIX C: POLES FOR THE MARKOVIAN AND THE NON-MARKOVIAN EXAMPLES

The poles s_n and the corresponding coefficients $\alpha_n^{(\pm)}$ and $\beta_n^{(\pm)}$ in Eqs. (12) and (13) determine the atomic and the field dynamics. However, the coefficients $\alpha_n^{(\pm)}$ and $\beta_n^{(\pm)}$ also account for the higher eigenfrequencies that cause an abrupt change at $t = d/v$, arising due to the time-delayed feedback. Since we are interested in the dynamics after $t = d/v$, we redefine the following coefficients:

$$\overline{\alpha}_n \equiv \alpha_n e^{s_n d/v}, \tag{C1}$$

$$\overline{\beta}_n \equiv \beta_n e^{s_n d/v}. \tag{C2}$$

The dynamics after $t = d/v$ is thus described as

$$c_{A2}(t) = \sum_{n=-\infty}^{\infty} \overline{\alpha}_n e^{s_n (t-d/v)}, \tag{C3}$$

$$c_{A3}(t) = \sum_{n=-\infty}^{\infty} \overline{\beta}_n e^{(s_n - i\omega_{23})(t-d/v)}. \tag{C4}$$

$\overline{\alpha}_n$ and $\overline{\beta}_n$ do not consider the high-frequency components constituting the abrupt change at $t = d/v$, and only account for the dynamics in the regime $t > d/v$.

Figures 5 and 6 show the poles s_n and the corresponding coefficients $\overline{\alpha}_n$ and $\overline{\beta}_n$ for Markovian and non-Markovian regimes, respectively. The real part of the poles represents the collective decay rate and the imaginary part represents collective shift of energy in the eigenmodes. We see that in the Markovian regime (Fig. 5) the high-frequency and fast decaying modes have negligible contribution. In contrast, the non-Markovian regime (Fig. 6) shows that the dominant poles occur in the range of frequencies between zero and ω_{23}, and decay rates that are enhanced beyond the Markovian limit.

APPENDIX D: COMPARISON OF SUPERDUPERRADIANCE AND DICKE SUPERRADIANCE IN LEVEL 2 DYNAMICS

The enhancement of decay rate of level 2 population for symmetrically correlated emitters in a non-Markovian regime exceeds the standard Dicke superradiant decay rate, whereas

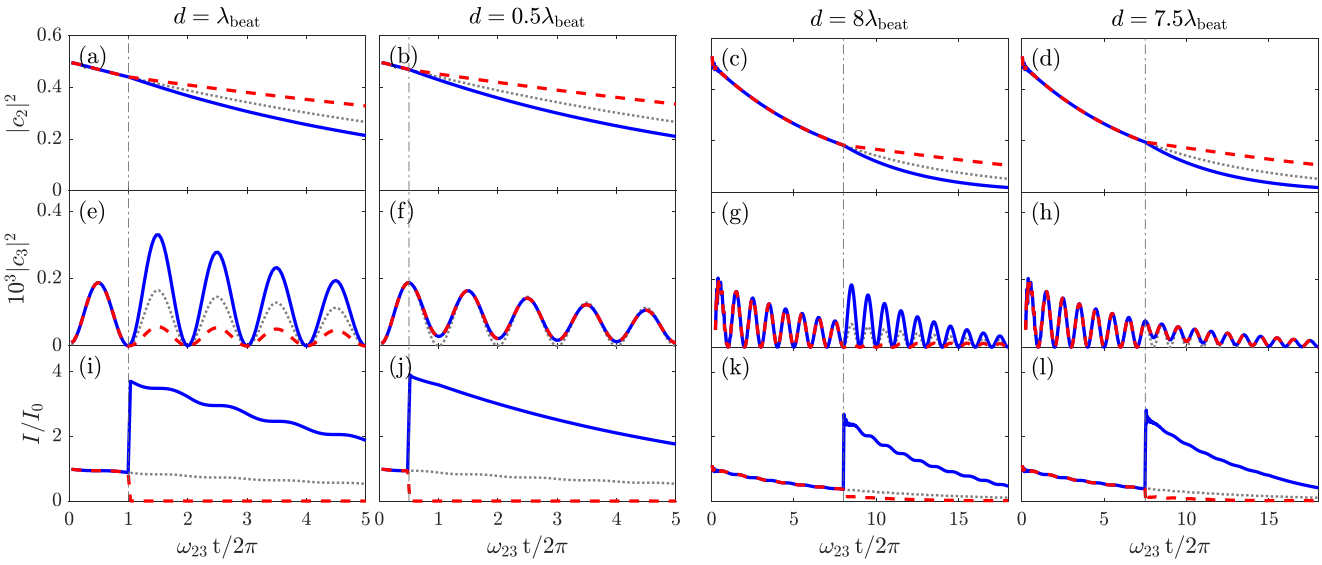

FIG. 8. The atom-field dynamics for coupling efficiency $\eta = 0.4$: (a)–(d) level 2 dynamics, (e)–(h) level 3 dynamics, and (i)–(l) field dynamics measured at $x \to x_B^+$ for interatomic separations (a), (e), (i) $d = \lambda_{\text{beat}}$, (b), (f), (j) $d = 0.5\lambda_{\text{beat}}$, (c), (g), (k) $d = 8\lambda_{\text{beat}}$, and (d), (h), (l) $d = 7.5\lambda_{\text{beat}}$. The solid blue curves are for the symmetric initial state, and the dashed red curves are for the antisymmetric initial state. The vertical dash-dotted lines indicate the times when the field emitted from one atom reaches the other atom. For comparison the single atom dynamics is drawn with the dotted gray lines. The level 3 population is scaled by a factor of 10^3 for clarity of illustration.

it is hard to tell just by looking at Figs. 4(a) and 4(b). Figure 7 shows a direct comparison of non-Markovian enhancement of decay for the case of $d = 8\lambda_{\text{beat}}$, to the standard Dicke superradiant decay and independent decay, demonstrating that retarded backaction may lead to a faster-than-superradiance decay.

APPENDIX E: MARKOVIAN AND NON-MARKOVIAN DYNAMICS FOR IMPERFECT COUPLING EFFICIENCY

The example of imperfect coupling efficiency of $\eta = 0.4$ is shown in Fig. 8. The general effect of having a finite coupling efficiency is that the interference between different atoms observed at the separation time is mitigated. In consequence, the level 2 dynamics shows reduced enhancement and suppression of decay rates for symmetric and antisymmetric initial states, respectively. Similarly, the level 3 dynamics for $d = n\lambda_{\text{beat}}$ shows less enhancement and suppression of quantum beats for symmetric and antisymmetric initial states, respectively. In the level 3 dynamics for $d = (n + \frac{1}{2})\lambda_{\text{beat}}$, destructive interference due to the out-of-phase photon from the other atom is also reduced. As a result, the intensity of light emitted from the system shows less enhancement or suppression of the decay rate and the quantum beats.

[1] E. T. Jaynes, in *Foundations of Radiation Theory and Quantum Electrodynamics*, edited by A. O. Barut (Springer, New York, 1980), pp. 37–43.
[2] R. H. Dicke, Phys. Rev. **93**, 99 (1954).
[3] G. S. Agarwal, Phys. Rev. A **15**, 2380 (1977).
[4] H. S. Han, A. Lee, K. Sinha, F. K. Fatemi, and S. L. Rolston, Phys. Rev. Lett. **127**, 073604 (2021).
[5] S. Haroche, in *High-Resolution Laser Spectroscopy*, edited by K. Shimoda (Springer-Verlag, Berlin, 1976), pp. 253–313.
[6] M. Gross, C. Fabre, P. Pillet, and S. Haroche, Phys. Rev. Lett. **36**, 1035 (1976).
[7] M. Gross and S. Haroche, Phys. Rep. **93**, 301 (1982).
[8] N. Skribanowitz, I. P. Herman, J. C. MacGillivray, and M. S. Feld, Phys. Rev. Lett. **30**, 309 (1973).
[9] D. Pavolini, A. Crubellier, P. Pillet, L. Cabaret, and S. Liberman, Phys. Rev. Lett. **54**, 1917 (1985).
[10] R. G. DeVoe and R. G. Brewer, Phys. Rev. Lett. **76**, 2049 (1996).
[11] A. S. Sheremet, M. I. Petrov, I. V. Iorsh, A. V. Poshakinskiy, and A. N. Poddubny, arXiv:2103.06824.
[12] V. A. Pivovarov, L. V. Gerasimov, J. Berroir, T. Ray, J. Laurat, A. Urvoy, and D. V. Kupriyanov, Phys. Rev. A **103**, 043716 (2021).
[13] A. Asenjo-Garcia, M. Moreno-Cardoner, A. Albrecht, H. J. Kimble, and D. E. Chang, Phys. Rev. X **7**, 031024 (2017).
[14] A. F. van Loo, A. Fedorov, K. Lalumiére, B. C. Sanders, A. Blais, and A. Wallraff, Science **342**, 1494 (2013).
[15] Y. Li and C. Argyropoulos, Opt. Express **24**, 26696 (2016).
[16] P. Solano, P. Barberis-Blostein, F. K. Fatemi, L. A. Orozco, and S. L. Rolston, Nat. Commun. **8**, 1857 (2017).
[17] J.-H. Kim, S. Aghaeimeibodi, C. J. K. Richardson, R. P. Leavitt, and E. Waks, Nano Lett. **18**, 4734 (2018).
[18] W. D. Newman, C. L. Cortes, A. Afshar, K. Cadien, A. Meldrum, R. Fedosejevs, and Z. Jacob, Sci. Adv. **4**, eaar5278 (2018).
[19] A. K. Boddeti, J. Guan, T. Sentz, X. Juarez, W. Newman, C. Cortes, T. W. Odom, and Z. Jacob, Nano Lett. **22**, 22 (2022).
[20] R. Pennetta, M. Blaha, A. Johnson, D. Lechner, P. Schneeweiss, J. Volz, and A. Rauschenbeutel, Phys. Rev. Lett. **128**, 073601 (2022).
[21] M. Zanner, T. Orell, C. M. F. Schneider, R. Albert, S. Oleschko, M. L. Juan, M. Silveri, and G. Kirchmair, Nat. Phys. **18**, 538 (2022).
[22] P. Solano, J. A. Grover, J. E. Hoffman, S. Ravets, F. K. Fatemi, L. A. Orozco, and S. L. Rolston, Adv. At. Mol. Opt. Phys. **66**, 439 (2017).
[23] D. E. Chang, L. Jiang, A. V. Gorshkov, and H. J. Kimble, New J. Phys. **14**, 063003 (2012).
[24] N. V. Corzo, B. Gouraud, A. Chandra, A. Goban, A. S. Sheremet, D. V. Kupriyanov, and J. Laurat, Phys. Rev. Lett. **117**, 133603 (2016).
[25] M. Mirhosseini, E. Kim, X. Zhang, A. Sipahigil, P. B. Dieterle, A. J. Keller, A. Asenjo-Garcia, D. E. Chang, and O. Painter, Nature (London) **569**, 692 (2019).
[26] L. Ostermann, H. Ritsch, and C. Genes, Phys. Rev. Lett. **111**, 123601 (2013).
[27] L. Henriet, J. S. Douglas, D. E. Chang, and A. Albrecht, Phys. Rev. A **99**, 023802 (2019).
[28] M. T. Manzoni, M. Moreno-Cardoner, A. Asenjo-Garcia, J. V. Porto, A. V. Gorshkov, and D. E. Chang, New J. Phys. **20**, 083048 (2018).
[29] F. Dinç and A. M. Brańczyk, Phys. Rev. Res. **1**, 032042(R) (2019).
[30] S. Rist, J. Eschner, M. Hennrich, and G. Morigi, Phys. Rev. A **78**, 013808 (2008).
[31] K. Sinha, A. González-Tudela, Y. Lu, and P. Solano, Phys. Rev. A **102**, 043718 (2020).
[32] K. Sinha, P. Meystre, E. A. Goldschmidt, F. K. Fatemi, S. L. Rolston, and P. Solano, Phys. Rev. Lett. **124**, 043603 (2020).
[33] K. Sinha, P. Meystre, and P. Solano, Nanophot. Mater. Dev. Syst. **11091**, 53 (2019).
[34] G. Calajó, Yao-Lung L. Fang, H. U. Baranger, and F. Ciccarello, Phys. Rev. Lett. **122**, 073601 (2019).
[35] R. Trivedi, D. Malz, S. Sun, S. Fan, and J. Vučković, Phys. Rev. A **104**, 013705 (2021).
[36] P. Yao and S. Hughes, Opt. Express **17**, 11505 (2009).
[37] G. C. Hegerfeldt and M. B. Plenio, Quantum Opt. **6**, 15 (1994).
[38] S. J. Srinivasan, A. J. Hoffman, J. M. Gambetta, and A. A. Houck, Phys. Rev. Lett. **106**, 083601 (2011).
[39] F. Dinç, A. M. Brańczyk, and I. Ercan, Quantum **3**, 213 (2019).
[40] P. Solano, P. Barberis-Blostein, and K. Sinha, arXiv:2108.12951.
[41] A. Asenjo-Garcia, H. J. Kimble, and D. E. Chang, Proc. Natl. Acad. Sci. USA **116**, 25503 (2019).
[42] N. J. Cerf, M. Bourennane, A. Karlsson, and N. Gisin, Phys. Rev. Lett. **88**, 127902 (2002).
[43] A. Vaziri, G. Weihs, and A. Zeilinger, Phys. Rev. Lett. **89**, 240401 (2002).
[44] H. Bechmann-Pasquinucci and W. Tittel, Phys. Rev. A **61**, 062308 (2000).

Research Article Vol. 33, No. 2 / 27 Jan 2025 / Optics Express 3013
Optics EXPRESS

Optical lattices with variable spacings generated by binary phase transmission gratings

HYOK SANG HAN,[1,*] AHREUM LEE,[1] SARTHAK SUBHANKAR,[1] S. L. ROLSTON,[1,2] AND FREDRIK K. FATEMI[2,3]

[1] Joint Quantum Institute, University of Maryland and the National Institute of Standards and Technology, College Park, Maryland 20742, USA
[2] DEVCOM Army Research Laboratory, Adelphi, Maryland 20783, USA
[3] Quantum Technology Center, University of Maryland, College Park, Maryland 20742, USA
[*] hhan123@umd.edu

Abstract: Optical accordion lattices are routinely used in quantum simulation and quantum computation experiments to tune optical lattice spacings. Here, we present a technique for creating tunable optical lattices using binary-phase transmission gratings. Lattices generated using this technique have high uniformity, contrast, lattice spacing tunability, and power efficiencies. These attributes are crucial for exploring collective quantum phenomena in highly ordered atomic arrays coupled to optical waveguides for quantum networking and quantum simulation. In this paper, we demonstrate adjustable-period lattices that are ideally suited for use with optical nanofibers.

1. Introduction

The study of highly ordered arrays of atoms is a rich and active area of research with applications in quantum optics, quantum computation, quantum simulation, and quantum networking [1–4]. There are two primary methods for creating ordered arrays. Optical lattices made by interfering beams have been the workhorse of efforts to simulate condensed matter systems with cold atoms [5,6]. Arrays of optical tweezers (tightly focused beams) have become a competitive platform for quantum computation [7–10]. Quantum optics of ordered arrays of atoms coupled to 1D nanophotonic waveguides [11–15] requires the ability to create arrays of many atoms over many lattice sites (range of a thousand) with precise control of the lattice constant commensurate with the emission wavelength to probe aspects of interference (e.g., super- or subradiance) [16–20].

While optical lattices made with fixed interfering beams provide a dense, large number of trapping sites, flexibility is constrained by tunable wavelength range. In contrast, tweezer arrays provide greater flexibility, but increasing the number of trapping sites with wavelength-scale trap spacing remains challenging. A need for both scalability and flexibility led to the creation of optical "accordion lattices," with the ability to change the angle of the interfering beams through a single control parameter [21–29]. Using movable free-space optics to tune the lattice spacings [21–25] allows large tuning range of the lattice spacings but introduces potential power imbalances and alignment sensitivity. Acousto-optic deflectors (AODs) provide fine control over the angle of the beams [26–28], but can degrade beam quality and tend to have large minimum lattice spacings, although the latter limitation is not intrinsic to AODs but arises from experimental designs that prioritize large dynamic tuning range.

Here, we present a simple, compact, and novel optical accordion lattice technique based on binary-phase transmission gratings to trap atoms that is ideally-suited for one-dimensional systems. The advantages of this approach are the high uniformity, contrast (>98%), tunability of the lattice spacings, and laser power efficiency (~ 80%). The technique benefits from imprinting the precision of the structure created by electron beam lithography onto the optical field. Phase plates with fixed lattice spacing have been previously employed to create periodic potentials for ultra-cold atomic gas [30]. In our implementation, the lattice spacing is adjustable by utilizing

#544727 https://doi.org/10.1364/OE.544727
Journal © 2025 Received 22 Oct 2024; revised 17 Dec 2024; accepted 21 Dec 2024; published 21 Jan 2025

Optics EXPRESS

the gradual variation in grating periods between the adjacent rows of the compact grating set, with the range limited only by the numerical aperture (NA) of the imaging system. Additionally, modifications to the optical lattice intensity distribution can be made by tailoring the beam profile at the transmission grating or inserting other custom phase plates without further realignment of the relay optics. While a similar approach can be made using a spatial light modulator (SLM) to generate a reconfigurable lattice potential [31], tunability and extent of the lattice are constrained by the array size of the SLM. Figure 1 shows our designed implementation with optical nanofiber, but the technique is not limited to this specific application.

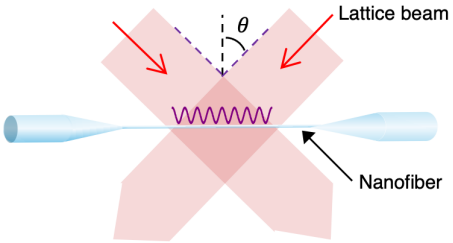

Fig. 1. An optical accordion lattice projected onto a nanophotonic waveguide, such as an optical nanofiber.

The paper is organized as follows. In Sec. 2, we develop a Fourier optics-based framework [32] to derive the properties of the optical lattice created using a diffraction grating. In Sec. 3, we present details on the experimental realization and characterization of the accordion lattices. The summary and concluding remarks are given in Sec. 4.

2. Theory

In our approach, shown in Fig. 2, the two beams are generated by diffraction of a laser beam passing through a binary phase transmission grating. The beams are relayed through a $4f-$ imaging system that only transmits the ± 1 diffracted orders. The far-field pattern of the electric field of light diffracted by a grating is given by the Fraunhofer diffraction integral:

$$\mathcal{E}(u) = \frac{\mathcal{E}_0 e^{ikz} e^{ikx^2/2z}}{i\lambda z} \int_{\infty}^{\infty} f(x') e^{-i2\pi u x'} dx', \tag{1}$$

where $u = x/(z\lambda)$, $\mathcal{E}_0$ is the electric field of the laser light illuminating the grating, λ is the wavelength of light, $k = 2\pi/\lambda$, and $f(x)$ is the structure function of the grating. The Fourier decomposition of the structure function is as follows:

$$f(x) = \sum_m a_m e^{-2\pi i m x/d_{\text{grt}}}, \tag{2}$$

where a_m is the mth Fourier coefficient with $m = 0, \pm 1, \pm 2, \ldots$, and d_{grt} is the grating period.

The structure function for a periodic binary phase transmission grating [33–36] in air/vacuum is (Fig. 2(c))

$$f(x) = \begin{cases} e^{i\varphi} & \text{if } x \in [0, l] \\ 1 & \text{if } x \in [l, d_{\text{grt}}] \end{cases}, \tag{3}$$

with

$$\varphi = \frac{2\pi h}{\lambda}(n_0 - 1), \tag{4}$$

Optics EXPRESS

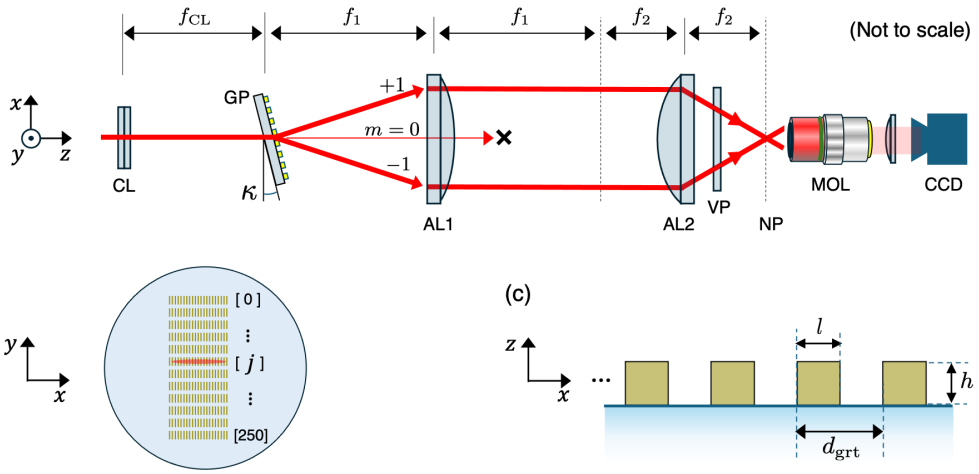

Fig. 2. (a) The spatially-filtered and plane-symmetric $4f$-imaging system for creating the optical accordion lattices. (b) The grating plate with the horizontal red stripe representing the beam illuminating the jth grating. (c) Cross-section of a binary phase transmission grating.

where h is the relief depth and n_0 is the refractive index of the grating material. The Fourier coefficient a_m for the binary phase transmission grating is

$$a_m = \frac{1}{d_{\text{grt}}} \int_0^{d_{\text{grt}}} f(x) e^{i2\pi m x/d_{\text{grt}}} dx \tag{5}$$

$$= -\frac{i\left(e^{i\varphi}\left(-1 + e^{2i\pi Dm}\right) - e^{2i\pi Dm} + e^{2i\pi m}\right)}{2\pi m}, \tag{6}$$

where $D = l/d_{\text{grt}}$ is the duty factor of the grating. The diffraction efficiency of the mth order is

$$\eta_m = |a_m|^2 = \frac{4}{\pi^2 m^2} \sin^2(\pi m D) \sin^2(\varphi/2). \tag{7}$$

For $D = 0.5$ and $\varphi = \pi$, the diffraction efficiency for all even diffraction orders is 0, $a_{\pm 1} = \mp 2i/\pi$, and $\eta_{\pm 1} = 40.5\%$. Additionally, the angle of the mth order diffracted beam (ξ_m) with respect to the optical axis is given by the Bragg condition:

$$\sin(\xi_m) = -\frac{m\lambda}{d_{\text{grt}}}. \tag{8}$$

The $4f-$ imaging system illustrated in Fig. 2 (assumed to be diffraction-limited) transmits only the first-order diffracted light. The intensity of the optical accordion lattice at the nanofiber plane NP is then [32]:

$$\mathcal{I}_{\text{lattice}}(x) = \frac{16\mathcal{E}_0^2}{\pi^2 M^2} \sin^2\left(\frac{2\pi}{M d_{\text{grt}}} x\right), \tag{9}$$

where $M = f_2/f_1$ is the magnification of the imaging system. The accordion lattice spacing is:

$$d_{\text{lat}} = M\frac{d_{\text{grt}}}{2}. \tag{10}$$

Note that the lattice spacing is independent of the wavelength of light used to generate the lattice.

Optics EXPRESS

For a grating rotated about the y-axis by a small angle κ, the lattice spacing is given by the following equation:

$$d_{\text{lat}} = M\frac{d_{\text{grt}}}{2}\cos\kappa. \tag{11}$$

Note that this rotation changes the phase φ in the structure function (Eq. (3)), which changes the diffraction efficiency (Eq. (7)). However, as shown in the next section, we only need to change κ within ± 0.1 rad for continuous fine-tuning of the lattice period, which leads to a negligible reduction (<0.01%) in the diffraction efficiency.

3. Experiment

In this section, we present details on the experimental realization and characterization of optical lattices using this approach. The optical system (Fig. 2 (a)) is specifically designed for our nanofiber experiment, which requires a large lattice extent (~ 2 mm) along the nanofiber direction (x-axis) and tight focus ($<10\,\mu$m) in the transverse direction (y-axis). The nanofiber is under high vacuum and located at the center of a 6" spherical octagonal chamber (Kimball Physics MCF600-SphOct-F2C8), requiring an imaging lens with a long working distance (>65 mm) and a large diameter (100 mm). While our specific implementation requires these larger diameter aspheric lenses due to experimental constraints, the technique is not restricted to large optics.

Laser light at $\lambda = 775$ nm is delivered to the imaging system by a single-mode polarization-maintaining fiber optic patch cable (Thorlabs P3-780PM-FC-2). The light is collimated (Thorlabs F810APC-780) and polarized along the y-axis. The laser beam with a waist of 3.8 mm and propagating along the z-axis is first focused in the y direction by a plano-convex cylindrical lens CL (Thorlabs LJ1653RM-B) with a focal length $f_{\text{CL}} = 200$ mm. The grating plate is placed at the focus of CL.

The grating plate GP is a compactly stacked array of 251 binary phase transmission gratings with different grating constants (see Fig. 2(b)). Each grating spatially modulates the optical path difference φ using silicon nitride (SiN) (yellow rectangles in Fig. 2(c)) patterned onto a 1-mm-thick quartz substrate (blue-shaded region in Fig. 2(c)) through electron beam lithography. The grating plate was fabricated in a cleanroom at DEVCOM Army Research Laboratory using the Raith EBPG5200 Plus electron beam system with patterning accuracy well below optical wavelengths. Given the refractive index of SiN is ≈2.0 at 780 nm, 390-nm-thick SiN deposition height (h) yields $\varphi \approx \pi$. Each grating spans a rectangular area of $10\,\text{mm} \times 100\,\mu$m, fully enclosing the beam profile ($w_x \times w_y = 3.8\,\text{mm} \times 20\,\mu$m) at the focus of CL.

The grating constant for each grating is

$$d_{\text{grt}}[j] = d_0 + j\delta, \tag{12}$$

where $d_0 = 3.0\,\mu$m and $\delta = 20$ nm are the designed offset and step size, and $j \in \mathbb{N}$ is the array index of the grating ranging from 0 to 250. Therefore, the designed accordion lattice spacing is

$$d_{\text{lat}}^{\text{dsgn}}[j] = \frac{M}{2}\cos\kappa(d_0 + j\delta), \tag{13}$$

where we have used Eq. (11) and Eq. (12).

The grating plate is mounted on a linear translation stage to choose a grating with $d_{\text{grt}}[j]$. The total diffraction efficiency in the $m = \pm 1$ is $\sim 80\%$. The first aspheric lens AL1 (Thorlabs AL100200-B, $f_1 = 200$, NA = 0.23) is placed f_1 away from the grating plate. We filter out all diffracted orders except the $m = \pm 1$ orders. The spatially filtered conjugate image of the grating is then imaged by the second aspheric lens AL2 (Thorlabs AL100100-B, $f_2 = 100$ mm, NA = 0.48) placed $f_1 + f_2$ from AL1 and f_2 away from the nanofiber image plane through a 6" CF flange viewport VP (Kurt. J. Lesker VPZL-600) placed 1 cm downstream of AL2. While the vacuum

Optics EXPRESS

chamber and the nanofiber were absent during this demonstration, VP was included to assess its impact on the lattice quality. At the NP, each lattice beam has a measured beam waist of 1.5 mm along the x-axis and 8 μm along the y-axis. This large aspect ratio of 190 : 1 allows us to generate lattices with approximately a thousand lattice sites along the nanofiber with good optical power efficiency.

To analyze the lattices, we use microscope objective lenses MOL (Mitutoyo P Plan 100×), a plano-convex lens (f = 200 mm) and a CCD camera to image the accordion lattice projected onto the NP. Background-subtracted images of accordion lattices resulting from gratings with index j = 15 and j = 250 are presented in Fig. 3. The axes are scaled to represent the structure at the NP, given a 100× magnification and a 3.45 μm camera pixel size. The background-subtracted images are integrated along y to generate a 1D profile along the x-axis, which is subsequently fit with a sinusoidal function which yields $d_{\mathrm{lat}}^{\mathrm{meas}}[j] = 0.80$ μm and 2.0 μm for j = 15 and j = 250, respectively, agreeing well with the grating specifications scaled by the magnification of the imaging system M = 0.5 and the grating rotation angle $\kappa = 0$. The contrast of the interference fringes is very high >0.98, which is important for quantum optics experiments.

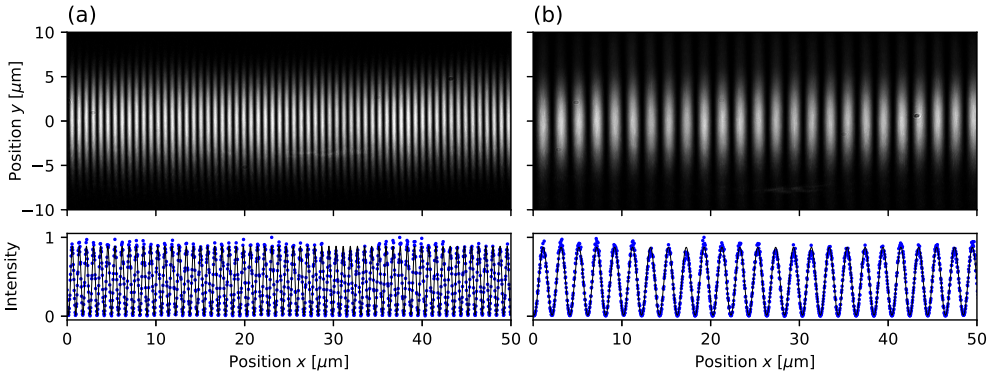

Fig. 3. Measured 2D intensity profile (top) and integrated column density profile (bottom) of an accordion lattice created using the (a) j = 15 and (b) j = 250 grating. (bottom) The blue dots represent data, and the black trace represents the fit.

We measure and fit images of optical lattices to extract the $d_{\mathrm{lat}}^{\mathrm{meas}}[j]$ for a range of grating indices j (in increments of 10), which are represented as blue circles in Fig. 4(a). We fit the measured lattice spacings using a linear fit (black solid line) $d_{\mathrm{lat}}^{\mathrm{meas}}[j] = (727 + 5.2j)$ nm. The red dashed line is a plot of the designed lattice spacing $d_{\mathrm{lat}}^{\mathrm{dsgn}}[j] = (750 + 5.0j)$ nm from Eq. (13) with M = 0.5 and $\kappa = 0$. We attribute the small discrepancy between the $d_{\mathrm{lat}}^{\mathrm{meas}}[j]$ and $d_{\mathrm{lat}}^{\mathrm{dsgn}}[j]$ to uncertainty in the exact magnification in the $4f-$imaging relay due to the thick aspheric lenses. The range of lattice spacings (0.8 - 2 μm) in this demonstration was chosen to meet our experimental requirements. The lattice spacing range, including the smallest spacing, can be customized by using different gratings and optics. The inset in Fig. 4(a) shows a montage of 31 lattices ($220 \leq j \leq 250$), where image rows are stacked vertically and aligned horizontally at $x = 0$, exhibiting a quasi-continuous variation in lattice spacing (1.9 - 2.0 μm).

The δ = 20 nm change in the period between the adjacent gratings leads to a 5 nm change in the optical lattice spacing with our choice of aspheric lenses. Sub-5 nm tuning of the lattice spacing can be achieved by rotating the grating plane about the y-axis by κ(<0.1 rad). In Fig. 4(b), we plot the measured $d_{\mathrm{lat}}^{\mathrm{meas}}[j]$ (filled circles) as a function of κ for three adjacent gratings. We fit the measured $d_{\mathrm{lat}}^{\mathrm{meas}}[j]$ using Eq. (13) with $Md_0/2$, and $M\delta/2$ as the fit parameters. The fits are represented as solid lines with $Md_0/2$ = 734 nm and $M\delta/2$ = 5.1 nm extracted from the fits.

Optics EXPRESS

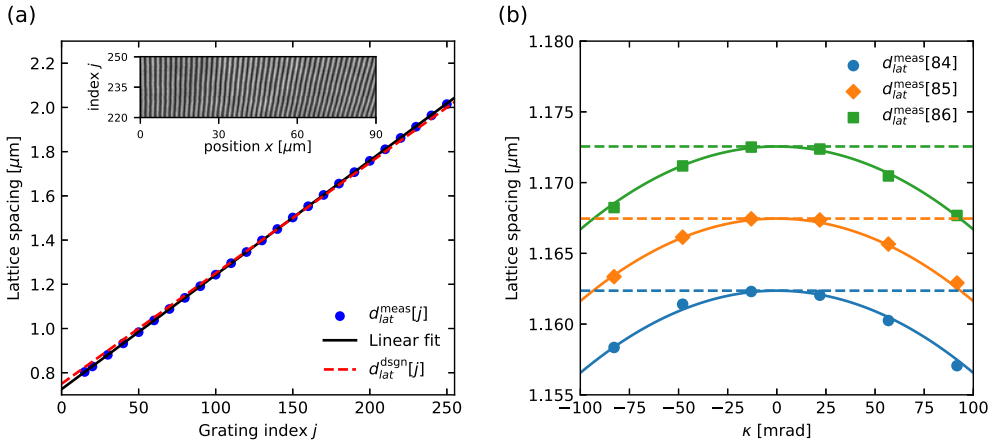

Fig. 4. (a) Measured lattice spacing $d_{\text{lat}}^{\text{meas}}[j]$ as a function of j with the black solid line representing a fit to the data and the red dashed line representing the ideal design $d_{\text{lat}}^{\text{dsgn}}[j]$. Inset: Vertically stitched lattice images for $220 \leq j \leq 250$, showing a gradual change in periodicity as j varies. (b) Measured $d_{\text{lat}}^{\text{meas}}[j]$ as a function of κ for $j = 84, 85, 86$. The solid lines are fit to the data using Eq. (13) with $Md_0/2$, and $M\delta/2$ as the fit parameters, and the dashed horizontal lines correspond to $d_{\text{lat}}[j]$ at $\kappa = 0$. The error bars are smaller than the data markers and are not visible in the plots.

All accordion lattice implementations are susceptible to aberration-induced changes in lattice spacing over the entire extent of the lattice. To inspect large-scale lattice uniformity, we analyze the lattice spacing over the entire 2-mm lattice region by translating the MOL stage along the x-axis in 0.5-mm increments. We observed a minor amount of lattice spacing variation $\partial d_{\text{lat}}^{\text{meas}}/\partial x = 2.05(7)$ nm/mm, corresponding to a 0.2% chirp over the entire 2-mm lattice region. This indicates that our approach yields high-quality lattices with thousands of sites. We attribute this minor frequency chirp to aberrations in the $4f-$ imaging system.

4. Conclusion and outlook

In this paper, we have presented a technique for generating optical accordion lattices which makes uniform, high-contrast lattice sites ($\sim 0.2\%$ chirp in the lattice frequency over the entire 2 mm lattice region with contrast larger than 98%) with highly tunable lattice spacings ($0.8 - 2$ μm) and high power efficiencies ($\sim 80\%$). We propagate laser light illuminating binary phase transmission gratings through a spatially filtered plane-symmetric $4f-$imaging system to create these lattices. The lattices have a large $190:1$ aspect ratio and are therefore ideal for interfacing atoms trapped in these lattices to longitudinally extended nanophotonic waveguides such as an optical nanofiber or a nanophotonic crystal waveguide. The number of lattice sites lies in the thousand range, making these lattices well-suited for exploring photon-mediated collective quantum phenomena arising from large, highly ordered arrays of atoms. Although our current implementation uses a set of gratings with discrete spacings, grating plates with continuously varying grating spacing can be fabricated. Such a grating plate combined with fast RF beam steering can allow for dynamic tuning of the spacing of these optical accordion lattices necessary for quantum gas and quantum optics experiments.

Funding. DEVCOM Army Research Laboratory (W911NF-24-2-0107); Joint Quantum Institute (70NANB16H168).

Acknowledgment. The authors thank Kanu Sinha and Shouvik Mukherjee for the valuable discussion, and Jason Sun for fabrication of the SiN grating.

Disclosures. The authors declare no conflicts of interest.

Optics EXPRESS

Data availability. Data underlying the results presented in this paper may be obtained from the authors upon reasonable request.

References

1. D. E. Chang, J. S. Douglas, A. González-Tudela, *et al.*, "Colloquium: Quantum matter built from nanoscopic lattices of atoms and photons," Rev. Mod. Phys. **90**(3), 031002 (2018).
2. D. Bluvstein, S. J. Evered, A. A. Geim, *et al.*, "Logical quantum processor based on reconfigurable atom arrays," Nature **626**(7997), 58–65 (2024).
3. E. Shahmoon, D. S. Wild, M. D. Lukin, *et al.*, "Cooperative resonances in light scattering from two-dimensional atomic arrays," Phys. Rev. Lett. **118**(11), 113601 (2017).
4. S. G. Menon, N. Glachman, M. Pompili, *et al.*, "An integrated atom array-nanophotonic chip platform with background-free imaging," Nat. Commun. **15**(1), 6156 (2024).
5. A. Hemmerich and T. W. Hänsch, "Two-dimensional atomic crystal bound by light," Phys. Rev. Lett. **70**(4), 410–413 (1993).
6. I. Bloch and M. Greiner, *Exploring quantum matter with ultracold atoms in optical lattices*, (Academic Press, 2005), pp. 1–47.
7. D. Barredo, S. de Léséleuc, V. Lienhard, *et al.*, "An atom-by-atom assembler of defect-free arbitrary two-dimensional atomic arrays," Science **354**(6315), 1021–1023 (2016).
8. M. Endres, H. Bernien, A. Keesling, *et al.*, "Atom-by-atom assembly of defect-free one-dimensional cold atom arrays," Science **354**(6315), 1024–1027 (2016).
9. A. M. Kaufman and K.-K. Ni, "Quantum science with optical tweezer arrays of ultracold atoms and molecules," Nat. Phys. **17**(12), 1324–1333 (2021).
10. D. Bluvstein, H. Levine, G. Semeghini, *et al.*, "A quantum processor based on coherent transport of entangled atom arrays," Nature **604**(7906), 451–456 (2022).
11. E. Vetsch, D. Reitz, G. Sagué, *et al.*, "Optical interface created by laser-cooled atoms trapped in the evanescent field surrounding an optical nanofiber," Phys. Rev. Lett. **104**(20), 203603 (2010).
12. A. Goban, K. S. Choi, D. J. Alton, *et al.*, "Demonstration of a state-insensitive, compensated nanofiber trap," Phys. Rev. Lett. **109**(3), 033603 (2012).
13. C. Lacroûte, K. S. Choi, A. Goban, *et al.*, "A state-insensitive, compensated nanofiber trap," New J. Phys. **14**(2), 023056 (2012).
14. J. Lee, J. A. Grover, J. E. Hoffman, *et al.*, "Inhomogeneous broadening of optical transitions of 87rb atoms in an optical nanofiber trap," J. Phys. B: At., Mol. Opt. Phys. **48**(16), 165004 (2015).
15. A. Goban, C.-L. Hung, J. D. Hood, *et al.*, "Superradiance for atoms trapped along a photonic crystal waveguide," Phys. Rev. Lett. **115**(6), 063601 (2015).
16. A. S. Sheremet, M. I. Petrov, I. V. Iorsh, *et al.*, "Waveguide quantum electrodynamics: Collective radiance and photon-photon correlations," Rev. Mod. Phys. **95**(1), 015002 (2023).
17. D. F. Kornovan, A. S. Sheremet, and M. I. Petrov, "Collective polaritonic modes in an array of two-level quantum emitters coupled to an optical nanofiber," Phys. Rev. B **94**(24), 245416 (2016).
18. N. V. Corzo, B. Gouraud, A. Chandra, *et al.*, "Large bragg reflection from one-dimensional chains of trapped atoms near a nanoscale waveguide," Phys. Rev. Lett. **117**(13), 133603 (2016).
19. A. Asenjo-Garcia, M. Moreno-Cardoner, A. Albrecht, *et al.*, "Exponential improvement in photon storage fidelities using subradiance and "selective radiance" in atomic arrays," Phys. Rev. X **7**(3), 031024 (2017).
20. A. Lee, H. S. Han, F. K. Fatemi, *et al.*, "Collective quantum beats from distant multilevel emitters," Phys. Rev. A **107**(1), 013701 (2023).
21. T. C. Li, H. Kelkar, D. Medellin, *et al.*, "Real-time control of the periodicity of a standing wave: an optical accordion," Opt. Express **16**(8), 5465–5470 (2008).
22. J. H. Huckans, I. B. Spielman, B. L. Tolra, *et al.*, "Quantum and classical dynamics of a bose-einstein condensate in a large-period optical lattice," Phys. Rev. A **80**(4), 043609 (2009).
23. J. L. Ville, T. Bienaimé, R. Saint-Jalm, *et al.*, "Loading and compression of a single two-dimensional bose gas in an optical accordion," Phys. Rev. A **95**(1), 013632 (2017).
24. L. Su, A. Douglas, M. Szurek, *et al.*, "Dipolar quantum solids emerging in a hubbard quantum simulator," Nature **622**(7984), 724–729 (2023).
25. L. Su, A. Douglas, M. Szurek, *et al.*, "Fast single atom imaging in optical lattice arrays," arXiv (2024).
26. R. A. Williams, J. D. Pillet, S. Al-Assam, *et al.*, "Dynamic optical lattices: two-dimensional rotating and accordion lattices for ultracold atoms," Opt. Express **16**(21), 16977–16983 (2008).
27. S. Al-Assam, R. A. Williams, and C. J. Foot, "Ultracold atoms in an optical lattice with dynamically variable periodicity," Phys. Rev. A **82**(2), 021604 (2010).
28. S. Wili, T. Esslinger, and K. Viebahn, "An accordion superlattice for controlling atom separation in optical potentials," New J. Phys. **25**(3), 033037 (2023).
29. J. Tao, Y. Wang, Y. He, *et al.*, "Wavelength-limited optical accordion," Opt. Express **26**(11), 14346–14355 (2018).
30. W. S. Bakr, J. I. Gillen, A. Peng, *et al.*, "A quantum gas microscope for detecting single atoms in a hubbard-regime optical lattice," Nature **462**(7269), 74–77 (2009).

Optics EXPRESS

31. P. J. Rodrigo, V. R. Daria, and J. Glückstad, "Dynamically reconfigurable optical lattices," Opt. Express **13**(5), 1384–1394 (2005).
32. C. S. Adams and I. G. Hughes, *Optics f2f: From Fourier to Fresnel* (Oxford University Press, 2018).
33. A. Y. Meshalkin, V. V. Podlipnov, A. V. Ustinov, *et al.*, "Analysis of diffraction efficiency of phase gratings in dependence of duty cycle and depth," J. Phys.: Conf. Ser. **1368**(2), 022047 (2019).
34. J. E. Harvey and R. N. Pfisterer, "Understanding diffraction grating behavior: including conical diffraction and Rayleigh anomalies from transmission gratings," Opt. Eng. **58**(08), 1 (2019).
35. H. Gross, *Handbook of Optical Systems*, vol. 1 (Wiley, 2005).
36. M. D. M. Sánchez-López, I. Moreno, and A. Martínez-García, "Teaching diffraction gratings by means of a phasor analysis," *Optics InfoBase Conference Papers.* pp. 1–12 (2009).

Bibliography

[1] E.T. Jaynes and F.W. Cummings. Comparison of quantum and semiclassical radiation theories with application to the beam maser. *Proceedings of the IEEE*, 51(1):89–109, 1963.

[2] Marlan O. Scully and M. Suhail Zubairy. *Quantum optics*. Cambridge University Press, Cambridge, 1997.

[3] H. J. Kimble, M. Dagenais, and L. Mandel. Photon antibunching in resonance fluorescence. *Phys. Rev. Lett.*, 39:691–695, Sep 1977.

[4] H. Paul. Photon antibunching. *Rev. Mod. Phys.*, 54:1061–1102, Oct 1982.

[5] D. F. Walls. Squeezed states of light. *Nature*, 306:141–146, Nov 1983.

[6] Stuart J. Freedman and John F. Clauser. Experimental test of local hidden-variable theories. *Phys. Rev. Lett.*, 28:938–941, Apr 1972.

[7] Pieter Kok, W. J. Munro, Kae Nemoto, T. C. Ralph, Jonathan P. Dowling, and G. J. Milburn. Linear optical quantum computing with photonic qubits. *Rev. Mod. Phys.*, 79:135–174, Jan 2007.

[8] H. J. Kimble. The quantum internet. *Nature*, 453:1023–1030, Jun 2008.

[9] Klemens Hammerer, Anders S. Sørensen, and Eugene S. Polzik. Quantum interface between light and atomic ensembles. *Rev. Mod. Phys.*, 82:1041–1093, Apr 2010.

[10] Peter Lodahl, Sahand Mahmoodian, and Søren Stobbe. Interfacing single photons and single quantum dots with photonic nanostructures. *Rev. Mod. Phys.*, 87:347–400, May 2015.

[11] Dolev Bluvstein, Simon J. Evered, Alexandra A. Geim, Sophie H. Li, Hengyun Zhou, Tom Manovitz, Sepehr Ebadi, Madelyn Cain, Marcin Kalinowski, Dominik Hangleiter, J. Pablo Bonilla Ataides, Nishad Maskara, Iris Cong, Xun Gao, Pedro Sales Rodriguez, Thomas Karolyshyn, Giulia Semeghini, Michael J. Gullans, Markus Greiner, Vladan Vuletić, and Mikhail D. Lukin. Logical quantum processor based on reconfigurable atom arrays. *Nature*, 626:58–65, Feb 2024.

[12] H. C. Nägerl, D. Leibfried, H. Rohde, G. Thalhammer, J. Eschner, F. Schmidt-Kaler, and R. Blatt. Laser addressing of individual ions in a linear ion trap. *Phys. Rev. A*, 60:145–148, Jul 1999.

[13] A. N. Vamivakas, M. Atatüre, J. Dreiser, S. T. Yilmaz, A. Badolato, A. K. Swan, B. B. Goldberg, A. Imamoğlu, and M. S. Ünlü. Strong extinction of a far-field laser beam by a single quantum dot. *Nano Letters*, 7(9):2892–2896, 2007. PMID: 17691853.

[14] Meng Khoon Tey, Zilong Chen, Syed Abdullah Aljunid, Brenda Chng, Florian Huber, Gleb Maslennikov, and Christian Kurtsiefer. Strong interaction between light and a single trapped atom without the need for a cavity. *Nature Physics*, 4:924–927, Dec 2008.

[15] G. Wrigge, I. Gerhardt, J. Hwang, G. Zumofen, and V. Sandoghdar. Efficient coupling of photons to a single molecule and the observation of its resonance fluorescence. *Nature Physics*, 4:60–66, Jan 2008.

[16] Michael Fleischhauer, Atac Imamoglu, and Jonathan P. Marangos. Electromagnetically induced transparency: Optics in coherent media. *Rev. Mod. Phys.*, 77:633–673, Jul 2005.

[17] Tasso R. M. Sales. Smallest focal spot. *Phys. Rev. Lett.*, 81:3844–3847, Nov 1998.

[18] S. J. van Enk and H. J. Kimble. Single atom in free space as a quantum aperture. *Phys. Rev. A*, 61:051802, Mar 2000.

[19] S. J. van Enk. Atoms, dipole waves, and strongly focused light beams. *Phys. Rev. A*, 69:043813, Apr 2004.

[20] R Miller, T E Northup, K M Birnbaum, A Boca, A D Boozer, and H J Kimble. Trapped atoms in cavity qed: coupling quantized light and matter. *Journal of Physics B: Atomic, Molecular and Optical Physics*, 38(9):S551, apr 2005.

[21] J. T. Shen and Shanhui Fan. Coherent photon transport from spontaneous emission in one-dimensional waveguides. *Opt. Lett.*, 30(15):2001–2003, Aug 2005.

[22] D. E. Chang, J. S. Douglas, A. González-Tudela, C.-L. Hung, and H. J. Kimble. Colloquium: Quantum matter built from nanoscopic lattices of atoms and photons. *Rev. Mod. Phys.*, 90:031002, Aug 2018.

[23] Alexandra S. Sheremet, Mihail I. Petrov, Ivan V. Iorsh, Alexander V. Poshakinskiy, and Alexander N. Poddubny. Waveguide quantum electrodynamics: Collective radiance and photon-photon correlations. *Rev. Mod. Phys.*, 95:015002, Mar 2023.

[24] Q. A. Turchette, C. J. Hood, W. Lange, H. Mabuchi, and H. J. Kimble. Measurement of conditional phase shifts for quantum logic. *Phys. Rev. Lett.*, 75:4710–4713, Dec 1995.

[25] Neil V. Corzo, Jérémy Raskop, Aveek Chandra, Alexandra S. Sheremet, Baptiste Gouraud, and Julien Laurat. Waveguide-coupled single collective excitation of atomic arrays. *Nature*, 566:359–362, Feb 2019.

[26] J. I. Cirac, P. Zoller, H. J. Kimble, and H. Mabuchi. Quantum state transfer and entanglement distribution among distant nodes in a quantum network. *Phys. Rev. Lett.*, 78:3221–3224, Apr 1997.

[27] A. D. Boozer, A. Boca, R. Miller, T. E. Northup, and H. J. Kimble. Reversible state transfer between light and a single trapped atom. *Phys. Rev. Lett.*, 98:193601, May 2007.

[28] Shinichi Sunami, Shiro Tamiya, Ryotaro Inoue, Hayata Yamasaki, and Akihisa Goban. Scalable networking of neutral-atom qubits: Nanofiber-based approach for multiprocessor fault-tolerant quantum computers. *PRX Quantum*, 6:010101, Feb 2025.

[29] J. E. Hoffman, S. Ravets, J. A. Grover, P. Solano, P. R. Kordell, J. D. Wong-Campos, L. A. Orozco, and S. L. Rolston. Ultrahigh transmission optical nanofibers. *AIP Advances*, 4(6):067124, Jun 2014.

[30] Wenchao Ge, Kurt Jacobs, Zachary Eldredge, Alexey V. Gorshkov, and Michael Foss-Feig. Distributed quantum metrology with linear networks and separable inputs. *Phys. Rev. Lett.*, 121:043604, Jul 2018.

[31] H J Kimble. Strong interactions of single atoms and photons in cavity qed. *Physica Scripta*, 1998(T76):127, jan 1998.

[32] Haruka Tanji-Suzuki, Ian D. Leroux, Monika H. Schleier-Smith, Marko Cetina, Andrew T. Grier, Jonathan Simon, and Vladan Vuletić. Chapter 4 - interaction between atomic ensembles and optical resonators: Classical description. In E. Arimondo, P.R. Berman, and C.C. Lin, editors, *Advances in Atomic, Molecular, and Optical Physics*, volume 60 of *Advances In Atomic, Molecular, and Optical Physics*, pages 201–237. Academic Press, 2011.

[33] Fam Le Kien and K. Hakuta. Cooperative enhancement of channeling of emission from atoms into a nanofiber. *Phys. Rev. A*, 77:013801, Jan 2008.

[34] K C Kao and T W Davies. Spectrophotometric studies of ultra low loss optical glasses i: single beam method. *Journal of Physics E: Scientific Instruments*, 1(11):1063, nov 1968.

[35] F. P. Kapron, D. B. Keck, and R. D. Maurer. Radiation losses in glass optical waveguides. *Applied Physics Letters*, 17(10):423–425, Nov 1970.

[36] S. Y. Siew, B. Li, F. Gao, H. Y. Zheng, W. Zhang, P. Guo, S. W. Xie, A. Song, B. Dong, L. W. Luo, C. Li, X. Luo, and G.-Q. Lo. Review of silicon photonics technology and platform development. *Journal of Lightwave Technology*, 39(13):4374–4389, 2021.

[37] Xing-Liang Dong, Peng-Bo Li, Zongping Gong, and Franco Nori. Waveguide qed with dissipative light-matter couplings. *Phys. Rev. Res.*, 7:L012036, Feb 2025.

[38] Hannes Pichler and Peter Zoller. Photonic circuits with time delays and quantum feedback. *Phys. Rev. Lett.*, 116:093601, Mar 2016.

[39] Hannes Pichler, Soonwon Choi, Peter Zoller, and Mikhail D. Lukin. Universal photonic quantum computation via time-delayed feedback. *Proceedings of the National Academy of Sciences*, 114(43):11362–11367, 2017.

[40] J. D. Thompson, T. G. Tiecke, N. P. de Leon, J. Feist, A. V. Akimov, M. Gullans, A. S. Zibrov, V. Vuletić, and M. D. Lukin. Coupling a single trapped atom to a nanoscale optical cavity. *Science*, 340(6137):1202–1205, Jun 2013.

[41] A. Goban, C.-L. Hung, S.-P. Yu, J.D. Hood, J.A. Muniz, J.H. Lee, M.J. Martin, A.C. McClung, K.S. Choi, D.E. Chang, O. Painter, and H.J. Kimble. Atom–light interactions in photonic crystals. *Nature Communications*, 5:3808, May 2014.

[42] A. Goban, C.-L. Hung, J. D. Hood, S.-P. Yu, J. A. Muniz, O. Painter, and H. J. Kimble. Superradiance for atoms trapped along a photonic crystal waveguide. *Phys. Rev. Lett.*, 115:063601, Aug 2015.

[43] Jed Rowland, Christopher Perrella, Andre N. Luiten, Rafal Gartman, Krzysztof T. Kaczmarek, Joshua Nunn, and Ben M. Sparkes. High-bandwidth warm-atom quantum memory using hollow-core photonic crystal fibers. *Phys. Rev. Appl.*, 21:014048, Jan 2024.

[44] Michael R Sprague, Duncan G England, Amir Abdolvand, Joshua Nunn, Xian-Min Jin, W Steven Kolthammer, Marco Barbieri, Bruno Rigal, Patrick S Michelberger, Tessa F M Champion, Philip St J Russell, and Ian A Walmsley. Efficient optical pumping and high optical depth in a hollow-core photonic-crystal fibre for a broadband quantum memory. *New Journal of Physics*, 15(5):055013, may 2013.

[45] T. Lund-Hansen, S. Stobbe, B. Julsgaard, H. Thyrrestrup, T. Sünner, M. Kamp, A. Forchel, and P. Lodahl. Experimental realization of highly efficient broadband coupling of single quantum dots to a photonic crystal waveguide. *Phys. Rev. Lett.*, 101:113903, Sep 2008.

[46] Marijn A. M. Versteegh, Michael E. Reimer, Klaus D. Jöns, Dan Dalacu, Philip J. Poole, Angelo Gulinatti, Andrea Giudice, and Val Zwiller. Observation of strongly entangled photon pairs from a nanowire quantum dot. *Nature Communications*, 5:5298, Oct 2014.

[47] L. Scarpelli, B. Lang, F. Masia, D. M. Beggs, E. A. Muljarov, A. B. Young, R. Oulton, M. Kamp, S. Höfling, C. Schneider, and W. Langbein. 99 *Phys. Rev. B*, 100:035311, Jul 2019.

[48] Hanna Le Jeannic, Tomás Ramos, Signe F. Simonsen, Tommaso Pregnolato, Zhe Liu, Rüdiger Schott, Andreas D. Wieck, Arne Ludwig, Nir Rotenberg, Juan José García-Ripoll, and Peter Lodahl. Experimental reconstruction of the few-photon nonlinear scattering matrix from a single quantum dot in a nanophotonic waveguide. *Phys. Rev. Lett.*, 126:023603, Jan 2021.

[49] Hanna Le Jeannic, Alexey Tiranov, Jacques Carolan, Tomás Ramos, Ying Wang, Martin Hayhurst Appel, Sven Scholz, Andreas D. Wieck, Arne Ludwig, Nir Rotenberg, Leonardo Midolo, Juan José García-Ripoll, Anders S. Sørensen, and Peter Lodahl. Dynamical photon–photon interaction mediated by a quantum emitter. *Nature Physics*, 18:1191–1195, Oct 2022.

[50] A. Sipahigil, R. E. Evans, D. D. Sukachev, M. J. Burek, J. Borregaard, M. K. Bhaskar, C. T. Nguyen, J. L. Pacheco, H. A. Atikian, C. Meuwly, R. M. Camacho, F. Jelezko, E. Bielejec,

H. Park, M. Lončar, and M. D. Lukin. An integrated diamond nanophotonics platform for quantum-optical networks. *Science*, 354(6314):847–850, 2016.

[51] M. K. Bhaskar, D. D. Sukachev, A. Sipahigil, R. E. Evans, M. J. Burek, C. T. Nguyen, L. J. Rogers, P. Siyushev, M. H. Metsch, H. Park, F. Jelezko, M. Lončar, and M. D. Lukin. Quantum nonlinear optics with a germanium-vacancy color center in a nanoscale diamond waveguide. *Phys. Rev. Lett.*, 118:223603, May 2017.

[52] Carlo Bradac, Weibo Gao, Jacopo Forneris, Matthew E. Trusheim, and Igor Aharonovich. Quantum nanophotonics with group iv defects in diamond. *Nature Communications*, 10:5625, Dec 2019.

[53] A. Wallraff, D. I. Schuster, A. Blais, L. Frunzio, R.-S. Huang, J. Majer, S. Kumar, S. M. Girvin, and R. J. Schoelkopf. Strong coupling of a single photon to a superconducting qubit using circuit quantum electrodynamics. *Nature*, 431:162–167, Sep 2004.

[54] Mohammad Mirhosseini, Eunjong Kim, Xueyue Zhang, Alp Sipahigil, Paul B. Dieterle, Andrew J. Keller, Ana Asenjo-Garcia, Darrick E. Chang, and Oskar Painter. Cavity quantum electrodynamics with atom-like mirrors. *Nature*, 569:692–697, May 2019.

[55] P. Solano, P. Barberis-Blostein, F. K. Fatemi, L. A. Orozco, and S. L. Rolston. Superradiance reveals infinite-range dipole interactions through a nanofiber. *Nature Communications*, 8:1857, Nov 2017.

[56] Arjan F. van Loo, Arkady Fedorov, Kevin Lalumière, Barry C. Sanders, Alexandre Blais, and Andreas Wallraff. Photon-mediated interactions between distant artificial atoms. *Science*, 342(6165):1494–1496, 2013.

[57] Zhen Wang, Hekang Li, Wei Feng, Xiaohui Song, Chao Song, Wuxin Liu, Qiujiang Guo, Xu Zhang, Hang Dong, Dongning Zheng, H. Wang, and Da-Wei Wang. Controllable switching between superradiant and subradiant states in a 10-qubit superconducting circuit. *Phys. Rev. Lett.*, 124:013601, Jan 2020.

[58] Kazuki Koshino, Shingo Kono, and Yasunobu Nakamura. Protection of a qubit via subradiance: A josephson quantum filter. *Phys. Rev. Appl.*, 13:014051, Jan 2020.

[59] S. J. Srinivasan, A. J. Hoffman, J. M. Gambetta, and A. A. Houck. Tunable coupling in circuit quantum electrodynamics using a superconducting charge qubit with a v-shaped energy level diagram. *Phys. Rev. Lett.*, 106:083601, Feb 2011.

[60] D. E. Chang, J. I. Cirac, and H. J. Kimble. Self-organization of atoms along a nanophotonic waveguide. *Phys. Rev. Lett.*, 110:113606, Mar 2013.

[61] Zachary Eldredge, Pablo Solano, Darrick Chang, and Alexey V. Gorshkov. Self-organization of atoms coupled to a chiral reservoir. *Phys. Rev. A*, 94:053855, Nov 2016.

[62] A. Gonzalez-Tudela, D. Martin-Cano, E. Moreno, L. Martin-Moreno, C. Tejedor, and F. J. Garcia-Vidal. Entanglement of two qubits mediated by one-dimensional plasmonic waveguides. *Phys. Rev. Lett.*, 106:020501, Jan 2011.

[63] Ephraim Shahmoon and Gershon Kurizki. Nonradiative interaction and entanglement between distant atoms. *Phys. Rev. A*, 87:033831, Mar 2013.

[64] Anton Frisk Kockum, Per Delsing, and Göran Johansson. Designing frequency-dependent relaxation rates and lamb shifts for a giant artificial atom. *Phys. Rev. A*, 90:013837, Jul 2014.

[65] Bharath Kannan, Max J. Ruckriegel, Daniel L. Campbell, Anton Frisk Kockum, Jochen Braumüller, David K. Kim, Morten Kjaergaard, Philip Krantz, Alexander Melville, Bethany M. Niedzielski, Antti Vepsäläinen, Roni Winik, Jonilyn L. Yoder, Franco Nori, Terry P. Orlando, Simon Gustavsson, and William D. Oliver. Waveguide quantum electrodynamics with superconducting artificial giant atoms. *Nature*, 583:775–779, Jul 2020.

[66] P. W. Milonni and P. L. Knight. Retardation in the resonant interaction of two identical atoms. *Phys. Rev. A*, 10:1096–1108, Oct 1974.

[67] Kanupriya Sinha, Pierre Meystre, Elizabeth A. Goldschmidt, Fredrik K. Fatemi, S. L. Rolston, and Pablo Solano. Non-markovian collective emission from macroscopically separated emitters. *Phys. Rev. Lett.*, 124:043603, Jan 2020.

[68] Kanupriya Sinha, Alejandro González-Tudela, Yong Lu, and Pablo Solano. Collective radiation from distant emitters. *Phys. Rev. A*, 102:043718, Oct 2020.

[69] Lei Qiao and Chang-Pu Sun. Atom-photon bound states and non-markovian cooperative dynamics in coupled-resonator waveguides. *Phys. Rev. A*, 100:063806, Dec 2019.

[70] Giuseppe Calajó, Yao-Lung L. Fang, Harold U. Baranger, and Francesco Ciccarello. Exciting a bound state in the continuum through multiphoton scattering plus delayed quantum feedback. *Phys. Rev. Lett.*, 122:073601, Feb 2019.

[71] Michael J. Morrissey, Kieran Deasy, Mary Frawley, Ravi Kumar, Eugen Prel, Laura Russell, Viet Giang Truong, and Síle Nic Chormaic. Spectroscopy, manipulation and trapping of neutral atoms, molecules, and other particles using optical nanofibers: A review. *Sensors*, 13(8):10449–10481, 2013.

[72] Thomas Nieddu, Vandna Gokhroo, and Síle Nic Chormaic. Optical nanofibres and neutral atoms. *Journal of Optics*, 18(5):053001, March 2016. Publisher: IOP Publishing.

[73] Pablo Solano, Jeffrey A. Grover, Jonathan E. Hoffman, Sylvain Ravets, Fredrik K. Fatemi, Luis A. Orozco, and Steven L. Rolston. Chapter seven - optical nanofibers: A new platform for quantum optics. volume 66 of *Advances In Atomic, Molecular, and Optical Physics*, pages 439–505. Academic Press, 2017.

[74] Kali P Nayak, Mark Sadgrove, Ramachandrarao Yalla, Fam Le Kien, and Kohzo Hakuta. Nanofiber quantum photonics. *Journal of Optics*, 20(7):073001, jun 2018.

[75] Wenfang Li, Dylan Brown, Alexey Vylegzhanin, Zohreh Shahrabifarahani, Aswathy Raj, Jinjin Du, and Síle Nic Chormaic. Atom-light interactions using optical nanofibres—a perspective. *Journal of Physics: Photonics*, 6(2):021002, apr 2024.

[76] V. V. Klimov and M. Ducloy. Spontaneous emission rate of an excited atom placed near a nanofiber. *Phys. Rev. A*, 69:013812, Jan 2004.

[77] Fam Le Kien, S. Dutta Gupta, V. I. Balykin, and K. Hakuta. Spontaneous emission of a cesium atom near a nanofiber: Efficient coupling of light to guided modes. *Phys. Rev. A*, 72:032509, Sep 2005.

[78] K. P. Nayak, P. N. Melentiev, M. Morinaga, Fam Le Kien, V. I. Balykin, and K. Hakuta. Optical nanofiber as an efficient tool for manipulating and probing atomic fluorescence. *Opt. Express*, 15(9):5431–5438, Apr 2007.

[79] G. Sagué, E. Vetsch, W. Alt, D. Meschede, and A. Rauschenbeutel. Cold-atom physics using ultrathin optical fibers: Light-induced dipole forces and surface interactions. *Phys. Rev. Lett.*, 99:163602, Oct 2007.

[80] Shinya Kato and Takao Aoki. Strong coupling between a trapped single atom and an all-fiber cavity. *Phys. Rev. Lett.*, 115:093603, Aug 2015.

[81] E. Vetsch, D. Reitz, G. Sagué, R. Schmidt, S. T. Dawkins, and A. Rauschenbeutel. Optical interface created by laser-cooled atoms trapped in the evanescent field surrounding an optical nanofiber. *Phys. Rev. Lett.*, 104:203603, May 2010.

[82] A. Goban, K. S. Choi, D. J. Alton, D. Ding, C. Lacroûte, M. Pototschnig, T. Thiele, N. P. Stern, and H. J. Kimble. Demonstration of a state-insensitive, compensated nanofiber trap. *Phys. Rev. Lett.*, 109:033603, Jul 2012.

[83] Pablo Solano, Fredrik K. Fatemi, Luis A. Orozco, and S. L. Rolston. Dynamics of trapped atoms around an optical nanofiber probed through polarimetry. *Opt. Lett.*, 42(12):2283–2286, Jun 2017.

[84] S. T. Dawkins, R. Mitsch, D. Reitz, E. Vetsch, and A. Rauschenbeutel. Dispersive optical interface based on nanofiber-trapped atoms. *Phys. Rev. Lett.*, 107:243601, Dec 2011.

[85] Zigeng Li, Xiaomiao Li, and Xiaolan Zhong. Strong photon blockade in an all-fiber emitter-cavity quantum electrodynamics system. *Phys. Rev. A*, 103:043724, Apr 2021.

[86] Limin Tong, Rafael R. Gattass, Jonathan B. Ashcom, Sailing He, Jingyi Lou, Mengyan Shen, Iva Maxwell, and Eric Mazur. Subwavelength-diameter silica wires for low-loss optical wave guiding. *Nature*, 426:816–819, Dec 2003.

[87] S.W. Harun, K.S. Lim, C.K. Tio, K. Dimyati, and H. Ahmad. Theoretical analysis and fabrication of tapered fiber. *Optik*, 124(6):538–543, 2013.

[88] Gilberto Brambilla, Vittoria Finazzi, and David J. Richardson. Ultra-low-loss optical fiber nanotapers. *Opt. Express*, 12(10):2258–2263, May 2004.

[89] G. Brambilla, Y. Jung, and F. Renna. Optical fiber microwires and nanowires manufactured by modified flame brushing technique: properties and applications. *Frontiers of Optoelectronics in China*, 3:61–66, Mar 2010.

[90] Jonathan M. Ward, Danny G. O'Shea, Brian J. Shortt, Michael J. Morrissey, Kieran Deasy, and Síle G. Nic Chormaic. Heat-and-pull rig for fiber taper fabrication. *Review of Scientific Instruments*, 77(8):083105, Aug 2006.

[91] Lu Ding, Cherif Belacel, Sara Ducci, Giuseppe Leo, and Ivan Favero. Ultralow loss single-mode silica tapers manufactured by a microheater. *Appl. Opt.*, 49(13):2441–2445, May 2010.

[92] Lei Shi, Xianfeng Chen, Hongjuan Liu, Yuping Chen, Zhiqing Ye, Weijun Liao, and Yuxing Xia. Fabrication of submicron-diameter silica fibers using electric strip heater. *Opt. Express*, 14(12):5055–5060, Jun 2006.

[93] Jihao Jia, Felix Tebbenjohanns, Thomas Hoinkes, Jürgen Volz, Arno Rauschenbeutel, and Philipp Schneeweiss. Measuring deviations from a perfectly circular cross-section of an optical nanofiber at the Ångström scale, 2025.

[94] J.D. Love and W.M. Henry. Quantifying loss minimisation in single-mode fibre tapers. *Electronics Letters*, 22:912–914, 1986.

[95] T.A. Birks and Y.W. Li. The shape of fiber tapers. *Journal of Lightwave Technology*, 10(4):432–438, 1992.

[96] Simon J. Evered, Dolev Bluvstein, Marcin Kalinowski, Sepehr Ebadi, Tom Manovitz, Hengyun Zhou, Sophie H. Li, Alexandra A. Geim, Tout T. Wang, Nishad Maskara, Harry Levine, Giulia Semeghini, Markus Greiner, Vladan Vuletić, and Mikhail D. Lukin. High-fidelity parallel entangling gates on a neutral-atom quantum computer. *Nature*, 622:268–272, Oct 2023.

[97] Jian Wang, Dong-Yu Huang, Xiao-Long Zhou, Ze-Min Shen, Si-Jian He, Qi-Yang Huang, Yi-Jia Liu, Chuan-Feng Li, and Guang-Can Guo. Ultrafast high-fidelity state readout of single neutral atom. *Phys. Rev. Lett.*, 134:240802, Jun 2025.

[98] E. Stourm, M. Lepers, J. Robert, S. Nic Chormaic, K. Mølmer, and E. Brion. Spontaneous emission and energy shifts of a rydberg rubidium atom close to an optical nanofiber. *Phys. Rev. A*, 101:052508, May 2020.

[99] Krishnapriya Subramonian Rajasree, Tridib Ray, Kristoffer Karlsson, Jesse L. Everett, and Síle Nic Chormaic. Generation of cold rydberg atoms at submicron distances from an optical nanofiber. *Phys. Rev. Res.*, 2:012038, Feb 2020.

[100] Alexey Vylegzhanin, Dylan J. Brown, Aswathy Raj, Danil F. Kornovan, Jesse L. Everett, Etienne Brion, Jacques Robert, and Síle Nic Chormaic. Excitation of 87rb rydberg atoms to ns and nd states ($n \leq 68$) via an optical nanofiber. *Optica Quantum*, 1(1):6–13, Oct 2023.

[101] R. Mitsch, C. Sayrin, B. Albrecht, P. Schneeweiss, and A. Rauschenbeutel. Quantum state-controlled directional spontaneous emission of photons into a nanophotonic waveguide. *Nature Communications*, 5:5713, Dec 2014.

[102] Peter Lodahl, Sahand Mahmoodian, Søren Stobbe, Arno Rauschenbeutel, Philipp Schneeweiss, Jürgen Volz, Hannes Pichler, and Peter Zoller. Chiral quantum optics. *Nature*, 541:473–480, Jan 2017.

[103] Jan Petersen, Jürgen Volz, and Arno Rauschenbeutel. Chiral nanophotonic waveguide interface based on spin-orbit interaction of light. *Science*, 346(6205):67–71, 2014.

[104] Tridib Ray, Ratnesh K Gupta, Vandna Gokhroo, Jesse L Everett, Thomas Nieddu, Krishnapriya S Rajasree, and Síle Nic Chormaic. Observation of the 87rb 5s1/2 to 4d3/2 electric quadrupole transition at 516.6 nm mediated via an optical nanofibre. *New Journal of Physics*, 22(6):062001, jun 2020.

[105] S. M. Hendrickson, M. M. Lai, T. B. Pittman, and J. D. Franson. Observation of two-photon absorption at low power levels using tapered optical fibers in rubidium vapor. *Phys. Rev. Lett.*, 105:173602, Oct 2010.

[106] S. M. Spillane, G. S. Pati, K. Salit, M. Hall, P. Kumar, R. G. Beausoleil, and M. S. Shahriar. Observation of nonlinear optical interactions of ultralow levels of light in a tapered optical nanofiber embedded in a hot rubidium vapor. *Phys. Rev. Lett.*, 100:233602, Jun 2008.

[107] Jianbin Zhang, Yi Kang, Xin Guo, Yuhang Li, Keying Liu, Yu Xie, Hao Wu, Dawei Cai, Jue Gong, Zhangxing Shi, Yingying Jin, Pan Wang, Wei Fang, Lei Zhang, and Limin Tong. High-power continuous-wave optical waveguiding in a silica micro/nanofibre. *Light: Science & Applications*, 12:89, Apr 2023.

[108] Neil V. Corzo, Baptiste Gouraud, Aveek Chandra, Akihisa Goban, Alexandra S. Sheremet, Dmitriy V. Kupriyanov, and Julien Laurat. Large bragg reflection from one-dimensional chains of trapped atoms near a nanoscale waveguide. *Phys. Rev. Lett.*, 117:133603, Sep 2016.

[109] Riccardo Pennetta, Martin Blaha, Aisling Johnson, Daniel Lechner, Philipp Schneeweiss, Jürgen Volz, and Arno Rauschenbeutel. Collective radiative dynamics of an ensemble of cold atoms coupled to an optical waveguide. *Phys. Rev. Lett.*, 128:073601, Feb 2022.

[110] D E Chang, L Jiang, A V Gorshkov, and H J Kimble. Cavity qed with atomic mirrors. *New Journal of Physics*, 14(6):063003, jun 2012.

[111] H. L. Sørensen, J.-B. Béguin, K. W. Kluge, I. Iakoupov, A. S. Sørensen, J. H. Müller, E. S. Polzik, and J. Appel. Coherent backscattering of light off one-dimensional atomic strings. *Phys. Rev. Lett.*, 117:133604, Sep 2016.

[112] Christian Liedl, Felix Tebbenjohanns, Constanze Bach, Sebastian Pucher, Arno Rauschenbeutel, and Philipp Schneeweiss. Observation of superradiant bursts in a cascaded quantum system. *Phys. Rev. X*, 14:011020, Feb 2024.

[113] R. H. Dicke. Coherence in spontaneous radiation processes. *Phys. Rev.*, 93:99–110, Jan 1954.

[114] M. Gross and S. Haroche. Superradiance: An essay on the theory of collective spontaneous emission. *Physics Reports*, 93(5):301–396, 1982.

[115] Marlan O. Scully, Edward S. Fry, C. H. Raymond Ooi, and Krzysztof Wódkiewicz. Directed spontaneous emission from an extended ensemble of n atoms: Timing is everything. *Phys. Rev. Lett.*, 96:010501, Jan 2006.

[116] Marlan O. Scully and Anatoly A. Svidzinsky. The super of superradiance. *Science*, 325(5947):1510–1511, 2009.

[117] J. P. Clemens, L. Horvath, B. C. Sanders, and H. J. Carmichael. Collective spontaneous emission from a line of atoms. *Phys. Rev. A*, 68:023809, Aug 2003.

[118] J. Eschner, Ch. Raab, F. Schmidt-Kaler, and R. Blatt. Light interference from single atoms and their mirror images. *Nature*, 413:495–498, Oct 2001.

[119] D. Plankensteiner, L. Ostermann, H. Ritsch, and C. Genes. Selective protected state preparation of coupled dissipative quantum emitters. *Scientific Reports*, 5:16231, Nov 2015.

[120] Justin G. Bohnet, Zilong Chen, Joshua M. Weiner, Dominic Meiser, Murray J. Holland, and James K. Thompson. A steady-state superradiant laser with less than one intracavity photon. *Nature*, 484:78–81, Apr 2012.

[121] Y. K. Wang and F. T. Hioe. Phase transition in the dicke model of superradiance. *Phys. Rev. A*, 7:831–836, Mar 1973.

[122] Kristian Baumann, Christine Guerlin, Ferdinand Brennecke, and Tilman Esslinger. Dicke quantum phase transition with a superfluid gas in an optical cavity. *Nature*, 464:1301–1306, Apr 2010.

[123] Dasom Kim, Sohail Dasgupta, Xiaoxuan Ma, Joong-Mok Park, Hao-Tian Wei, Xinwei Li, Liang Luo, Jacques Doumani, Wanting Yang, Di Cheng, Richard H. J. Kim, Henry O. Everitt, Shojiro Kimura, Hiroyuki Nojiri, Jigang Wang, Shixun Cao, Motoaki Bamba, Kaden R. A. Hazzard, and Junichiro Kono. Observation of the magnonic dicke superradiant phase transition. *Science Advances*, 11(14):eadt1691, 2025.

[124] William Guerin, Michelle O. Araújo, and Robin Kaiser. Subradiance in a large cloud of cold atoms. *Phys. Rev. Lett.*, 116:083601, Feb 2016.

[125] S. J. Roof, K. J. Kemp, M. D. Havey, and I. M. Sokolov. Observation of single-photon superradiance and the cooperative lamb shift in an extended sample of cold atoms. *Phys. Rev. Lett.*, 117:073003, Aug 2016.

[126] Michelle O. Araújo, Ivor Krešić, Robin Kaiser, and William Guerin. Superradiance in a large and dilute cloud of cold atoms in the linear-optics regime. *Phys. Rev. Lett.*, 117:073002, Aug 2016.

[127] R. G. DeVoe and R. G. Brewer. Observation of superradiant and subradiant spontaneous emission of two trapped ions. *Phys. Rev. Lett.*, 76:2049–2052, Mar 1996.

[128] Michael Scheibner, Thomas Schmidt, Lukas Worschech, Alfred Forchel, Gerd Bacher, Thorsten Passow, and Detlef Hommel. Superradiance of quantum dots. *Nature Physics*, 3:106–110, Feb 2007.

[129] Alexey Tiranov, Vasiliki Angelopoulou, Cornelis Jacobus van Diepen, Björn Schrinski, Oliver August Dall'Alba Sandberg, Ying Wang, Leonardo Midolo, Sven Scholz, Andreas Dirk Wieck, Arne Ludwig, Anders Søndberg Sørensen, and Peter Lodahl. Collective super- and subradiant dynamics between distant optical quantum emitters. *Science*, 379(6630):389–393, 2023.

[130] A. Asenjo-Garcia, J. D. Hood, D. E. Chang, and H. J. Kimble. Atom-light interactions in quasi-one-dimensional nanostructures: A green's-function perspective. *Phys. Rev. A*, 95:033818, Mar 2017.

[131] Janne Ruostekoski and Juha Javanainen. Arrays of strongly coupled atoms in a one-dimensional waveguide. *Phys. Rev. A*, 96:033857, Sep 2017.

[132] Hashem Zoubi and Helmut Ritsch. Lifetime and emission characteristics of collective electronic excitations in two-dimensional optical lattices. *Phys. Rev. A*, 83:063831, Jun 2011.

[133] Eric Sierra, Stuart J. Masson, and Ana Asenjo-Garcia. Dicke superradiance in ordered lattices: Dimensionality matters. *Phys. Rev. Res.*, 4:023207, Jun 2022.

[134] Stuart J. Masson and Ana Asenjo-Garcia. Universality of dicke superradiance in arrays of quantum emitters. *Nature Communications*, 13:2285, Apr 2022.

[135] Janne Ruostekoski and Juha Javanainen. Emergence of correlated optics in one-dimensional waveguides for classical and quantum atomic gases. *Phys. Rev. Lett.*, 117:143602, Sep 2016.

[136] Hyok Sang Han, Ahreum Lee, Kanupriya Sinha, Fredrik K. Fatemi, and S. L. Rolston. Observation of vacuum-induced collective quantum beats. *Phys. Rev. Lett.*, 127:073604, Aug 2021.

[137] Xinchao Zhou, Hikaru Tamura, Tzu-Han Chang, and Chen-Lung Hung. Trapped atoms and superradiance on an integrated nanophotonic microring circuit. *Phys. Rev. X*, 14:031004, Jul 2024.

[138] Fam Le Kien, S. Dutta Gupta, K. P. Nayak, and K. Hakuta. Nanofiber-mediated radiative transfer between two distant atoms. *Phys. Rev. A*, 72:063815, Dec 2005.

[139] D. F. Kornovan, A. S. Sheremet, and M. I. Petrov. Collective polaritonic modes in an array of two-level quantum emitters coupled to an optical nanofiber. *Phys. Rev. B*, 94:245416, Dec 2016.

[140] A. Asenjo-Garcia, M. Moreno-Cardoner, A. Albrecht, H. J. Kimble, and D. E. Chang. Exponential improvement in photon storage fidelities using subradiance and "selective radiance" in atomic arrays. *Phys. Rev. X*, 7:031024, Aug 2017.

[141] D. F. Kornovan, N. V. Corzo, J. Laurat, and A. S. Sheremet. Extremely subradiant states in a periodic one-dimensional atomic array. *Phys. Rev. A*, 100:063832, Dec 2019.

[142] Robert J. Bettles, Simon A. Gardiner, and Charles S. Adams. Cooperative eigenmodes and scattering in one-dimensional atomic arrays. *Phys. Rev. A*, 94:043844, Oct 2016.

[143] R. T. Sutherland and F. Robicheaux. Collective dipole-dipole interactions in an atomic array. *Phys. Rev. A*, 94:013847, Jul 2016.

[144] H. P. Breuer and F. Petruccione. *The theory of open quantum systems*. Oxford University Press, 2002.

[145] Heinz-Peter Breuer, Elsi-Mari Laine, Jyrki Piilo, and Bassano Vacchini. Colloquium: Non-markovian dynamics in open quantum systems. *Rev. Mod. Phys.*, 88:021002, Apr 2016.

[146] Inés de Vega and Daniel Alonso. Dynamics of non-markovian open quantum systems. *Rev. Mod. Phys.*, 89:015001, Jan 2017.

[147] Haiyang Zhang, Xiaoxiang Han, Guoqing Zhang, Lianbi Li, Lin Cheng, Jun Wang, Yunjie Zhang, Yanwen Xia, and Caijuan Xia. Non-markovian noise mitigation in quantum teleportation: enhancing fidelity and entanglement. *Scientific Reports*, 14:23885, Oct 2024.

[148] Tomás Ramos, Benoît Vermersch, Philipp Hauke, Hannes Pichler, and Peter Zoller. Non-markovian dynamics in chiral quantum networks with spins and photons. *Phys. Rev. A*, 93:062104, Jun 2016.

[149] R. J. Cook and P. W. Milonni. Quantum theory of an atom near partially reflecting walls. *Phys. Rev. A*, 35:5081–5087, Jun 1987.

[150] U. Dorner and P. Zoller. Laser-driven atoms in half-cavities. *Phys. Rev. A*, 66:023816, Aug 2002.

[151] Tommaso Tufarelli, M. S. Kim, and Francesco Ciccarello. Non-markovianity of a quantum emitter in front of a mirror. *Phys. Rev. A*, 90:012113, July 2014.

[152] Emil Raaholt Ingelsten, Anton Frisk Kockum, and Ariadna Soro. Avoiding decoherence with giant atoms in a two-dimensional structured environment. *Phys. Rev. Res.*, 6:043222, Dec 2024.

[153] Ahreum Lee, Hyok Sang Han, Fredrik K. Fatemi, S. L. Rolston, and Kanu Sinha. Collective quantum beats from distant multilevel emitters. *Phys. Rev. A*, 107:013701, Jan 2023.

[154] Hyok Sang Han, Ahreum Lee, Sarthak Subhankar, S. L. Rolston, and Fredrik K. Fatemi. Optical lattices with variable spacings generated by binary phase transmission gratings. *Opt. Express*, 33(2):3013–3020, Jan 2025.

[155] Jonathan E. Hoffman. Optical nanofiber fabrication and analysis towards coupling atoms to superconducting qubits. 2014.

[156] Jeffrey A. Grover. Atom-trapping and photon-counting experiments with optical nanofibers. 2015.

[157] Wolfgang Petrich, Michael H. Anderson, Jason R. Ensher, and Eric A. Cornell. Behavior of atoms in a compressed magneto-optical trap. *J. Opt. Soc. Am. B*, 11(8):1332–1335, Aug 1994.

[158] Daniel A. Steck. "Rubidium 85 D Line Data," available online at `http://steck.us/alkalidata`. (revision 2.2.1, 21 November 2019).

[159] P. T. Starkey, C. J. Billington, S. P. Johnstone, M. Jasperse, K. Helmerson, L. D. Turner, and R. P. Anderson. A scripted control system for autonomous hardware-timed experiments. *Review of Scientific Instruments*, 84(8):085111, Aug 2013.

[160] E. T. Jaynes in. *Foundations of Radiation Theory and Quantum Electrodynamics*. Springer US, Boston, MA, 1980.

[161] S. Haroche, J. A. Paisner, and A. L. Schawlow. Hyperfine quantum beats observed in cs vapor under pulsed dye laser excitation. *Phys. Rev. Lett.*, 30:948–951, May 1973.

[162] C. G. Wade, N. Šibalić, J. Keaveney, C. S. Adams, and K. J. Weatherill. Probing an excited-state atomic transition using hyperfine quantum-beat spectroscopy. *Phys. Rev. A*, 90:033424, Sep 2014.

[163] E. Hack and J. R. Huber. Quantum beat spectroscopy of molecules. *International Reviews in Physical Chemistry*, 10(3):287–317, 1991.

[164] H. Stolz, V. Langer, E. Schreiber, S. Permogorov, and W. von der Osten. Picosecond quantum-beat spectroscopy of bound excitons in cds. *Phys. Rev. Lett.*, 67:679–682, Aug 1991.

[165] I. E. Kozin, V. G. Davydov, I. V. Ignatiev, A. V. Kavokin, K. V. Kavokin, G. Malpuech, Hong-Wen Ren, M. Sugisaki, S. Sugou, and Y. Masumoto. Zero-field spin quantum beats in charged quantum dots. *Phys. Rev. B*, 65:241312(R), Jun 2002.

[166] J. Bylsma, P. Dey, J. Paul, S. Hoogland, E. H. Sargent, J. M. Luther, M. C. Beard, and D. Karaiskaj. Quantum beats due to excitonic ground-state splitting in colloidal quantum dots. *Phys. Rev. B*, 86:125322, Sep 2012.

[167] Gerhard C. Hegerfeldt and Martin B. Plenio. Coherence with incoherent light: A new type of quantum beat for a single atom. *Phys. Rev. A*, 47:2186–2190, Mar 1993.

[168] G. C. Hegerfeldt and M. B. Plenio. Quantum beats revisited: a quantum jump approach. *Quantum Opt.*, 6:15, 1994.

[169] T. P. Altenmuller. Are there quantum beats from vacuum-induced coherence. *Zeit. fur Physik D*, 34:157, 1995.

[170] Zhiming Wu, Jiahua Li, and Ying Wu. Vacuum-induced quantum-beat-enabled photon antibunching. *Phys. Rev. A*, 108:023727, Aug 2023.

[171] Zhiming Wu, Jiahua Li, and Ying Wu. Phase-engineered photon correlations in weakly coupled nanofiber cavity qed. *Phys. Rev. A*, 109:033709, Mar 2024.

[172] Maximilian Zanner, Tuure Orell, Christian M. F. Schneider, Romain Albert, Stefan Oleschko, Mathieu L. Juan, Matti Silveri, and Gerhard Kirchmair. Coherent control of a multi-qubit dark state in waveguide quantum electrodynamics. *Nature Physics*, 18:538–543, May 2022.

[173] K. Sinha, P. Meystre, and P. Solano. Non-markovian dynamics of collective atomic states coupled to a waveguide. *Nanophotonic Materials, Devices, and Systems*, 11091:53 – 59, 2019.

[174] Francois Dubin, Daniel Rotter, Manas Mukherjee, Carlos Russo, Jürgen Eschner, and Rainer Blatt. Photon correlation versus interference of single-atom fluorescence in a half-cavity. *Phys. Rev. Lett.*, 98:183003, May 2007.

[175] H. J. Kimble, M. Dagenais, and L. Mandel. Multiatom and transit-time effects on photon-correlation measurements in resonance fluorescence. *Phys. Rev. A*, 18:201–207, July 1978.

[176] H J Carmichael, P Drummond, P Meystre, and D F Walls. Intensity correlations in resonance fluorescence with atomic number fluctuations. *Journal of Physics A: Mathematical and General*, 11(5):L121–L126, May 1978.

[177] Philippe Grangier, Gérard Roger, Alain Aspect, Antoine Heidmann, and Serge Reynaud. Observation of photon antibunching in phase-matched multiatom resonance fluorescence. *Phys. Rev. Lett.*, 57:687–690, Aug 1986.

[178] Fam Le Kien and K. Hakuta. Correlations between photons emitted by multiatom fluorescence into a nanofiber. *Phys. Rev. A*, 77:033826, Mar 2008.

[179] Markus Hennrich, Axel Kuhn, and Gerhard Rempe. Transition from antibunching to bunching in cavity qed. *Phys. Rev. Lett.*, 94:053604, Feb 2005.

[180] J. A. Grover, P. Solano, L. A. Orozco, and S. L. Rolston. Photon-correlation measurements of atomic-cloud temperature using an optical nanofiber. *Phys. Rev. A*, 92:013850, Jul 2015.

[181] Rodney Loudon. *The Quantum Theory of Light*. Oxford University Press, 2000.

[182] K. P. Nayak, Fam Le Kien, M. Morinaga, and K. Hakuta. Antibunching and bunching of photons in resonance fluorescence from a few atoms into guided modes of an optical nanofiber. *Phys. Rev. A*, 79:021801, Feb 2009.

[183] Fam Le Kien, V. I. Balykin, and K. Hakuta. Atom trap and waveguide using a two-color evanescent light field around a subwavelength-diameter optical fiber. *Phys. Rev. A*, 70:063403, Dec 2004.

[184] Kali P. Nayak, Jie Wang, and Jameesh Keloth. Real-time observation of single atoms trapped and interfaced to a nanofiber cavity. *Phys. Rev. Lett.*, 123:213602, Nov 2019.

[185] Rudolf Grimm, Matthias Weidemüller, and Yurii B. Ovchinnikov. Optical dipole traps for neutral atoms. volume 42 of *Advances In Atomic, Molecular, and Optical Physics*, pages 95–170. Academic Press, 2000.

[186] Paul D. Lett, Richard N. Watts, Christoph I. Westbrook, William D. Phillips, Phillip L. Gould, and Harold J. Metcalf. Observation of atoms laser cooled below the doppler limit. *Phys. Rev. Lett.*, 61:169–172, Jul 1988.

[187] J. Dalibard and C. Cohen-Tannoudji. Laser cooling below the doppler limit by polarization gradients: simple theoretical models. *J. Opt. Soc. Am. B*, 6(11):2023–2045, Nov 1989.

[188] Amnon Yariv and Pochi Yeh. *Photonics: Optical Electronics in Modern Communications*. Oxford University Press, 2007.

[189] Fam Le Kien, J.Q. Liang, K. Hakuta, and V.I. Balykin. Field intensity distributions and polarization orientations in a vacuum-clad subwavelength-diameter optical fiber. *Optics Communications*, 242(4):445–455, 2004.

[190] Eugen Vetsch. Optical interface based on a nanofiber atom-trap. 2010.

[191] Pablo Solano. Quantum optics in optical nanofibers. 2017.